Universidad de Cantabria

E.T.S Ingenieros de Caminos, Canales y Puertos

Dpto. de Ciencias y Técnicas del Agua y del Medio Ambiente

Doctoral Thesis

Metodología para la Predicción Numérica de Plumas de Flotabilidad Negativa Procedentes de Vertidos de Salmuera: Calibración y Validación con Datos Experimentales y de Campo

Methodology for the Numerical Prediction of Negatively-Buoyant Plumes from Brine Discharges. Calibration and Validation with Experimental and Field Data

Author:
Beatriz Pérez Díaz

Supervisors:
Dra. Sonia Castanedo Bárcena
Dra. Pilar Palomar Herrero

Environmental Hydraulics Institute "IH Cantabria"

June 2017

A mi familia

Don't believe what your eyes are telling you.
All they show is limitation.
Look with your understanding.
Find out what you already know and you will see the way to fly.

Richard Bach
Jonathan Livingston Seagull

Acknowledgements

Una vez acabada esta tesis, mirando atrás en el tiempo, me doy cuenta de que han sido muchas las personas que han participado en su desarrollo, tanto a nivel personal como a nivel profesional, a todas ellas, gracias.

En primer lugar, gracias a mis directoras de tesis, Sonia Castanedo y Pilar Palomar, por compartir conmigo sus conocimientos y experiencia, y por todos sus consejos. Sonia, gracias por tu confianza y apoyo a lo largo de estos años, gracias por orientarme, guiarme, y por estar siempre cerca con una sonrisa. Pilar, gracias por tu entusiasmo y tu energía, por ser tan humana y por hacerme "salir con ganas" de todas nuestras conversaciones. Quiero agradecer a Raúl Medina por darme la oportunidad de formar parte del IH Cantabria, y por estar siempre disponible para cualquiera de mis dudas. Agradezco también al Ministerio de Economía, Industría y Competitividad la beca de Formación de Personal Investigador que ha permitido la realización de esta tesis.

Parte fundamental de este trabajo ha sido desarrollado gracias al equipo de laboratorio, Ana Álvarez y Pilar Palomar. Gracias por todas las horas de trabajo duro bajo la luz del láser. Ana, especialmente agradecida contigo por no bajar el ritmo de ese trabajo, tan físico, en ningún momento; eres una heroína, ya no sólo para Teo.

Esta tesis no podría obtener la mención internacional sin mi estancia en el centro I+D HR Wallingford (Reino Unido), gracias a la ayuda del Ministerio de Economía, Industría y Competitividad para la realización de estancias predoctorales. I would like to thank the whole Hydrodynamics and Metocean group of HR Wallingford. Specially, thanks to Matthew Wood and Florence Henno, for make the placement possible, for their support and contributions and, above all, for being the perfect hosts. Thank you!

Quiero agradecer a todos los compañeros del IH Cantabria que de una u otra manera han estado presentes en este camino, haciendo que el trabajo sea más fácil. Gracias a todo el equipo de administración por su buen hacer; a Iñaki, Sheila, Rafa y Javi por su ayuda, siempre cargada de paciencia y buen humor; a Nico, Jorge y Bea por estar ahí desde tiempos camineros; y a María, Andrés, Pablo y Lucía por ser una mano amiga. Muchas gracias también a toda la tercera planta y, en especial, al grupo OCEANO por todos los buenos momentos vividos

y por los ánimos en esta última etapa. Javi G, gracias por esa cabeza que tienes, capaz de enlazar los temas más interesantes.

Agradecimientos también para Íñigo, Elsa y Paula, por ser parte de la sesión de risoterapia a nuestra particular hora del "tupper". Gracias por todos los temas inimaginables e inagotables de conversación, por todas las risas y el buen humor. A ti, Paula, gracias por cuidar de mi esta última temporada, por estar siempre pendiente y por haberme dejado descubrir lo especial que eres.

Por supuesto, gracias a todos los amigos con los que tan buenos ratos he pasado, ¡idos preparando para el ansiado verano de 2017!. Gracias a Elvi y Marta, por vuestras distintas y maravillosas formas de dar cariño. Zeng, a ti, gracias por ser tan buen compañero y abrirnos las puertas de tu casa, aquí tienes la tuya para siempre. Muchas gracias Manu, porque contigo es imposible aburrirse y por todo tu conocimiento bien trasmitido. A dos de mis "docto", Lara y Fátima, gracias por ser tan auténticas y ponerle corazón a todo. Gracias a Alba, por tu romántica racionalidad y por mostrarme un Mogro que ya no me imagino sin ti. Finalmente, y de forma muy especial, gracias a Chisco y Miri, para vosotros no creo que exista forma de expresar mi gratitud, habéis sido mis hermanos, mi oxígeno, gracias y mil veces gracias.

No puedo olvidarme de los amigos que siguen estando ahí, desde los distintos inicios universitarios: Ele, Nati, Jose, Patri y Belen. Gracias por estar siempre pendientes y por vuestras palabras de ánimo.

Gracias a mi gente: Rosa, Dero, Peru, Joa, Marta, Cris, Egüen y Ronny. Gracias por ser mi conexión con la realidad, por todo vuestro cariño y por estar siempre ahí. En particular, gracias a Dero, por ser mi compañera de aventuras y desventuras estudiantiles, y por tu opinión, siempre bien fundamentada; y a Rosa, gracias por haber aparecido aquella tarde de verano en mi casa y no haberte separado nunca de mi.

No puede faltar aquí el reconocimiento a mi familia, mis padres, mi hermano y mis tías, gracias por apoyarme siempre. A mis padres, gracias por ser ejemplo de esfuerzo y dedicación, que es y será el germen de cualquier meta que alcance en esta vida.

Y por último, gracias Paco, por tu generosidad incondicional, por tu paciencia infinita y por creer siempre en mi. Gracias por ser mi constante, mi calma, y en definitiva, por hacerme tan feliz.

Contents

List of Figures

List of Tables

Chapter 0

Resumen

De acuerdo con la normativa de estudios de doctorado de la Universidad de Cantabria en relación a los requerimientos exigidos para aquellas tesis redactadas en un idioma diferente al español, aprobada por Junta de Gobierno de 12 de marzo de 1999 y actualizada a 18 de diciembre de 2013, a continuación se presenta un resumen del documento original redactado en inglés. Dicho resumen condensa los aspectos más importantes del presente trabajo de investigación. A pesar de ello, dada la naturaleza propia de un resumen, este apartado no supone una traducción literal, por lo que se remite al lector a la versión en inglés para una información más detallada.

I. Introducción

I.A. Motivación y antecedentes

La escasez de agua en zonas costeras densamente pobladas ha promovido la construcción de numerosas plantas de desalinización de agua de mar para abastecer de agua dulce a la población local. Debido a ello, en las últimas décadas, la desalación se ha convertido en una alternativa fundamental a las fuentes convencionales de agua dulce en zonas como las regiones costeras del Mediterráneo y del Medio Oriente o la costa de California, China y Australia (Cánovas Cuenca (2012); Laspidou et al. (2010) y Dawoud and Al Mulla (2012)). Hoy en día, la tecnología de desalinización más ampliamente utilizada es la ósmosis inversa

(SWRO), cuyo principal subproducto es la salmuera, un efluente hipersalino habitualmente descargado en el mar. Dicho efluente constituye un potencial impacto negativo sobre ecosistemas marinos estenohalinos como la Posidonia (Lattemann and Höpner (2008); Sánchez-Lizaso et al. (2008) y Laspidou et al. (2010)), y, además, puede generar problemas de recirculación de la planta desaladora en el caso de que el mismo alcance la toma de agua de mar.

En décadas anteriores, debido a la ausencia de regulación con respecto a los vertidos de salmuera al mar, el tipo de descarga más comúnmente empleada ha sido la descarga superficial directa (véanse ejemplos de la Figura 0.1a). Sin embargo, en los últimos años, pruebas fehacientes del impacto nocivo de este tipo de vertidos sobre el medio marino han generado un aumento de las preocupaciones medioambientales. Como consecuencia, las plantas de desalinización construidas recientemente utilizan sistemas de descargas más sofisticados mediante chorros sumergidos inclinados (véanse ejemplos de la Figura 0.1b), los cuales favorecen la dilución de la salmuera gracias a la cantidad de movimiento generada por el propio chorro.

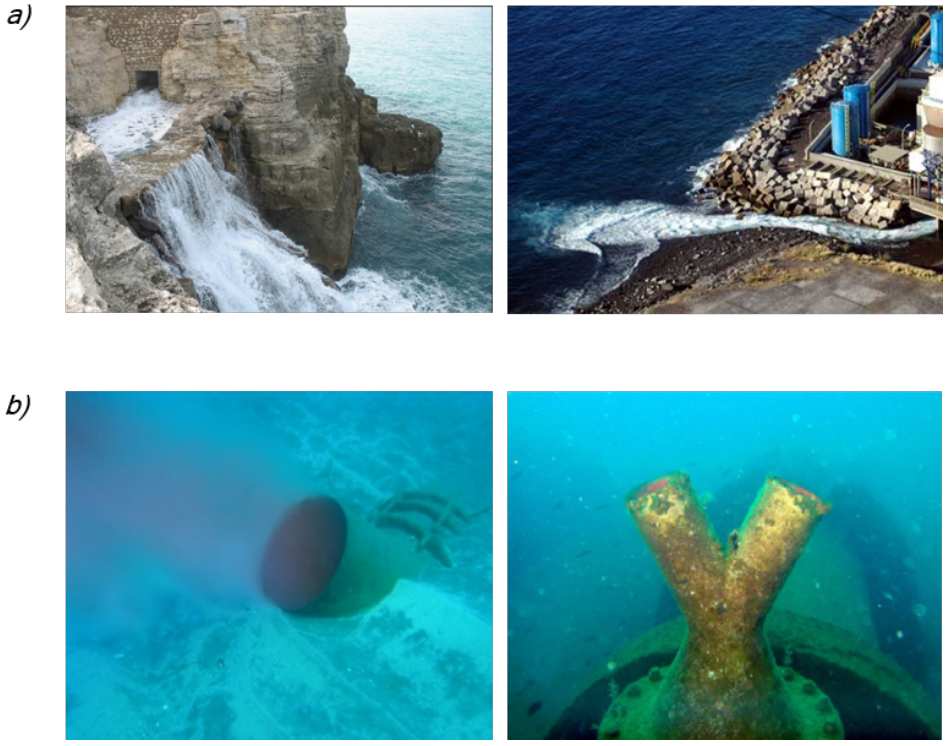

Figura 0.1: Configuraciones de vertidos de salmuera: a) descargas directas superficiales, b) descargas mediante chorros sumergidos inclinados. Ejemplos de plantas desaladoras españolas. Fuente: CEDEX, ITC, Taxón S.L

El comportamiento de las descargas de salmuera dentro del ambiente marino está gobernado por la flotabilidad negativa de la salmuera (es decir, por su mayor densidad que el agua circundante). Sin embargo, en el propio desarrollo y evolución del vertido se pueden diferenciar dos regiones principales en función de la proximidad al punto de descarga: la región de campo cercano y la región de campo lejano (comunmente denominadas regiones NF y FF por sus siglas en inglés: Near Field y Far Field). Habitualmente estas dos regiones se estudian de manera independiente debido a las diferentes escalas espaciales y temporales de los procesos de transporte y mezcla implicados (véase la Figura 0.2). La región de campo cercano se caracteriza por una mezcla inicial que depende de la configuración de la descarga de salmuera y de las propiedades intrínsecas tanto del efluente como del medio receptor (en este caso, el mar). En esta región, las características de flujo y mezcla están dominadas por pequeñas escalas ($\sim$ metros y $\sim$ minutos), y en ella se dan las tasas de dilución más altas debido a los efectos turbulentos de gran escala. Posteriormente, en la región de campo lejano la salmuera se transforma en una corriente de densidad que viaja por los fondos marinos con una pequeña tasa de dilución en comparación con la región de campo cercano. En este caso, la mezcla depende de las condiciones ambientales (batimetría, corrientes, oleaje, viento, etc.) y las diferencias entre las propiedades de flujo de la corriente de densidad salina y el agua circundante. En esta región, donde las características de flujo y mezcla están dominadas por grandes escalas, la extensión espacial y temporal de la corriente de densidad puede ser del orden de kilómetros y horas. En la Figura 0.3 se muestra un diagrama del comportamiento tanto en campo cercano como en campo lejano de una descarga de salmuera mediante chorro sumergido.

Dado que las tasas de dilución más altas se obtienen en la región de campo cercano, los esfuerzos de la comunidad científica se han centrado principalmente en el estudio de esta región (experimental y numéricamente) así como en el desarrollo de herramientas útiles y metodologías validadas para diseñar configuraciones óptimas de descarga de salmuera (véase Palomar (2014)). El criterio de optimización de estas metodologías de diseño consiste en lograr una dilución máxima que cumpla con los requisitos medioambientales dentro de la propia región de campo cercano. Sin embargo, existen ocasiones en las que también se requiere el estudio de la región de campo lejano, tales como: (1) cuando la dilución mínima exigida no se consigue en la región predecesora de campo cercano; (2) ante la existencia de ecosistemas sensibles lejos del punto de descarga, pero dentro del área potencial de impacto de la corriente de densidad; (3) cuando existe riesgo de impacto de la

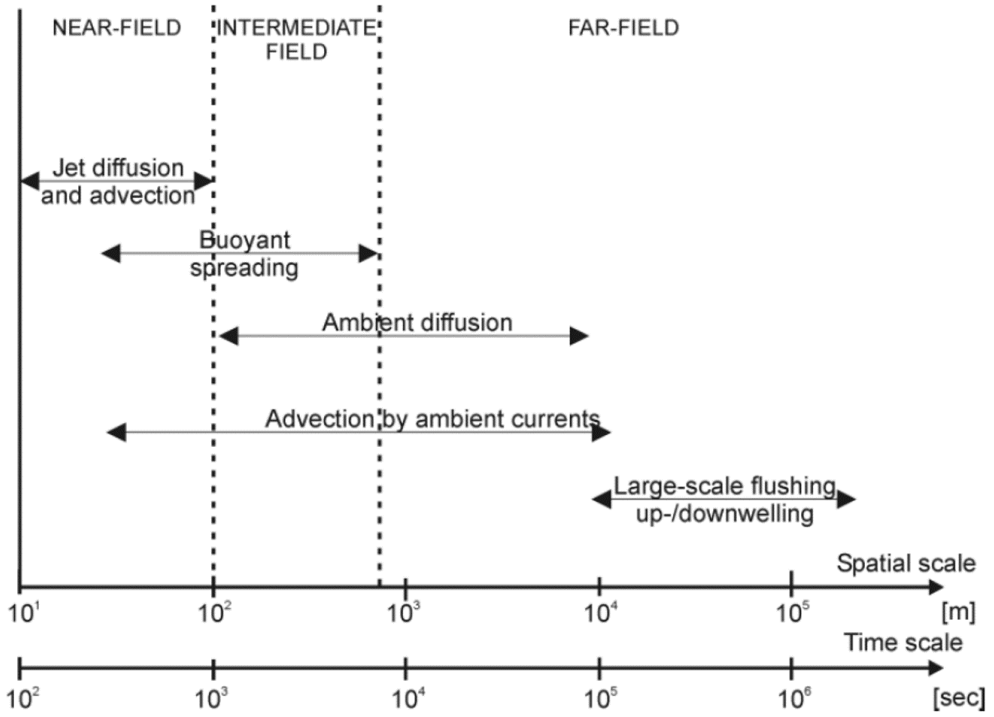

Figura 0.2: Escalas temporales y espaciales de los procesos de transporte y mezcla relacionados con descargas aguas residuales. Fuente: Gerhard H. Jirka, Abrahan, G. and Harleman (1976) and Fischer (1979)

corriente de densidad en la toma de agua de la desaladora; (4) ante la existencia de contaminantes químicos en el efluente de descarga, cuyo comportamiento se rige por diferentes escalas espacio-temporales; (5) en vertidos directos superficiales, por ejemplo, en playas, y la salmuera se comporta casi en su totalidad como una corriente de densidad propia del campo lejano.

En las situaciones enumeradas anteriormente, se requiere predecir el comportamiento del efluente no sólo en campo cercano sino también en campo lejano, donde se forma la corriente de densidad. Debido a las grandes diferencias en las escalas espacio-temporales mencionadas, así como a los diferentes factores condicionantes que rigen su comportamiento, las herramientas de simulación hidrodinámica disponibles para simular correcta y eficientemente ambas regiones son de diferente naturaleza. Por lo tanto, además de un modelado fiable del campo cercano y lejano, se ha de utilizar una correcta metodología de acoplamiento entre ambos modelos con el fin de obtener una predicción del comportamiento global de los vertidos de salmuera.

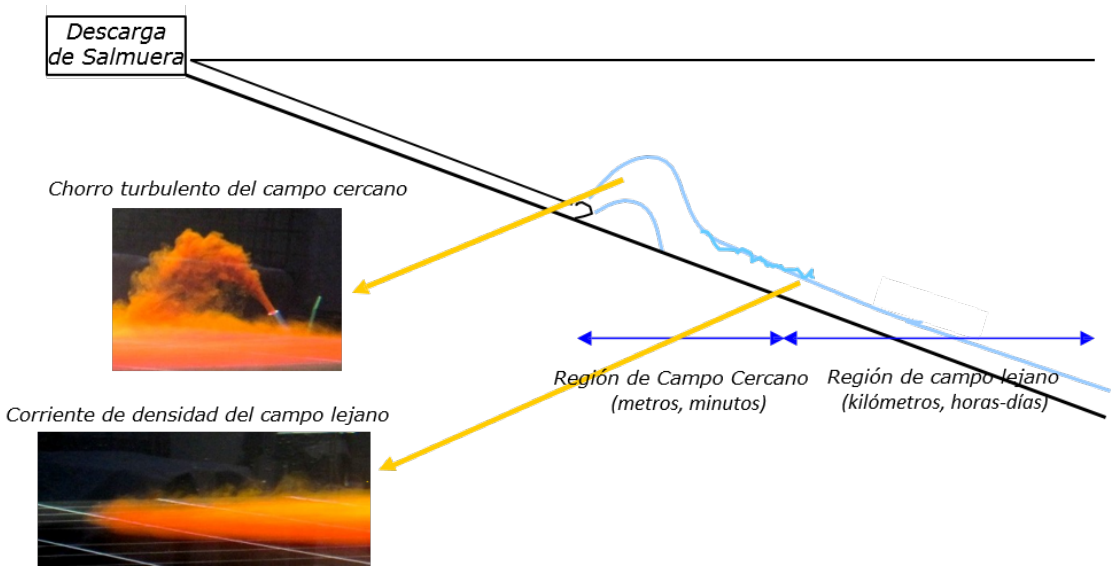

Figura 0.3: Diagrama del comportamiento en campo cercano y lejano de una descarga de salmuera mediante chorro sumergido. Fuente: Palomar (2014)

I.B. Estado del conocimiento

En esta sección se presenta una breve descripción del contexto en que se enmarcan: la caracterización experimental de la corriente de densidad característica del campo lejano, su modelado numérico y la metodología de acoplamiento entre el campo cercano y el campo lejano.

Caracterización experimental del campo lejano

En las últimas décadas, debido a las cada vez más presentes corrientes de densidad de naturaleza industrial en el medioambiente (Simpson (1982, 1997) y Huppert (2006)), varios estudios han intentado comprender el su comportamiento mediante estudios experimentales de laboratorio.

Atendiendo a la continuidad del régimen de flujo, en la literatura científica se han abordado dos tipos de experimentos. Por un lado, se han estudiado las corrientes de densidad generadas por un volumen finito de efluente (p.e. Kneller et al. (1999)). Los análisis de este tipo de experimentos se han centrado en el estudio detallado de la dinámica de las estructuras que aparecen en el frente de las corrientes de densidad (p.e. Huppert and Simpson (2006); Maxworthy and Nokes (2007); Nogueira et al. (2014); Nokes et al. (2010); Özgökmen and Chassignet (2002) y Ottolenghi et al. (2016)). La otra vertiente experimental se ha centrado en analizar el

comportamiento estable y cuasi-estacionario del cuerpo de la corriente de densidad generada por vertidos de caudal constante (p.e. Ellison and Turner (1959); Garcia (1993) y Hosseini et al. (2006)). Recientemente, Sequeiros (2012) recopiló una extensa base de datos de medidas de velocidad y concentración medias de corrientes de densidad de diversa naturaleza obtenidas de diferentes trabajos publicados. Por otra parte, aprovechando técnicas de medición de alta resolución, algunos estudios han focalizado sus esfuerzos en el análisis detallado de la estructura turbulenta de estos flujos (p.e. Gerber et al. (2011)), comparando el comportamiento de las corrientes de densidad de sustancias disueltas (como las hipersalinas) y las de partículas suspendidas (como las turbidíticas) (Gray et al. (2006) y Islam and Imran (2010)).

Otros estudios experimentales como Cenedese and Adduce (2008), se centraron en la caracterización del mecanismo de mezcla mediante la cuantificación de la incorporación (o arrastre) del fluido circundante en la corriente de densidad. Habitualmente este término es conocido por su expresión en inglés, "Entrainment" (Princevac et al. (2005); Turner (1986) y Wells et al. (2010)). Los trabajos desarrollados por Cenedese et al. (2010); Kashefipour et al. (2010) y Chowdhury and Testik (2014) recogen un gran número de parametrizaciones de "Entrainment" desarrolladas en las últimas décadas, todas ellas en función del número de Richardson (es decir, la relación entre la energía potencial y cinética del flujo). La mayor parte de estas parametrizaciones se han obtenido a partir de corrientes de densidad bidimensionales, es decir, confinadas lateralmente, existiendo un menor número de parametrizaciones a partir de corrientes no confinadas (p.e. Britter and Simpson (1978) y Patterson et al. (2006)). El trabajo de La Rocca et al. (2008) muestra experimentos de corrientes de densidad no confinadas, sin embargo el objeto de su estudio fue la velocidad de avance del frente en vez de el citado "Entrainment". Para conocimiento de los autores, únicamente las recientes publicaciones de MacDonald and Chen (2012) y Yuan et al. (2013) han tratado de aislar el efecto del esparcimiento lateral en la tasa de mezcla o "Entrainment".

Dado que las corrientes de densidad características de la región de campo lejano de los vertidos de salmuera son habitualmente corrientes no confinadas, la presente tesis trata de superar las deficiencias encontradas en cuanto a su caracterización experimental mediante avanzadas técnicas ópticas "Particle Image Velocimetry" (PIV) y "Planar Laser Induced Fluorescense" (PLIF) (Martin and Garcia (2008) y Liao and Cowen (2010)).

Caracterización numérica del campo lejano

Debido al creciente interés en predecir el comportamiento de las corrientes de densidad en el medio marino, el modelado numérico de este tipo de flujo está en auge. Existen fundamentalmente, dos tipos de aproximaciones numéricas para predecir numéricamente este tipo de flujos: los modelos integrales y aquellos que resuelven la estructura vertical del flujo. El concepto de los modelos integrales para predecir estas corrientes fue introducido por Ellison1959 y posteriormente desarrollado por Alavian (1986) y Parker et al. (1986). En general, estos modelos integrales asumen la hipótesis de distribución de presión hidrostática y resuelven las ecuaciones de hidrodinámica integradas en profundidad. Por otro lado, aquellos modelos que resuelven la estructura vertical del flujo se basan en la resolución de las ecuaciones de la hidrodinámica (es decir, continuidad y Navier-Stokes) con distinto grado de simplificación.

Desde que Ellison and Turner (1959) asentara sus bases, los modelos integrales se han desarrollado significativamente, centrándose principalmente en las corrientes de turbidíticas lateralmente confinadas (Akiyama and Stefan (1985); Bradford et al. (1997); Choi (1999); Choi and Garcia (1995); Garcia (1993); Imran et al. (1998); Parker et al. (1986) y Ungarish (2007a)). Respecto a las corrientes de densidad no confinadas, Ungarish (2007b) y La Rocca et al. (2008) realizaron análisis numéricos para la validación de sus aproximaciones integrales con datos experimentales. Recientemente, La Rocca and Pinzon (2010) y La Rocca et al. (2012) propusieron el uso de modelos integrales que dividen la columna de agua en dos capas (denominados “double-layer shallow water models”) y Adduce et al. (2012) presentó una modificación considerando una nueva parametrización del “Entrainment” como parámetro de calibración de estos modelos.

Comunmente, la distribución vertical de las corrientes de densidad se ha analizado numéricamente con modelos hidrodinámicos que resuelven las ecuaciones Navier-Stokes teniendo en cuenta la aproximación de Reynolds (RANS, siglas procedentes de la expresión en inglés: Reynolds Average Navier Stokes). Estos modelos requieren un modelo de turbulencia (o cierre de las ecuaciones) para estimar las tensiones turbulentas de Reynolds, así como la definición de una ley de fricción en los contornos sólidos de estudio. Stacey and Bowen (1988a,b) resolvió la distribución vertical de una serie de corrientes turbidíticas utilizando como Modelo de de Cierre de Turbulencia (TCM) un modelo de longitud de mezcla. Otros autores

emplearon el modelo κ - ε (Rodi (1984)) como TCM (por ejemplo, Brø rs and Eidsvik (1992); Eidsvik and Brø rs (1989) y Choi and Garcia (2002)). En los últimos años, algunos trabajos relacionados con la simulación de corrientes de densidad han utilizado modelos complejos DNS (siglas procedentes de la expresión en inglés: Direct Numerical Simulation) como Birman et al. (2005); Cantero et al. (2006); Härtel et al. (2000); Lowe et al. (2005) y Cantero et al. (2007)), sin embargo, en escalas reales de campo estas últimas simulaciones son, a día de hoy, inabordables computacionalmente. El trabajo presentado en Paik et al. (2009) mostró que, considerando mallas de cálculo suficientemente finas, los modelos que resuelven las ecuaciones URANS (siglas procedentes de la expresión en inglés: Unesteady Reynolds Average Navier Stokes) con un modelo de cierre de turbulencia LRN-κ - ε (es decir, para flujos de bajo número de Reynodls)(Citet Hwang1998) pueden alcanzar resultados similares a simulaciones las DNS y LES (siglas procedentes de la expresión en inglés: Large Eddy Simulation).

Mientras los modelos integrales proporcionan resultados aceptables (del orden de magnitud) para aplicaciones sencillas en cuanto a las condiciones del medio, los modelos más sofisticados (DNS y LES) pueden proporcionar resultados más ajustados a la realidad pero en tiempos de cálculo normalmente inasequibles para aplicaciones a escala de campo. Bombardelli and García (2002) evaluaron la evolución de corrientes de densidad en el río Chicago utilizando un modelo hidrodinámico tridimensional de complejidad intermedia. Kulis and Hodges (2006) realizaron un análisis de sensibilidad numérica atendiendo al número de capas sigma para simular la corriente de densidad de la Bahía de Corpus Christi utilizando un modelo hidrodinámico tridimensional que resuelve las ecuaciones RANS, teniendo en cuenta la aproximación de Boussinesq y la hipótesis de presión hidrostática (es decir, ecuaciones para la resolución de aguas poco profundas). Utilizando modelos hidrodinámicos tridimensionales similares, Firoozabadi et al. (2009) y Mahgoub et al. (2015) reprodujeron corrientes de densidad generadas en laboratorio y validaron los resultados numéricos con los correspondientes datos experimentales. Sin embargo, ninguno de los trabajos revisados relacionados con la simulación de corrientes de densidad con modelos hidrodinámicos tridimensionales han sido completamente validados teniendo en cuenta tanto el esparcimiento de la corriente como la estructura vertical de las principales magnitudes, es decir, velocidad y concentración.

Con el fin de simular adecuadamente y en tiempos asumibles las corrientes de

densidad no confinadas como las generadas en la región de campo lejano de los vertidos de salmuera, esta tesis realiza un análisis de sensibilidad atendiendo a los aspectos numéricos de un modelo hidrodinámico tridimensional que resuelve las ecuaciones de ondas largas. Además, ante la carencia de trabajos de validación en la literatura científica a este respecto, la presente tesis asume el reto de validar la configuración de modelado propuesta comparando los resultados numéricos con datos experimentales de corrientes de densidad generadas en laboratorio.

Modelado acoplado del campo cercano y campo lejano

La cada vez más creciente instalación de nuevos dispositivos de vertidos que favorecen la mezcla del efluente hipersalino en la región de campo cercano ha motivado que la mayor parte de los estudios científicos recientes se centren en el estudio del modelado numérico de esta región. Un menor número de estudios se ha centrado en el procedimiento de acople entre herramientas numéricas de campo cercano y lejano.

Atendiendo a la región de campo cercano, el uso de varias herramientas como VISJET (Cheung et al. (2000)), CORMIX (Doneker and Jirka (2001)) y VISUAL-PLUMES (Frick (2004)) se ha extendido en los últimos años para proporcionar una predicción aproximada del comportamiento de los vertidos mediante chorro sumergido. Sin embargo, estas herramientas, basadas en el análisis dimensional y la integración de ecuaciones diferenciales, fueron programadas y validadas para simular vertidos de flotabilidad positiva y análisis recientes en el Instituto de Hidráulica Ambiental de la Universidad de Cantabria, han demostrado importantes limitaciones y un mal ajuste para vertidos de flotabilidad negativa (Palomar (2014)). Por esta razón, recientemente, se han desarrollado en el Instituto de Hidráulica Ambiental (Palomar et al. (2013)), nuevas herramientas de modelado de vertido de salmuera, BrIHne (www.BrIHne.ihcantabria.com), validadas con datos experimentales muy precisos. Otros trabajos de investigación como Oliver et al. (2008); Plumb (2008) y Garcia Alba (2011) utilizaron modelos más avanzados como CFD FLUENT para analizar este tipo de vertidos. Sin embargo, aunque se puede extraer información más detallada de ellos, estos modelos tienen un gran coste computacional en comparación con las herramientas basadas en el análisis dimensional y la integración de ecuaciones.

En cuanto al procedimiento de acople entre modelos de campo cercano y lejano, la mayoría de los trabajos existentes en la literatura científica se han enfocado en el estudio de vertidos de flotabilidad positiva, como los vertidos de aguas residuales. Estos trabajos han utilizado como modelos de campo cercano las herramientas comerciales citadas anteriormente y como modelos de campo lejano modelos hidrodinámicos tridimensionales que tienen en cuenta las condiciones del medio, como el modelo Delft3D-Flow (Roelvink and Van Banning (1994) y Hydraulics (2005)). A grandes rasgos, se han utilizado dos tipos de procedimientos de acople entre estos modelos, el acoplamiento "pasivo" y el acoplamiento "activo". La versión más reciente del acoplamiento "pasivo" consiste en introducir los valores de concentración y caudal obtenidos por el modelo de campo cercano al final de esta región, en las localizaciones correspondientes del dominino de cálculo del modelo de campo lejano (Zhang and Adams (1999)). Choi and Lee (2007) denomina a este procedimiento como "Diluted Source at Trapped Level" (DSTL) y fue utilizado por Bleninger (2006) para acoplar la herramienta de campo cercano CORMIX con el modelo de campo lejano Delft3D-FLOW. Este tipo de acoplamientos son adecuados para vertidos de poco caudal, en los que se puede considerar que la región de campo cercano no afectará a las carácterísticas hidrodinámicas del medio (Stamou and Nikiforakis (2013)). Para vertidos de elevado caudal, cuyos caudales de descarga pueden afectar signicativamente a la hidrodinámica de la zona, Choi and Lee (2007) y Stamou and Nikiforakis (2013) desarrollaron procedimientos de acoplamiento "activos" capaces de introducir la influencia del campo cercano en las aguas receptoras mediante un conjunto de sumideros-fuentes a lo largo de la trayectoria del chorro. Aunque Nikiforakis and Stamou (2015) adaptó el procedimiento de acoplamiento "activo" desarrollado por Stamou and Nikiforakis (2013) para vertidos de flotabilidad negativa, este procedimiento no ha sido validado con mediciones de campo. Únicamente Wood et al. (2014) presentó un trabajo de validación utilizando tanto procedimientos de acoplamiento "activos" como "pasivos", llegando a la conclusión de que los precedimientos "pasivos" son recomendables para el modelado de vertidos hipersalinos procedente de operaciones de lixiviación.

En esta tesis se propone una metodología de modelado acoplado utilizando modelos fiables de campo cercano y lejano, BrIHne y TELEMAC-3D, respectivamente, para predecir el comportamiento continuo en ambas regiones de vertidos de salmuera a través de chorros sumergidos. La metodología se valida mediante la comparación

de los resultados numéricos con mediciones en campo de salinidad en la corriente de densidad del vertido de salmuera de una planta desaladora.

I.C. Objetivos

El objetivo general de esta tesis es profundizar en el conocimiento del comportamiento de los efluentes de la salmuera en aguas costeras, así como en su modelado, que permitirá predecir su alcance en zonas alejadas del punto de vertido. Para lograr este objetivo general, se abordarán tres objetivos específicos:

- **Objetivo 1: Profundizar en el estudio del comportamiento de las corrientes de densidad salina no confinadas** y evaluar la influencia de las condiciones iniciales de descarga mediante un análisis experimental que utiliza avanzadas técnicas ópticas de medida.
- **Objetivo 2: Establecer una configuración numérica óptima para el modelado de corrientes de densidad no confinadas**, con apoyo de bases de datos experimentales para la validación.
- **Objetivo 3: Implementar una metodología de acople entre los modelos de campo cercano y lejano** utilizando la configuración numérica propuesta en el Objetivo 2, que permita predecir el comportamiento global de los efluentes de salmuera, y su validación con datos de campo.

I.D. Organización de la tesis

La estructura de la tesis está organizada de la siguiente manera:

El **Capítulo 1**, describe la motivación de esta investigación y proporciona algunos antecedentes para una mejor comprensión de las siguientes secciones. Al final del mismo, se describen los objetivos específicos expuestos anteriormente y las secciones en que se abordan.

Los tres capítulos siguientes (**Capítulos 2, 3 y 4**) abordan los objetivos específicos de la tesis. Cada uno de los capítulos incluye un resumen, una introducción, una descripción del marco metodológico, así como los resultados y conclusiones principales. A continuación se describe un breve resumen de la investigación realizada en cada capítulo:

- **Capítulo 2. Caracterización global PIV-PLIF de corrientes de densidad salina no confinadas bajo diferentes condiciones**

  El presente capítulo muestra una caracterización global experimental de las propiedades de flujo cuasi-estacionarias de las corrientes salinas no confinadas usando técnicas óptimas no intrusivas PIV-PLIF ("Particle Image Velocimetry"-"Planar Laser Induced Fluorescense"). Se incluye el estudio de la influencia de la pendiente del fondo y las condiciones iniciales de descarga (el caudal, el espesor y la concentración salina) sobre el comportamiento de la corriente de densidad. La base de datos de alta resolución presentada en este capítulo es una herramienta clave para la calibración/validación de diferentes aproximaciones numéricas, como los modelos integrales y los modelos hidrodinámicos tridimensionales.

- **Capítulo 3. Modelado hidrodinámico de corrientes de densidad no confinadas: optimización de la configuración numérica**

  En este capítulo se muestra un análisis de sensibilidad de los diferentes aspectos numéricos que influyen en el modelado de corrientes de densidad mediante modelos hidrodinámicos tridimensionales (p.e. la discretización del dominio, la definición de la fuente/descarga, la asunción de hipótesis hidrostática, los esquemas advectivos y los modelos de turbulencia). A través de dicho análisis, se proporcionan una serie de recomendaciones para todos los aspectos numéricos clave de modelado para optimizar la simulación de este tipo de flujos. Finalmente, estas recomendaciones son validadas con la base de datos experimental obtenida de los ensayos PIV-PLIF, descritos en el anterior capítulo y otros datos experimentales de trabajos previos. Por lo tanto, este estudio representa un primer paso hacia la validación de estos modelos hidrodinámicos tridimensionales para resolver flujos de corriente de densidad a escala de campo.

- **Capítulo 4. Metodología de modelado acoplado de los vertidos de salmuera al mar. Caso de validación: planta de desaladora de Maspalomas**

  Este capítulo presenta una metodología de modelado acoplado utilizando modelos validados (p.e. BrIHne y TELEMAC-3D) para predecir el comportamiento del campo cercano y del campo lejano de los vertidos de salmuera

de una manera integral. Además, la metodología desarrollada se valida mediante la comparación de los resultados numéricos, bajo diferentes condiciones ambientales y de vertido, con mediciones en campo de salinidad en la corriente de densidad del vertido de la planta desaladora de Maspalomas (Canarias, España). Por lo tanto, esta metodología constituye una herramienta clave para la predicción de estos vertidos de flotabilidad negativa en la fase de optimización del diseño de vertidos, así como para estudiar el area de impacto de los mismos bajo diferentes condiciones ambientales.

Finalmente, el último capítulo (**Capítulo 5**) resume las conclusiones obtenidas en la presente tesis y marca las futuras líneas de investigación.

II. Caracterización global PIV-PLIF de corrientes de densidad no confinadas [1]

Una vez revisado el estado del conocimiento atendiendo a la caracterización experimental de las corrientes de densidad de flotabilidad negativa (véase la Sección I.B), el presente capítulo presenta el conjunto de ensayos realizados en el Instituto de Hidráulica Ambiental bajo el marco de esta tesis. diseñados especialmente para subsanar las lagunas identificadas en el análisis del estado del conocimiento. Teniendo en cuenta que el estudio se centra en las corrientes de densidad de vertidos de salmuera, los flujos experimentados corresponden a corrientes salinas no confinadas sobre pendientes suaves que imitan a los fondos marinos de las zonas costeras donde se descargan estos vertidos. Por otro lado, las técnicas de medición avanzadas PIV-PLIF, permitiran obtener una caracterización global tanto en términos de cobertura espacial, como en términos de las magnitudes estudiadas: velocidad y concentración.

Las siguientes secciones describen brevemente los experimentos, así como las técnicas de medición utilizadas y el análisis de sus resultados.

[1] Este sub-apartado resume de manera concisa la metodología y los resultados del Capítulo 2 del documento en inglés, que a su vez es una adaptación de los artículos "Pérez-Díaz, B., Palomar, P., Castanedo, S. y Álvarez, A. (2016). Caracterización experimental del campo lejano de los vertidos de salmuera al mar (2016). RIBAGUA - Revista Iberoamericana del Agua 3, 66-75" y "Pérez-Díaz, B., Palomar, P. and Castanedo, S. (2017). PIV-PLIF global characterization of non-confined saline density currents under different flow conditions. Journal of Geophysical Research - Oceans (under review)". Las conclusiones y aportaciones del capítulo se resumen en la Sección V

II.A. Método experimental

Los ensayos se llevaron a cabo en el laboratorio del IH Cantabria, en un tanque de $3x3x1\,m^3$ con dos paredes acristaladas, simulando un vertido sumergido continuo de salmuera en un medio receptor homogéneo y en reposo. El dispositivo de vertido consistió en una arqueta de metacrilato con una ranura en el fondo de altura regulable apoyada sobre un falso fondo de plástico (rozamiento casi despreciable) dispuesto a 30 cm del fondo real del tanque y a 20 cm de las paredes. De esta manera, el vertido hipersalino queda almacenado bajo el falso fondo, evitando el riesgo de contaminación de la propia pluma y permitiendo así el estudio de plumas no confinadas, es decir tridimensionales.

Para grabar las imágenes instantáneas PIV-PLIF, se utilizaron dos cámaras "Imager ProX 4M (CCD)". Ambas cámaras se colocaron contiguamente, con una pequeña zona de solape, para poder capturar la máxima extensión posible (∼1400mm). Para cada caso PIV-PLIF, se tomaron, al menos, 1800 imágenes a 5 Hz de frecuencia, una vez alcanzado el comportamiento totalmente desarrollado de la corriente dedensidad, es decir un comportamiento estacionario del cuerpo de la corriente. En la Figura 0.4 se muestra un esquema de las corrientes de densidad no confinadas generadas por este tipo de plumas hipersalinas. La nomenclatura empleada en esta figura es la utilizada a lo largo de todo el capítulo.

Tabla 0.1: Principales características de las configuraciones de los experimentos de laboratorio

CASOS	Dimensiones ranura $(b_0 \cdot h_0)$ m	Profundidad agua (Ha_0) m	Pendiente (α) %	Diferencia densidad $(\rho_a - \rho_0)$ Kg/m^3	Caudal descarga (Q_0) l/min
CASO1	$0.100 \cdot 0.026$	0.460	1.0	3.145	14.600
CASO2	$0.100 \cdot 0.016$	0.460	1.0	3.100	15.100
CASO3	$0.100 \cdot 0.026$	0.460	1.0	3.130	19.200
CASO4	$0.100 \cdot 0.026$	0.420	2.5	3.070	14.980
CASO5	$0.100 \cdot 0.026$	0.360	4.5	3.140	14.09
CASO6	$0.100 \cdot 0.026$	0.460	1.0	11.080	14.890

La Tabla 0.1 resume las condiciones experimentales y parámetros iniciales de las corrientes de densidad en este estudio. Para establecer esta casuística, fueron necesarias pruebas previas que asegurasen buenas mediciones PIV-PLIF y al mismo tiempo un comportamiento de tipo pluma hipersalina característica de la región de campo lejano. El $CASO1$ es el caso base, a partir del cual se generan el resto de

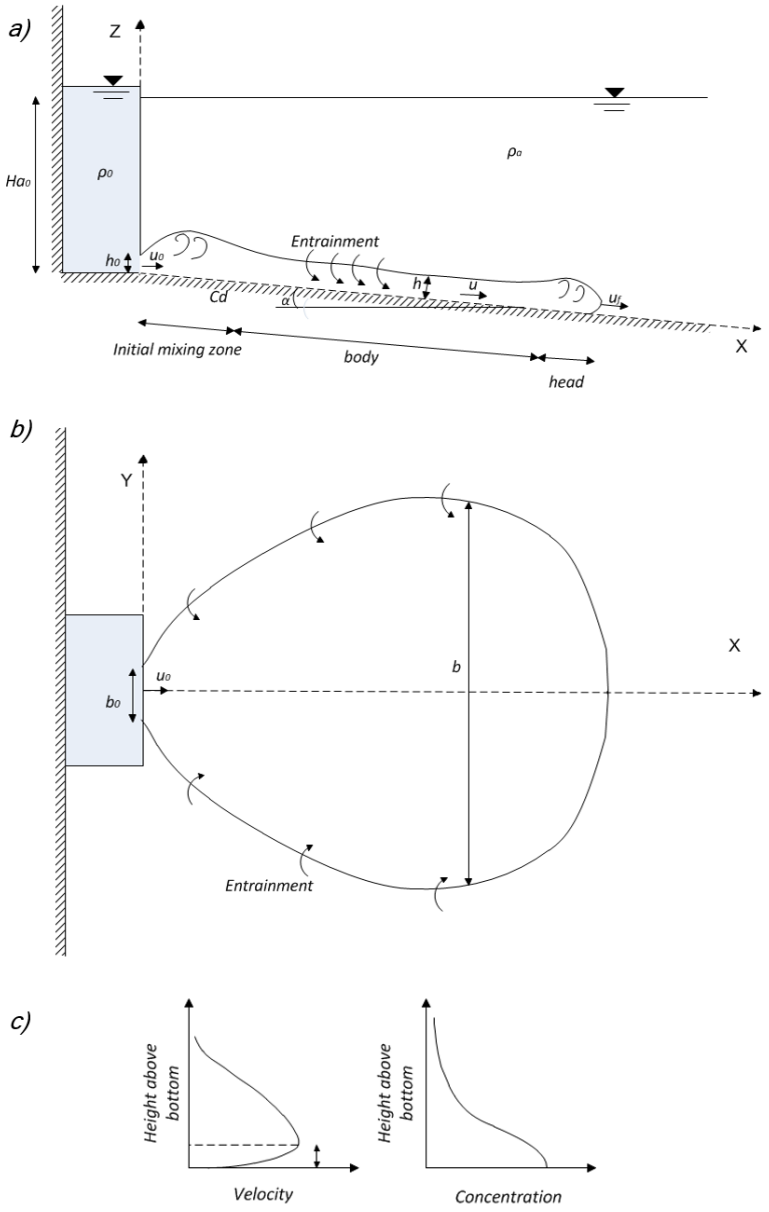

Figura 0.4: Esquema de una corriente de densidad hipersalina no confinada: a) vista de perfil longitudinal; b) vista en planta; c) perfiles transversales de velocidad y concentración

casos, modificando únicamente una de sus variables objeto de estudio: el espesor inicial del vertido, el caudal de descarga, la pendiente en el fondo, o la diferencia de densidad entre el medio receptor y el vertido.

II.B. Resultados

Los campos instantáneos de velocidades y concentraciones obtenidos en el plano de simetría resultan de la correcta interpretación y el acople de las parejas de imágenes

contiguas (tomadas por las cámaras descritas en la sección previa). Puesto que el objetivo de estudio de este capítulo es la caracterización de las corrientes de densidad una vez alcanzan su estado completamente desarrollado (es decir, el cuerpo de la corriente, y no la cabeza de esparcimiento) y estacionario, se obtienen los campos medios de las variables fundamentales de estos flujos: las componentes horizontal y vertical de la velocidad media (U_X y U_Z), las componentes vertical y horizontal de la fluctuación de la velocidad media (U'_X y U'_Y), la concentración media (C), la fluctuación de la concentración media (C') y la dilución media ($S \simeq C_o/C$). La Figura 0.5 presenta todos los campos promediados detallados para el $CASO1$.

Aprovechando las ventajas que ofrecen las técnicas PIV-PLIF frente a las clásicas medidas puntuales en el espacio, este estudio caracteriza el comportamiento de las corrientes de densidad de manera continua en el espacio. De esta manera se han podido extraer perfiles longitudinales (véase la Figura 0.6) de las variables más representativas de los flujos estudiados: la componente horizontal de la velocidad máxima normalizada ($U_{X_{max}}/U_0$) y la dilución mínima (S_{min}). La Figura 0.6 muestra la existencia de grandes gradientes en los perfiles longitudinales de velocidades y de dilución (primeros 400mm-600mm) hasta alcanzar un estado cuasi-estable a partir del cual la tasa de dilución es mínima y se mantiene en un valor casi constante. Este estado se denominará "Estado Normal" a lo largo del resto de documento, y es debido a dos razones fundamentales: 1) la corriente de densidad comienza a ser insensible al esparcimiento lateral en su plano de simetría longitudinal (eje de mayores concentraciones, y por tanto menores diluciones); y 2) la estratificación vertical estable que se alcanza debido al intercambio entre las fuerzas inerciales y de flotabilidad (Britter and Linden (1980)).

En la literatura científica (Alavian (1986); Morton et al. (1956); Parker et al. (1986) y Fukuoka, S. and Fukushima (1980)) la tasa de mezcla debida a la incorporación del fluido del medio receptor en la corriente de densidad es comúnmente denominada coeficiente de "Entrainment", E. Un gran número de publicaciones científicas han centrado sus investigaciones en la caracterización de esta tasa de dilución para corrientes de densidad bidimensionales (lateralmente confinadas), por tanto en la caracterización del coeficiente E vertical. Dicha caracterización ha consistido fundamentalmente en la búsqueda de parametrizaciones del coeficiente E vertical en función del número adimensional de Richardson (Ri) que representa la relación entre la energía potencial y cinética del flujo. A mayores valroes de

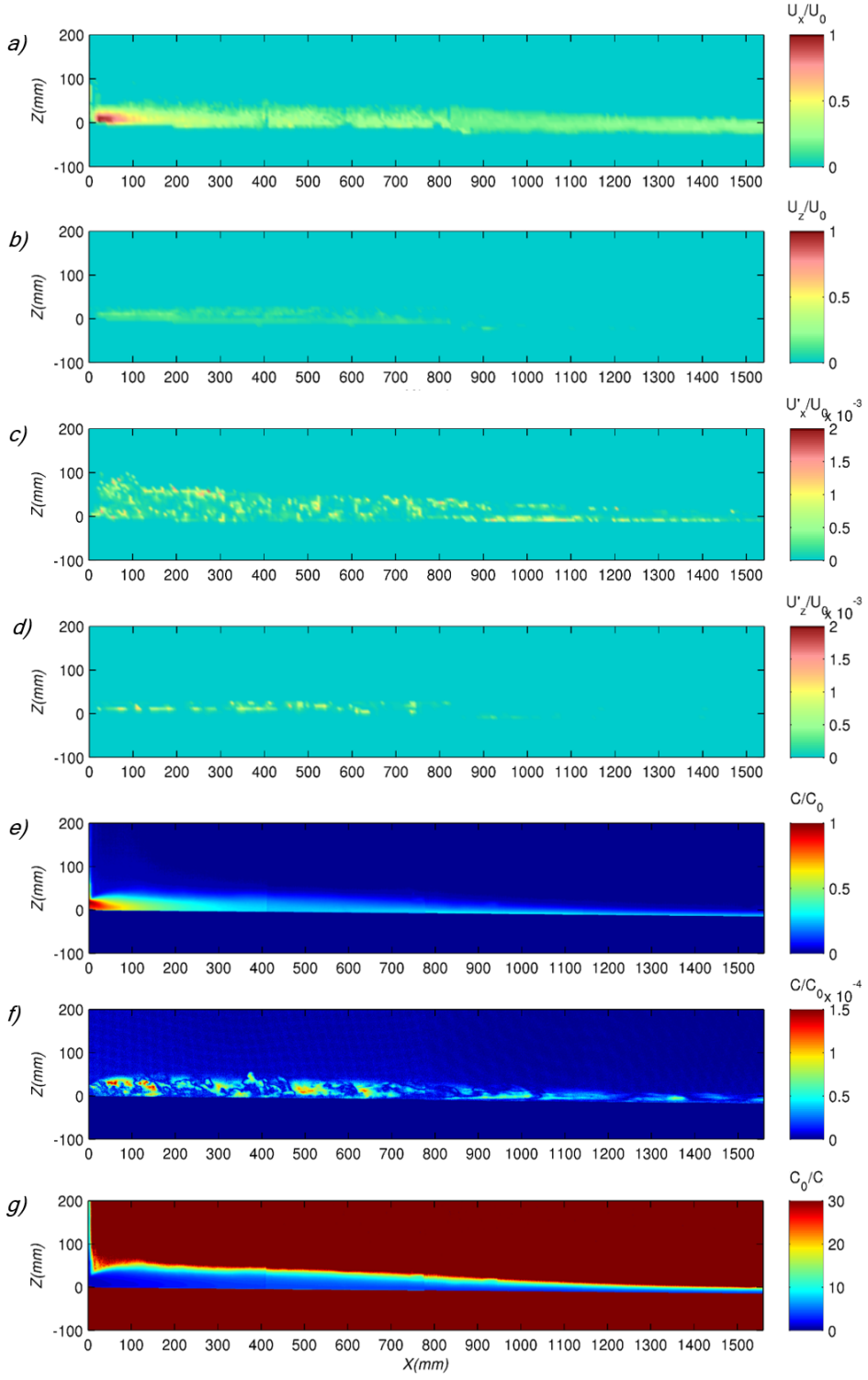

Figura 0.5: Campos de flujos normalizados del $CASO1$: a) velocidad media horizontal; b) velocidad media vertical; c) fluctuación de velocidad media horizontal; d) fluctuación de velocidad media vertical; e) concentración media; f) fluctuación de concentración; g) dilución media.

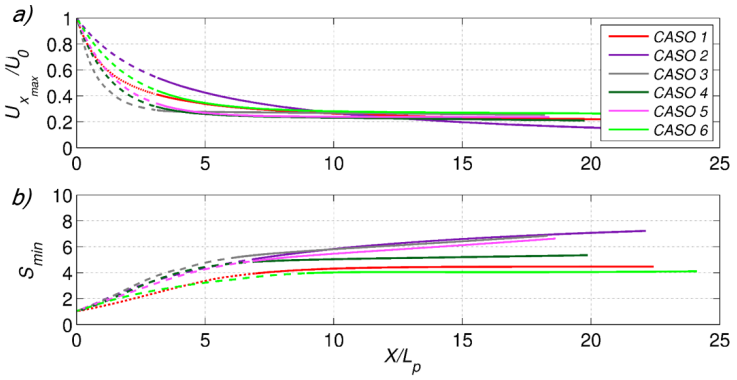

Figura 0.6: Perfiles longitudinales de: a) velocidad horizontal máxima normalizada; b) dilución mínima

Ri existe una menor dilución, llegando a ser inexistente para valores $Ri > 1$. Algunas de esas parametrizaciones quedan recopiladas en el trabajo de Chowdhury and Testik (2014). Tomando como ejemplo el trabajo de Dallimore et al. (2001) y Kulis and Hodges (2006), se ha calculado experimentalmente el valor del "Entrainment" a partir de la distancia aguas abajo en la que se puede asumir el "Estado Normal" para cada caso. Como se puede apreciar en la validación de la Figura 0.7, los valores de E obtenidos de los experimentos llevados a cabo, validan con los resultados de las corrientes confinadas experimentadas por otros autores, lo cual indica que efectivamente la región caracterizada como "Estado Normal" en el plano de simetría de estas corrientes de densidad tiene comportamiento de corriente bidimensional (o confinada), es decir, su principal mecanismo de mezcla es a través del flujo vertical.

Comparando los valores de obtenidos para los casos experimentados en este estudio (véase la Tabla 0.1), se llega a la conclusión de que aquellos con mayor cantidad de movimiento inicial (es decir, con mayores velocidades iniciales generadas por menores espesores iniciales y mayores caudales, $CASO2$ y $CASO3$) y mayores pendientes ($CASO4$ y $CASO5$) favorecen la dilución frente al caso base ($CASO1$). En cambio, el caso con mayor diferencia de densidad ($CASO6$) obtiene menor tasa de dilución. Para todos los casos estudiados el rango de valores obtenido oscila entre $1 \cdot 10^{-2}$ a $4 \cdot 10^{-2}$, valores correspondientes al $CASO6$ y $CASO5$, respectivamente.

Como resultado del análisis de la estructura vertical media, la Figura 0.8 presenta los perfiles transversales adimensionalizados a distintas distancias del punto de

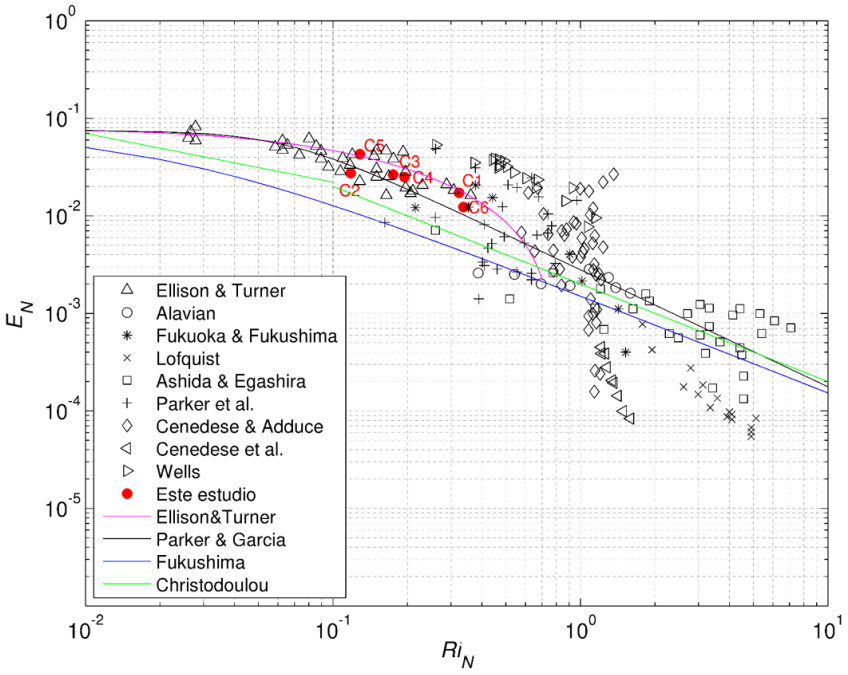

Figura 0.7: Medidas del coeficiente "Entrainemnt" (E) en función del número de Richardson (Ri) y parametrizaciones del estado del conocimiento (Kashefipour et al. (2010))

descarga, tanto para concentración como para velocidad, de uno de los casos estudiados. Como se observa todos ellos son autosimilares, convergiendo en una misma curva de ajuste polinómica. Dicha autosimilitud permite establecer unos coeficientes de forma que definen la distribución de las variables en el perfil $S1$ y $S2$ (Parker et al. (1987) y Garcia (1993)). Para todos los casos experimentados, una vez alcanzado el "Estado Normal", los coeficientes de forma toman valores en el rango de 0.7-0.86 y 0.57-0.77, respectivamente. Estos valores corresponden a perfiles suaves de concentración y velocidad, comunes para corrientes salinas.

Adicionalmente, del análisis de la estructura vertical turbulenta de las corrientes generadas (para una revisión completa del trabajo, se remite al lector al Capítulo 2 redactado en inglés), se deduce el colapso de las escalas de turbulencia de mayor escala inmediatamente aguas abajo de la descarga (también apreciable en los campos de flujo de la Figura 0.5c, d y f). Asímismo, en estos perfiles se reconoce un patrón común respecto a la localización de la zona de mínima turbulencia, la cual se ubica a la misma altura respecto del fondo que las máximas velocidades. Bajo esta ubicación se encuentra la zona donde las fluctuaciones de la concentración son mínimas, es decir donde existe menor transferencia de masa por difusión turbulenta.

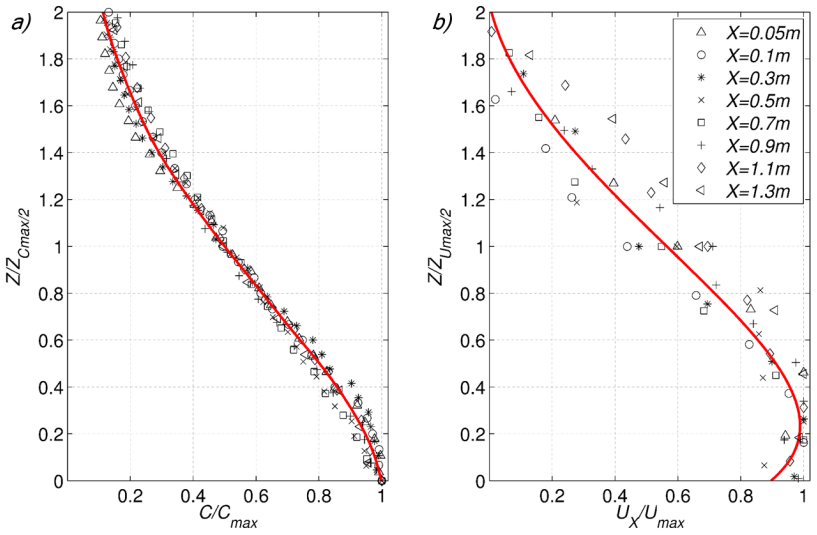

Figura 0.8: Perfiles autosimilares para el $CASO1$: a) concentración media; b) componente horizontal de la velocidad media. Los símbolos representan las medidas PIV-PLIF y la línea continua representa la curva polinómica de ajuste

Finalmente, se aplica un modelo de ecuaciones integradas para resolver este tipo de flujos no confinados basado en Alavian (1986). Para simular las corrientes generadas con este modelo se utilizaron los valores de los parámetros de calibración (E, $S1$ y $S2$) extraídos de este análisis experimental. Tras la comparación de los resultados numéricos y los experimentales se concluye que esta aproximación numérica para las corrientes de densidad objeto de este estudio, en términos generales, sobrevalora la velocidad y la dilución, e infravalora su esparcimiento lateral. Por lo tanto, se concluye que este modelo no es capaz de predecir correctamente el comportamiento de corrientes de densidad no confinadas.

III. Modelado numérico de corrientes de densidad no confinadas [2]

Teniendo en cuenta el objetivo final de esta tesis, es decir, tratar de predecir la evolución de los vertidos de salmuera a escala de campo, así como la revisión de las ventajas e inconvenientes de las herramientas numéricas del estado del

[2]Este sub-apartado resume de manera concisa la metodología y los resultados del Capítulo 3 del documento en inglés, que a su vez es una adaptación del artículo "Pérez-Díaz, B., Castanedo, S and Palomar, P. (2017). Modelling non-confined density currents using 3D hydrodynamic models: finding the key numerical set-up. Journal of Geophysical Research - Oceans (submitted)". Las conclusiones y aportaciones del capítulo se resumen en la Sección V

conocimiento, este capítulo se centra en el establecimiento de una serie de recomendaciones de buena práctica referentes a la configuración de los modelos hidrodinámicos tridimensionales para simular correctamente las corrientes de densidad propias del campo lejano de estos vertidos. Este objetivo específico se lleva a cabo a través de un análisis de sensibilidad de los diferentes aspectos numéricos que influyen en la simulación de este tipo de flujos.

Las siguientes secciones describen de manera resumida el citado análisis de sensiblidad, así como la validación de las recomendaciones establecidas mediante la reproducción numérica de corrientes de densidad obtenidas experimentalmente (las generadas bajo el marco de esta tesis y descritas en el capítulo previo (Pérez-Díaz et al. (2016b)) y las expuestas en Choi and Garcia (2001)).

III.A. Análisis de sensibilidad

Dentro de la gran oferta de modelos hidrodinámicos tridimensionales disponibles, este estudio selecciona el modelo de elementos finitos semi-implícito TELEMAC-3D (Hervouet (2007) y LNHE and Laboratory (2007)) por presentar ciertas ventajas frente al resto. Algún ejemplo de estas ventajas es el hecho de que utilice mallas no estructuradas, permita el uso del sistema de coordenadas verticales sigma (fácilmente redistribuibles) y su organizado código programado en Fortran90, que permite al usuario modificar fácilmente aspectos numéricos como los coeficientes asociados a los modelos de turbulencia, la activación de la hipótesis hidrostática, los esquemas numéricos, etc.

Tomando como partida una simulación base que trata de reproducir el $CASO1$ de los experimentos de laboratorio expuestos en el Capítulo 2 de esta tesis (véase Tabla 0.1 y Figura 0.4), el análisis de sensiblidad llevado a cabo consiste en la ejecución de varias simulaciones que varían un único aspecto numérico manteniendo el resto invariante. Los aspectos numéricos tenidos en cuenta en este análisis, así como las opciones consideradas respecto a cada uno de ellos, se exmem en la Tabla 0.2.

La relevancia de cada aspecto numérico en la predicción del comportamiento de las corrientes de densidad se analiza mediante comparación de los resultados numéricos de las principales magnitudes características, como son la evolución temporal de la dispersión espacial en planta de la corriente y la evolución espacial

TABLA 0.2: Aspectos numéricos del análisis de sensibilidad y sus opciones consideradas

Aspecto Numérico	Abreviatura	Opciones
Discretización horizontal	Δx	amplio rango de Δx en función de b_o
Discretización vertical	Δz	amplio rango de Δz en función de h_o
Definición de la fuente	Sce	información de Q o $Q\&V$
Hipótesis hidrostátia	Hyd	con o sin hipótesis
TCM[a]horizontal	$TCMh$	Cst.[b], Smago.[c], κ-ε
TCM vertical	$TCMv$	Cst., ML[d], κ-ε
Esquema advectivo κ-ε	$AdSch_{\kappa\varepsilon}$	Charcs.[e], $2^{nd}O$-KP[f]

[a] Modelo de Cierre de Turbulencia; [b] Modelo Constante; [c] Modelo Smagorinsky; [d] Modelos de Longitud de Mezcla; [e] Método de las características; [f] esquema de 2^o orden *Kurganov and Petrova*

de la velocidad (U) y la dilución (S) en el seno de la corriente de densidad (en su plano de simetría). Respecto a la comparación de estas últimas magnitudes U y S, algunas comparaciones se han basado en los valores extremos de las mismas (velocidades máximas U_{max} y diluciones mínimas S_{min}) y a su distribución vertical en la columna de agua, mientras otras comparaciones se han centrado en la tasa de dilución ("Entrainment") una vez alcanzado el "Estado Normal".

Las principales recomendaciones establecidas a raíz de este análisis, por ser parte fundamental de las conclusiones generales de esta tesis, se detallan en la Sección V donde se recogen las conclusiones de la presente tesis.

III.B. Resultados y validación

El análisis de sensiblidad llevado a cabo para simular las corrientes de densidad objeto de estudio, proporciona la selección óptima de los aspectos numéricos evaluados. De acuerdo con la nomenclatura utilizada en la sección anterior, la configuración propuesta queda resumida en la Tabla 0.3.

TABLA 0.3: Configuración del modelo hidrodinámico tridimensional propuesta para simular corrientes de densidad

$\boldsymbol{\Delta x}$	$\boldsymbol{\Delta z}$	$\boldsymbol{Sce}$	$\boldsymbol{Hyd}$	$\boldsymbol{TCMh}$	$\boldsymbol{TCMv}$	$\boldsymbol{AdSch_{\kappa\varepsilon}}$
$\Delta x_1 \leq bo/4$	$\Delta z_{min} \leq ho/16$	$Q\&V$	con	Cst.	κ-ε c_μ=0.2, $c_{3\varepsilon}$=0.7	Más conserv. (p.e. $2^{nd}O$-KP)

En las Figuras 0.9, 0.10 y 0.11 se presentan las comparativas de los resultados numéricos de la simulación de la corriente de densidad $CASO1$ (véase Tabla 0.1) frente a los datos experimentales correspondientes. La Figura 0.9 muestra la buena concordancia entre la base de datos numérica y la experimental en cuanto a los perfiles verticales de velocidad y concentración a diferentes distancias aguas abajo de la descarga. Por otro lado, la Figura 0.10a muestra la correcta predicción de la posición frontal X_f (o avance) de la corriente, la cual se predice con un error normalizado $NRMSE_{X_f exp}$ inferior al 6%. Atendiendo a la evolución en el plano de simetría de la velocidad máxima U_{max} y dilución mínima S_{min}, la Figura 0.10b muestra un ajuste con errores normalizados en torno al 4% para la velocidad y menores al 1.3% para la dilución. Finalmente, la Figura 0.11 presenta una comparación del avance de la corriente visto en planta y perfil para diferentes instantes de tiempo. Se ha de tener en cuenta, que las magnitudes de espacio y tiempo se encuentran adimensionalizadas por unas escalas características para este tipo de corrientes (Chu and Jirka (1987) y Choi and Garcia (2001)) las cuales se definen para cada caso de estudio según: $L_p = Q_0^{3/5}/Bf_0^{1/5}$ y $T_p = Q_0^{4/5}/Bf_0^{3/5}$, donde $Bf_0 = Q_0 g(\rho_o - \rho_a)/\rho_a$.

Para asegurar que la configuración propuesta es válida para simular corrientes de densidad generadas por diferentes condiciones de descarga, se llevaron a cabo sendas simulaciones con el fin de reproducir el resto de experimentos de laboratorio presentados en el Capítulo 2 (véase Tabla 0.1). Asímismo, se realizaron simulaciones tratando de imitar las corrientes de densidad mostradas en Choi and Garcia (2001). En ambos casos hubo una gran concordancia entre los resultados numéricos y los experimentales (para una revisión completa del trabajo, se remite al lector al apítulo 3 de esta tesis).

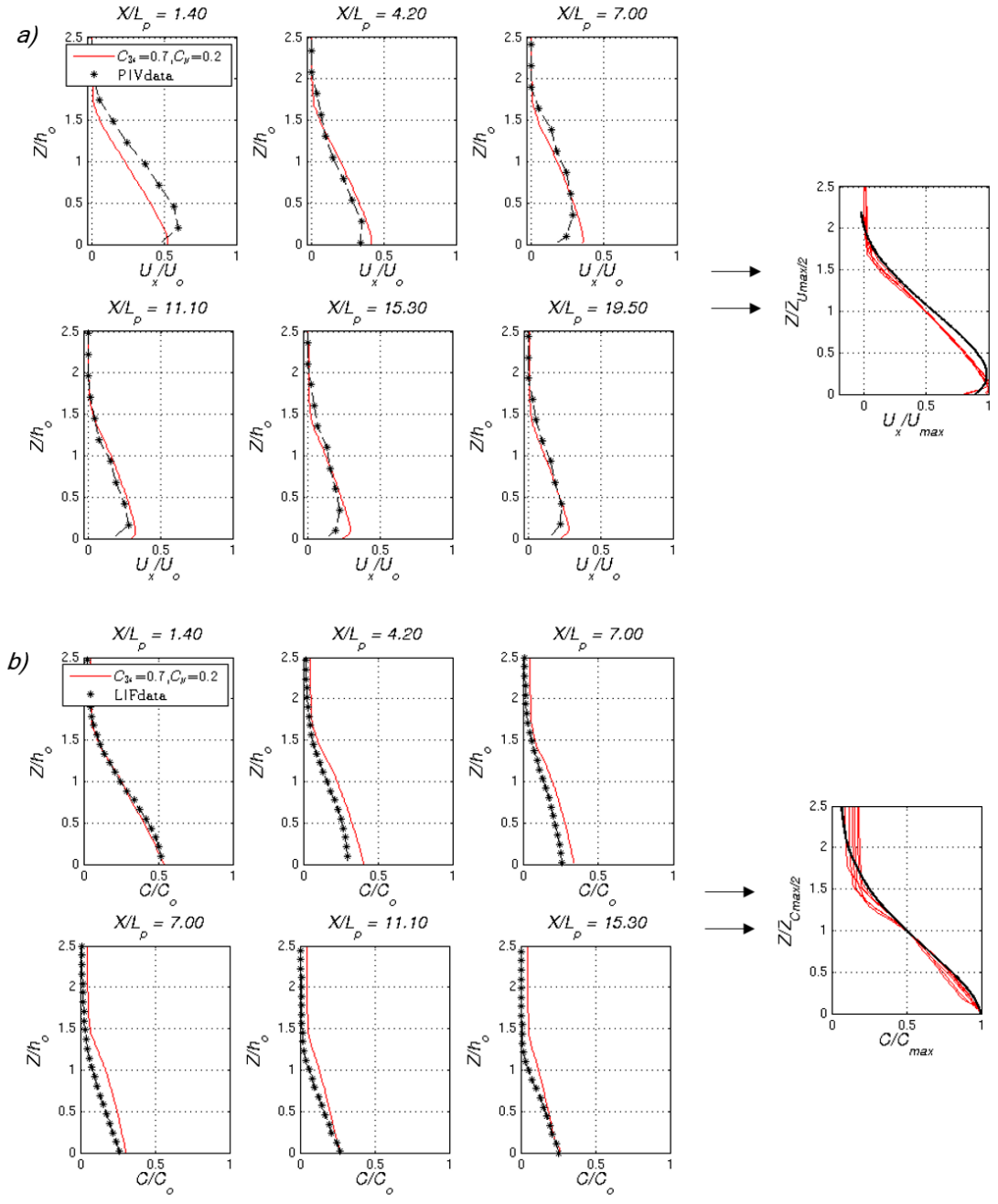

Figura 0.9: Comparativa de los perfiles verticales de a) velocidad horizontal y b) concentración salina, a distintas distancias aguas abajo de la descargas, además de sus correspondientes perfiles de autosimilitud. Las líneas rojas representan los resultados numéricos y las líneas negras punteadas los datos experimentales

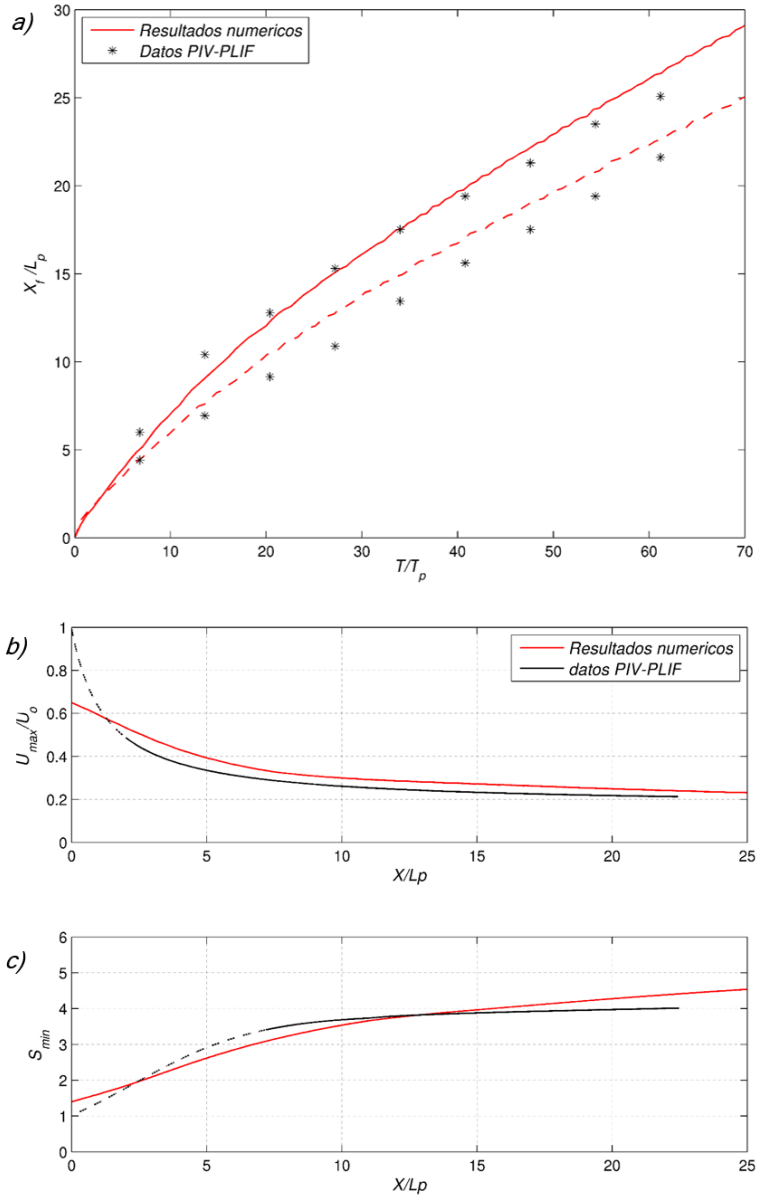

Figura 0.10: Comparativa de a) la evolución de la posición frontal de la corriente de densidad y b) la evolución en el plano de simetría de la velocidad máxima y la dilución mínima. Las líneas rojas representan los resultados numéricos y los asteriscos y líneas negras los datos experimentales

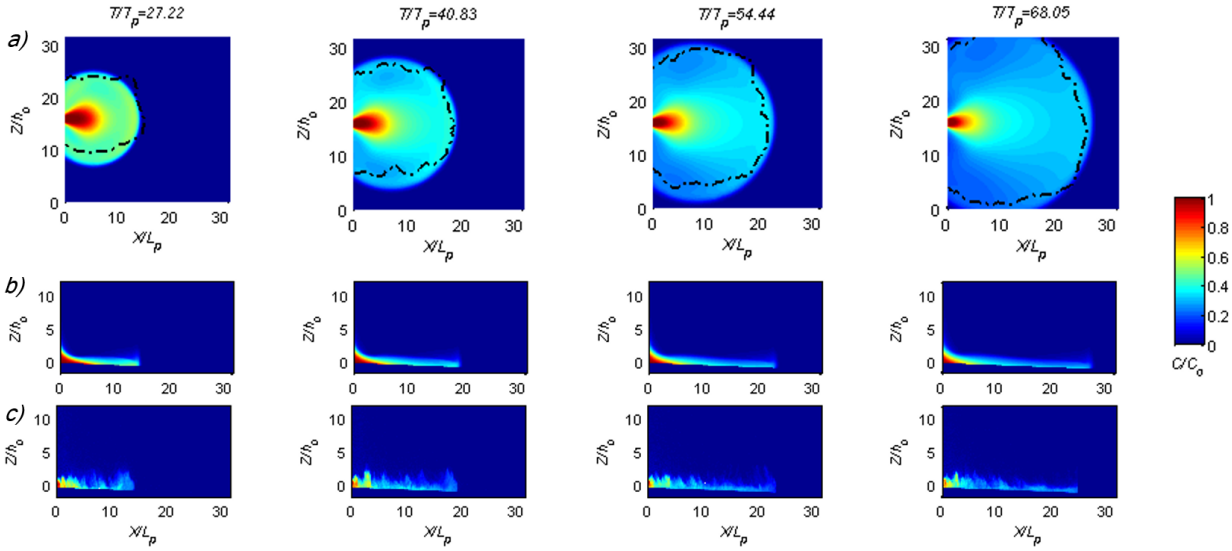

Figura 0.11: Comparativa del avance de la corriente de densidad en diferentes instantes: a) vista en planta (el campo de colores representa los resultados numéricos y las líneas punteadas en negro, los datos experimentales); b) vista en perfil de los resultados numéricos; c) vista en perfil de los datos experimentales

IV. Metodología de modelado acoplado para vertidos de salmuera [34]

Este capítulo presenta una metodología de modelado acoplado para los vertidos objeto de estudio de esta tesis, cuyo procedimiento de acople está basando en un tipo de acoplamiento "pasivo" (DSTL, Choi and Lee (2007)). Debido a que la correcta predicción de este tipo de vertidos no sólo depende del procedimiento de acople entre estos modelos, sino que depende fundamentalmente de la precisión del modelado numérico tanto del campo cercano como lejano, el principal valor añadido de esta metodología radica en que hace uso de modelos o configuraciones de los mismos expresamente validados para este tipo de flujos de flotabilidad negativa. Los modelos utilizados son: las herramientas BrIHne para la simulación del campo cercano (Palomar (2014)), y el modelo hidrodinámico tridimensional

[3]Este sub-apartado resume de manera concisa la metodología y los resultados del Capítulo 4 del documento en inglés, que a su vez esta siendo preparado para ser enviado a una revista científica de revisión por pares. Las conclusiones y aportaciones del capítulo se resumen en la Sección V

[4]Parte del trabajo mostrado en este sub-apartado (i.e. en el Capítulo 4) fue desarrollado durante una estancia de tres meses en el centro I+D HR Wallingford, el cual forma parte del consorcio de gestion del conjunto de programas TELEMAC-MASCARET

TELEMAC-3D para la simulación del campo lejano (véase Capítulo 3 de esta tesis).

El presente trabajo solventa una de las principales carencias detectadas en el estado del conocimiento, siendo ésta la falta de aplicación y validación de las metodologías existentes para casos reales de vertidos de salmuera a escala de campo. Bajo este marco, la metodología descrita se valida mediante la comparación de sus resultados con mediciones de salinidad en la corriente de densidad generada por el vertido de una planta desaladora ubicada en la costa de Gran Canaria, España.

IV.A. Metodología de acoplamiento

La metodología propuesta para evaluar el impacto potencial de los vertidos de salmuera en el medioambiente queda reflejada en el diagrama de la Figura 0.12. En este diagrama, el recuadro naranja de línea punteada recoge los principales pasos de esta metodología: la caracterización medioambiental, tanto a escala regional como a escala local, el modelado del campo cercano (NF), el procedimiento de acople y, finalmente, el modelado del campo lejano (FF) y la visualización de sus resultados. Los pasos metodológicos mencionados son detallados en este capítulo, primero, de manera teórica y, después, de manera práctica mediante la aplicación paso a paso de la metodología al caso de estudio.

Las bases de datos necesarias para llevar a cabo dicha metodología son: (1) la correspondiente a la planta desaladora, como la ubicación de la descarga, las características de la salmuera y las características del dispositivo de descarga; y (2) la referente al medio receptor como la batimetría y la información meteoceánica en la zona de descarga. Mientras las base de datos referente a la planta desaladora alimenta directamente al modelado NF, la base de datos del medio receptor constituye la información requerida por el paso previo, la caracterización mediambiental, el cual genera datos de entrada tanto para el modelado NF como para el modelado FF.

Por tanto, este primer paso de caracterización medioambiental, consiste en analizar las características del medio receptor tanto a escala local, donde se localiza el dispositivo de descarga (es decir, la region de NF), como a escala regional, donde se espera que impacte la corriente de densidad (es decir, la región de FF). La caracterización local consiste en analizar, a la profundidad de la boca del dispositivo,

la velocidad, temperatura y salinidad del agua receptora. Por otro lado, la caracterización regional consiste en analizar la hidrodinámica del área de estudio (es decir, el nivel del mar, las corrientes, la temperatura y la salinidad), así como las condiciones atmosféricas fundamentales (es decir, la presión atmosférica a nivel del

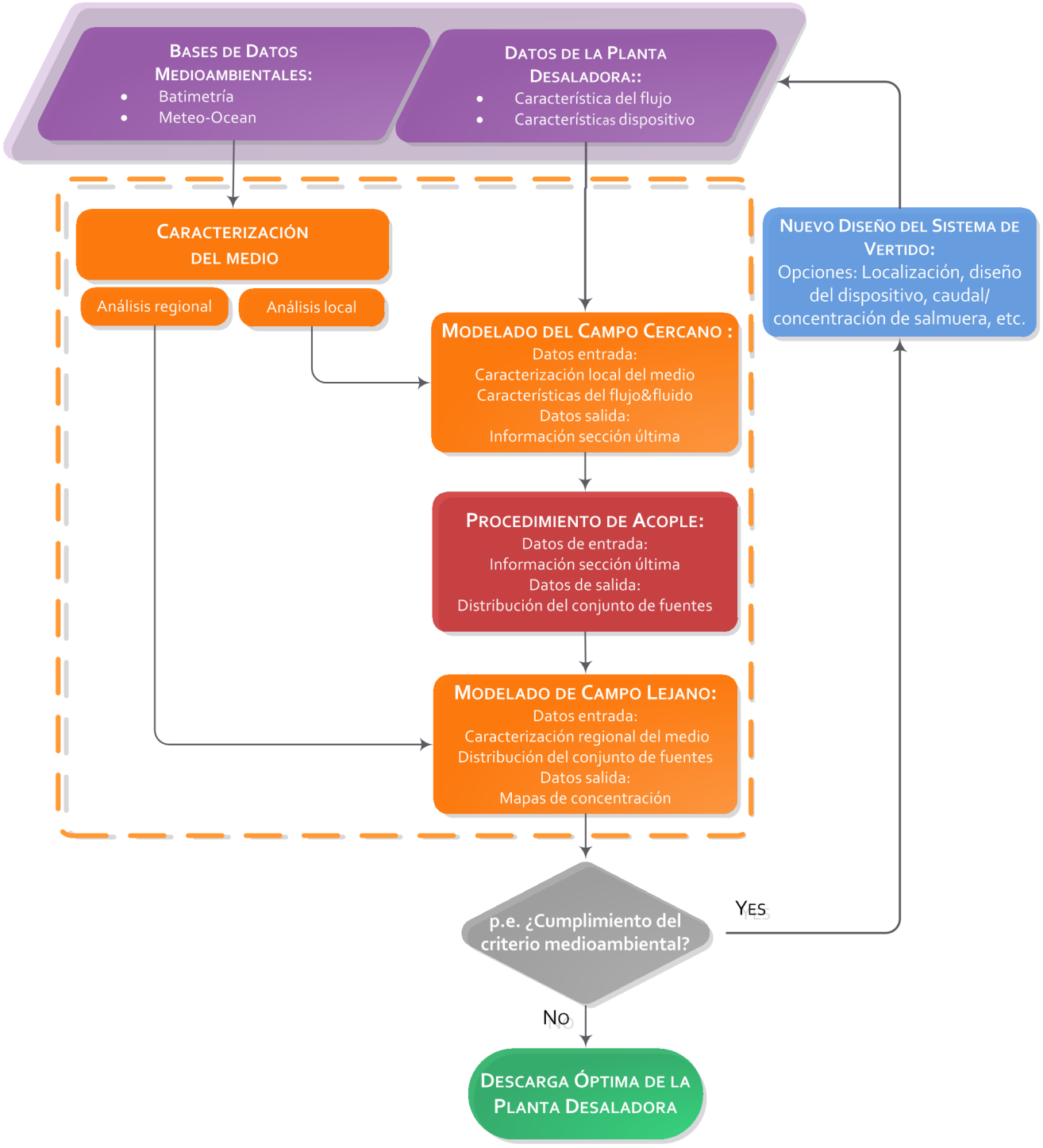

Figura 0.12: Esquema de la metodología para la predicción global de los vertidos de salmuera

mar y el viento). A partir de este análisis regional se generarán las condiciones de contorno y forzamientos atmosféricos para el modelo hidrodinámico tridimensional con el que se modela el FF.

Los siguiente pasos de la metodología propuesta, es decir, el modelado NF, el procedimiento de acople y el modelado FF, son los encargados de llevar a cabo la predicción del comportamiento del vertido propiamente dicha. Para ello, se hace uso de las herramientas numéricas mencionadas, BrIHne y TELEMAC-3D, así como de una estrategia de acoplamiento expuesta a continuación.

El procedimiento de acople entre ambos modelos, es decir en la estrategia numérica encargada de dar continuidad y dinamismo del modelado de estos vertidos, se basa en la conversión de los datos de salida del modelo NF en datos de entrada del modelo FF. Este procedimiento queda detallado con base en sus principales aspectos dinámicos, temporales y espaciales:

- Aspectos dinámicos:

  El procedimiento de acople utilizado consiste en especificar una descarga tipo fuente en aquellos nodos del dominio de cálculo del campo lejano situados al final de la región del campo cercano. Las magnitudes de la descarga a especificar en el domino del campo lejano dependerán de la información de salida del la herramienta BrIHne utilizada (BrIHne-Jet, BrIHne-MJets, o BrIHne-Jet-Spreading). No obstante, las magnitudes fundamentales serán el caudal (Q_{oFF}) y la concentración salina (C_{oFF}), las cuales, teniendo en cuenta el factor de dilución predicho por la herramienta de campo cercano (S) al final del mismo, quedarán definidas por $Q_{oFF} = S \cdot Q_o$ y $C_{oFF} = (C_o - C_a)/S + C_a$, donde Q_o y C_o son el caudal y la concentración del vertido inicial, respectivamente, y C_a la concentración salina del medio receptor.

- Aspectos temporales:

  La variabilidad temporal de estas descargas/fuentes al inicio del campo lejano, es decir, el paso de tiempo del procedimiento de acople (Δt_{CP}), será dependiente de la variabilidad de los datos de salida del modelado NF (Δt_{NF}) y del paso de tiempo de cálculo del modelo hidrodinámico (Δt_{FF}) según la expresión: Δt_{CP}=max(Δt_{NF},Δt_{FF}). Puesto que Δt_{FF} es habitualmente del orden de segundos, Δt_{CP} será, en la mayoría de los casos, equivalente a la variabilidad temporal de los datos de salida del modelado NF, Δt_{NF}. Por

tanto, el paso de tiempo del procedimiento de acople (Δt_{CP}) dependerá de la resolución temporal de los datos de entrada de la planta desaladora, y, en el caso de tener en cuenta la influencia de la velocidad del medio receptor en el modelado NF, de la variabilidad de dicha condición ambiental.

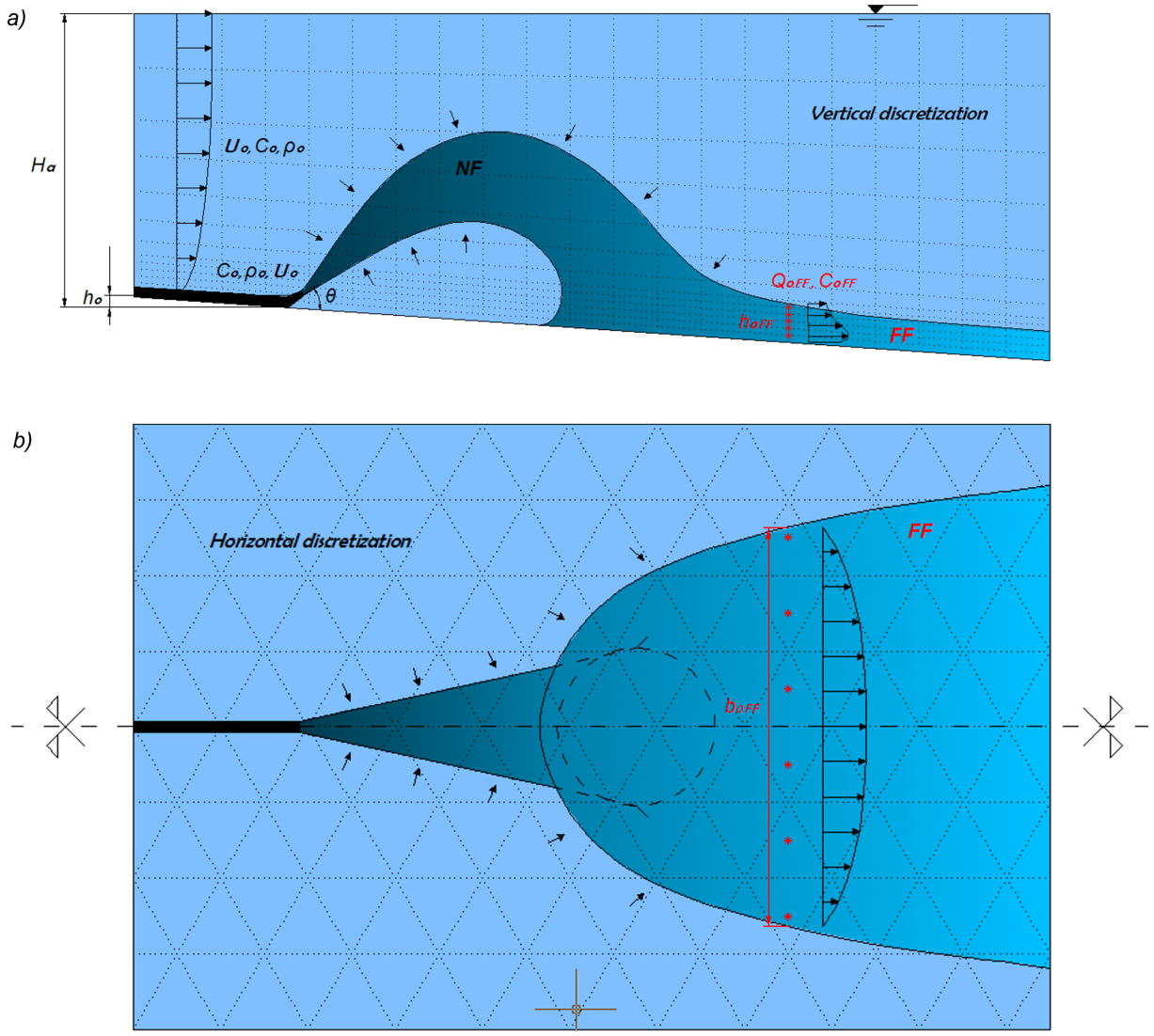

Figura 0.13: Esquema del procedimiento de acople: a) vista en perfil y b) vista en planta

- Aspectos espaciales:

  Teniendo en consideración la aproximación de forma de ranura (Bleninger (2006)) en la última sección de la región de campo cercano ($b_{oFF} \times h_{oFF}$,), así como las recomendaciones para el correcto modelado del campo lejano establecidas en el Capítulo 2, la descarga en el dominio de cálculo del FF

quedará repartida en un número de fuentes determinado (N_s) según la discretización de la zona (véase la Figura 0.13). Por regla general, el caudal y la concentración de cada una de estas fuentes quedará definido por las siguientes expresiones: $Q_i = Q_{oFF}/N_s$ y $C_i = C_{oFF}$. No obstante, en el caso de que la herramienta utilizada para modelar el NF haya sido BrIHne-Jet-Spreading, la cual aporta información de la distribución vertical de la concentración y el caudal en la última región del NF (Palomar (2014)), las magnitudes características de cada una de las fuentes (Q_i y C_i) se establecerán en función de dicha distribución. La Figura 0.13 muestra un esquema en planta y en perfil del procedimiento de acople.

IV.B. Resultados y validación

Gracias a las campañas de campo realizadas en el marco del proyecto I+D Venturi (http://www.proyectoventuri.com/), cuyo objetivo, entre otros, era evaluar la afección de la corriente de densidad generada por el vertido de la planta desaladora de Maspalomas en Gran Canaria, este capítulo lleva a cabo la validación de la metodología propuesta comparando sus resultados con las mediciones realizadas en 7 campañas de campo (en distintos periodos desde el año 2009 al 2011). Por tanto, la validación se realiza para distintas condiciones meteoceánicas y de producción de salmuera de la desaladora.

Cabe resaltar que, durante los periodos de estas campañas, además de la medición de la salinidad en el fondo del área de impacto de la salmuera, se midió el perfil de corriente en un punto en la cercanías del dispositivo de vertido. Gracias a estas mediciones, se llevó a cabo una validación de los resultados numéricos, para la cual se utilizaron dos técnicas: downscalling dinámico mediante el modelo híbrido ROMS-TELEMAC-3D, y el citado downscalling dinámico adaptado para incluir la asimilación de datos medidos. La Figura 0.14 presenta los resultados de ambas validaciones, las cuales, muestran siempre errores $RMSE$ menores de 0.038 m/s.

Debido a que la única referencia temporal de los datos de salinidad de cada campaña es el periodo en el que se ha realizado la misma, es decir, no hay información sobre el instante temporal en el que se midió la salinidad en cada punto, la validación se realizó considerando los valores máximos de salinidad alcanzados en el periodo correspondiente. De esta manera, un resultado coherente sería aquel

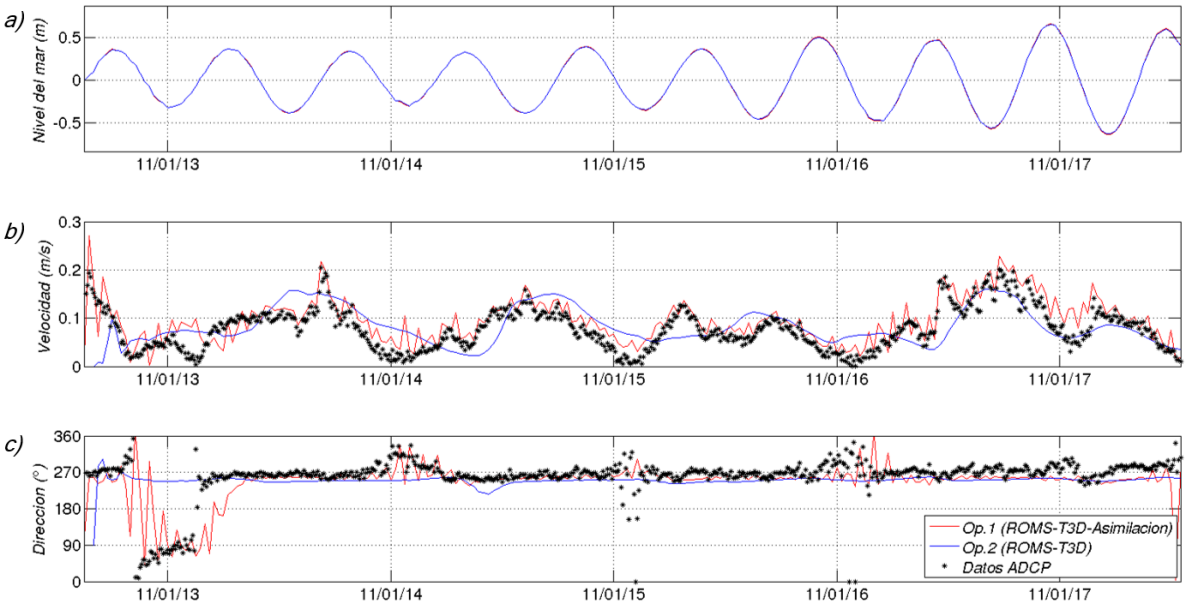

Figura 0.14: Comparación entre los datos medidos por un ADCP en las cercanías al punto de vertido y los resultados numéricos de la caracterización hidrodinámica: a) altura del nivel del mar, b) modulo de velocidad y c) dirección de velocidad

en el que los valores de salinidad medidos dentro de la corriente de densidad sean iguales o inferiores a los valores máximos obtenidos de la modelización numérica.

La Figura 0.15 muestra el mapa de salinidad máxima resultante de la aplicación de la metodología propuesta para una de las campañas, así como las correspondientes mediciones puntuales. A modo de resultado de validación de todas las campañas, la Tabla 0.4 proporciona el porcentaje de las medidas de salinidad que se encuentran dentro de la correspondiente isohalina resultado (para ello se consideran líneas isohalinas equidistantes entre sí 1 *psu*). El menor porcentaje se obtuvo para la campaña $C1$ con un valor de 86.4%, pero se ha de señalar que este caso fue uno de las campañas en que hubo menor número de puntos de medida. Adicionalmente, durante una de las campañas, se realizaron medidas de salinidad en la columna de agua en un punto para un instante determinado. La Figura 0.16 muestra la distribución en planta de la corriente de densidad modelada para ese instante, y la buena correlación obtenida en el perfil de salinidad.

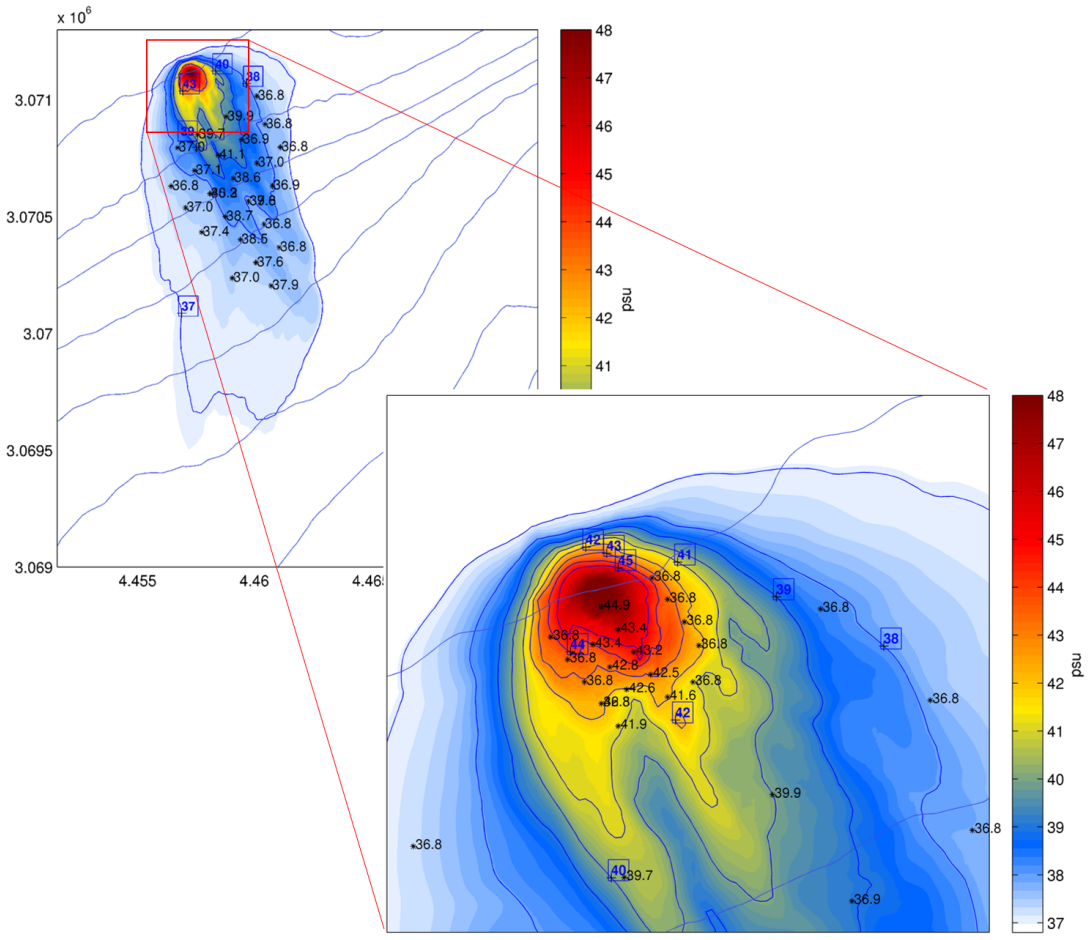

Figura 0.15: Salinidad máxima en el fondo resultante de la aplicación de la metodología propuesta (mapa de colores y líneas de contorno isohalinas) y medidas instantáneas de salinidad (asteriscos) de la campaña *C*7

TABLA 0.4: Porcentaje de valores de salinidad medidos dentro de de la correspondiente línea isohalina

	C1	C2	C3	C4	C5	C6	C7
porcentaje	86.4	92.5	91.6	93.7	100.0	93.5	92.8

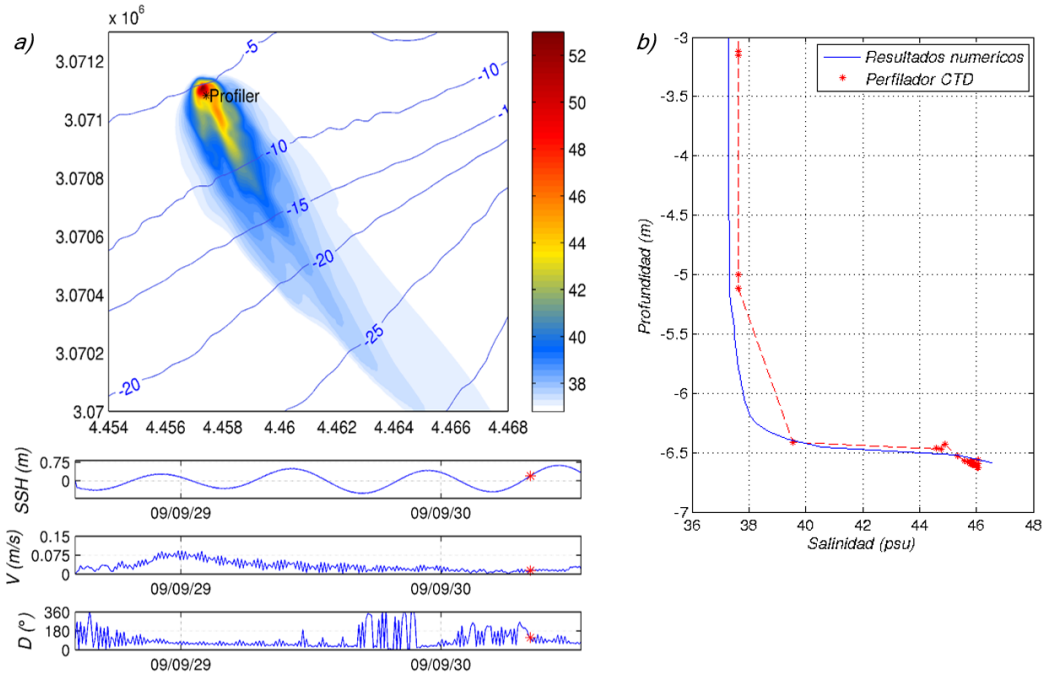

Figura 0.16: a) Mapa de salinidad en el fondo para el instante 30/09/2009 08:16-08:17 (Campaña *C4*) y localización del dispositivo de medida; b) comparación del perfil de salinidad entre las mediciones y los resultados numéricos

V. Conclusiones generales y futuras líneas de investigación

V.A. Conclusiones

El objetivo fundamental de esta tesis ha sido ampliar el conocimiento sobre el comportamiento y modelado numérico en campo lejano de los vertidos de salmuera al mar, así como en el acoplamiento entre los modelos de campo cercano y lejano para su predicción integral.

Este objetivo general se ha alcanzado por medio de la consecución de tres objetivos específicos previamente establecidos en la Introducción. En esta sección se resumen las principales conclusiones obtenidas:

Objetivo 1: Profundizar en el estudio del comportamiento de las corrientes de densidad salina no confinadas

Este objetivo específico fue satisfactoriamente alcanzado gracias a los datos experimentales obtenidos mediante técnicas de medida PIV-PLIF, las cuales resultaron ser un método eficaz para el análisis detallado (de alta resolución temporal y espacial) del comportamiento de corrientes de densidad. Gracias al estudio pormenorizado de los campos de flujo obtenidos en los planos de simetría de las corrientes generadas en el laboratorio, se obtuvo una perspectiva espacial global del comportamiento de los procesos de transporte y mezcla de estas corrientes:

- Del análisis de los campos medios de velocidad se deduce que la misma disminuye bruscamente en los inicios de la corriente de densidad debido a la fricción con el fondo, el fluido circundante en reposo y a su expansión lateral. De la misma manera, las fluctuaciones turbulentas también presentan valores más altos en la zona cercana a la ranura de descarga, desvaneciendose rápidamente aguas abajo revelando el colapso de las escalas de turbulencia de mayor escala. Puesto que se observaron resultados análogos en los campos de concentración, se deduce que la transferencia de masa por difusión turbulenta tiene lugar en las cercanías a la ranura de descarga, donde existe el mayor esfuerzo cortante entre ambos fluidos

- Analizando la estructura vertical de las principales magnitudes, velocidad y concentración, se concluye que este tipo de flujos presentan propiedades autosimilares a cualquier distancia aguas abajo. Los valores de parámetros de forma atendiendo a los perfiles de concentración son $S1 : 0.7 - 0.86$; $S2 : 0,57 - 0,77$. Estos valores que corresponden a perfiles con forma suave, propios de corrientes de densidad en régimen supercrítico.

- El análisis de la estructura vertical de las fluctuaciones turbulentas de la velocidad en diferentes localizaciones aguas abajo de la descarga, muestra que la zona común de mínima turbulencia se ubica a la misma altura respecto del fondo que las máximas velocidades. Bajo esta ubicación se encuentra la zona donde las fluctuaciones de la concentración son mínimas, es decir donde existe menor transferencia de masa por difusión turbulenta.

- Mediante un análisis (en ordenes de magnitud) del intercambio de energía existente en el seno de las corrientes de densidad estudiadas, se observa que

las mismas presentan un estratificación estable (con rango de número de Richardson de 10^{-1} a 1) con números de Schmidt cercanos a 1.

- A través de la evaluación de los perfiles longitudinales de velocidad y concentración máxima, se observa la exitencia de un "Estado Normal" a partir de una distancia aguas abajo de la ranura de descarga común para las corrientes generadas.

- Una vez alcanzado el "Estado Normal" citado, se observa que las tasas de dilución (expresadas cuantitativamente en función del parámetro "Entrainment" E_N) alcanzan un valor cuasi constante. Debido a que los valores de E_N obtenidos coinciden con parametrizaciones existentes en la literatura científica deducidas a partir de corrientes de densidad confinadas, este estudio demuestra que la dilución obtenida en el plano de simetría de corrientes de densidad no confinadas es fundamentalmente resultado de los mecanismos de mezcla verticales y no resultado de la mezcla lateral (lo cual coincide con las observaciones de Yuan et al. (2013))

- De la comparación de los valores de la tasa de dilución obtenida una vez alcanzado el "Estado Normal" (es decir, el parámetro E_N), se concluye que las mayores pendientes del fondo y las descargas con mayor cantidad de movimiento inicial favorecen la dilución. Concretamente se muestra que la dilución mínima obtenida en la última sección (S_{minF}) de las corrientes de densidad estudiadas aumenta en torno a $1,6$ veces cuando la cantidad de movimiento inicial se duplica y en torno a $1,6$ veces para cada unidad porcentual que aumenta la pendiente del fondo. Por el contrario, S_{minF} se ve reducida en torno a $\sim 0,9$ veces cuando la flotabilidad inicial se triplica.

- Mediante la comparación de los resultados numéricos obtenidos de la aplicación del modelo de ecuaciones integradas basado en Alavian (1986) y las mediciones de las corrientes de densidad estudiadas, se concluye que este modelo no es capaz de predecir correctamente el comportamiento de dichas corrientes no confinadas

Objetivo 2: Establecer una configuración numérica óptima para el modelado de corrientes de densidad no confinadas

Un exahustivo análisis de sensibilidad a los principales aspectos numéricos que pueden afectar a la correcta predicción de este tipo de flujos, así como la validación de sendos resultados numéricos con sus correspondientes datos experimentales, ha permitido, efectivamente, establecer la configuración numérica clave para el modelado de corrientes de densidad con modelos hidrodinámicos tridimensionales. A continuación se detalla dicha configuración en forma de recomendaciones numéricas:

- Es necesario contar con una alta discretización horizontal fundamentalmente en las cercanias de la descarga-fuente, por lo que es aconsejable utilizar mallas no estructuradas que permitan diferentes resoluciones horizontales en el dominio de estudio para así hacer computacionalmente viables (en cuanto a tiempos de ejecución) las simulaciones numéricas a escala de campo. Suponiendo una descarga en forma de ranura (dimensiones $b_0 \times h_0$), una resolución horizontal mínima de al menos el ancho de la ranura b_0 es necesaria para tratar de conservar la de cantidad de movimiento y de masa.

- Asímismo, una alta resolución vertical es necesaria para evitar difusión numérica. Teniendo en cuenta el tipo de corrientes de densidad objeto de estudio en este trabajo, el espaciamiento vertical debe ser al menos de $h_0/16$ en la totalidad del espesor de la corriente de densidad, para lo cual es necesario utilizar coordenada vertical de tipo sigma. Dado que mantener esta resolución tan fina en la columna de agua en todo el domino de estudio seria computacionalmente prohibitivo, se recomienda un espaciamiento vertical gradual, perdiendo resolución hacia la superficie.

- A la hora de definir la/s fuente/s de la descarga, se recomienda aportar información al modelo tanto del caudal de descarga como de la velocidad de la descarga ($Q\&V$).

- Se considera que la hipótesis de presión hidrostática es asumida correctamente para aquellos casos con batimetrías sin grandes gradientes, lo cual reducirá significativamente los tiempos de ejecución (tiempos $1.5 \sim 2$ veces menores que los casos equivalentes que no asumen la citada hipótesis).

- Se recomienda el uso del modelo de turbulencia Constante en la dimensión horizontal ($TCMh$), variando los valores de sus coeficientes (es decir, eddys viscossity y diffusivity) según la discretización horizontal.
- Debido a la demostrada influencia del modelo vertical de turbulencia ($TCMv$) en la reproducción de este tipo de flujos, se ha de prestar especial atención a su elección. Tanto el modelo Constante, los modelos de longitud de mezcla como el modelo κ - ε pueden ser correctamente utilizados tras un previo proceso de calibración. Específicamente, para los casos analizados en este estudio, el modelo κ - ε calibrado (constantes empíricas $c_{3\varepsilon}$ y $c_{\ mu}$ igual a ~ 0.7 y ~ 0.2, respectivamente) en conjunción con el esquema de advección más conservador para las ecuaciones κ - ε, proporciona los mejores resultados. Debe tenerse en cuenta que el uso del modelo de turbulencia κ - ε, que añade dos ecuaciones más al sistema de ecuaciones a resolver, es computacionalmente más demandante que el resto de los modelos. Tanto el modelo de longitud de mezcla como el modelo Constante pueden dar buenos resultados en un plazo de tiempo más razonable para aplicaciones de campo.

Los resultados de la validación llevada a cabo en este estudio demuestran que, mediante la aplicación de estas pautas/recomendaciones numéricas, los modelos hidrodinámicos tridimensionales como TELEMAC-3D pueden reproducir el comportamiento de las corrientes de densidad bajo condiciones controladas de laboratorio con errores inferiores a 1.3% para los valores de dilución máxima y 6% para los valores de velocidad máxima.

Objetivo 3: Implementar una metodología de acople entre los modelos de campo cercano y lejano

Finalmente, esta tesis implementa una metodología numérica para predecir el comportamiento global de los vertidos de salmuera mediante chorro sumergido. Dicha metodología incluye desde la caracterización ambiental (condiciones oceanográficas y atmosféricas) hasta el modelado del campo cercano y su acoplamiento al modelado del campo lejano, haciendo uso de los modelos previamente validados BrIHne y TELEMAC-3D.

Por último, la validación llevada a cabo mediante la aplicación de la metodología al caso de estudio de los vertidos de la desaladora de Maspalomas (Canarias,

España) y la comparación de sus resultados con mediciones de campo, demuestra la aplicabilidad de la misma para casos reales a escala de campo. De esta validación se extraen las siguientes conclusiones específicas:

- La técnica de "downscalling dinámico" utilizada para obtener la caracterización del medio en la zona de interés mediante el modelo híbrido ROMS-TELEMAC-3D, proporciona valores de $RMSE$ de la velocidad en las cercanías a la localización de descarga inferiores a 0.038 m/s. Este valor de $RMSE$ despreciable frente a la velocidad media obtenida en la zona, asegura una correcta predicción de las condiciones hidrodinámicas que pueden afectar a la corriente de densidad hipersalina generada.

- Atendiendo a la validación en términos de alcance de la corriente de densidad, la metodología propuesta predice correctamente el comportamiento de la corriente bajo diferentes condiciones del medio, la cual llega a alcanzar zonas alejadas hasta 1500 metros de la localización de la descarga con excesos de salinidad mayores a 1 psu (siempre en favor de la pendiente). Asímismo, se validaron los resultados de salinidad en zonas más cercanas al punto de descarga.

- Mediante un conjunto de medidas de salinidad tomadas en un determinado instante a diferentes profundiades, se comprueba que la metodología propuesta también predice adecuadamente tanto el espesor de la corriente de densidad como la distribución de la concentración de sal en la columna de agua.

- Debido a los buenos resultados obtenidos, se concluye que el procedimiento de acople utilizado en esa metodología, es decir, un acoplamiento "pasivo" en el que la información de la sección última del campo cercano se reparte en el dominio de cálculo del campo lejano siguiendo las recomendaciones establecidas en el Capítulo 3 de esta tesis, es un procedimiento de acople óptimo para este tipo de vertidos.

V.B. Futuras líneas de investigación

Los estudios llevados a cabo durante esta tesis han conducido al planteamiento de las siguientes líneas de investigación.

Atendiendo a la caracterización experimental:

- Teniendo en cuenta que la batimetría es uno de los factores determinantes en la evolución del comportamiento de las corrientes de densidad hipersalina, sería recomendable realizar experimentos adicionales con una amplia gama de pendientes del fondo y con obstáculos que imiten gradientes de batimetría acusados, que son comunes en los fondos marinos irregulares.

- Para una mejor evaluación de la dispersión lateral de corrientes de densidad salina no confinadas, sería recomendable repetir los experimentos presentados en esta tesis tomando medidas PIV-PLIF en planos perpendiculares al plano de simetría (es decir, perpendiculares a la dirección principal del flujo). Otra opción sería aplicar técnicas de medición PIV-PLIF tridimensionales.

- Teniendo en cuenta el comportamiento de los efluentes de la salmuera tanto en la región de campo cercano como en de campo lejano, es aconsejable diseñar y llevar a cabo un conjunto de experimentos que cubran ambas regiones bajo diferentes condiciones iniciales de descarga y del medio receptor. Recientemente, Palomar (2014) y Costa González (2016), estudiaron en detalle la región intermedia asociada al final del campo cercano, sin embargo, un estudio más exhaustivo considerando la región de campo lejano es aún necesario.

Atendiendo al modelado numérico del campo lejano:

- Mediante la realización de pruebas de sensibilidad numérica adicionales bajo una amplia gama de condiciones de descarga inicial, establecer una regla general que permita definir la discretización horizontal y vertical mínima necesaria al inicio de la región de campo lejano. Dicha regla general podría sustentarse en base a algún parámetro significativo relacionado con los procesos de mezcla como son los números adimensionales de Richardson o Péclet.

- Debido a que en las regiones donde existen acusados gradientes batimétricos la difusión numérica puede convertirse, erróneamente, en el proceso de mezcla gobernante, es necesario realizar pruebas de sensibilidad adicionales respecto a la discretización del dominio, los modelos de turbulencia y la validez de la asunción de la hipotesis de presión hidrostática.

- Se propone investigar el uso de discretizaciones verticales flexibles capaces de evolucionar en el tiempo y en el espacio en función de una variable física, en este caso, el gradiente de densidad. El modelo hidrodinámico utilizado en este estudio, TELEMAC-3D, cuenta con dicha opción, denominado método AMR (procedente de las siglas en inglés de "Automatic Mesh Redistribution method"), basado en una generalización del tradicional sistema de coordenadas sigma (Mead et al. (2011)).

- Pruebas de sensibilidad adicionales considerando el modelo de cierre de turbulencia LRN-κ - ε (es decir, para flujos de bajo número de Reynodls)(Hwang and Lin (1998)), mediante el cual se puede mejorar el modelado de las capas más profundas, es decir las adheridas a los fondos marinos (capa límite)(Paik et al. (2009)).

Atendiendo al modelado numérico acoplado de la región de campo cercano y lejano:

- Llevar a cabo un estudio comparativo entre los procedimientos de acoplamiento "pasivo" y "activo" para distintos vertidos de salmuera que difieran en el caudal de descarga.

- Adaptar la metodología de acople propuesta a vertidos de flotabilidad positiva, como los vertidos de aguas residuales urbanas o vertidos térmicos. De esta manera, tras un estudio de validación similar al expuesto en esta tesis para vertidos de flotabilidad negativa, se desarrollaría una herramienta genérica y por tanto útil, para estudiar vertidos de cualquier índole (dentro de los vertidos de sustancias disueltas).

- Ya que los modelos hidrodinámicos tridimensionales como TELEMAC-3D están robustamente acoplados a modelos del estado del arte que resuelven otras dinámicas, como los modelos de calidad de aguas, oleaje y atmosféricos; la presente metodología podría adaptarse para considerar condiciones ambientales adicionales en el caso de ser significativas en la mezcla de este tipo de vertidos.

Chapter 1

Introduction

1.1. Motivation and background

The scarcity of water in highly populated areas near the coast has promoted the construction of many seawater desalination plants to supply with fresh water the local population. Thus, in the last decades, desalination is becoming a fundamental alternative to conventional water sources in coastal areas such as the Mediterranean and the Middle East regions or the coastal waters of California, China and Australia (Cánovas Cuenca (2012); Laspidou et al. (2010) and Dawoud and Al Mulla (2012)). At the time of this thesis, the most important and highest yielding desalination technology worldwide is the seawater reverse osmosis (SWRO), whose main sub-product is brine, an hypersaline effluent which is discharged into the sea and may cause harmful impact on stenohaline marine ecosystems such as Posidonia seagrass (Lattemann and Höpner (2008); Sánchez-Lizaso et al. (2008) and Laspidou et al. (2010), as well as recirculation problems (i.e. brine effluent discharged can reach the seawater intake of the desalination plant affecting the desalination technology efficiency).

So far, due to the lack of regulation regarding brine discharges, diverse discharge configurations, mostly direct surface discharges (e.g. in Figure 1.1a), have been used worldwide. However, environmental concerns regarding brine discharges have increased in the last decade. As a consequence, the recently constructed desalination plants discharge the brine mostly through submerged jet configurations (see an example in Figure 1.1b) in order to increase the momentum gradient between fluids, hence to increase the turbulence and to favour the mixing with receiving

fluid (i.e. the dilution of the brine). Nowadays, the most recent large desalination plants have been designed with brine discharges through submerged multiport inclined jets, in which brine is sometimes also pre-diluted with seawater to increase dilution previously to the discharge.

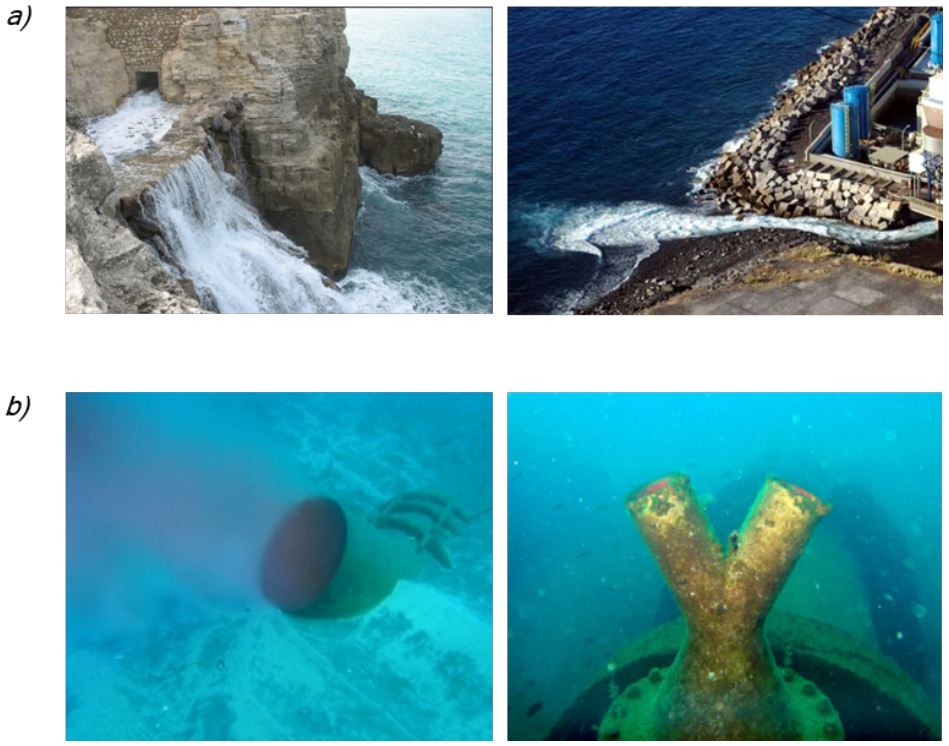

Figure 1.1: Brine discharge configurations: a) direct surface discharges, b) submerged jet discharges. Examples in Spanish desalination plants. Source: CEDEX, ITC, Taxón S.L

The behavior of brine discharges within the marine environment is governed by the negative buoyancy of brine (i.e. more dense than de surrounding water). Nevertheless, two main regions can be differentiated according to the proximity to the discharge point (i.e. according to the spatial and temporal scales of the transport and mixing processes involved) in the developed flow, the so-called Near Field (NF) and Far Field (FF) regions (see Figure 1.2). The NF region is characterized by initial mixing that depends on the brine discharge configuration and the effluent and ambient properties. In this region, flow and mixing characteristics are dominated by small scales (∼metres and ∼minutes), and the highest dilution rates (i.e. mixing rates) due to turbulence effects are found. After an intermediate field, in the FF region the brine turns into a density current that flows down to the seabed with a small dilution rate compared to the NF region. Mixing depends

on the ambient conditions (bathymetry, currents, waves, wind, etc.) and the differences between the flow properties of the saline density current and the receiving waters. In this region, where the flow and mixing characteristics are dominated by large scales, the spatial and temporal extent of the density current can be of the order of kilometers and hours, respectively. Figure 1.3 shows a diagram of the behavior of a submerged jet brine discharge, the most increasingly used discharge configuration, in the NF and FF regions.

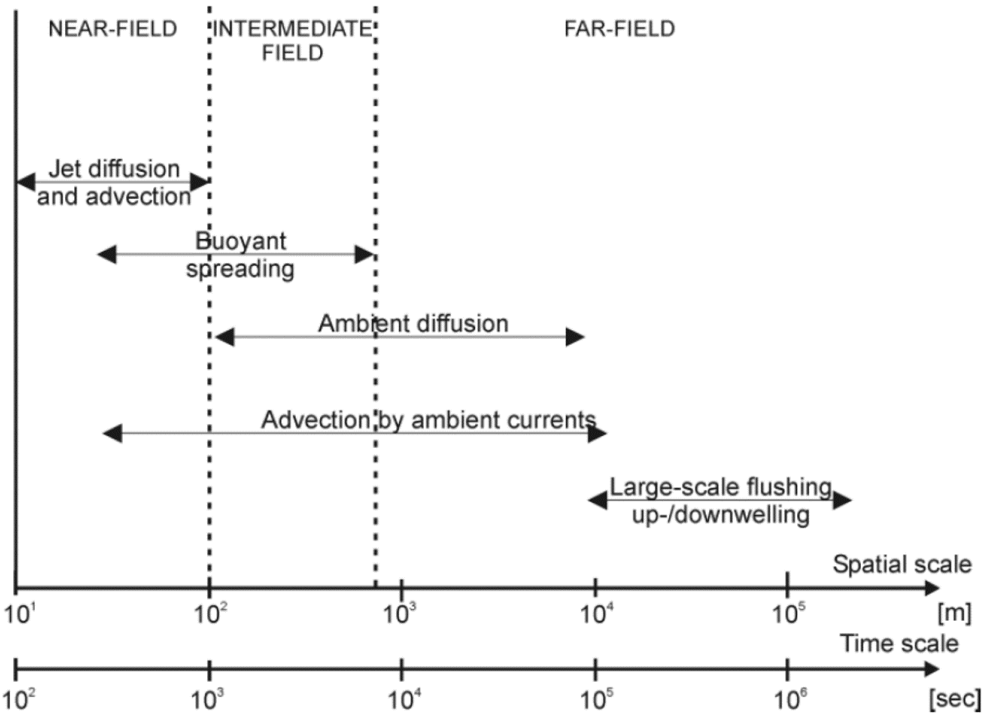

Figure 1.2: Typical temporal and spatial scales for transport and mixing processes related to coastal wastewater discharges. Source: Gerhard H. Jirka, Abrahan, G. and Harleman (1976) and Fischer (1979)

Since the highest dilution rates are obtained in the NF region, the efforts of the scientific community have been mainly focused on the study of this region (experimentally and numerically) and on developing useful modelling validated tools and methodologies to design optimum brine discharge configurations (e.g. Palomar (2014)). Therefore, these optimum discharge configurations or outfall devices are specially designed to achieve maximum dilution and to meet environmental requirements within the NF region.

However, there are cases where the study of the saline density current of the FF region is also required such as those where: (1) minimum dilution required is not achieved in the NF region, (2) there are sensitive ecosystems to brine far

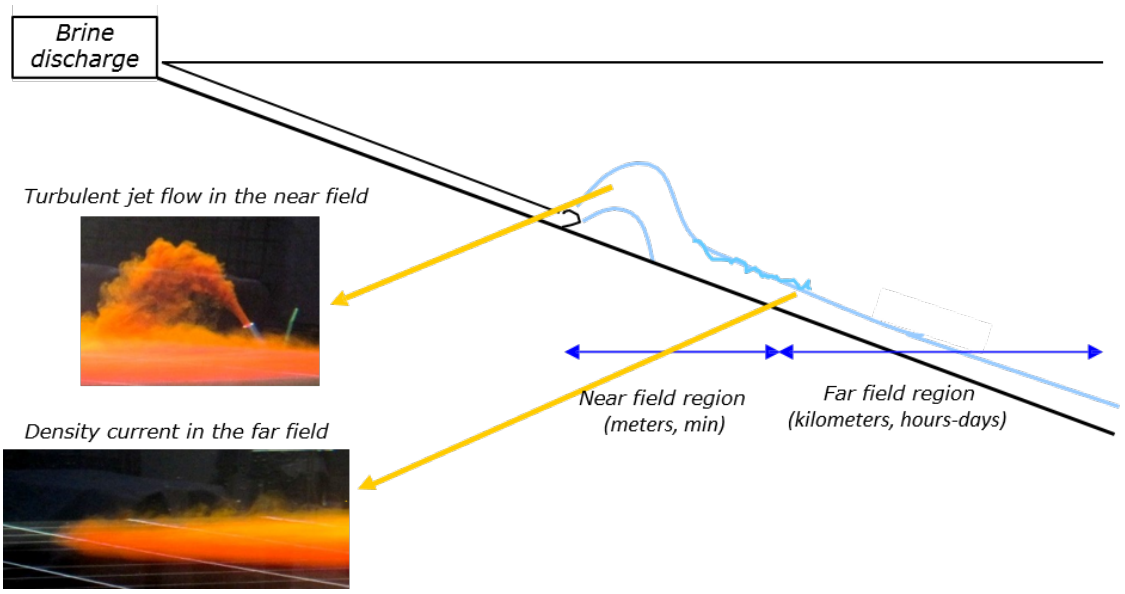

Figure 1.3: Diagram of the behavior of a submerged jet brine discharge in the NF and FF regions. Source: Palomar (2014)

from the discharge point but within the potential impact area of the FF, (3) there is a risk of recirculation problems, i.e. brine effluent discharged can reach the seawater intake, (4) the effluent has chemical pollutants which behavior are governed by different chemical reaction kinetics (e.g. those present in the sub-product of thermal desalination plants, or in membrane cleaning waters of SWRO desalination plants), (5) the discharge configuration consists of a still existing flow-by-gravity discharge which makes the brine behaves as a density current since the beginning.

In these cases, to assess the potential negative impact of brine discharges, a global hydrodynamic study that allow to predict the complex brine effluent behavior far from the discharge point (i.e. both NF and FF regions) is required. Due to the large differences in time and spatial scales mentioned as well as the different conditioning factors, the NF and FF regions have to be separately predicted by using different modelling tools. Therefore, a reliable FF modelling as well as a reliable coupling procedure between NF and FF models is needed to obtain a prediction of the global behavior of brine discharges, covering distance far from the disposal point.

1.2. State of the art

In this section a brief description of the context that involves the three main aspects that this thesis addresses is provided: the FF experimental characterization, the FF numerical modelling and the NF and FF coupled modelling.

1.2.1. FF experimental characterization

For some time now, due to the numerous natural and industrial occurrences of density current motions in the environment (Simpson (1982, 1997) and Huppert (2006)), several studies have aimed at understanding the behavior of these flows, such as saline or turbidity density currents, by means of laboratory experimental studies.

Different experiments and analysis have been addressed in the scientific literature regarding the continuity of the flow regime. Lock-exchange flows (i.e. those generated by fixed volume) in horizontal flumes (Kneller et al. (1999)) were extensively studied focusing on the dynamics of the current head and its evolution (Huppert and Simpson (2006); Maxworthy and Nokes (2007); Nogueira et al. (2014); Nokes et al. (2010); Özgökmen and Chassignet (2002) and Ottolenghi et al. (2016)). On the other hand, constant-flux release experiments have been mainly focused on analyzing the quasi-steady state conditions within the current body. Ellison and Turner (1959) and other later works (Garcia (1993); Parker et al. (1987) and Hosseini et al. (2006)) obtained the quasi-steady (or equilibrium) mean flow properties, such as the mean vertical structure (or cross sections) of velocity and concentration. More recently, Sequeiros (2012) compiled an extensive database of velocity and concentration measurements of density currents of diverse nature obtained from different published works. Moreover, taking advantage of high-resolution measuring techniques, a considerable amount of studies has been focused on the turbulent structure of these quasi-steady state flows (Gerber et al. (2011)), comparing the behavior of saline and turbidity density currents (Gray et al. (2006) and Islam and Imran (2010)).

To elucidate the quasi-steady characteristics of the mixing mechanism in this kind of constant-flux currents, experimental studies such as Cenedese and Adduce (2008) and field studies such as Dallimore et al. (2001); Hebbert et al. (1979)

and Fernandez and Imberger (2006) were undertaken based on the analysis of the entrainment of the surrounding fluid into the density current (Princevac et al. (2005); Turner (1986) and Wells et al. (2010)). Cenedese et al. (2010); Kashefipour et al. (2010) and Chowdhury and Testik (2014) gathered the large number of entrainment parameterizations that have been developed during the last decades, all of them being functions of the Richardson number (the ratio of the buoyancy term to the flow gradient term). Some of these parameterizations also reflect the influence of the bottom topography in terms of bottom friction coefficient, C_D, and bottom slope, α. Nevertheless, most of the aforementioned entrainment parameterizations have been obtained from experimental two-dimensional density currents (i.e. laterally confined). For non-confined density currents, some studies used axisymmetric configurations which were forced to spread cylindrically (Britter and Simpson (1978) and Patterson et al. (2006)) while others such as La Rocca et al. (2008) used initially channelized discharge configurations. However, these works studied the front spreading characteristics locally, and not the general entrainment characterization. As far as the authors of this present work are aware, only MacDonald and Chen (2012) and Yuan et al. (2013) have tried to isolate the effect of spreading on the mixing mechanism in thermal density currents, in addition to analyzing the quasi-steady state vertical structure.

To overcome the shortcomings regarding the spatial coverage of the available data in the scientific literature, even more evident taking into account non confined density currents as those generated in the FF region of brine discharges, the present thesis shows an experimental characterization of the guasi-steady flow properties of saline density currents using PIV (Particle Image Velocimetry) and PLIF (Planar Laser Induced Fluorescence) measurement techniques (Martin and Garcia (2008) and Liao and Cowen (2010)).

1.2.2. FF numerical modelling

Due to the growing interest in predicting behavior of humand-induced density current on the environment, major efforts have been undertaken to numerically reproduce their behavior using different modelling techniques. As a broad classification, two modelling techniques are available for studying these flows numerically: integral models, and those which solve the vertical structure of the flow. The concept of the integral model for density currents was introduced by Ellison and

Turner (1959) and further developed by Alavian (1986) and Parker et al. (1986), among others. In general, integral models assume a hydrostatic pressure distribution within the current and use vertical depth-integrated equations. On the other hand, those models which solve the vertical structure of the flow are based on the resolution of 3D Navier-Stokes (N-S) equations with different degrees of simplification.

Since Ellison and Turner (1959), integral models have been significantly developed, mainly focusing on turbidity currents (Akiyama and Stefan (1985); Bradford et al. (1997); Choi and Garcia (1995); Garcia (1993); Imran et al. (1998); Parker et al. (1986) and Choi (1999)). Recently these models have been designated as single or double-layer shallow water models depending on whether they consider only the heavier layer (e.g. Ungarish (2007a)) or divide the entire depth into two layers (Ungarish (2008)). Taking into account three-dimensional (i.e. non-confined) density currents, Ungarish (2007b) and La Rocca et al. (2008) performed numerical analysis to validate their single-layer shallow water models against experimental data. La Rocca and Pinzon (2010) and La Rocca et al. (2012) proposed using double-layer shallow water models for three-dimensional density currents, and Adduce et al. (2012) presented a modification considering a new entrainment formulae between the two fluids.

The vertical distribution of the main variables of density current has been numerically analyzed with hydrodynamic models that solve N-S equations taking into account the Reynolds approximation (Reynolds Averaged Navier-Stokes Equations, or RANS). In these applications, a turbulence closure model is required to estimate the Reynolds stress in conjunction with wall functions. Stacey and Bowen (1988a,b) solved the vertical distribution of one-dimensional turbidity currents using a mixing length model as the Turbulence Closure Model (TCM). Other authors employ the κ-ε model (Rodi (1984)) as the TCM (e.g. Brø rs and Eidsvik (1992); Eidsvik and Brø rs (1989) and Choi and Garcia (2002)). The κ-ε TCM has also been applied to density currents plunging into reservoirs by Farrell and Stefan (1988) and Bournet et al. (1999). In recent years, a number of Direct Numerical Simulations (DNSs) of density currents have been reported in the literature (e.g. Birman et al. (2005); Cantero et al. (2006); Härtel et al. (2000); Lowe et al. (2005) and Cantero et al. (2007)). Since DNSs are prohibitively expensive in terms of computational time, specially when considering field-scale simulations, other authors like Patterson et al. (2005) and Patterson et al. (2006) conducted

bi- and three-dimensional simulations of axisymmetric density currents using an implicit Large-Eddy Simulation (LES) (Almgren et al. (1996)), relying on the use of Subgrid Scale modelling (SGS). However, Paik et al. (2009) revealed that, for moderately fine computational meshes, the Unsteady Reynolds Averaged Navier-Stokes (URANS) equations closed with a buoyancy corrected Low-Reynolds Number (LRN) κ-ε (Hwang and Lin (1998)) can achieve similar results to DNS and LES simulations.

Integral models are acceptable for those field-scale practical purposes in water resources management where only a coarse approximation of the characteristic flow quantities at an equilibrium state is required. One the other hand, the most sophisticated numerical approximations (e.g. DNS and LES) are highly time-demanding computationally demanding and they are therefore usually applied at laboratory scale under controlled conditions. Bombardelli and García (2002) assessed the potential development of density currents in the Chicago River using an intermediate complexity 3D hydrodynamic model in order to capture the spatial variability and complexity. Kulis and Hodges (2006) carried out a layer-number sensitivity test to simulate a density current in Corpus Christi Bay in Texas using a sigma-coordinate 3D hydrodynamic model based on RANS equations and taking into account the Boussinesq approximation and the Hydrostatic hypothesis. Applying similar 3D hydrodynamic models, Firoozabadi et al. (2009) and Mahgoub et al. (2015) simulated density currents and validated their results against laboratory measurements. However, none of the reviewed works related to density currents simulations with 3D hydrodynamic models are fully validated, i.e. considering both the spreading and the vertical structure of the main flow variables (velocity and concentration).

In this thesis, a sensitivity analysis related to the numerical aspects of a 3D hydrodynamic model based on 3D shallow water equations are conducted to properly simulate non-confined density currents such as those generated in the FF region of brine discharges.

1.2.3. NF-FF coupled modelling

In recent years, due to the increasingly installation of new discharge devices that enhance the mixing of the effluent in the NF region(i.e. submerged jets), several studies have been focussed on the numerical modelling of this region and, to a

lesser extent, on the coupled modelling procedure between numerical tools for both the NF and FF region.

Regarding the NF region, several commercial software have been used to provide an approximate prediction of submerged discharges behaviour: VISJET (Cheung et al. (2000)), CORMIX (Doneker and Jirka (2001)) and VISUAL-PLUMES (Frick (2004)). Although these tools, based on dimensional analysis and integration of differential equations, were programmed and validated for simulating the flow of positively-jets, they have been also used for modelling negatively buoyant jets arising from brine discharges. More recently, a new set of tools called BrIHne (www.BrIHne.ihcantabria.com), based on mathematical approaches scientifically supported for brine effluents (Palomar et al. (2013)), have been developed and validated with experimental tests (Palomar (2014)). Several research works such as Oliver et al. (2008); Plumb (2008) and Garcia Alba (2011) used computational fluid mechanics advanced models as the CFD FLUENT to achieve approximate predictions for single port discharges. However, although very refined information can be extracted from them, these models are still very time-consuming compared to the integral model approach.

In the scientific literature there are a few research works regarding the coupling procedures of NF and FF models, mainly focused on waste water and thermal single port discharges (i.e. positively buoyant effluents). Most of the FF models used in these coupling procedures are those that take into account the real ambient conditions (i.e. bathymetry and meteo-ocean conditions), such as the 3D hydrodynamic models Delft3D-Flow (Roelvink and Van Banning (1994) and Hydraulics (2005)) and TELEMAC-3D (Hervouet (2007)). Overall, there are two main coupling strategies, the "passive" and "active" coupling. The most current and realistic version of "passive" coupling consist of introducing the values of diluted concentration and/or flow rates determined by the NF model at specific locations of the FF model as source terms (Zhang and Adams (1999)). Choi and Lee (2007) refers to this procedure as "Diluted Source at Trapped Level" (DSTL) and was applied in the algorithm developed by Bleninger (2006) to couple the NF model CORMIX and the FF model Delft3D (Hydraulics Delft (2001)). It is noteworthy that "passive" couplings are suitable for relatively small discharges, whose NF characteristics do not change the flow characteristics of the FF (Stamou and Nikiforakis (2013)). For thermal discharges, whose large flow rates may affect significantly the flow field in FF and vice versa, Choi and Lee (2007) and Stamou

and Nikiforakis (2013) developed similar "active" couplings that are capable to introduce the NF action on the ambient flow by a collection of sink/sources along the jet trajectory and a diluted source at the terminal level. Although Nikiforakis and Stamou (2015) adapted the coupling procedure developed by Stamou and Nikiforakis (2013) for brine discharges, this procedure has not been validated with real field measurements of this kind of effluents. Recently, NF and FF modelling using coupling procedures has been validated for brine discharges by Wood et al. (2014). The authors considered brine generated from salt cavern leaching operations, which result in high salinity, or "hypersaline" brines. They found that "passive" coupling with TELEMAC-3D produced good comparisons with field measurements of salinity in the FF region.

Due to the fact that there are few coupling procedures, and they are not validated for negatively-buoyant discharges from desalination plants, the present thesis propose a coupled modelling methodology using separately validated models BrIHne and TELEMAC-3D taking into account a "passive" strategy. In addition, the methodology is validated through concentration field measurements from a real desalination plant.

1.3. Objetives of the thesis

The general objective of this thesis is to deepen into the knowledge of the behaviour of negatively-buoyant plumes within coastal waters as well as into their numerical modelling in order to predict their behaviour. To achieve this general objective, three specific goals will be addressed:

- **Objetive 1: To deep into the knowledge of the behaviour of non-confined saline density currents** and to assess the influence of the initial conditions through an experimental analysis using advanced optical techniques.
- **Objetive 2: To establish an optimum numerical set-up to model non-confined saline density currents** and its validation with experimental databases.
- **Objetive 3: To implement a coupling methodology between NF and FF models** using the previous proposed numerical set-up to predict

the global brine effluent behavior and to validate the procedure with field data.

1.4. Layout of the thesis

The structure of the thesis is organised as follows:

The present chapter (**Chapter 1**), describes the motivation for this research and provides some background for a better understanding of the next sections. At the end of this chapter, the specific objectives outlined above and the sections where they are addressed, are described.

The following three chapters (**Chapters 2, 3 and 4**) address the specific objectives of the thesis. Each of the chapters includes an abstract, an introduction, a description of the methodology framework, as well as the results and main conclusions. Following, a brief abstract of the research carried out at each chapter is described:

- **Chapter 2. PIV-PLIF global characterization of non-confined saline density currents under different flow conditions**

  This chapter shows an experimental global characterization of the quasi-steady flow properties of non-confined constant-flux saline currents using non-intrusive PIV (Particle Image Velocimetry) and PLIF (Planar Laser Induced Fluorescence) techniques carried out in the IH Cantabria's facilities. In addition, this characterization includes the study of the influence of the bottom slope and the initial flow conditions such as the flow rate, the thickness and the saline concentration, on the density current behavior.The high-quality database presented in this chapter is a key tool for calibration/validation of different numerical approximations, such as integral models and 3-Dimensional hydrodynamic modelling.

  The work developed in this chapter has been submitted to Journal of Geophysical Research - Oceans:

  Pérez-Díaz, B., Palomar, P. and Castanedo, S. (2017). PIV-PLIF global characterization of non-confined saline density currents under different flow conditions.

- **Chapter 3. Modelling non-confined density currents using 3D hydrodynamic models: finding the key numerical set-up**

  This chapter focuses on the establishment of a proper configuration of 3D hydrodynamic models to reproduce the transport and mixing processes that occur in density current flows. Through a comprehensive sensitivity analysis based on the reproduction of a density current, a set of recommendations regarding the main numerical aspects such as the domain discretization, the momentum-source specification, the hydrostatic hypothesis and the turbulence closure models are compiled in this study. Finally, these recommendations are applied to reproduce a set of laboratory-generated density currents such as those detailed in Chapter 2, and their results are validated against their corresponding measurements, showing a good compliance in the evoluction of the main variables' values. This study therefore represents a first step towards the validation of 3D hydrodynamic models used to solve real field-scale saline current flows.

  The work developed in this chapter has been submitted to Journal of Geophysical Research - Oceans:

  Pérez-Díaz, B., Castanedo, S. and Palomar, P. (2017). Modelling non-confined density currents using 3D hydrodynamic models: finding the key numerical set-up.

- **Chapter 4. Coupled modelling methodology of brine discharges. Validation case: Maspalomas desalination plant**

  This chapter presents a coupled modelling methodology using *ad hoc* validated models (i.e. BrIHne and TELEMAC-3D) to accurately predict the Near Field (NF) and Far Field (FF) behavior of brine discharges in an integrated way. Furthermore, the developed methodology is validated against concentration measurements in the brine plume generated by the discharge of Maspalomas desalination plant (Canary Island, Spain) under different environmental conditions. Therefore, this contribution constitutes and advance in predicting the evolution of negatively-buoyant discharges, which is fundamental in the outfall design phase of a desalination plant whose objective is to mitigate the negative effect of brine both in the NF and FF regions.

  This study is under preparation to be submitted for publication in a SCI journal.

Finally, the last chapter (**Chapter 5**) summarizes all conclusions obtained from the present thesis and also suggests future research topics as a continuation of this work.

Chapter 2

PIV-PLIF global characterization of non-confined saline density currents under different flow conditions [1]

Abstract

Saline density currents are a growing worldwide environmental concern due to their increasing occurrence generated by brine discharges and their negative impact on marine ecosystems. The present paper shows an experimental characterization of the quasi-steady flow properties of non-confined constant-flux saline currents using non-intrusive PIV (Particle Image Velocimetry) and PLIF (Planar Laser Induced Fluorescence) techniques. The synchronized nature and the full coverage of the measurements present a novelty in comparison with the previous published works. This global characterization includes the study of the influence of the bottom slope and the initial flow conditions such as the flow rate, the thickness and the saline concentration, on the plume behavior. The results achieved reveal the self-similarity of the mean variables' cross sections and the collapse of higher length scales of turbulence along the density currents. In addition, this study

[1] This chapter is based on: Pérez-Díaz, B., Palomar, P. and Castanedo, S. (2017). PIV-PLIF global characterization of non-confined saline density currents under different flow conditions. Submitted in Journal of Geophysical Research - Oceans (in second review at the time of the thesis publication)

finds the existence of a "Normal Status" from which the vertical mixing becomes the main mixing mechanism in the plane of symmetry of the currents. Regarding the impact of the initial conditions aforementioned, the results show that the mixing increases with higher flow rates and steeper slopes (between $1.15 - 1.6$ times the dilution of the base case) and decreases with higher saline concentration. Finally, a comparison between a wide spread numerical approximation for non-confined density currents and the measured data reveals that the lateral spreading approximation needs to be reformulated. The high-quality database presented in this study is a key tool for future calibration/validation of different numerical approximations, such as 3-Dimensional hydrodynamic modelling.

2.1. Introduction

Density currents, also known as gravity currents, are primarily horizontal flows driven by buoyancy, i.e. by the density difference between the environmental fluid and the current, as well as by the hydrodynamic conditions of the surrounding area. There are numerous natural and industrial occurrences of density current motions caused by different types of discharges in the environment (Simpson (1982, 1997) and Huppert (2006)). Several classifications of these horizontal flows can be made in broad terms regarding their general behavior (e.g. free-surface, neutral and bottom density currents) and the fluid nature (e.g. thermal, saline and turbidity currents). In recent years, brine discharges from desalination plants have become a significant concern worldwide due to its potential negative impact on the protected marine ecosystems. It is therefore important to delve into the behavior and properties of these flows, not only in the near field, but also in the far field region, where the bottom saline density currents generated can travel long distances before their total dilution with potential effects on stenohaline species. Since the behavior of these non-confined saline currents is largely dependent on the bathymetry and the initial flow conditions, this contribution analyzes globally, in spatial terms, the dynamic and mixing evolution of a set of laboratory generated density currents, by varying conditions such as the bottom slope, the buoyancy and the momentum flux.

Taking into account the continuity of the flow regime in density current experiments, i.e. those generated by fixed volume (lock-exchange) or constant-flux

releases, different analysis have been addressed in the scientific literature. Lock-exchange flows in horizontal flumes (Kneller et al. (1999)) were extensively studied focusing on the dynamics of the current head and its evolution (Huppert and Simpson (2006); Maxworthy and Nokes (2007); Nogueira et al. (2014); Nokes et al. (2010); Özgökmen and Chassignet (2002) and Ottolenghi et al. (2016)). On the other hand, constant-flux release experiments have been mainly focused on analyzing the quasi-steady state conditions within the current body. Ellison and Turner (1959) and other later works (Garcia (1993); Parker et al. (1987) and Hosseini et al. (2006)) obtained the quasi-steady (or equilibrium) mean flow properties, such as the mean vertical structure (or cross sections) of velocity and concentration. More recently, Sequeiros (2012) compiled an extensive database of velocity and concentration measurements of density currents of diverse nature (e.g. turbidity, thermal and saline currents; lock-exchange and constant-flux currents), obtained from different published works. Thanks to this, a Froude-number-based iterative method was presented to estimate the quasi-steady state conditions of turbidity currents considering crucial parameters such as the bottom slope angle (α) and the friction coefficient (C_D). Moreover, taking advantage of high-resolution measuring techniques, a considerable amount of studies have been focused on the turbulent structure of these quasi-steady state flows (Gerber et al. (2011)), comparing the behavior of saline and turbidity density currents (Gray et al. (2006) and Islam and Imran (2010)).

To elucidate the quasi-steady characteristics of the mixing mechanism in this kind of constant-flux currents, experimental studies such as Cenedese and Adduce (2008) and field studies such as Dallimore et al. (2001); Hebbert et al. (1979) and Fernandez and Imberger (2006) were undertaken based on the analysis of the entrainment of the surrounding fluid into the density current (Princevac et al. (2005); Turner (1986) and Wells et al. (2010)). Cenedese et al. (2010); Kashefipour et al. (2010) and Chowdhury and Testik (2014) gathered the large number of entrainment parameterizations that have been developed during the last decades, all of them being functions of the Richardson number (the ratio of the buoyancy term to the flow gradient term). Some of these parameterizations also reflect the influence of the bottom topography in terms of C_D and α. Nevertheless, most of the aforementioned entrainment parameterizations have been obtained from experimental two-dimensional density currents (i.e. laterally confined). For non-confined density currents, some studies used axisymmetric configurations which were forced to spread cylindrically (Britter and Simpson (1978) and Patterson

et al. (2006)) while others such as La Rocca et al. (2008) used initially channelized discharge configurations. However, these works studied the front spreading characteristics locally, and not the general entrainment characterization. As far as the authors of this present work are aware, only MacDonald and Chen (2012) and Yuan et al. (2013) have tried to isolate the effect of spreading on the mixing mechanism in thermal density currents, in addition to analyzing the quasi-steady state vertical structure. They concluded that the non-confined density currents achieve more dilution and have smoother (i.e. less stepped) vertical profiles than confined density currents. However they disagree about the impact of lateral spreading on the local mixing efficiency (i.e. the entrainment rate).

Regarding the numerical prediction of the downstream evolution of density currents, two approaches based on the Navier-Stokes equations have been studied: integral models (e.g. models developed by Alavian (1986); Ellison and Turner (1959); Garcia and Parsons (1996) and La Rocca and Pinzon (2010)) and 3-Dimensional hydrodynamic models (Dallimore et al. (2003) and Bleninger (2006)). Studies such as Choi and Garcia (2002); Gerber et al. (2011) and La Rocca and Pinzon (2010) and Mahgoub et al. (2015) obtained a good agreement between experimental data and numerical results regarding the vertical structure or the width-spreading rate (in the non-confined configurations) at some distances from the discharge. However, non of them has so far been fully validated in terms of the quasi-steady spatial evolution because of the lack of a global characterization of the body of the density currents. Accordingly, a more comprehensive analysis of the real processes that occur within density currents is needed to facilitate the reliable prediction of their behavior.

To overcome the detected shortcoming regarding the spatial coverage of the available data, even more evident taking into account non-confined density currents, the present study reveals a flow-field, vertical and longitudinal analysis of the dynamic and mixing evolution (i.e. velocity and density evolution) of a set of laboratory-generated density currents. At the same time, focusing on the parameters that impact on the behavior of saline currents from constant-flux brine discharges, that is, the bathymetry and the initial flow conditions, the second objective of this study is to isolate the effects of these parameters. These two aims are addressed by performing a set of experiments of constant-flux non-confined density currents, varying the bottom slope, the flow rate, the thickness and the saline concentration of the density current. The experiments were carried out at

the IHCantabria's facilities using PIV and PLIF techniques, which provide a high-quality measurements of velocity and concentration (Martin and Garcia (2008) and Liao and Cowen (2010)).

The manuscript is organized as follows: The experimental set up and procedures are described in Section 2.2. Flow characterization and analysis are presented in Sections 2.3 and 2.4. This characterization includes the flow fields of mean velocity and mean concentration, the evolution of mean and turbulence vertical structure and the longitudinal profiles of the variables' maximum values at the cross-sections. Furthermore, a wide spread numerical approximation for non-confined saline currents is compared with the experimental data obtained. Summary and conclusions are presented in section 2.5.

2.2. Experimental set-up

The experimental apparatus used to generate steady density currents comprised a $3x3x1\ m^3$ steel test tank with tow glass-walls, a 1000 *liter* plastic effluent storage tank and a steel 100 *liter* constant head tank. The storage and the constant head tanks were connected to each other by a pump for re-circulating the effluent (mixing of fresh water, salt, dye tracer and small particles) and to ensure a steady flow. The effluent was gravity discharged from the constant head tank into the test tank which was with freshwater to simulate the receiving body. An ultrasonic flow-meter with a measuring range $\pm 0.02 - \pm 32\ m/s$ and an accuracy of ± 1 % measured and controlled the flow rate. The steel test tank incorporated two lateral glass windows; one was used to illuminate the laser sheet and the other to allow recording of the images. To simulate the seabed, a plastic plate was installed inside the test tank 30 *cm* above the bottom and 20 *cm* from the walls. The space beneath the plastic plate was designed to function as a brine trap, to enable the study of non-confined gravity currents.

Figure 2.1a shows a schematic diagram of the experimental setup. In addition, Figure 2.1b shows the detail of the discharge device, a transparent methacrylate tank with a height-adjustable slot at the bottom. In this configuration, the gravity current is discharged from the right side. In the results analysis, a Cartesian

coordinate system (X, Z) is considered with the origin at the center of the discharge slot, with the X-axis pointing to the right and the positive Z-axis pointing upwards.

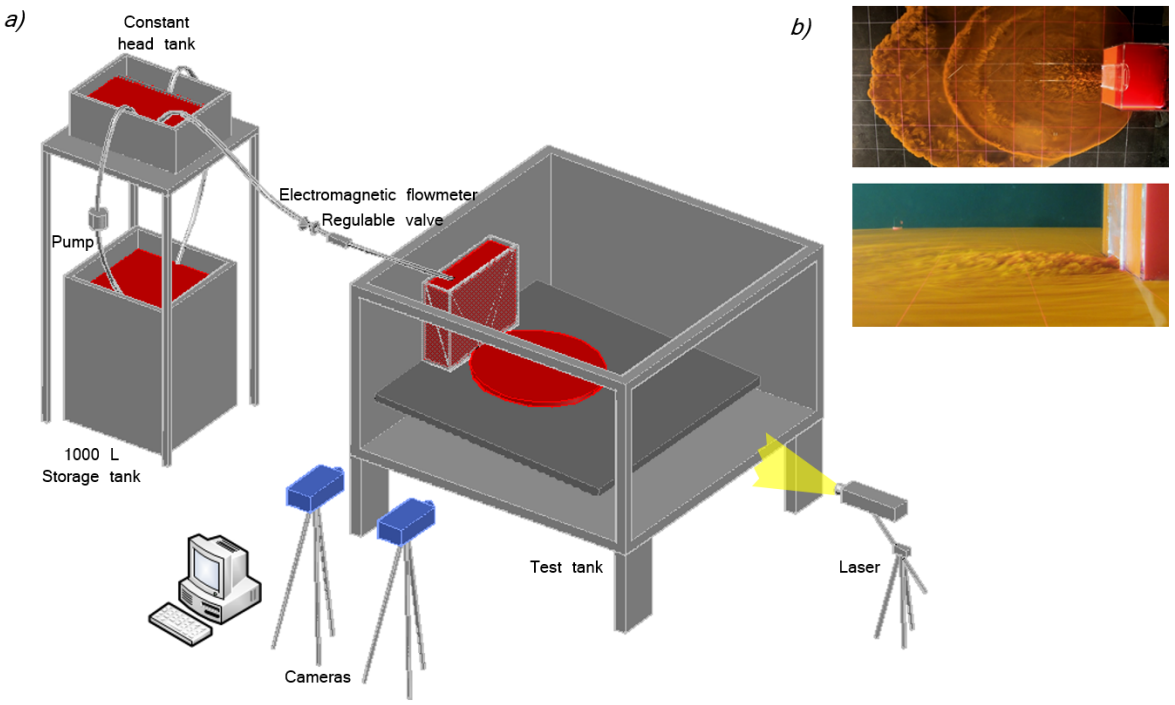

Figure 2.1: a) Schematic diagram of the PIV-LIF experimental set-up; b) Photographs of the discharge device

For the PIV-LIF measurement equipment, a Q-switched double pulse Nd-Yag laser was used to illuminate the flow. LaVision Imager ProX 4 Charge Coupled Devices (CCD) cameras with a resolution of 2048 × 2048 *pixels* were deployed to record the images, and LaVision-Davis software was used for image postprocessing. The laser sheet passes vertically through the center of the discharge slot, i.e. the density current's plane of symmetry. Green light was released with a 532 nm wavelength and a 30 Hz pulse repetition rate at each cavity. The cameras were mounted with a Nikon AF Nikkor 50 mm $1:1:8D$ objective with an aperture varying between 1.8 and 2.2 mm. In order to capture the maximum coverage area, both synchronised cameras were adjacently situated with an overlapping zone. Thus, each PIV and PLIF image covered approximately 700 mm. The effects of geometric distortion resulting from small angles in the camera alignment were corrected during processing and post-processing.

To ensure the quality of the velocity and concentration measurements within the flow, a proper selection of PIV and PLIF test paramenters is essential. For the

PIV measurements, PSP-50 polyamide particles with a 50 μm diameter, a density of 1030 Kg/m^3 and a much lower settle velocity (0.03 mm/s) than the lowest expected flow velocity were used (the effective particle image diameter was between 2 and 3 *pixels* in all cases, in agreement with Westerweel (1993) and Willert (1996)); the interrogation window was 16×16 *pixels* and the separation time between laser pulses, dt, was 15.000 μs close to the discharge slot and 30.000 μs in the area farther from the slot, where flow velocities are lower; finally, a standard cyclic FFT correlation function with a two-iteration multi-pass approach was applied to postprocess the images. For the PLIF measurements, Rhodamine $6G$ ($C_{28}H_{31}ClN_2O_3$) was used as a dye tracer (Crimaldi (2008)). By applying the procedure proposed by Ferrier et al. (1993), dye concentration values of around $12\mu g/L$ were found to be an adequate initial concentration for correct measurements along the full saline plume with negligible attenuation. The raw images recorded by the PLIF cameras were corrected before being transformed into concentration by subtracting the "dark" image (from the surrounding scattered light) and by applying transversal and longitudinal correction operators because of the Gaussian distribution of the laser beam (laser sheet correction) and longitudinal attenuation (following the Bouguer-Beer Law), respectively.

For each PIV and PLIF test, at least 1800 images, each with a frequency of 5 Hz, were captured to characterise the current behavior. The first 500 images were removed to ensure at steady state. A statistical convergence analysis showed that the remaining 1300 images were enough to guarantee the convergence of statistics.

Figures 2.2a, 2.2b and 2.2c show the scheme of the non-confined density current tested. The discharge design parameters displayed are: the slot width (b_0), the slot height (h_o), the discharge velocity (u_o), the density of the effluent (ρ_0) and of the receiving water (ρ_a), the water depth (H_a) and the slope angle (α). The main features of the generated saline current are the thickness (h), the width (b) and the main velocity (u). Since the PIV and PLIF techniques in this study were applied to characterize the longitudinal profile (Figure 2.2a), additional experiments were carried out to study the lateral spreading of the density current (Figure 2.2b). These experiments consisted of taking photos every 10 *seconds* with a camera located at the upper part of the test tank which was able to capture the whole plan view (see Figure 2.3). In these cases, the effluent was dyed with a high concentration of Rhodamine 6G to obtain a good visual definition of the lateral spreading.

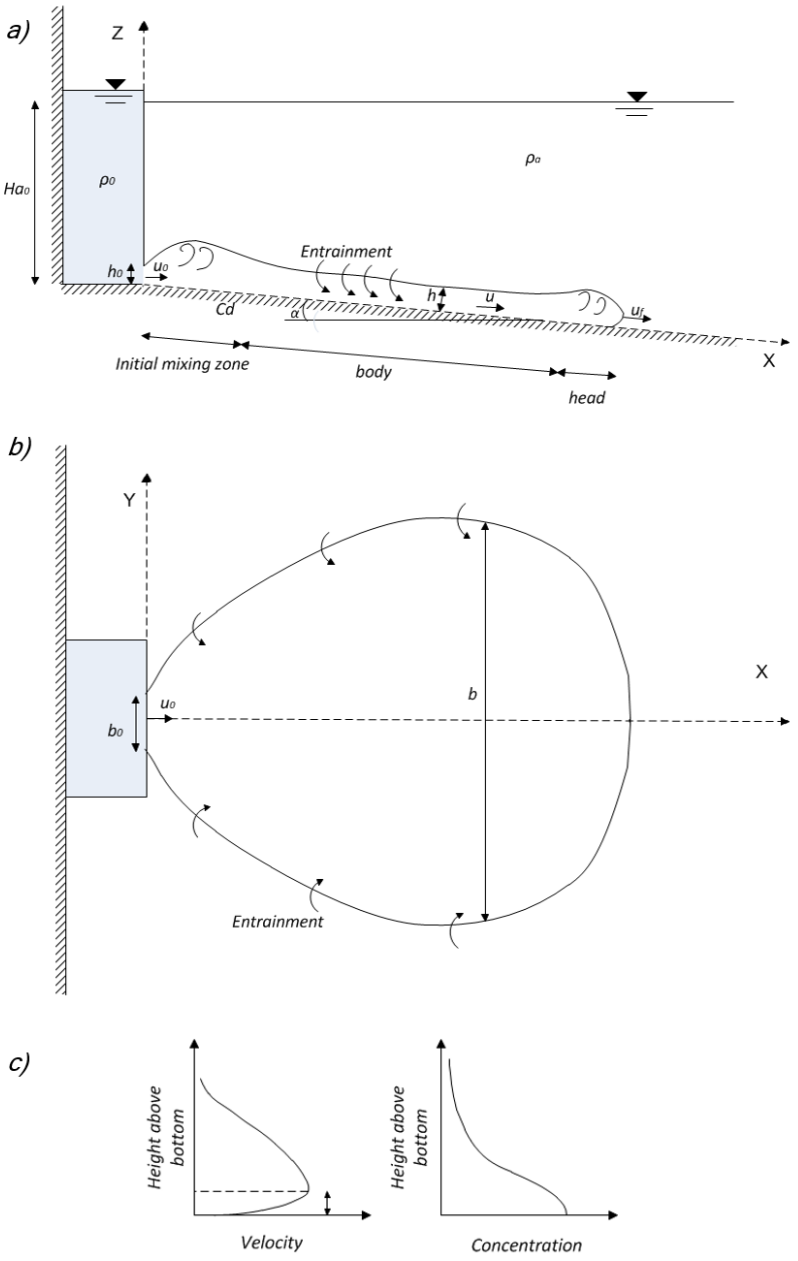

Figure 2.2: Scheme of the non-confined constant-flux density current: a) longitudinal profile view; b) plan view; c) cross sections of velocity and concentration

The characteristics of the final tests are summarized in Table 2.1. These tests combine high quality PIV-PLIF measurements with realistic plume conditions according to previous works studying the end of the near field region of brine discharges (Palomar (2014)). Thus, conditions close to the start of the far field region were considered to design the test cases.

CASE1 is the reference case on which all other cases were modified in one of the initial parameters (thickness h_0, flow rate Q_0, slope α or density difference

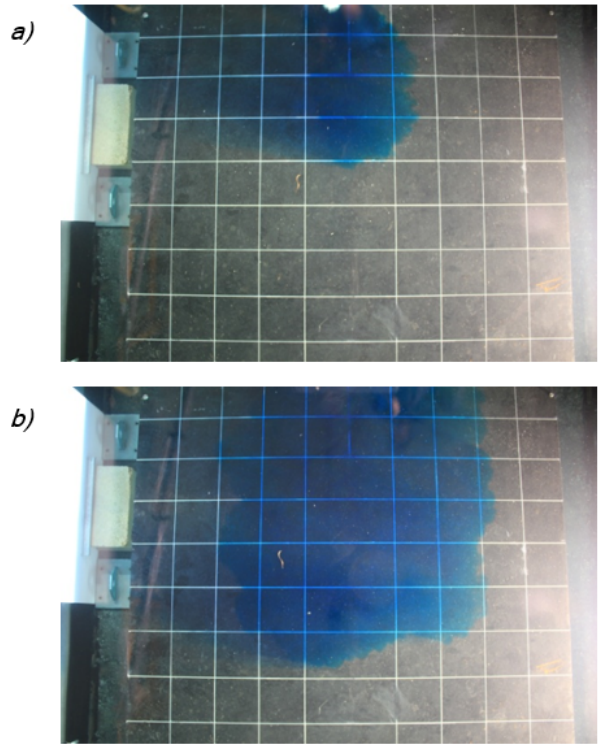

Figure 2.3: Spreading evolution photographs of *CASE1* at: a) 20 s and b) 60 s. Each square painted on the bottom is 0.2 $m/side$.

$\rho_a - \rho_0$). *CASE1*, *CASE2*, *CASE3* and *CASE6* represent comparable density currents with different initial Momentum fluxes ($Mf_0 = b_0 h_0 u_o^2$) and Buoyancy fluxes ($Bf_0 = b_0 h_0 U_o g(\rho_a - \rho_0)/\rho_a$) on an almost horizontal slope. *CASE4* and *CASE5* represent dynamically invariant cases from *CASE1* with two different slopes (2.5% and 4.5%, respectively). Different values of initial Momentum and Buoyancy fluxes were made by varying the initial density difference (*CASE1* and *CASE6*) and the initial velocity discharge (u_0), using the initial plume thickness (*CASE1* and *CASE2*) and the flow rate (*CASE1* and *CASE3*). The discharge slot width (b_0) and the bottom friction coefficient (C_D) were invariant parameters. For all the density current test cases, the Reynolds number ($Re_0 = u_0 h_0/\nu$, where ν is the fluid viscosity) was greater than 1000. Therefore, under laboratory conditions, a fully turbulent flow was considered in all cases (Cenedese and Adduce (2008)). The values of the initial bulk Richardson number ($Ri_{b0} = h_0 g_0{}' \cos\alpha/u_0^2$, where $g_0{}' = g(\rho_a - \rho_0)/\rho_a$ is the initial reduced gravity of the current) ranged between 0.017 and 0.296, so all the generated flows were supercritical ($Ri \leq 1$).

TABLE 2.1: Configurations tested to characterize the saline density currents

CASES	Slot dimensions $(b_0 \cdot h_0)$ m	Water depth (Ha_0) m	Slope (α) %	Density difference $(\rho_a - \rho_0)$ Kg/m^3	Discharge flow-rate (Q_0) l/min	Discharge velocity (u_0) m/s	Momentum flux (Mf_0) cm^4/s^2	Buoyancy flux (Bf_0) cm^4/s^3	Reynolds number (Re_0) -	Richardson number (Ri_{b0}) -	Length scale (L_p) m
CASE1	$0.100 \cdot 0.026$	0.460	1.0	3.145	14.600	0.095	2289	749	2424	0.088	0.072
CASE2	$0.100 \cdot 0.016$	0.460	1.0	3.100	15.100	0.164	4112	765	2515	0.017	0.073
CASE3	$0.100 \cdot 0.026$	0.460	1.0	3.130	19.200	0.125	3979	984	3197	0.050	0.080
CASE4	$0.100 \cdot 0.026$	0.420	2.5	3.070	14.980	0.098	2471	753	2494	0.082	0.073
CASE5	$0.100 \cdot 0.026$	0.360	4.5	3.140	14.09	0.098	2489	775	2512	0.082	0.073
CASE6	$0.100 \cdot 0.026$	0.460	1.0	11.080	14.890	0.097	2398	2700	2499	0.296	0.056

The last parameter shown in Table 2.1 is the characteristic length scale of plume-like behavior flows (Chu and Jirka (1987) and Choi and Garcia (2001)), $L_p = Q_0^{3/5}/Bf_0^{1/5}$. This length scale is obtained by considering the volume flux and the buoyancy flux as the characteristic dimensional variables, and can be successfully used to correlate the experimental data using dimensionless analysis (see Choi and Garcia (2001)). As can be observed in Table 2.1, the L_p value is very small in all the tests, showing that the plume reaches the buoyancy-dominated conditions very close to the slot discharge point. To provide a better interpretation of the results, length data are non-dimensionalized by L_p in this study.

2.3. Density current flow characterization

This section characterizes the full stationary density current flow based on the obtained PIV-PLIF experimental data. To study the hydrodynamic and mixing processes, the mean (local time-averaged) and turbulent fluctuation flow fields, the cross sections (vertical structure) and the longitudinal profiles along the saline density current are presented.

2.3.1. Flow fields

As previously mentioned, flow fields are presented by the union of two consecutive camera images with an overlapping zone. Figure 2.4 shows an example of the composition result of two snapshot of the concentration flow fields corresponding to $CASE1$. The high spatial resolution allows us to observe flow details as Kelvin-Helmholtz instabilities along the interface between the flowing current and the stagnant surrounding water (Chowdhury and Testik (2014) and Simpson (1997)). These instabilities are formed between fluids of different densities moving at different velocities, with dynamics depending on the ratio between the buoyancy term (the stabilizing force) and the flow gradient term (the destabilizing force), i.e. the Richardson number (Smyth and Moum (2000)). In addition, the gravitational lobe-cleft instability at the current front can be observed in Figure 2.4 (the aim of study of previous experiments, e.g. Britter and Simpson (1978)).

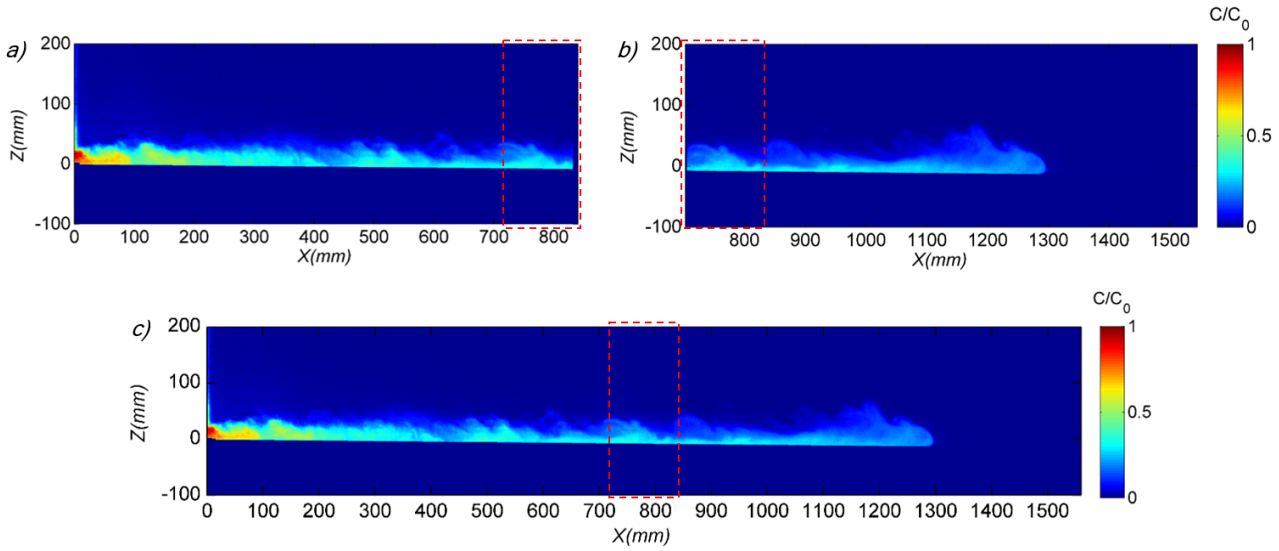

Figure 2.4: Snapshot normalized concentration images of *CASE1*: a) from Camera 1; b) from Camera 2; c) from the union of images of Camera 1 and 2. The red dashed lines correspond to the overlap region between cameras

Figure 2.5 displays the time-averaged flow fields obtained from the velocity and concentration measurements for *CASE1*. The local mean variables are obtained from the PIV and PLIF instantaneous images by applying the following expressions:

$$U_X = \frac{1}{N}\sum_{i=1}^{N} u_{xi} \tag{2.1}$$

$$U_Z = \frac{1}{N}\sum_{i=1}^{N} u_{zi} \tag{2.2}$$

$$C = \frac{1}{N}\sum_{i=1}^{N} c_i \tag{2.3}$$

$$U'_X = \frac{1}{N}\sum_{i=1}^{N} \sqrt{(u_{xi} - U_X)^2} \tag{2.4}$$

$$U'_Z = \frac{1}{N}\sum_{i=1}^{N} \sqrt{(u_{zi} - U_Z)^2} \tag{2.5}$$

$$C' = \frac{1}{N}\sum_{i=1}^{N} \sqrt{(c_i - C)^2}, \tag{2.6}$$

where: u_{xi} and u_{zi} are the instantaneous values of the horizontal and vertical velocities respectively; c_i is the instantaneous value of concentration; and N is

the number of images. Figures 2.5a and 2.5b shows the horizontal (U_X) and vertical (U_Z) components of the mean velocity results. The horizontal (U'_X) and vertical (U'_Z) components of the velocity fluctuation are also included in Figures 2.5c and d. Velocities are normalized with the discharge value (U_0) and represented using the same scale. From concentration measurements, Figures 2.5e and 2.5f represent the mean concentration (C) and turbulent concentration fluctuation (C') normalized with the discharge concentration (C_0). Finally, Figure 2.5g shows the mean dilution (S) obtained from the following expression:

$$S = \frac{C_0 - C_a}{C - C_a}, \tag{2.7}$$

where C_0 is the initial brine concentration, C_a is the surrounding fluid concentration and C is the mean concentration at each point of the flow.

According to Figures 2.5a and 2.5b, the horizontal motion is predominant along the saline density current while the vertical component is almost negligible. The noticeable decrement of the horizontal mean velocity along the flow is due to the bottom friction and the surrounding stagnant fluid. Regarding velocity turbulent fluctuations (Figure 2.5c and 2.5d), values are higher close to the discharge slot, where the widest turbulence kinetic energy spectrum is present. Velocity fluctuations decay along the density current revealing the collapse of the higher length scales of turbulence. Velocity fluctuation fields show values several orders of magnitude lower than the mean velocity flows, revealing that the far field region (plume-like behavior) is achieved almost from the slot discharge. The vertical component of velocity fluctuation (Figure 2.5d), generated by the bottom friction and the Kelvin-Helmholtz instabilities, presents slightly lower values than the horizontal component and diminishes more rapidly. These vertical fluctuations are responsible for the mixing between fluids along the interface.

Similarly to velocity flow fields, mean concentration (Figure 2.5e) and concentration fluctuations (Figure 2.5f), rapidly decrease along the current, being very low downstream. This concentration reduction, is due to entrainment of the surrounding fluid into the current layer and also confirms the collapse of the higher length scales of turbulence.

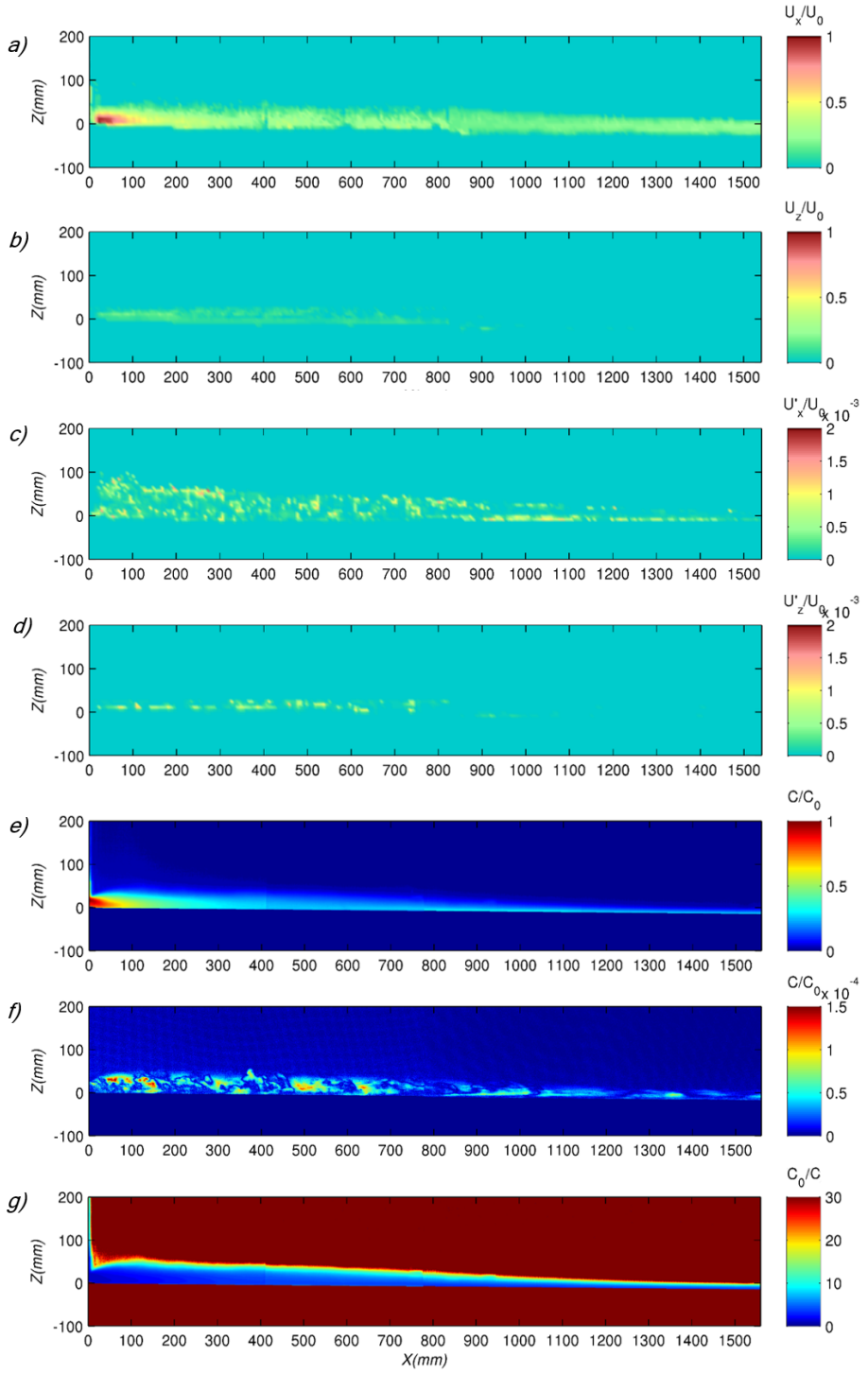

Figure 2.5: Normalized flow fields of the *CASE1* saline current: a) horizontal mean velocity; b) vertical mean velocity; c) horizontal component of velocity fluctuation; d) vertical component of velocity fluctuation; e) mean concentration; f) concentration fluctuation; and g) mean dilution

2.3.2. Vertical structure

In this section, the velocity and concentration vertical structure of a dense current developed on an inclined surface is studied. Thanks to the high PIV and PLIF measurement resolution, a detailed description of the mean and turbulent components of these main variables is presented.

2.3.2.1. Mean flow

Figure 2.6a shows the downstream variation of the horizontal mean velocity (U_x) for *CASE1*. As the figure shows, the velocity cross profile in saline density currents includes two regions: a thinner inner region and a thicker outer region that are separated by the maximum velocity (U_{Xmax}) (see Figure 2.2c). The inner region has a positive velocity gradient whereas the outer region has a negative velocity gradient, behaving like a shear layer. The vertical distance to the bottom of the velocity maximum is controlled by the upper and lower boundary drag and shear at the two boundaries and the velocity gradient (Hosseini et al. (2006)). In the present study, the maximum velocity was found to be at a distance from the bottom (h_{Umax}) between $0.25 - 0.30$ hu in all cases (where hu is the layer thickness regarding velocity measurements)(see Figure 2.6a). This range of values is in agreement with the results obtained by Islam and Imran (2010) and with the equation proposed by Sequeiros (2012) that relates the ratio h_{Umax}/hu to the Froude number of density current.

The downstream variation of mean concentration (C) cross profiles is plotted in Figure 2.6b showing a smooth shape typical of saline density currents. These profiles are characterized by a steep concentration gradient near the bottom boundary that falls off rapidly near the vertical location of the velocity maximum.

To study the self-similarity properties in cross profiles of saline density current, the mean velocity and concentration profiles have been normalized by the corresponding maximum values U_{Xmax} and C_{Xmax} (see Figure 2.7). The vertical coordinates are normalized by $Z_{U_{Xmax}/2}$ and $Z_{C_{max}/2}$, which represent the height at which U_X drops to half U_{Xmax} and the height at which C drops to half C_{max}, respectively. In these plots, the Z axis zero value represents the bottom. The length scales $Z_{U_{Xmax}/2}$ and $Z_{C_{max}/2}$ are used in wall jet and density currents analysis because

these U and C profiles collapse well when normalized with these variables (e.g. Gerber et al. (2011); Gray et al. (2006) and Palomar (2014)).

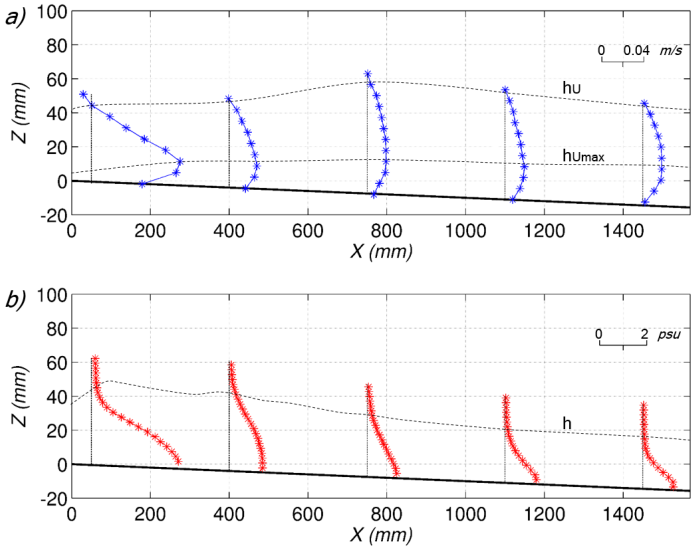

Figure 2.6: Downstream variation of *CASE1* cross profiles: a) horizontal mean velocity, b) concentration

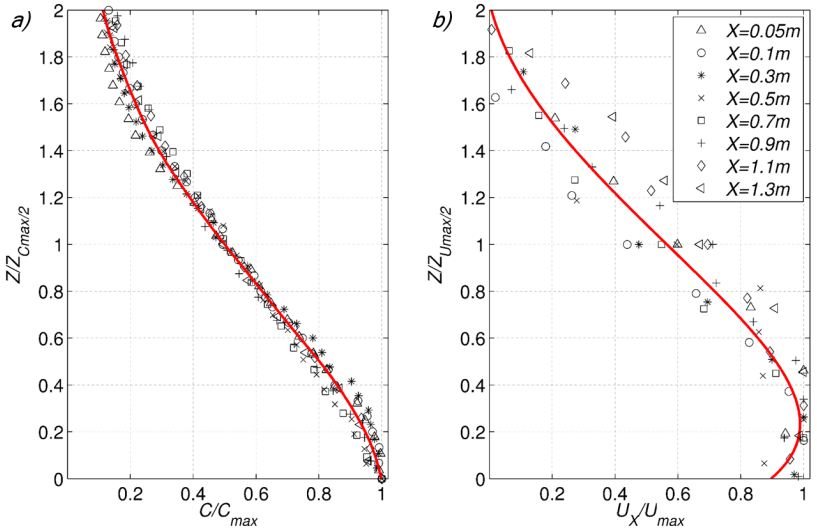

Figure 2.7: Similarity profiles of *CASE1*: a) mean concentration; b) mean horizontal velocity. Symbols represent measurements, and the line is the best fitting polynomial curve

As Figures 2.7a and 2.7b show, the normalized mean horizontal velocity and mean concentration cross profiles collapse well into a single profile. Consequently, the self-similarity hypothesis can be assumed for these variables along the density current studied, according to the results obtained by Garcia (1993); Parker et al. (1987) and Hosseini et al. (2006).

Previous studies (Alavian (1986); Ellison and Turner (1959) and Garcia and Parsons (1996)) proposed empirical shape parameters for mean cross sections. These parameters allow us to obtain approximate the vertical distributions to be applied in integral equations models. The shape parameters are defined by the equations:

$$S_1 = \frac{1}{Bh}\int_0^\infty \beta \, \mathrm{d}z, \tag{2.8}$$

$$S_2 = \frac{2}{Bh^2}\int_0^\infty \beta z \, \mathrm{d}z, \tag{2.9}$$

where z represents the vertical coordinate; β is the density fraction ($\beta = (\rho - \rho_a)/\rho_a$); and B is the characteristic density fraction of the current, considering the thickness (h). The values of S_1 and S_2 gives the extent of the dense layer compared to the vertical extent of motion. The values of these parameters depend on the chosen B and h characteristic values. In the present study, B was calculated considering both the maximum (ρ_{max}) and the mean (ρ_{mean}) density values within the current thickness h regarding the concentration profiles. The density current thickness at each cross section is considered that within which the concentration value is less than 10 % of the maximum concentration value. Due to the negligible difference among the collapse curves for each case, it can be inferred that common empirical shape parameters can be provided for the present tests. Figure 2.8 shows the downstream evolution of the aforementioned shape parameters experimentally obtained for $CASE1$. As can be observed, S_1 and S_2 tend to a constant value at some distance from the slot discharge. This is consistent with the similar appearance among the concentration profiles furthest downstream presented in Figure 2.6b. Table 2.2 presents the value ranges of the shape parameters for the cases studied.

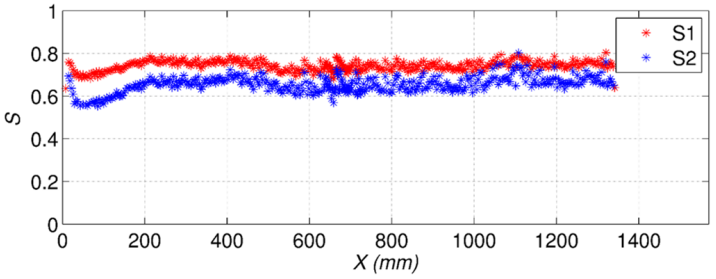

Figure 2.8: Shape parameters

Some turbidity current studies (Parker et al. (1986, 1987)) used top-hat assumption (shape parameter values equal to 1) values, which implies that the concentration profile has a stepped profile, characterized by a nearly constant current density extending vertically up to the velocity maximum location. The present saline density currents have a smooth concentration profile with shape parameters more similar to other saline density current experiments (see Table 2.2).

Table 2.2: Shape Parameters

	S_1	S_2	Type
Ellison&Turner(1959)	0.60/0.90	0.20/0.30	saline
Alavian(1986)	0.35/0.84	0.10/0.43	saline
Parker et al.(1987)	0.99	1.00	turbidity
García(1993)	0.99	0.79	saline
This study	0.70/0.86	0.57/0.77	saline

Since the smooth-profile density currents generated in this study are in supercritical regime ($Fr > 1$, equivalent to $Ri < 1$), it appears that there might be a relation between flow regime of the density currents and the shape of their profiles. In fact, more recently published experimental studies such as Sequeiros et al. (2010) conclude that those density currents in subcritical regimes ($Fr < 1$, equivalent to $Ri > 1$) reveal a steeper profile than their counterparts in supercritical regimes. The latter agrees with the results obtained in the present study and the experimental observations of Cortés et al. (2014), which shows that supercritical density currents are more likely to split into two parts at a stratified water body than subcritical ones, due to the fact that they have a diffuse density interface, that is, a smooth concentration profile, instead of a sharp, more step-like concentration profile. On the other hand, other justification for the smooth profile presented in these experiments can be the non-confined nature of the density currents. Although for positively buoyant currents, Yuan et al. (2013) obtains differences between the velocity and concentration profiles of confined and non-confined thermal currents. They find that non-confined currents have smooth velocity and concentration profiles that extend to the surface, whereas the confined current profiles are uniform near the surface (i.e. more step-like profile). Therefore, the smooth profiles of the density currents studied in the present paper can be due to both their non-confined nature and their supercritical regime.

2.3.2.2. Turbulence structure

Taking into account the flow fields of velocity and concentration fluctuations obtained by equations (2.4), (2.5) and (2.6), this section presents the analysis of the vertical turbulence structure of the density current.

The study of the horizontal and vertical components of velocity fluctuation of the mean flow, i.e. the study of Reynolds stress components, helps us to understand the role played by bottom friction and fluid entrainment in bottom density currents. The Reynolds stress components for unit volume of incompressible Newtonian fluid (τ_{ij}) that can be measured in the vertical symmetry plane of the generated density currents are:

$$\begin{aligned} \tau_{XX} &= -\rho\, U'_X U'_X\,, \\ \tau_{ZZ} &= -\rho\, U'_Z U'_Z\,, \\ \tau_{XZ} &= -\rho\, U'_X U'_Z\,, \end{aligned} \tag{2.10}$$

where the first two components (τ_{XX} and τ_{ZZ}) are normal stresses in the horizontal (streamwise) and vertical directions, respectively, while the third component (τ_{XZ}) is a shear stress (i.e. a tangential stress). Islam and Imran (2010) observed that the vertical (τ_{ZZ}) and the lateral (τ_{YY}) components are smaller than the horizontal streamwise component (τ_{XX}) in bi-dimensional saline and turbidity currents (laterally confined). Since Planar PIV was applied in the present study about tri-dimensional saline current, the Reynolds stress lateral component (τ_{YY}) cannot be calculated. In this case, it is expected to be more similar to the horizontal streamwise component (τ_{XX}) than in previous studies such as Islam and Imran (2010), due to the non-lateral confined currents tested. The vertical component (τ_{ZZ}) is around one order of magnitude smaller than the τ_{XX} in the cases tested (see Figure 2.5d). Considering this fact and the mathematical expression of turbulent kinetic energy per unit volume (equation 2.11), it is expected to have a similar distribution to the most important component $U'_X U'_X$:

$$T_{ke} = \frac{1}{2}\rho\,\left(U'_X U'_X + U'_Y U'_Y + U'_Z U'_Z\right). \tag{2.11}$$

Figure 2.9b presents the normalized downstream evolution of the main Reynolds stress component i.e., the normalized streamwise Reynolds stress component ($\tau_{XX}/\,\rho U^2_{Xmax}$), at three different locations for *CASE1*. In order to contrast the turbulent behavior

and the mean flow characteristics, the streamwise velocity component (U_X/U_0) and its vertical gradient ($\partial U_X/\partial Z$) are plotted at the same locations (Figures 2.9a and 2.9c, respectively).

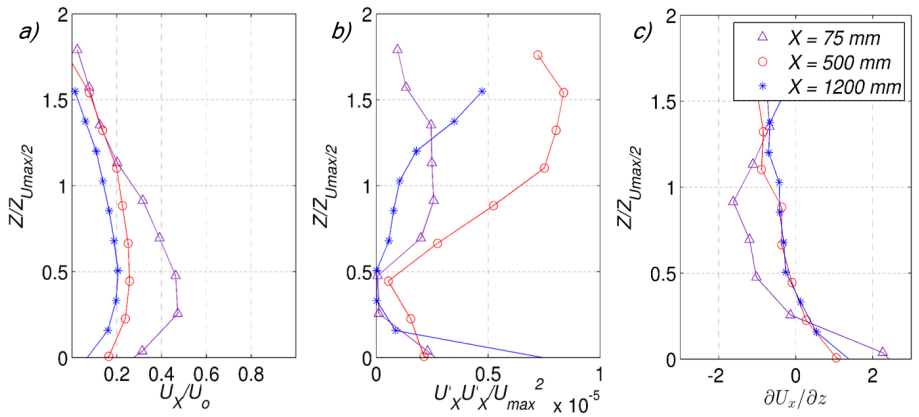

Figure 2.9: Normalized profiles of hydrodynamic variables along the density current: a) Mean horizontal velocity component; b) horizontal Reynolds stress component; and c) vertical gradient of the mean horizontal velocity

Figure 2.9b shows a turbulent structure with two peaks corresponding to the lower and upper flow boundaries and a zone of minimum turbulence (i.e. minimum fluctuations and hence, Reynolds stress) at the location of the maximum velocity. This structure is consistent with Gray et al. (2006); Islam and Imran (2010) and Gerber et al. (2011). The vertical gradient of the mean horizontal velocity ($\partial U_X/\partial Z$) is related to the loss of momentum due to the friction with the bottom and the surrounding fluid at rest. The gradient slope is larger at the bottom at the three studied locations, revealing that bottom friction plays an important role in the momentum damping.

Similarly, Figure 2.10 shows the variables related to concentration at the same three locations for *CASE1*. Concentration fluctuation decreases along the density current, in agreement with Gerber et al. (2011), presenting different peaks depending on the location. In the zone closest to the discharge slot, the concentration fluctuation has an outer peak corresponding to the outer Reynolds stress peak ($\tau_{XX}/\,\rho U^2_{Xmax}$) shown in Figure 2.9b, and a local minimum located just below the velocity maximum corresponding to a slow diffusion zone (Buckee et al. (2009)). At farther locations, the outer peak has spread out and decreased in magnitude. As can be observed in Figure 2.10, the concentration fluctuations do not present self-similarity properties.

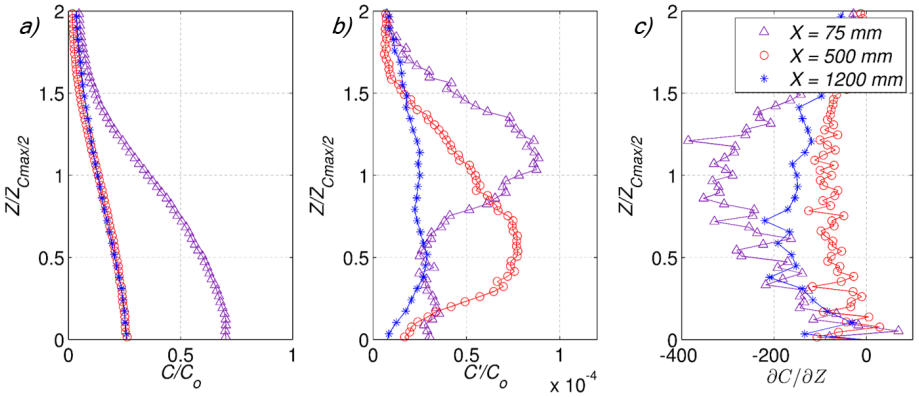

Figure 2.10: Normalized profiles of: a) mean concentration; b) concentration fluctuation; and c) vertical gradient of the mean concentration

Turbulence profiles corresponding to the entire casuistry were studied, however, given the non-remarkable differences among them, the profiles from *CASE1* are presented as a general example.

In order to better understand the anisotropic nature of the stable body associated with the studied density currents, the order of magnitude of the buoyancy production of turbulent kinetic energy (G) (equation 2.12) and the shear production of turbulent kinetic energy (P) (equation 2.13) are presented in Table 2.3. Both terms are related through the following flux Richardson number expression (Tennekes and Lumley (1972)):

$$G = -\frac{g}{\rho} U'_Z \frac{\partial \rho}{\partial Z} \tag{2.12}$$

$$P = -U'_X U'_Z \frac{\partial U}{\partial Z} \tag{2.13}$$

$$Ri_f = \frac{G}{P} = \frac{g}{\rho} \frac{U'_Z \, \partial \rho / \partial Z}{U'_X U'_Z \, \partial U / \partial Z} \tag{2.14}$$

where $\partial \rho / \partial Z$ can be considered equivalent to $\partial C / \partial Z$ taking into account that, in these controlled laboratory experiments, the density difference is only caused by different saline concentrations. The buoyancy production term (G) acts as a sink term in the vertical flux transport, damping the higher length scales of turbulence (see Figure 1a of Smyth and Moum (2000)), i.e. minimising the shear production term (P). By means of this energy exchange, the studied density currents reach a stable stratification, which is characteristic of flow motions where Ri_f is equal to or greater than 10^{-1} (Smyth and Moum (2000)).

TABLE 2.3: Orders of magnitude of the parameters involved in the flux Richardson number expression (2.14)

U'_X (m/s)	U'_Z (m/s)	$\partial U/\partial Z$ (s^{-1})	C' (psu)	$\partial C/\partial Z$ (psu/m)	G (m^2/s^3)	P (m^2/s^3)
10^{-5}	10^{-6}	10^{0}	10^{-3}	10^{2}	10^{-11}	10^{-10}

Taking into account the anisotropic properties of this kind of supercritical flow, the boundary-layer approximation (Rodi and Chow (1980)) can be applied, reducing the governing equations (Navier-Stokes equations with Reynolds and Boussinesq approximations). This approximation assumes that the velocity component of the main flow direction is much greater than the components in the other directions, and that the diffusive transport in the main direction is negligible relative to convection. Following these simplifications, the vertical turbulence issue of the resultant equation system is solved using well-known eddy viscosity (ν_t) and eddy diffusivity (Γ) concepts according to the expressions:

$$-U'_X U'_Z = \nu_t \frac{\partial U}{\partial Z} \tag{2.15}$$

$$-C' U'_Z = \Gamma \frac{\partial C}{\partial Z} \tag{2.16}$$

$$\sigma_t = \frac{\nu_t}{\Gamma} \tag{2.17}$$

These parameters represent the proportionality factors between the Reynolds shear stress and the mean velocity vertical gradient (ν_t), and between the vertical Reynolds flux and the vertical gradient of the transported quantity (Γ). The ratio between both parameters, known as the Schmidt number, can be included in the Richardson flux expression as follows:

$$Ri_f = \sigma_t \frac{g}{\rho} \frac{\partial \rho/\partial Z}{(\partial U/\partial Z)^2} \simeq Ri_g \tag{2.18}$$

where Ri_g is the gradient Richardson number (comparable to the initially defined bulk Richardson number Ri_b), approximately the same as Ri_f due to $\sigma_t \simeq 1$. The latter assumption is reliable when absolute values of Ri_f are small (10^{-1}), as it has been shown to be for the studied flows. The eddy viscosity and diffusivity parameters can be solved by different Turbulence Closure Models (TCM) which are widely studied in the literature (Rodi and Chow (1980)). However, the verification of the Schmidt number values for these kinds of flows, $\sigma_t \simeq 1$ (Turner (1973)), is valuable information for future numerical validation research with advanced

numerical modelling.

2.3.3. Longitudinal profiles

By taking advantage of the PIV-PLIF techniques over classical spatial dispersed measurements, this study characterises the density current behavior by means of continuous spatial assessment. Accordingly, this section presents the longitudinal profiles of the maximum velocity (U_{Xmax}) and the minimum dilution (S_{min}) (i.e. the lines that join the points of maximum mean velocity and concentration of the cross sections).

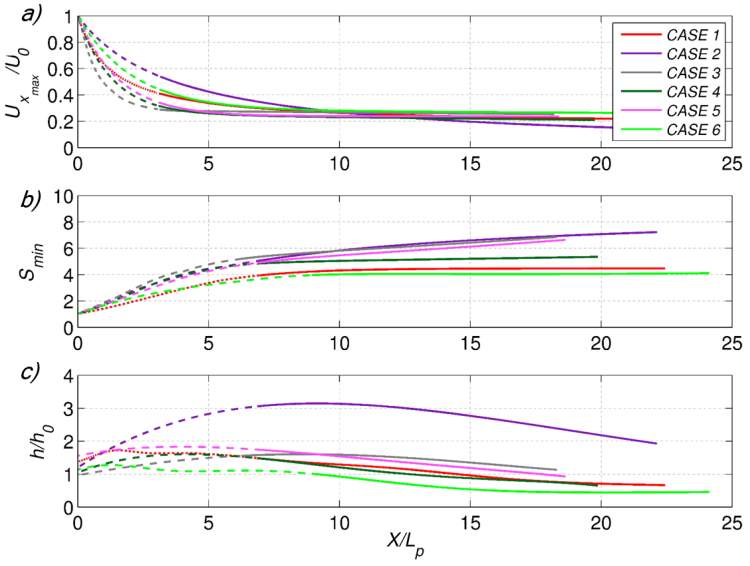

Figure 2.11: Longitudinal profiles of: a) normalized maximum horizontal velocity; b) minimum dilution; and c) thickness

Figures 2.11a and 2.11b show the normalized maximum velocity (U_{max}/U_0) and the minimum dilution (S_{min}) values along the dimensionless longitudinal profile of the saline plumes tested. In addition, the normalized thickness (h/h_0) dimensionless longitudinal profiles are shown in Figure 2.11c again for all the cases tested. These longitudinal profiles are the result of fitting curves obtained from measured values and cover the full zone experimentally characterized using PIV and PLIF.

According to Figure 2.11a, the normalized maximum velocity rapidly decreases along the first $400 - 600\ mm$ ($5 - 7\ X/L_p$), depending on the study case, after which it then diminishes at a slower rate before stabilizing around a nearly constant value. In agreement with the velocity longitudinal profiles, the evolution

of the minimum dilution (S_{min}) (see Figure 2.11b) reveals high dilution rates in the region close to the discharge slot, reducing to a smaller value later on. The initial high dilution rates are due to the higher length scales of turbulence which drive up the mixing and to the lateral spreading of the currents. On the basis of these observations, it can be posited that the non-confined saline density currents studied in the present work show a "Normal Status" in the plane of symmetry at a certain downstream distance from the discharge slot. The most remarkable results regarding the normalized thickness (h/h_0) revealed in Figure 2.11c are the the highest values reached by the case with higher Momentum flux (Mf_0) (*CASE2*) and the lower values reached by the case with the highest Buoyancy flux (Bf_0) (*CASE6*).

TABLE 2.4: General flow parameters for each study case beyond their "Normal Status" are reached

CASES	S_{minN}	$(U_{Xmax}/U_0)_N$	Ri_{bN}	S_{minF}	S_{minF}/S_{minF_b}
CASE1	3.796	0.239	0.324	4.350	S_{min_b}
CASE2	6.438	0.211	0.115	7.225	1.661
CASE3	6.210	0.250	0.128	6.802	1.563
CASE4	5.165	0.223	0.204	5.350	1.229
CASE5	5.954	0.237	0.126	6.635	1.525
CASE6	4.076	0.267	0.318	4.08	0.938

The "Normal Status" is reached at the downstream distance at which the minimum dilution longitudinal profiles reach a quasi-constant increase rate (see Figure 2.11), corresponding also to almost stable values of the dimensionless bulk Richardson number. The main reasons for the occurrence of this "Normal Status" observed in the plane of symmetry are: (1) density currents start to become insensitive to the lateral spreading (i.e. lateral mixing); (2) the vertical stable stratification reached by means of the energy exchange described in section 2.3.2.2, i.e. the exchange between the driving (buoyancy) and resisting (inertial) forces (Britter (1979)). Table 2.4 summarizes the density currents' characteristics once reaching the "Normal Status", denoted by sub-index $_N$. Although all the cases are in supercritical regime ($Ri < 1$), in cases with higher Ri_{bN} (*CASE1* and *CASE6*) the buoyancy forces are more significant than in the others, so lower rates of dilution are obtained. In contrast, in *CASE2* and *CASE3*, the significance of the shear stress is largely maintained, thus, the rate of dilution is higher than in the base *CASE1*. For those cases over a sloping bottom, *CASE4* and *CASE5*, the gravitational force (the component of the weight of the density current fluid in the downslope direction), together with the buoyancy and inertial forces, governs

the propagation dynamics of the density current (Tsihrintzis and Alavian (1996)), making the dilution rate larger than in base *CASE1*.

Table 2.4 also shows the final dilution obtained at the last section of the density currents (S_{minF}) characterized in the present tests, and, by establishing the value of *CASE1* as the base case (S_{minF_b}), the comparison-dilution rates (S_{minF}/S_{minF_b}). This dilution ratio reveals that the total dilution obtained in the symmetry longitudinal profile is around 1.6 times the S_{minFb} in the cases with approximately twice the Momentum flux (*CASE2* and *CASE3*), whereas approximately 1.15 times the S_{minF_b} for each unit (in percentage) of increment of the bottom slope (*CASE4* and *CASE5*) and 0.9 times the S_{minF_b} for cases with more than three times the Buoyancy flux (*CASE6*). Finally, considering that brine discharges systems have to be designed to obtain the highest dilution, it can be concluded that discharges with the greatest Momentum flux (Mf_0), the lowest Buoyancy flux (Bf_0) and over steeper slopes (tests within a range from 1% to 4.5%) enhance the dilution.

2.3.3.1. Mixing process: Entrainment

To obtain the mixing rate between the density current and the surrounding fluid, the vertical entrainment assumption has been generally considered since the study published by Morton et al. (1956). This assumption states that the entrainment velocity across the interface is proportional to the characteristic velocity of the flow. The constant of proportionality is known as the Entrainment coefficient (E).

In order to estimate the Entrainment coefficient from flow measurements, two different methods are found in the density current literature. One entrainment coefficient estimation derives from vertical mass fluxes (Strang and Fernando (2001) and Wells et al. (2010)) and an alternate version is based on volume conservation (Dallimore et al. (2001)). The good agreement between the two methods was checked by Dallimore et al. (2001) using measurements in the center longitudinal axis of a real saline underflow in lake Ogawara, which the author treats as a laterally confined density current in a channel (bi-dimensional). In the present work, the second method was chosen, taking advantage of the high resolution of the concentration measurements. In addition, by using this procedure both entrainments, lateral and vertical, are reflected. This method is based on the equations

for conservation of volume (2.19) and solute mass conservation (2.20):

$$\frac{d(Uh)}{dx} = EU \tag{2.19}$$

$$U\beta h = constant \tag{2.20}$$

where U, β, and h are the mean values of velocity, fractional density ($\beta = (\rho - \rho_a)/\rho_a$) generated by saline concentration, and layer depth at the selected location, respectively. Combining (2.19) and (2.20) leads to equation (2.21), where dC/dx is the variation in concentration when travelling with the mean velocity. By assuming similarity of the concentration profiles (shown in section 2.3.2), C can be set proportional to C_{max}.

$$E = -\frac{h}{C}\frac{dC}{dx} = -\frac{h}{C_{max}}\frac{dC_{max}}{dx} \tag{2.21}$$

Figure 2.12 shows the Entrainment coefficient evolution of *CASE1* calculated as explained above. The results obtained by applying Dallimore et al. (2001) are shown by asterisks, while the line represents the fitting curve. Higher values of entrainment are observed near the discharge slot, corresponding to the initial region of lateral spreading and with lower Richardson number values. According to the dilution rate, Entrainment coefficient values reaches a constant ratio corresponding to the "Normal Status". By analogy, this stable value is denoted as the normal Entrainment coefficient (E_N) and is defined as a single average value from this "Normal Status" location to the end of the density current. Table 2.5 gathers the normal Entrainment coefficient values obtained from the present density currents generated by different flow conditions. Similar to the conclusions achieved in the previous section in terms of minimum dilution (S_{minF}), the differences among the normal Entrainment coefficients (E_N) reveal that steeper slopes (tests within a range from 1% to 4.5%) and initial higher momentum fluxes favor the dilution of saline density currents.

TABLE 2.5: Vertical Normal Entrainment (E_N) coefficient for each study case beyond their "Normal Status" are reached

$CASES$	$CASE1$	$CASE2$	$CASE3$	$CASE4$	$CASE5$	$CASE6$
E_N	0.015	0.027	0.026	0.025	0.039	0.011

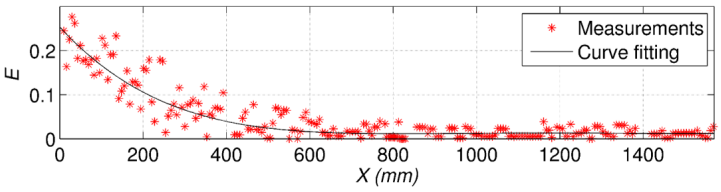

Figure 2.12: Entrainment coefficient evolution of *CASE1*. The asterisks represent the results of applying the Dallimore et al. (2001) procedure and the black line represents the fitting curve to these values

Several Entrainment coefficient parameterizations were deduced from laboratory studies for different kinds of density currents in previous works (gathered in Table 1 of Kashefipour et al. (2010)). All of them are in the form $E = E(Ri)$, establishing that as Ri increases, the entrainment of ambient water into the dense density current decreases and vice versa. Some of these parameterizations include the bed roughness effect ($E = E(Ri, C_D)$, where C_D is the bottom friction coefficient). However, Fernandez and Imberger (2006) concluded that entrainment parameterizations in the form $E = E(Ri)$ better predict the experimental observations for cases where $Ri < 10$, which is the study case. It is noteworthy that in the present experiments, since the characteristics of the bottom plastic material in the test tank always remained constant, bed roughness was not an initial condition variable. However, an order of magnitude of the C_D of the bottom plastic material can be calculated by using the measured Reynolds stresses ($C_D = u_*^2/U^2 = (U'_X U'^2_Z + \cancel{U'_Y U'^2_Z})^{1/2}/U^2 \simeq 10^-7$) demonstrating its low value. Finally, Wells et al. (2010) proposed a parameterization of E incorporating turbulence flux, length and velocity scales. They propose three scaling regimes and the present density currents are in the one referred to a large Froude numbers (i.e. small Ri numbers) which predicts E values almost constant.

As a validation of the E_N-Ri_{bN} values obtained from the study cases, Figure 2.13 shows a graph of the available observations of Entrainment coefficient versus the Ri number. In addition, some parameterizations from Table 1 of Kashefipour et al. (2010)) are included. The present experiments of non-confined density currents reveal similar E_N values to those at the same regime (small Ri numbers) corresponding to confined density currents, such as those of Ellison and Turner (1959); Fukuoka, S. and Fukushima (1980) and Parker et al. (1986). The latter confirms the previous assumption that once the flow reaches each "Normal Status" the dilution evolution in the vertical symmetry plane is insensitive to the non-confined

nature of the density currents. This reinforces the conclusion of Yuan et al. (2013), which indicated that lateral spreading does not modify the local mixing rate.

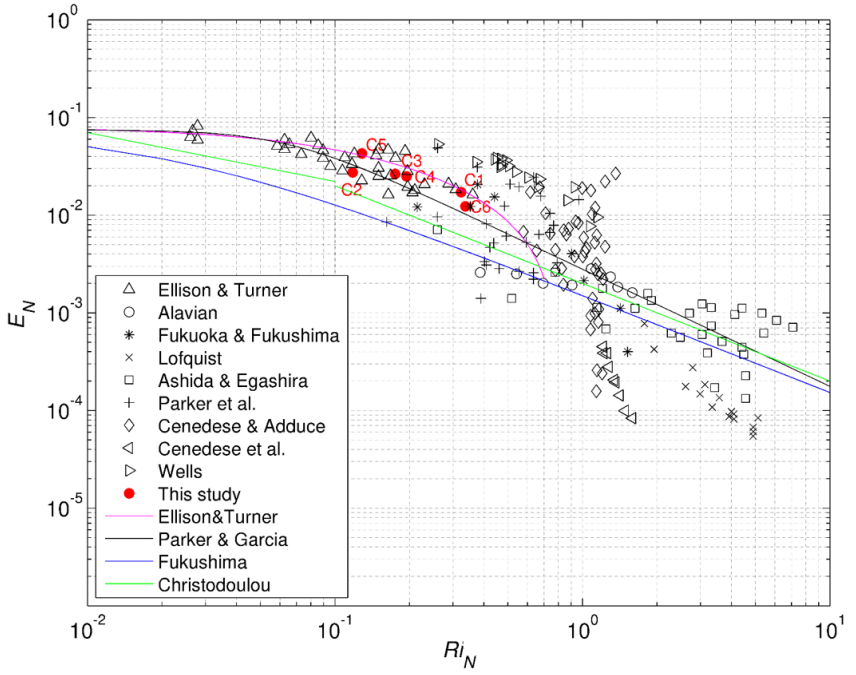

Figure 2.13: Measurements of the Entrainment Coefficient (E) plotted as a function of the Richardson number, and some entrainment parameterization detailed in Kashefipour et al. (2010)

2.4. Integral equation model *Vs* measured data

In this section, the results provided by a simplified numerical approximation based on the integration of the non-confined plume differential equations across sections (Ellison and Turner (1959); Garcia and Parsons (1996) are compared with Alavian (1986)) and the measured data, from the present study and from Choi and Garcia (2001), is presented.

To study the spatial development of the steady state of non-confined density currents, Alavian (1986) proposed the following differential equation system (equations (2.22), (2.23) and (2.24)) including the width evolution (b) of the density current as a variable. It is noteworthy that this approximation (equation (2.22)) assumes the same Entrainment coefficient for lateral and vertical mixing mechanisms.

$$\frac{d(Ubh)}{dx} = EU(b + 2h) \tag{2.22}$$

$$U\beta bh = constant \tag{2.23}$$

$$\frac{d(U^2)}{dX} = S_1 g\beta bh\sin\alpha - \frac{1}{2}S_2 g\frac{d(\beta bh^2)}{dx}\cos\alpha - C_D U^2 b \tag{2.24}$$

To validate this integral equation model with the present measured data, velocity and dilution predictions are compared to the PIV and PLIF measurements in the symmetry longitudinal profile, while the lateral spreading is compared with the plan view photographs as shown in Figure 2.3.

Figure 2.14 shows the evolution of the dilution (S), velocity (U) and width (b) obtained from the equation system (2.22)-(2.23)-(2.24) of three density currents simulating the initial conditions of some of the configurations examined in this study (*CASE1*, *CASE2* and *CASE5*). The E, S_1, S_2 and C_D used are those experimentally calculated. In order to graphically compare the numerical and experimental results, Figure 2.14 also shows the corresponding experimental values of measured variables, S and U.

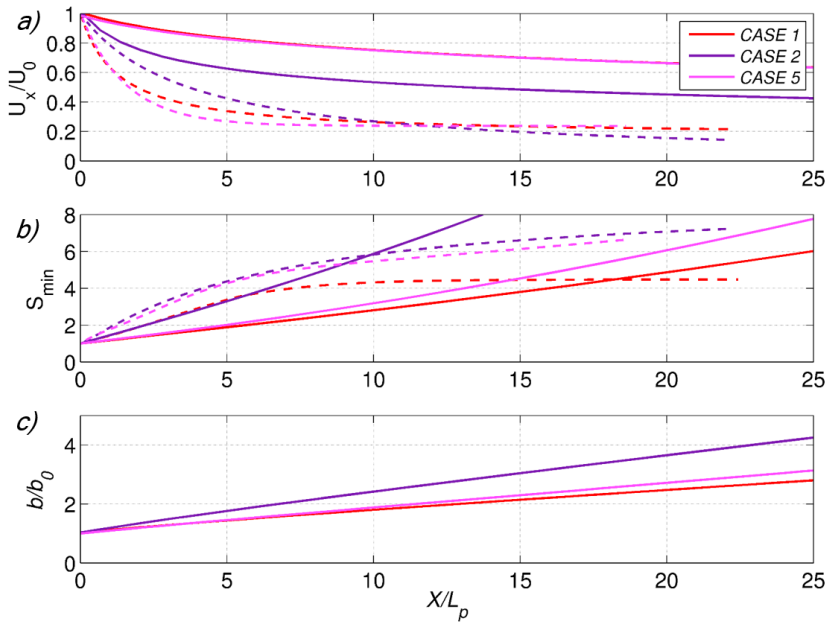

Figure 2.14: Longitudinal profiles comparison between numerical and experimental results. The dashed lines are from the experimental measurements and the continuous lines are obtained from the numerical approximations

Overall, the numerical approximation overestimates the velocity values and presents a different behavioral pattern regarding the dilution (underestimating close to the discharge slot and overestimating at the farthest points). These inconsistencies reveal that the aforementioned tree-dimensional approximation is not appropriate

for predicting the behavior of the assessed supercritical density currents in this study. Alavian (1986) presents the previous equation system to predict its experimental density currents (see Table 1 of Alavian (1986)), which flow over steep slopes (5°, 10° and 15°) and have lower buoyancy flux values and initial lower Reynolds numbers (near subcritical and laminar regimes) than the present cases. In those experiments, Alavian (1986) observes that the density current width converges at a constant value almost from the beginning of the discharge (see Figures 3 and 4 of Alavian (1986)). Lateral spreading was not the aim of the PIV-PLIF study, but thanks to the plan view photographs, a qualitatively analysis was done. As can be seen in Figure 2.3 for *CASE1*, from the beginning, the width observed is greater (each square painted in the bottom has 0.2 $m/side$, i.e. 2 $b/b_0/side$) than that numerically calculated (see Figure 2.14c). Photographs reveal that the *CASE1* density current reaches the lateral boundaries, which means $b/b_o > 10$.

To continue with the validation of the (Alavian, 1986) numerical approximation, the model results were compared with the experimental database published by Choi and Garcia (2001). This published work carried out experiments in a $2.44x3.66x1.22\ m^3$ tank to study the spreading rates of non-confined density currents over sloping beds. The chosen experimental density current was one generated on an incline of 2° called DEN1, the most similar configuration to the present cases. The flow initial parameters are summarized in Table 1 of Choi and Garcia (2001), which indicates that the flow is turbulent and supercritical. Table 2.6 reveals the experimental values of width b/b_o ($b_o = 0.1\ m$) and front velocity U_f/U_o ($U_o = 0.16\ m/s$) at the farthest measured point from the source ($X \simeq 2700\ mm$), and the corresponding values obtained by the three-dimensional numerical approximation analyzed. The discrepancy between the results confirms that this three-dimensional numerical approximation can not be used as a rule of thumb, i.e. lateral and vertical Entrainment coefficients can not be the same. In addition, it is observed that supercritical density currents, such as those in the present and Choi and Garcia (2001) experiments, have greater spreading lateral rates than those predicted by Alavian (1986)'s approximation.

TABLE 2.6: Comparison between experimental and numerical results

Experimental data		Numerical data	
U_f/U_o	b/b_o	U/U_o	b/b_o
0.187	20	0.5	5

Therefore, it can be concluded that future research regarding the numerical simulation of these flows with integral equation models should be focused on searching for a good lateral spreading approximation, based on the development of a new Entrainment parameterization which varies spatially. However, these integral equation models are restricted to simplified cases or to provide an order of magnitude. To more accurately model the behavior of density currents in real environments, largely dependent on the irregular bathymetry and on the receiving water´s hydrodynamics, more complex numerical approximations, such as 3-Dimensional hydrodynamic models should be another complementary research line (see Dallimore et al. (2003) and Bleninger (2006)).

2.5. Summary and conclusions

An experimental study to characterize the behavior of non-confined saline density currents in calm receiving water was presented using synchronized PIV and PLIF. The work is focused on the quasi-steady flow properties of the current body generated by a constant flux release. By means of the full spatial coverage of the PIV and PLIF measurements, this work presented a novel global analysis of this kind of density currents, different from previous published works. In addition, a broad range of different initial conditions (varying the flow rate, thickness, bottom slope and excess density) were tested, motivated by their occurrence in the far field of actual marine brine discharges.

In virtue of the detailed examination of the flow fields obtained from PIV and PLIF measurements in the planes of symmetry, a global spatial outlook of the behavior of these kind of saline density currents tested was obtained. The main findings were then gathered:

- The direct analysis of the mean flow fields revealed that the main component (U_X) of the mean velocity decreases sharply along the non-confined density current due to the influence of friction with the surrounding stagnant fluid, bottom friction and lateral spreading. Velocity turbulent fluctuations (U'_X and U'_Z) present higher values too in the zone close to the discharge slot, and they rapidly decay downstream of the flow, revealing the collapse of higher length scales of turbulence. Analogous results were shown about concentration fields. Therefore, turbulent mass transport is significantly

close to the discharge slot, where the higher Momentum flux takes place, but rapidly decays along the saline current.

- Taking into account the vertical structure, mean flow cross profiles revealed that these kinds of flows present self-similarity properties. Concentration shape parameters took values around $S1 : 0.7 - 0.86$; $S2 : 0.57 - 0.77$ for the cases tested. These values correspond to supercritical density currents with smooth shape concentration profiles. The analysis of the turbulence structure at different downstream locations showed a common zone of minimum turbulence, occurring at the position of maximum velocity. Just below this position, the concentration fluctuation presents its minimum, related to a slow diffusion zone (area with less turbulent mass transport). In addition, by means of an order of magnitude analysis of the energy exchange, the study density currents (range of Ri_b from 10^{-1} to 1) revealed a stable stratification with Schmidt numbers (σ_t) close to 1.

- Through the assessment of the longitudinal profiles of maximum values of horizontal mean velocity (U_X) and mean concentration (C), a "Normal Status" was observed to be reached at an almost common distance from the source for all the casuistry tested. From this "Normal Status", the U_X and the dilution rate (designed as the Normal Entrainment coefficient E_N) reach a quasi-constant value. Since the E_N values obtained agrees well with several existing parameterizations for confined density currents, this study reveals that vertical mixing beyond the "Normal Status" is the main mixing mechanism in the plane of symmetry for non-confined density currents (agreeing with Yuan et al. (2013))

Apart from the previous conclusions regarding the general behavior of the whole set of the density currents generated, a comparison between them, in terms of the final minimum dilution (S_{minF}) and the Normal Entrainment coefficient (E_N), was reported. As a general finding, it can be concluded that steeper slopes (tests within a range from 1% to 4.5%) and higher initial momentum fluxes enhance the dilution of saline density currents. More specifically, the final minimum dilution obtained at the last section of density currents (S_{minF}) was found to increase around 1.6 times when the Momentum flux was doubled and around 1.6 times for each percentage unit of increment of bottom slope. Contrarily, the S_{minF} was reduced ~ 0.9 times when the Buoyancy flux was tripled.

Finally, a comparison between the three-dimensional integrated equation approximation model proposed by Alavian (1986) and the PIV and PLIF experimental data of the present work shows that the model cannot correctly simulate the behavior of these non-confined density currents. Taking into account this conclusion, this PIV and PLIF database has an important additional value to facilitate the calibration/validation of new simplified methods and more complex numerical approximation such as hydrodynamic modelling tools. Although these advanced numerical tools are capable of evaluating the influence of real hydrodynamic conditions of the receiving coastal waters and real bathymetries, their calibration with the generated PIV and LIF database of saline density currents generated under controlled laboratory conditions will be a definitive step to continue with real applications.

Chapter 3

Modelling non-confined density currents using 3D hydrodynamic models: finding the key numerical set-up [1]

Abstract

The potential negative impact of human-induced density currents on the marine ecosystems, such as those generated by brine discharges, has resulted in an increasingly interest in obtaining accurate predictions of their behavior. Accordingly, the present contribution focuses on the establishment of a proper configuration of 3D hydrodynamic models to reproduce the transport and mixing processes that occur in these types of flows. Through a comprehensive sensitivity analysis based on the reproduction of several laboratory-generated density currents, a set of recommendations regarding the main numerical aspects such as the domain discretization, the momentum-source specification, the hydrostatic hypothesis and the turbulence closure models are compiled in this study. Finally, the proposed numerical modelling set-up is validated through different experimental data showing a good compliance in the evolution ofthe main variables' values (errors of less than

[1] This chapter is based on: Pérez-Díaz, B., Castanedo, S. and Palomar, P. (2017). Modelling non-confined density currents using 3D hydrodynamic models: finding the key numerical set-up. Submitted in Journal of Geophysical Research - Oceans

1.3% for dilution and 6% for velocity). This contribution therefore represents a first step towards the validation of these 3D hydrodynamic models used to solve real field-scale saline current flows.

3.1. Introduction

Bottom density-driven flows, generally called density or gravity currents, are continuous underflows which move downslope due to their negatively-buoyant characteristic, i.e. because they are heavier than the surrounding fluid. This phenomena occurs widely in natural environments, caused by either human activities or natural processes (Huppert (2006); Simpson (1997)). Nowadays, in the coastal and marine environment, some of the most common density currents are those generated by brine discharges from desalination plants. Hodges et al. (2011) makes an analogy between the behavior of a natural salt wedge and these brine discharges into shallow waters, both of which are governed by the density difference and the hydrodynamic of the surrounding area (Shao et al. (2008)) as well as by the bottom slope. Due to the potential negative impact of these human-induced currents on the environment, there is an increasingly widespread interest in obtaining accurate predictions of their behavior. Towards this end, the present work focuses on the establishment of a proper configuration of those numerical models that consider the main transport and mixing processes which occur in these kind of flows.

Dense underflows have been widely investigated in laboratory experiments (Alavian (1986); Ellison and Turner (1959); Garcia (1993) and Gerber et al. (2011)) and field studies (Dallimore et al. (2001); Fernandez and Imberger (2006); Hebbert et al. (1979); Hodges et al. (2011) and Pérez-Díaz et al. (2016a)). Major efforts have also been undertaken to predict the behavior of these currents using different modelling techniques and through comparisons with previous laboratory experiments (Choi (1999) and La Rocca et al. (2008)). As a broad classification, two modelling techniques are available for studying these flows numerically: integral models, and those which solve the vertical structure of the flow. The concept of the integral model for density currents was introduced by Ellison and Turner (1959) and further developed by Alavian (1986) and Parker et al. (1986), among others. In general, these integral models assume a hydrostatic pressure distribution within the current and use vertical depth-integrated equations. On the other hand, those

models which solve the vertical structure of the flow are based on the resolution of 3D Navier-Stokes (N-S) equations with different degrees of simplification.

Since Ellison and Turner (1959), integral models have been significantly developed, mainly focusing on turbidity currents (Akiyama and Stefan (1985); Bradford et al. (1997); Choi and Garcia (1995); Garcia (1993); Imran et al. (1998); Parker et al. (1986) and Choi (1999)). Recently these models have been designated as single or double-layer shallow water models depending on whether they consider only the heavier layer or divide the entire depth into two layers. Recently, Ungarish (2007a) investigated two-dimensional density currents with a wide range of depths and density differences using a single-layer shallow water model. The same author, in his subsequent work (Ungarish (2008)), studied these same types of flows using a double-layer model. Taking into account three-dimensional (i.e. non-confined) density currents, Ungarish (2007b) and La Rocca et al. (2008) performed numerical analysis to validate their single-layer shallow water models against experimental data. La Rocca and Pinzon (2010) and La Rocca et al. (2012) proposed using double-layer shallow water models for three-dimensional density currents, and Adduce et al. (2012) presented a modification considering a new entrainment formulae between the two fluids.

The vertical distribution of the main variables of density current has been numerically analyzed with hydrodynamic models that solve N-S equations taking into account the Reynolds approximation (Reynolds Averaged Navier-Stokes Equations, or RANS). In these applications, a turbulence closure model is required to estimate the Reynolds stress in conjunction with wall functions. Stacey and Bowen (1988a,b) solved the vertical distribution of one-dimensional turbidity currents using a mixing length model as the Turbulence Closure Model (TCM). Other authors employ the κ-ε model (Rodi (1984)) as the TCM (e.g. Brø rs and Eidsvik (1992); Eidsvik and Brø rs (1989) and Choi and Garcia (2002)). The κ-ε TCM has also been applied to density currents plunging into reservoirs by Farrell and Stefan (1988) and Bournet et al. (1999). In recent years, a number of Direct Numerical Simulations (DNSs) of density currents have been reported in the literature (e.g. Birman et al. (2005); Cantero et al. (2006); Härtel et al. (2000); Lowe et al. (2005) and Cantero et al. (2007)). These more sophisticated simulations are capable of capturing the interfacial vortex dynamics such like Kelvin-Helmholtz instabilities and the formation of the lobe-cleft structure at the current head. Since DNSs are prohibitively expensive in terms of computational time, specially when

considering field-scale simulations, other authors like Patterson et al. (2005) and Patterson et al. (2006) conducted bi- and three-dimensional simulations of axisymmetric density currents using an implicit Large-Eddy Simulation (LES) (Almgren et al. (1996)), relying on the use of Subgrid Scale modelling (SGS). However, Paik et al. (2009) revealed that, for moderately fine computational meshes, the Unsteady Reynolds Averaged Navier-Stokes (URANS) equations closed with a buoyancy corrected Low-Reynolds Number (LRN) κ-ε (Hwang and Lin (1998)) can achieve similar results to DNS and LES simulations.

Integral models are acceptable for those field-scale practical purposes in water resources management where only a coarse approximation of the characteristic flow quantities at an equilibrium state is required. On the other hand, the most complex numerical approximations (e.g. DNS and LES) are highly time-demanding computationally and they are therefore usually applied at laboratory scale under controlled conditions. Bombardelli and García (2002) assessed the potential development of density currents in the Chicago River using an intermediate complexity 3D hydrodynamic model in order to capture the spatial variability and complexity. Kulis and Hodges (2006) carried out a layer-number sensitivity test to numerically simulate a density current in Corpus Christi Bay in Texas using a sigma-coordinate 3D hydrodynamic model based on RANS equations and taking into account the Boussinesq approximation and the Hydrostatic hypothesis. Applying similar 3D hydrodynamic models, Firoozabadi et al. (2009) and Mahgoub et al. (2015) simulated density currents and validated their results against laboratory measurements. Firoozabadi et al. (2009) validated the vertical structure of the velocity at one position within a bi-dimensional density current and the evolution of the current height testing different configurations of the LRN κ-ε TCM selected (Launder and Spalding (1974)). Mahgoub et al. (2015) validated the spreading of three-dimensional density currents, assessing the importance of taking the hydrostatic hypothesis into account. To the authors' knowledge, none of the reviewed works related to density currents simulations with 3D hydrodynamic models are fully validated, i.e. considering both the spreading and the vertical structure of the main flow variables (velocity and concentration).

In this research, a set of sensitivity tests related to the numerical aspects of a 3D hydrodynamic model based on 3D shallow water equations are conducted to properly simulate non-confined density currents such as those generated in the far field region of brine discharges. The simulations are fully calibrated and validated

against measurements from Chapter 2 (Pérez-Díaz et al. (2017b)) and other authors (Choi and Garcia (2001)). Hence, as a novel contribution, the present work outlines an optimum modelling set-up to predict the behavior of these kind of flows using 3D hydrodynamic models, which are also capable of simulating the real environmental conditions present in coastal areas, such as tidal currents, which are highly influential in the evolution of density currents (Shao et al. (2008)).

The manuscript is organized as follows. The hydrodynamic model is described in Section 3.2. The sensitivity analysis to different numerical aspects is shown in Section 3.3. In Section 3.4, the proposed modelling set-up is summarized and the comparison between simulated and measured data is evaluated. In Section 3.5, further validations with published density current data under different flow conditions are delineated. Finally, conclusions are presented in section 3.6.

3.2. Numerical model

Numerical models capable of simulating the hydrodynamic and transport-diffusion processes that occurs in coastal areas at meter scale (from 1 up to 4 orders of magnitude) in the whole water column are commonly called 3D hydrodynamic models (or 3D hydrodynamic and transport models). They can usually be applied in many fields, especially those related to rivers, seas, estuaries and lakes. ROMS (Shchepetkin and McWilliams (2005)), Delft3D-Flow (Roelvink and Van Banning (1994) and Hydraulics (2005)), SELFE (Zhang and Baptista (2008)) and TELEMAC-3D (Hervouet (2007) and LNHE and Laboratory (2007)) are examples of 3D hydrodynamic models that can take into account processes such as: bottom friction, turbulence, sources and sinks of water, wind, air pressure, Coriolis force; diffusion of tracers and heat, sources and sinks of tracers and heat, production and decay of tracers; density-induced flow driven by salinity, temperature and sediments and thermal exchanges with the atmosphere; and dry areas (e.g. tidal flats) in the computational domain.

Amongst the available options, TELEMAC-3D model has been chosen for this work due to some of its special features: a large number of subroutines based on the a huge amount of scientific literature to reproduce processes at different scales; clearly structured Fortran90 source code that enables easy user-programming and

modification of subroutines; the option of switching-off the hydrostatic assumption; sigma-layer coordinate (i.e. terrain-following) in the vertical domain discretization; and unstructured horizontal domain discretization, that facilitate working with variable spacing meshes, and hence, obtaining computationally-efficient high resolution results in specific areas (e.g. areas of sources and sinks of water).A brief description of those parts of the model that play an important role in reproducing the behavior reproduction of density currents is listed hereunder.

TELEMAC-3D code solves the three-dimensional hydrodynamic equations (i.e. continuity, momentum and transport equations) considering the Reynolds approximation and by assuming the density difference in the continuity equation (i.e. incompressible fluid), and in the inertial and viscous terms of the momentum equations to be negligible, but included in the buoyancy force term (i.e. Boussinesq approximation). In addition, the basic code version of TELEMAC-3D uses the hydrostatic pressure hypothesis, which assumes that the vertical accelerations are negligible compared to the gravitational acceleration. After including previous assumptions, the simplified equation system can be set as follows:

$$\frac{\partial U_X}{\partial x} + \frac{\partial U_Y}{\partial y} + \frac{\partial U_Z}{\partial z} = Sce \tag{3.1}$$

$$\frac{\partial U_X}{\partial t} + U_X\frac{\partial U_X}{\partial x} + U_Y\frac{\partial U_X}{\partial y} + U_Z\frac{\partial U_X}{\partial z} = F_X - \frac{1}{\rho}\frac{\partial P}{\partial x} + \frac{\partial}{\partial x}\left(2\nu_{th}\frac{\partial U_X}{\partial x}\right) + \frac{\partial}{\partial y}\left(\nu_{th}\left(\frac{\partial U_X}{\partial y} + \frac{\partial U_Y}{\partial x}\right)\right) + \frac{\partial}{\partial z}\left(\nu_{tv}\frac{\partial U_X}{\partial z} + \nu_{th}\frac{\partial U_Z}{\partial x}\right) \tag{3.2}$$

$$\frac{\partial U_Y}{\partial t} + U_X\frac{\partial U_Y}{\partial x} + U_Y\frac{\partial U_Y}{\partial y} + U_Z\frac{\partial U_Y}{\partial z} = F_Y - \frac{1}{\rho}\frac{\partial P}{\partial y} + \frac{\partial}{\partial x}\left(\nu_{th}\left(\frac{\partial U_Y}{\partial x} + \frac{\partial U_X}{\partial y}\right)\right) + \frac{\partial}{\partial y}\left(2\nu_{th}\frac{\partial U_Y}{\partial y}\right) + \frac{\partial}{\partial z}\left(\nu_{tv}\frac{\partial U_Y}{\partial z} + \nu_{th}\frac{\partial U_Z}{\partial y}\right) \tag{3.3}$$

$$\frac{\partial P}{\partial z} = -\rho g \tag{3.4}$$

$$\frac{\partial T}{\partial t} + U_X\frac{\partial T}{\partial x} + U_Y\frac{\partial T}{\partial y} + U_Z\frac{\partial T}{\partial z} = \frac{\partial}{\partial x}\left(\Gamma_h\frac{\partial T}{\partial x}\right) + \frac{\partial}{\partial y}\left(\Gamma_h\frac{\partial T}{\partial y}\right) + \frac{\partial}{\partial z}\left(\Gamma_v\frac{\partial T}{\partial z}\right) + Q \tag{3.5}$$

These equations are continuity (3.1); the momentum equations for each Cartesian coordinate (3.2), (3.2) and (3.4); and the transport-diffusion equation (3.5). These

equations form a system with 5 unknowns: the Cartesian velocity components U_X, U_Y and U_Z, the pressure P, and the concentration of the conservative tracer T, such as salinity or temperature. In study cases with more than one tracer, one diffusion-transport equation is added per new tracer. The numerical coefficients ν_{th} and ν_{tv} are the horizontal and vertical turbulent viscosity coefficients (also called eddy viscosities), respectively, resulting from the Boussinesq approach (Joseph Boussinesq (1877)) used to model the Reynolds stresses, that is, to assess the turbulent diffusion. The coefficients Γ_h and Γ_v represent the equivalents of the corresponding eddy viscosity for tracer magnitudes, called eddy diffusivities. The previous coefficients (viscosities and diffusivities) are related to them by the Prandtl number (P_{rt}) for temperature or the Schmidt number (σ_c) for salinity, whose values depend on the kind of flow. *Sce* is the source or sink term of the flow-discharge. F_X and F_Y are the source or the sink terms and momentum body forces (e.g. Coriolis force, bottom friction, sources and sinks, wind, atmospheric pressure). Q is the source value of the tracer and ρ and g are the density and the gravitational acceleration, respectively. By developing the vertical coordinate equation (3.4) taking into account the Boussinesq decomposition of ρ, i.e. $\rho = \rho_0 + \Delta\rho$, the pressure at elevation z can be written as follows:

$$P = P_{atm} + \rho_0 g(Z_s - z) + \rho_0 g \int_z^{Z_s} \frac{\Delta\rho}{\rho_0} dz \tag{3.6}$$

where Z_s is the free surface elevation, P_{atm} is the atmospheric pressure, and $\Delta\rho$ is the density difference. Finally, to compute the density variations $\Delta\rho$, TELEMAC-3D applies a temperature and salinity density function that uses a reference density calculated by the UNESCO state equation under certain conditions: temperature of 4°C and zero salinity.

Several turbulence closure models (TCMs) can be used to estimate the eddy viscosities and diffusivities, such as zero-equation models (based on an algebraic relation), single equation models (based on a combination of an algebraic relation and an equation), two-equation models (based on two transport-diffusion equations) or even more complex models (e.g. the Reynolds stress model). In this work three common TCMs are used: for zero-equation models, the Constant turbulence model and the mixing length models (Smagorinsky, Prandtl's Mixing-Length model and Nezu and Nakagawa's Mixing-Length model); and for the more complex two-equation model, the κ-ε model. The simplest TCM, the Constant model, consists of defining constant eddy viscosities and diffusivities according to

the mesh-grid resolution and the characteristic velocity of the type of flow motion being studied (Madsen et al. (1988)). Mixing-Length and Smagorinsky TCMs are based on the mixing length concept proposed by Prandtl in 1925. While Mixing-Length TCMs such as the standard Prandtl model (Rodi (1984)) and the Nezu and Nakagawa model (Nezu and Nakagawa (1993)) are only applied as vertical TCM since they fix the characteristic mixing length as a function of the water depth and the distance to the bottom, the Smagorinsky model (Smagorinsky (1963)) belongs to the category of sub-grid turbulence models, where mixing length is dependent on the mesh-grid and a dimensionless coefficient according to the type of flow (anisotropic or isotropic flow). Finally, the most complex TCM used in this work is the two-equation κ-ε model. Herein, the eddy viscosities are evaluated by applying the following Kolmogorov-Prandtl relationship per direction:

$$\nu_t = c_\mu \frac{\kappa^2}{\varepsilon} \tag{3.7}$$

where κ is the turbulence kinetic energy, ε is the turbulence kinetic energy dissipation rate and c_μ is an empirical constant. This TCM added two more equations to the system which are (in conservative form and with the Einstein tensor notation):

$$\frac{\partial \kappa}{\partial t} + U_i \frac{\partial \kappa}{\partial x_i} = \frac{\partial}{\partial x_i}\left(\frac{\nu_t}{\sigma_\kappa}\frac{\partial \kappa}{\partial x_i}\right) + P - G - \varepsilon \tag{3.8}$$

$$\frac{\partial \varepsilon}{\partial t} + U_i \frac{\partial \varepsilon}{\partial x_i} = \frac{\partial}{\partial x_i}\left(\frac{\nu_t}{\sigma_\varepsilon}\frac{\partial \varepsilon}{\partial x_i}\right) + c_{1\varepsilon}\frac{\varepsilon}{\kappa}[P + (1 - c_{3\varepsilon})G] - c_{2\varepsilon}\frac{\varepsilon^2}{\kappa} \tag{3.9}$$

where the production terms denoted by the shear P and by the buoyancy G are estimated by:

$$P = \nu_t \left(\frac{\partial U_i}{\partial x_j} + \frac{\partial U_j}{\partial x_i}\right)\frac{\partial U_i}{\partial x_j} = 2\nu_t D_{ij} D_{ij} \tag{3.10}$$

$$G = \beta g \frac{\nu_t}{\sigma_c}\frac{\partial T}{\partial x_i} \tag{3.11}$$

where, indices i and j vary from 1 to 3 according to the direction, and β represents the fractional density, i.e. the volume expansion. The κ-ε model contains several empirical constants obtained by comprehensive data-fitting for a wide range of turbulent flows. Rodi (1984) compiled the following standard values:

$$c_\mu = 0.09;\ \ \sigma_\varepsilon = 1.00;\ \ \sigma_\kappa = 1.30;\ \ c_{1\varepsilon} = 1.44;\ \ c_{2\varepsilon} = 1.92;\ \ c_{3\varepsilon} \approx 0 - 1 \tag{3.12}$$

Among the empirical constans, $c_{3\varepsilon}$, associated with the buoyancy term G in equation (3.9) is originally established equal to 1 for stable situations, i.e. if G is negative, and equal to 0 for unstable stratifications (Launder and Spalding (1974); Viollet (1988)). However, this empirical coefficient $c_{3\varepsilon}$ as well as c_μ are both quite uncertain. Discussions and numerical tests on these constants is addressed in subsequent sections.

TELEMAC-3D solves the previous equations by means of a semi-implicit finite-element method, and its basic algorithm is split into three computational steps. In the first step, the advected velocity components are computed by solving only the advection terms in the momentum equations. The second step calculates the new velocity components from the advected velocities, and taking into account of the diffusion terms and the source terms in the momentum equations. In the third step the water depth from the vertical integration of the continuity equation and the momentum equation is computed including only the pressure-continuity terms.

The procedure for taking the advection terms into account is individualized for each variable to be processed (i.e. velocities, depth, tracers, turbulence kinetic energy and its dissipation rate). While the method of characteristics (Hervouet (2007)) is generally used for the velocities calculation, more conservative and monotonic schemes are used for the depth and the tracers (LNHE and Laboratory (2007)). Focusing on the advection scheme for tracers, in this case the salinity, the present study considers a second-order central-upwind scheme originally based on Kurganov and Petrova (2007)'s scheme and adapted by Bourban (2013). For κ-ε variables, the default advection scheme established by TELEMAC-3D is the method of characteristics. However, a sensitivity test based on the advection scheme for these variables ($AdSche_{\kappa\varepsilon}$) is later considered. Finally, from the options offered by TELEMAC-3D, the iterative solver used to solve the linear systems generated for each variable in this work are based on the conjugate gradient method. The relative accuracies, the number of iterations and the pre-conditionings of the matrices are established in accordance with the suggestions in the TELEMAC-3D user manual (LNHE and Laboratory (2007)).

3.3. Sensitivity analysis

This section presents the sensitivity analysis which tests the impact of different state-of-the-art numerical aspects on the simulation of a density current. In order to finally calibrate the model, the *CASE1* configuration tested and measured in the laboratory experiments of Chapter 2 is considered throughout this sensitivity analysis. Specifically, this experiment consisted of a laboratory-generated saline density current that evolves over a gentle slope bottom (1%). The saline effluent of this *CASE1* configuration was discharged through a rectangular slot measuring 0.1×0.026 m, simulating the beginning of the far field region of common brine discharges from submerged jets, i.e. the end section of the near field region known as the spreading layer (Papakonstantis and Christodoulou (2010) and Palomar (2014)). The main characteristics of the *CASE1* configuration are listed in Table 3.1 and outlined in Figure 3.1.

TABLE 3.1: Main characteristics of the laboratory configuration

Characteristics[a]	*CASE1*
Slot dimensions ($b_0 \times h_0$)	0.100×0.026 m
Water depth (Ha_0)	0.46 m
Slope (α)	1 %
Density difference ($\Delta\rho = \rho_0 - \rho_a$)	3.145 Kg/m^3
Discharge flow-rate ($Q_0 = U_0 b_0 h_0$)	14.6 l/min
Buoyancy flux ($Bf_0 = Q_0 g \Delta\rho/\rho_a$)	749 cm^4/s^3

[a] Meaning of symbols:
b_o: slot width; h_o: slot height; ρ_o: effluent density; ρ_a: ambient density; U_o, discharge velocity; g: gravity.

The initial and boundary conditions of the TELEMAC-3D application are defined with the aim of numerically simulating the real conditions of the experimental set-up (see Figure 3.1). Accordingly, the numerical application is initialized with a constant elevation value corresponding to Ha_0, zero velocities (stagnant receiving water), and constant values for each tracer studied (more details in Chapter 2). For the boundary conditions, the free-surface, open-boundaries (i.e. liquid-boundaries), and the bottom and rigid walls are taken into account. At the free-surface boundary, the rigid-lid approximation is made, which includes zero gradients and zero fluxes perpendicular to the boundary (i.e. $\partial U_i/\partial z = \partial\kappa/\partial z = \partial\varepsilon/\partial z = \partial T/\partial z = 0$). At the open-boundaries, the streamwise gradients of all the variables (i.e. velocities, tracer and fluxes) are set to zero and a prescribed elevation is applied. Strictly speaking, the boundary conditions for velocity on a

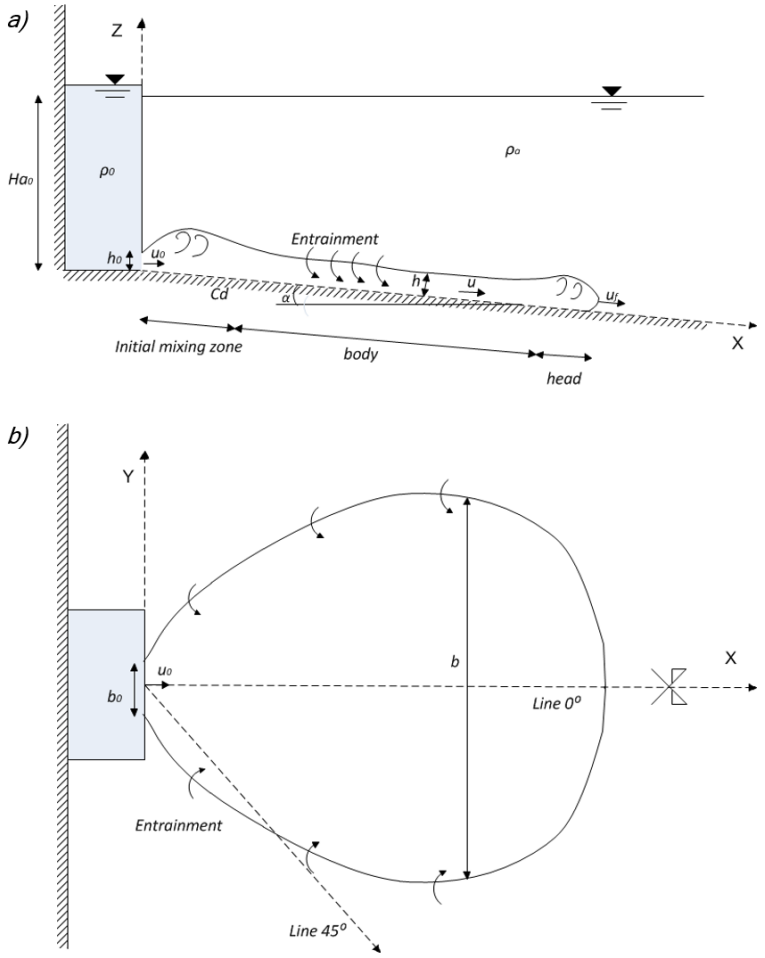

Figure 3.1: Scheme of a non-confined density current: a) longitudinal profile view; b) plan view. Source: Pérez-Díaz et al. (2017b)

rigid wall is a no-slip condition (i.e. dirichlet conditions $U_i = 0$). However, due to the turbulence and the existence of a boundary layer, the velocity near the bottom-wall quickly becomes non-zero, and the no-slip condition is replaced by a tangential stress (i.e. $\tau = \mu \frac{\partial \overrightarrow{U}}{\partial n}$) due to the friction on the bottom. This tangential stress is replicated by a turbulence model for the bottom using the friction or shear velocity $\tau = -\rho(U^*)^2$ and the distance to the bottom z. Assuming the flow is hydraulically rough (i.e. the characteristic roughness size of the bottom is greater than the thickness of the viscous sub-layer, Hervouet (2007)), the velocity profile near the bottom is defined by a logarithmic law function of the Nikuradse coefficient k_s, which represents the roughness size. Since the bottom material used in the experiments was plastic, the Nikuradse coefficient takes well-known values around $\sim 0.01 \times 10^{-3}$ m. At the rigid vertical walls, slip conditions are

also assumed, but in this case the tangential stress is set to zero. Tracer concentration gradients are also set to zero for the rigid walls (bottom and vertical rigid walls). For the turbulence kinetic energy κ and its dissipation rate ε, the boundary conditions defined by Rodi (1984) for rigid walls are considered.

It is worth highlighting that while in other numerical experiments (e.g. Firoozabadi et al. (2009)) the dense fluid enters the domain through an open-liquid boundary with the slot dimensions, in this work the saline flow rate is entered using punctual source terms. The number of source terms is determined by the slot dimensions and the domain discretization. This way, the findings of this study can be applied to future field applications like brine discharges from desalination plants, where the saline outflows are typically located within the study domain, not in the boundaries.

Due to the fact that these types of hydrodynamic models and their mesh-grid tools are designed and generally configured (e.g. accuracies and number of iterations) to model coastal and ocean processes, laboratory tests have to be scaled up to avoid numerical problems. Applying Froude similarity (i.e. the relevant forces are the inertial and gravity forces, Heller (2011)), mechanical similarity (i.e. geometric, kinematic and dynamic similarity) is expected to be achieved and therefore less scale-effects are expected to be obtain. However, since the Reynolds number Re of the case studied is not high enough (i.e. $Re >> 2000$) to directly neglect the viscous force, a previous sensitivity analysis varying the scale $Sc_F = L_{NUM}/L_{LAB}$ (taking into account the Froude similarity) is performed. The scale factors studied are: $Sc_F = 1; 10; 20; 50; 80; 100; 200; 1000$. This analysis reveals that, converting all the results to the same scale, the relative difference of the main quantities (concentration and velocity) amongst the scale-sensitivity cases (at geometrically equivalent locations) is always lower than 2%. This negligible difference, which is due to numerical and scale effects, leads to the conclusion that the Froude similarity can safely be assumed. Thereafter, a $Sc_F = 100$ scale factor is selected, this way, the modelled density currents (i.e. $CASE1_{Sc_F100}$) have features characteristic to the far field region of a brine discharge. Thereafter, $Sc_F = 100$ scale factor is selected, this way, the modeled density currents (i.e. CASE1 Sc˙F100) have features characteristic of the far field region of a brine discharge.

The methodology of the sensitivity analysis presented in the following sections consists of carrying out several simulations varying one numerical aspect while

keeping the rest unchanged. The significance of the numerical aspect under consideration in the prediction of density current behavior is analysed by comparing the numerical results of characteristic magnitudes such as the horizontal density current spreading, and the velocity (U) and the dilution (S) evolution within the density current. The dilution is calculated following the expression:

$$S = \frac{C_0 - C_a}{C - C_a}, \tag{3.13}$$

where C_0 is the initial salinity concentration of the source, C_a is the surrounding fluid salinity concentration and C is the salinity concentration at the study point within the density current.

Table 3.2 summarizes the numerical aspects and their options considered in this study. The selection of these numerical aspects is made as a function of the most common options of hydrodynamic models like TELEMAC-3D and a previous rough analysis used to define the most influential aspects. As can be seen, the scaling analysis mentioned is not included in the sensitivity analysis since it is generally not a concern to simulating field-scale density currents.

TABLE 3.2: Numerical aspects and their options

Numerical aspect	Abbreviation	Options
Horizontal discretization	Δx	wide range of Δx function of b_o
Vertical discretization	Δz	wide range of Δz function of h_o
Source input	Sce	information of Q or $Q\&V$
Hydrostatic Hypothesis	Hyd	with or without the hypothesis
Horizontal TCM	$TCMh$	Cst.[a], Smago.[b], κ-ε
Vertical TCM	$TCMv$	Cst., ML[c], κ-ε
Advection Scheme κ-ε	$AdSch_{\kappa\varepsilon}$	Charcs.[d], $2^{nd}O$-KP[e]

[a] Constant model; [b] Smagorinsky model; [c] Mixing-Length models; [d] Method of Characteristics; [e] 2^{nd} order *Kurganov and Petrova* scheme

3.3.1. Domain Discretization

The appropriate design of the computational mesh-grid is critical to simulate real physical processes while avoiding numerical effects. As a general rule, a fine domain discretization (i.e. high resolution) of the mesh-grid is needed when high spatial-temporal gradients of the variables modelled are expected. For negatively-buoyant density current flows, the high variability areas are the bottom part of the mesh-grid and the surroundings of the discharge location. This section shows the

results of the domain discretization sensitivity tests for *CASE1*, which varies both horizontal and vertical discretization, leaving the rest of the numerical aspects constant according to Table 3.3.

TABLE 3.3: Numerical aspects in the Domain Discretization sensitivity tests

$\boldsymbol{\Delta x}$	$\boldsymbol{\Delta z}$	***Sce***	***Hyd***	***TCMh***	***TCMv***	$\boldsymbol{AdSch_{\kappa\varepsilon}}$
Δx_1=$[bo/20, bo]$ Δx_2=$[bo/4, 3bo]$	Δz_{min}=$[ho/40, ho]$	$Q\&V$	with	Cst.	ML Prandtl	-

First, the sensitivity to the horizontal discretization is studied. For this purpose, the vertical discretization near the bottom is set as fine as Kulis and Hodges (2006) recommend, Δz=$ho/20$. According to Table 3.3, two horizontal discretization parameters are defined: Δx_1, the highest resolution near the discharge location, and Δx_2, the lowest resolution in the area furthest part from the discharge location. In order to compare the horizontal spreading for the different tests, the Figure 3.2a shows the front positions versus time in the plane of symmetry and in the plane at 45° to the symmetry plane (see line 0° and line 45° in Figure 3.1). These spatial and temporal quantities are normalized by the characteristic length and time scales of plume-like behavior flows (Chu and Jirka (1987) and Choi and Garcia (2001)), $L_p = Q_0^{3/5}/Bf_0^{1/5}$ and $T_p = Q_0^{4/5}/Bf_0^{3/5}$ (see Table 3.1). Furthermore, 3.2b and 3.2c show the longitudinal profile of normalized maximum velocity ($Umax/U_0$) and minimum dilution ($Smin$), respectively, used to analyze the evolution of the density current in the worst streamline, i.e. where the dilution of the density current is the lowest. To be consistent with the analysis of the behavior within the density current body carried out in Chapter 2, the longitudinal profiles presented in Figure 3.2b are considered from the instant that the density current is thoroughly developed in the study domain.

Figure 3.2a shows that for values of Δx_1 less than half of the horizontal slot dimension, i.e. $bo/2$, the spreading converges to similar values for all the cases. Paying attention to the longitudinal profile of the normalized maximum velocity in Figure 3.2b, higher differences can be observed in the region close to the discharge point. Taking the test with the lowest value of Δx_1 as the reference (values closer to the one), it can be seen that a discretization of at least $\Delta x_1 < b_0/4$ is needed to capture the flow motion in the discharge surroundings. Additional tests varying Δx_2 from $b_0/4$ to $3b_o$ reveal that in areas far from the discharge location, the

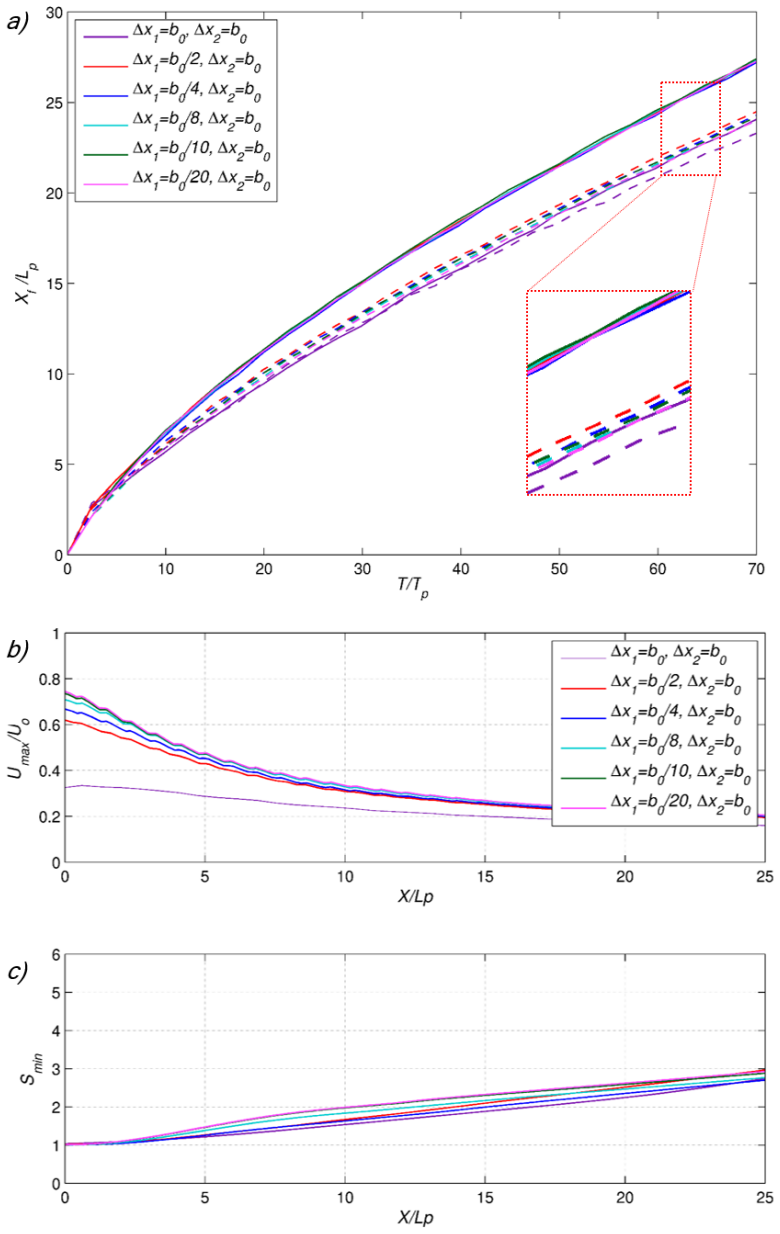

Figure 3.2: Horizontal discretization sensitivity tests: a) dimensionless front position versus dimensionless time in line 0° (continuous line) and in line 45° (dashed line); b) longitudinal profile of normalized maximum velocity; c) longitudinal profile of minimum dilution

horizontal discretization can be coarser and the results do not show significant differences. This way, the computational time can be minimized, but due to the large horizontal discretization variability, special attention must be paid to the $TCMh$ if it is set as Constant. In such cases, it is recommended to take different eddys coefficient values along the study domain according the mesh-grid resolution (Madsen et al. (1988)).

Secondly, the sensitivity to the vertical discretization is analyzed. Following Kulis and Hodges (2006) methodology, several tests are conducted both with and without the $TCMv$ over a wide range of vertical discretizations: Δz_{min}=$[h_0/40, h_0]$. In order to generate time-affordable simulations, the highest resolution for each case (i.e. the lowest values of Δz, Δz_{min}) is established in the region twice the height h_0 above the bottom, and from that depth to the surface the spacing is gradually increased by a factor of 1.5. The results of these tests, with and without $TCMv$, are used to evaluate the relationship between modelled mixing and numerical mixing at different discretizations. Calculating the vertical Entrainment coefficient (E) in the symmetrycal longitudinal profile (line 0°) for both types of tests provides a quantitative measure of the mixing. The Entrainment coefficient is calculated from the salinity longitudinal profile using the method of Dallimore et al. (2001), explained in Chapter 2. Figure 3.3 shows the value of the average Normal Entrainment coefficient E_N versus the number of vertical layers within the density current $N_{Zh} = h_0/\Delta z_{min}$ for different horizontal discretizations. E_N represents a single average value calculated from $X/L_P = 15$ in order to eliminate the effects of the density current's initial adjustment to the "Normal Status" (see Chapter 2).

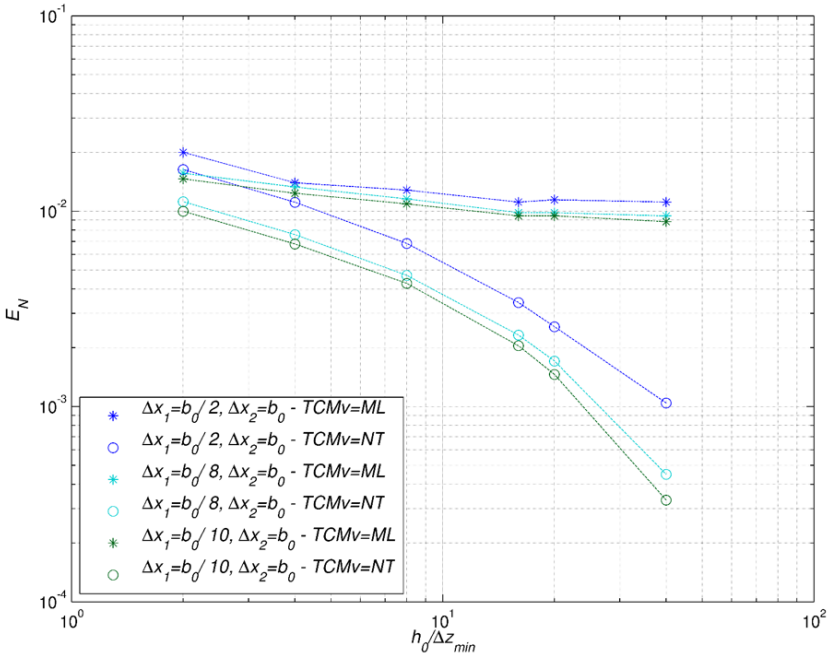

Figure 3.3: Vertical discretization sensitivity tests: Normal Entrainment versus vertical discretization for different horizontal discretization

In cases with the $TCMv$ turned off (no-turbulence NT tests), all mixing should be due to molecular Brownian motion. Since in these NT tests the kinematic viscosity (i.e. molecular) coefficient is set to 10^{-9} m^2/s, the vertical mixing should be essentially zero. Therefore, any mixing calculated in the NT tests can be considered as being due to numerical effects, so-called numerical diffusion. Figure 3.3 shows that, with the exception of the most coarsely resolved tests, the turbulent entrainment rates (i.e. entrainment rates of cases with the $TCMv$ turned on as ML) converge on the order of 10^{-2}, while the numerical entrainment rates (i.e. entrainment rates of cases with the $TCMv$ turned off, NT) increases nearly logarithmically as the vertical resolution coarsens, that is, the number of layers within the current is reduced. At a threshold of $h_0/\Delta z_{min}$ between 4-8, the numerical entrainment rates reaches the same order of magnitude as the turbulent entrainment rates. Thus, as the numerical entrainment rate increases (for fewer layers within the current), it begins to dominate the global modelled entrainment rate (i.e. turbulent plus numerical entrainment). It is noteworthy that when considering the horizontal resolution sensitivity tests for the each of the corresponding number of layers within the current, the previous pattern is maintained, always obtaining higher entrainment rates in tests with coarser horizontal resolutions. Therefore, it can be concluded that Figure 3.3 demonstrates that both the horizontal and the vertical resolution impact on the mixing modelled: the higher the resolution, the lower the numerical diffusion. Establishing a threshold such that the numerical diffusion should be around an order of magnitude below the global mixing to consider its effect negligible, Figure 3.3 indicates that values of $h_0/\Delta z_{min}$ between 16-20 are needed to minimize the numerical errors associated with numerical diffusion.

3.3.2. Source input and hydrostatic hypothesis

Once a suitable computational mesh-grid is defined, those numerical aspects that can also have an impact on the initial region of the density current are studied. As cited in the Section 3.2, TELEMAC-3D hydrodynamic model has the option to not assume the hydrostatic hypothesis, a simplification mainly valid for anisotropic flows where the horizontal motion scales are substantially larger than the vertical motion scales. Since density currents are mainly horizontal flows, the hydrostatic hypothesis appears to be properly assumed. However, as Mahgoub et al. (2015) highlighted, vertical accelerations might not be negligible compared

to gravitational acceleration in the starting region of the density current due to a kind of near field local effects found in this region. Numerically, without this hydrostatic hypothesis, the vertical momentum equation (3.4) is fully solved without any simplification, and the pressure (equation (3.6)) is split up into a hydrostatic pressure and a dynamic pressure term. On the other hand, TELEMAC-3D, like other similar hydrodynamic models, has the option of specifying only the liquid flow rate Q or specifying the liquid flow rate and the injection velocity ($Q\&V$). This section presents the analysis of the impact of these numerical aspects on the behavior of density currents. Table 3.4 presents the options selected for the rest of the numerical aspects.

TABLE 3.4: Numerical aspects in the Source-input & Hydrostatic-hypothesis sensitivity tests

$\boldsymbol{\Delta x}$	$\boldsymbol{\Delta z}$	***Sce***	***Hyd***	***TCMh***	***TCMv***	$\boldsymbol{AdSch_{\kappa\varepsilon}}$
Δx_1=$bo/8$ Δx_2=bo	Δz_{min}=$ho/20$	Q-$Q\&V$	with-without	Cst.	ML Prandtl	-

It is important to note that, although physically there is only one source of $h_0 \times b_0$ dimensions, due to the domain discretization, numerically it is transformed in several punctual source terms. For instance, 160 puntual sources of a liquid flow rate of $Q_0/160$ are needed for the specifications showed in Table 3.4 (Δx_1=$bo/8$ and Δz_{min}=$ho/20$).

Following the graphics presented in Figure 3.2, Figure 3.4 shows the impact of the source specification type and the hydrostatic hypothesis on the horizontal spreading and the symmetrical longitudinal profiles of maximum velocity and minimum dilution for the density current studied. For the source specification, $Q\&V$ information is needed to capture the flow motion in the discharge surroundings, U_{max}/U_o shows values closer one. The assumption of the hydrostatic hypothesis has a lower impact, but tests without the hypothesis obtain values of U_{max}/U_o closer to the one. Nevertheless, the non-hydrostatic simulations require some numerical corrections to fulfil the stability criterion (e.g. to apply a high implicitation coefficient for velocities and pressure, and to consider a TELEMAC-3D correction that deletes spurious free surface oscillations). These corrections, and the fact that a more complex system has to be solved, makes the application 1.5$\sim$2 times more time-consuming to obtain an almost negligible improvement. Thus, keeping in

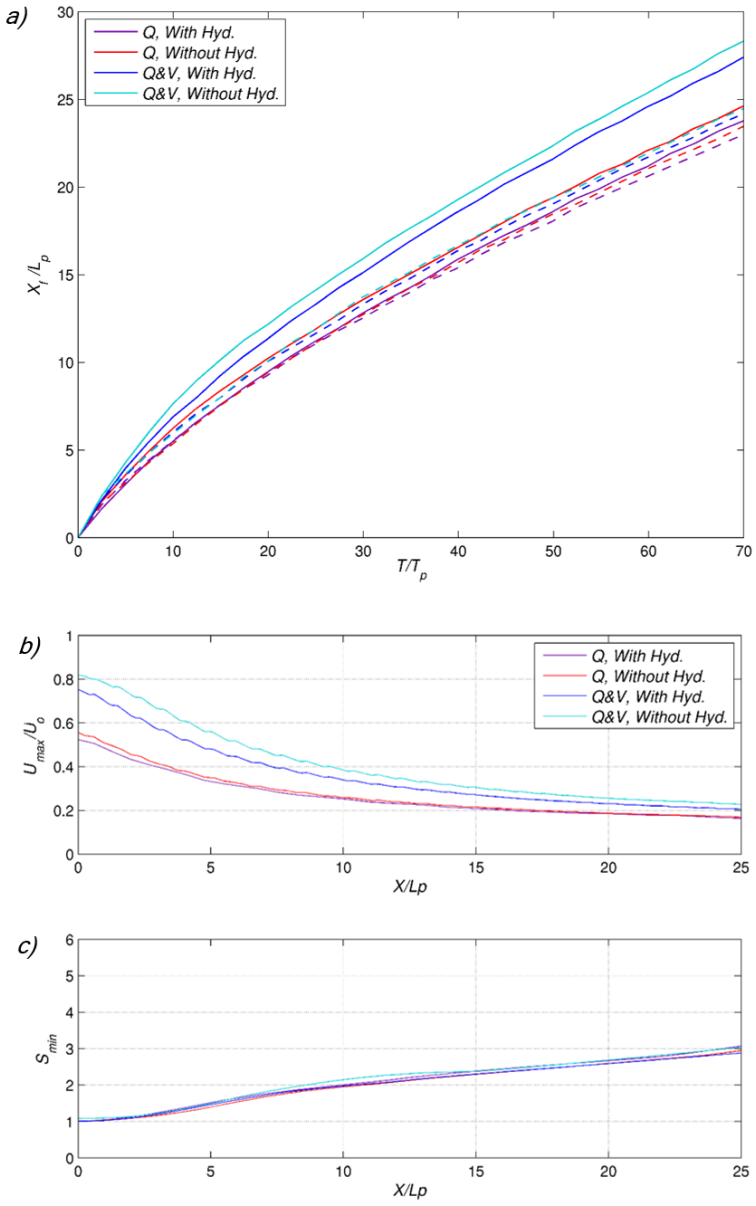

Figure 3.4: Source-input & Hydrostatic-hypothesis sensitivity tests: a) dimensionless front position versus dimensionless time in line 0° (continuous line) and in line 45° (dashed line); b) longitudinal profile of normalized maximum velocity; c) longitudinal profile of minimum dilution

mind field-scale applications with more complex environmental conditions than this box case, the hydrostatic hypothesis is considered well assumed.

3.3.3. Turbulence modelling

On the basis of the previous sensitivity tests, this section presents the findings concerning several of the well-known turbulence modelling options briefly described in section 3.2: Constant, Smagorinsky, Mixing-Length and $\kappa\varepsilon$ turbulence closure models (TCMs). Table 3.5 summarizes both the fixed numerical aspects (Δx, Δz, *Sce* and *Hyd*) and the options taken into account in this sensitivity test ($TCMh$, $TCMv$ and $AdSche_{\kappa\varepsilon}$).

TABLE 3.5: Numerical aspects in the Turbulence Modelling sensitivity tests

$\boldsymbol{\Delta x}$	$\boldsymbol{\Delta z}$	***Sce***	***Hyd***	$\boldsymbol{TCMh}$	$\boldsymbol{TCMv}$	$\boldsymbol{AdSch_{\kappa\varepsilon}}$
Δx_1=$bo/8$ Δx_2=bo	Δz_{min}=$ho/20$	$Q\&V$	with	Cst., Smago.	Cst., ML, κ-ε	Charcs., $2^{nd}O$-KP

For the turbulence closure model in the horizontal direction ($TCMh$), it is common for hydrodynamic models to use a Constant turbulence model. Thus, the user has to calibrate the horizontal eddy viscosity ν_{th} depending on the particular flow being studied and the domain discretization (Madsen et al. (1988)). However, taking advantage of the options programmed into TELEMAC-3D, simulations varying the $TCMh$ between the Constant and the Smagorinsky model are compared. For the study case, keeping the $TCMv$ as the Prandtl Mixing Length model, the results do not present any appreciable differences. In these tests, ν_{th} is defined according to the variable mesh-grid resolution (it takes scaled-down absolute values from 4.7×10^{-5} to 1.6 10^{-4} m/s^2), and the calibration parameter of the Smagorinsky model (C_s) is defined as 0.1, a common value for anisotropic flows (e.g. flow in a canal). The κ-ε model was also set as the $TCMh$ model but in this case the κ-ε model is mandatory for the $TCMv$, so the influence of the $TCMh$ could not be extracted. In addition, the simulations became so time-consuming and unstable (due to numerical problems at the liquid boundaries with the Neumann boundary conditions for the κ and ε equations) that this option for the $TCMh$ is not considered.

Due to the stratified nature of these types of flows, the turbulence closure model in the vertical direction ($TCMv$) is a key numerical aspect for accurately predicting the behavior of density currents. To analyze how the $TCMv$'s influence on the vertical structure of the flow, Figures 3.5, 3.6 and 3.7 shows the downstream

variation of the velocity cross profiles (the main velocity component, U_x) and salinity (C) along the symmetry plane (see line 0° in Figure 3.1) for each $TCMv$ case: Constant, Mixing Length and κ-ε models. For all simulations, the $TCMh$ is held as Constant according to the previous criteria. Furthermore, these figures present the normalized cross profiles which collapse into a single profile, called a similarity profile (see Ellison and Turner (1959); Garcia (1993); Parker et al. (1987)). In addition to the numerical results, measured data obtained using PIV-PLIF techniques (Pérez-Díaz et al. (2017b)) is also displayed. In the similarity cross profiles the black thick black represents the best fitting polynomial curve to the measured data (see Chapter 2).

Figure 3.5 shows the cross profiles from different simulations with Constant $TCMv$, varying ν_{tv} values from $\nu_{th}/1000$ to $\nu_{th}/10$. In these simulations the eddy diffusivity Γ is defined by the Schmidt number ($\sigma_c = \nu_{tv}/\Gamma_v$) which is considered to take values close to one for these types of flows. Both the velocity and the concentration cross profiles reveal that the simulation $\nu_{tv} = \nu_{th}/10$ better fits the experimental data. However, this simulation does not present a good shape-approximation in the first cross sections, i.e. those with higher momentum and concentration. In the remainder of the cross sections, the velocity agrees with the experimental data, while the dilution is underestimated (i.e. higher concentrations than expected). As can be seen in the similarity cross profiles, the normalized mean horizontal velocity and mean concentration cross profiles collapse well into single profiles which agree with the experimental similarity profiles.

Figure 3.6 shows the cross profiles for the $TCMv$ Mixing Length models, varying between the Prandtl and the Nezu and Nakagawa models. For these cases, the damping function addressed by Munk and Anderson (1948) is used to govern the vertical mass and momentum exchanges. The results of the two simulations are almost identical, showing logarithmic velocity and concentration profiles in most part of the density current body. Near the bottom, the agreement between the $TCMv$, the damping function and the turbulence model for the bottom based on the previously defined roughness size (i.e. the Nikuradse coefficient) can be observed. While the velocity cross profiles match fairly well with the experimental data along the whole density current body, the concentration profiles significantly underestimate the dilution in the region close to the bottom. Unlike the previous case, the normalized mean horizontal velocity and mean concentration cross

profiles collapse into single profiles but they disagrees with the the experimental similarity profiles.

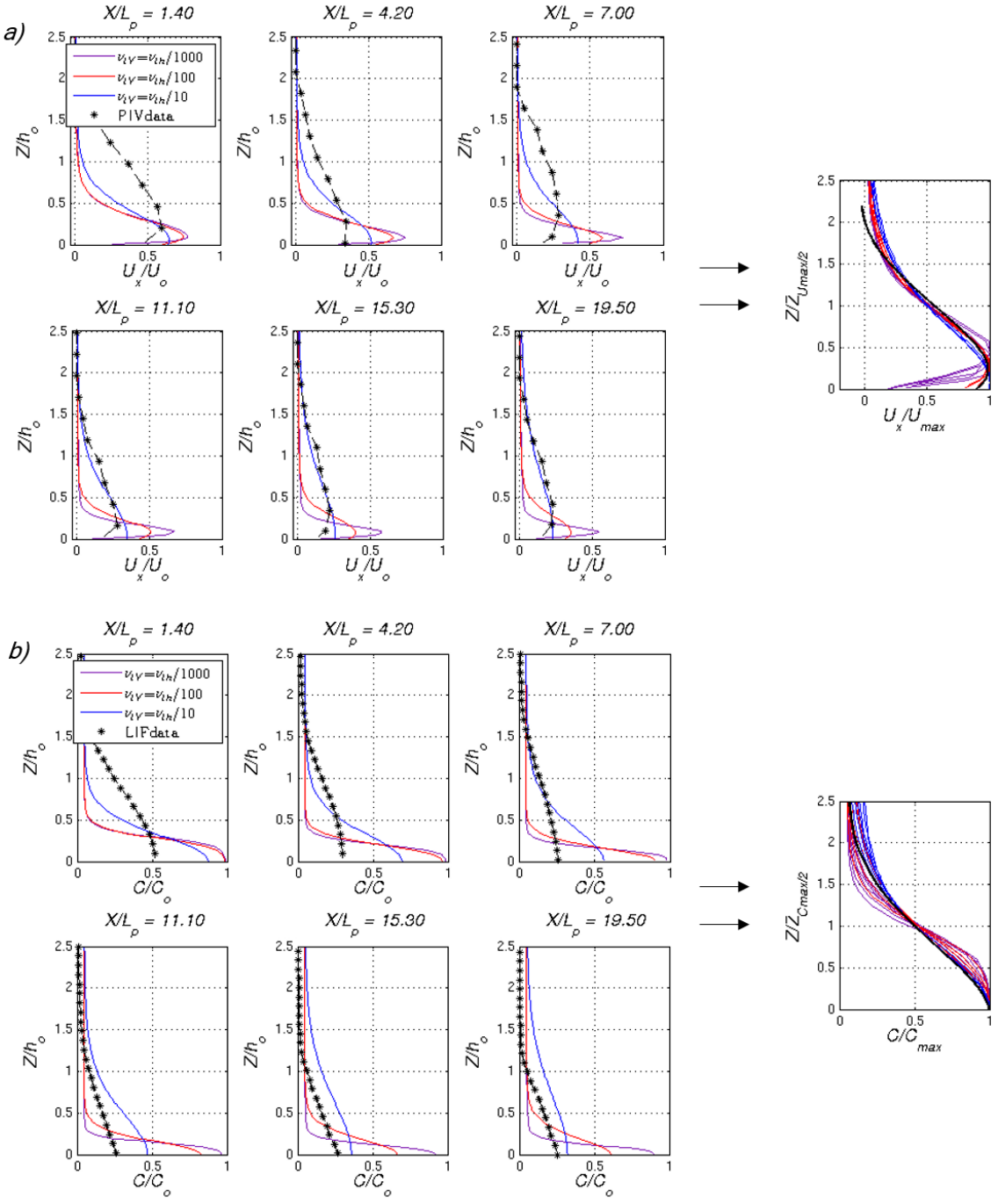

Figure 3.5: Downstream variation and similarity cross profiles for cases with $TCMv = Cst.$: a) horizontal velocity and b) salinity concentration

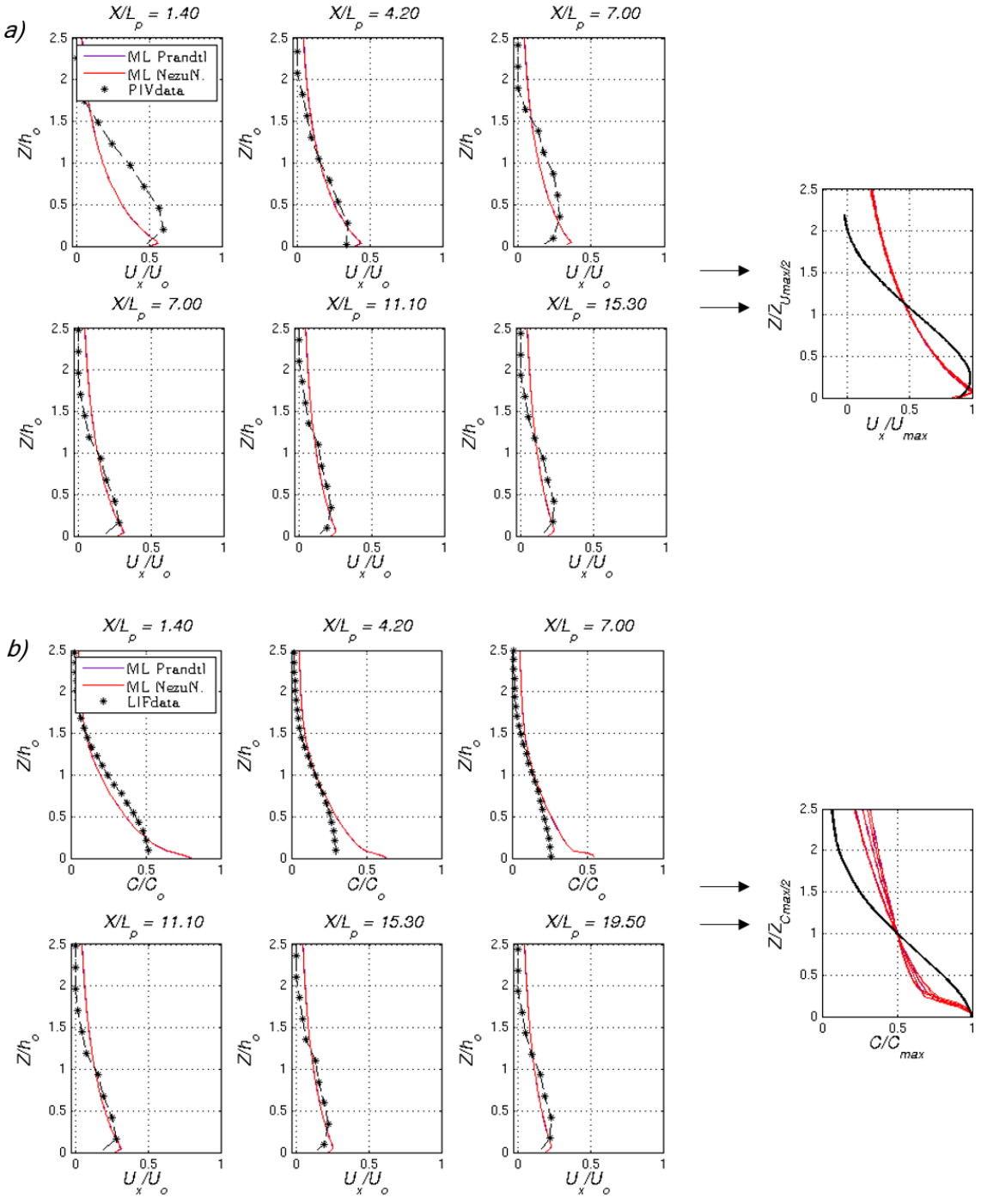

Figure 3.6: Downstream variation and similarity cross profiles for cases with $TCMv = ML$.: a) horizontal velocity and b) salinity concentration

Figure 3.7 shows the cross profiles from two simulations with the κ-ε $TCMv$. The difference between the two simulations is the advection scheme selected ($AdSch_{\kappa\varepsilon}$). Whereas in one case the method of characteristics is used, in the other case, the most conservative scheme programmed in TELEMAC-3D is selected (2^{nd}-KP). The characteristic method is recommended by LNHE and Laboratory (2007), since it has provided satisfactory results in many instances and it is the quickest. Nevertheless, due to the unique nature of these kinds of flows, where the buoyancy force is a driven force, i.e. the accurate definition of the mass-tracer quantities is fundamental, the more conservative scheme cited is also used to distinguish the influence of the advection scheme. Figure 3.7 reveals that both simulations overestimate the velocity and concentration near the bottom at all the locations studied, although the shape profile obtained is noticeably different from one case to the other. Regarding the cross profiles similarity, where a proper shape comparison can be undertaken, they reveal that the simulation with the most conservative advection scheme presents better results according to the experimental similarity curve.

Taking the similarity cross profiles into account, i.e. the profile shape profile, the Constant and κ-ε $TCMv$ are the models that best capture the vertical structure of thee density current. Since the Constant model only has the ν_{tv} as a calibration parameter, and the results presented in Figure 3.5 for $\nu_{tv} = \nu_{th}/10$ are its best results, the attention is focused on the κ-ε $TCMv$. As described in section 3.2, both the κ-ε model contains several empirical constants obtained by data fitting for a wide range of flows. Among these empirical constants, the $c_{3\varepsilon}$ and c_μ have demonstrated influence in the modelling of density currents and their values have been the subject of some controversy. For the $c_{3\varepsilon}$ constant, Hossain and Rodi (1982); Rodi (1987) and Choi and Garcia (2002) have suggested that $c_{3\varepsilon}$ values ranging from 1 to 0.6 give a good agreement with experimental results for density currents. On the other hand, the standard value of the other controversial empirical constant ($c_\mu = 0.09$) was chosen on the basis of experiments in flows in which the production P and dissipation ε of the turbulence energy were in approximate balance. In weak shear flows, for example, far-field jets and plumes where the velocity difference across the flow is only a small fraction of the convection velocity, P is significantly different from ε and c_μ was found to take different values (Rodi (1975)). Rodi (1972) correlated the experimental data and proposed a function $c_\mu = f(\overline{P/\varepsilon})$, which is valid only for thin shear layers (like the density currents studied).

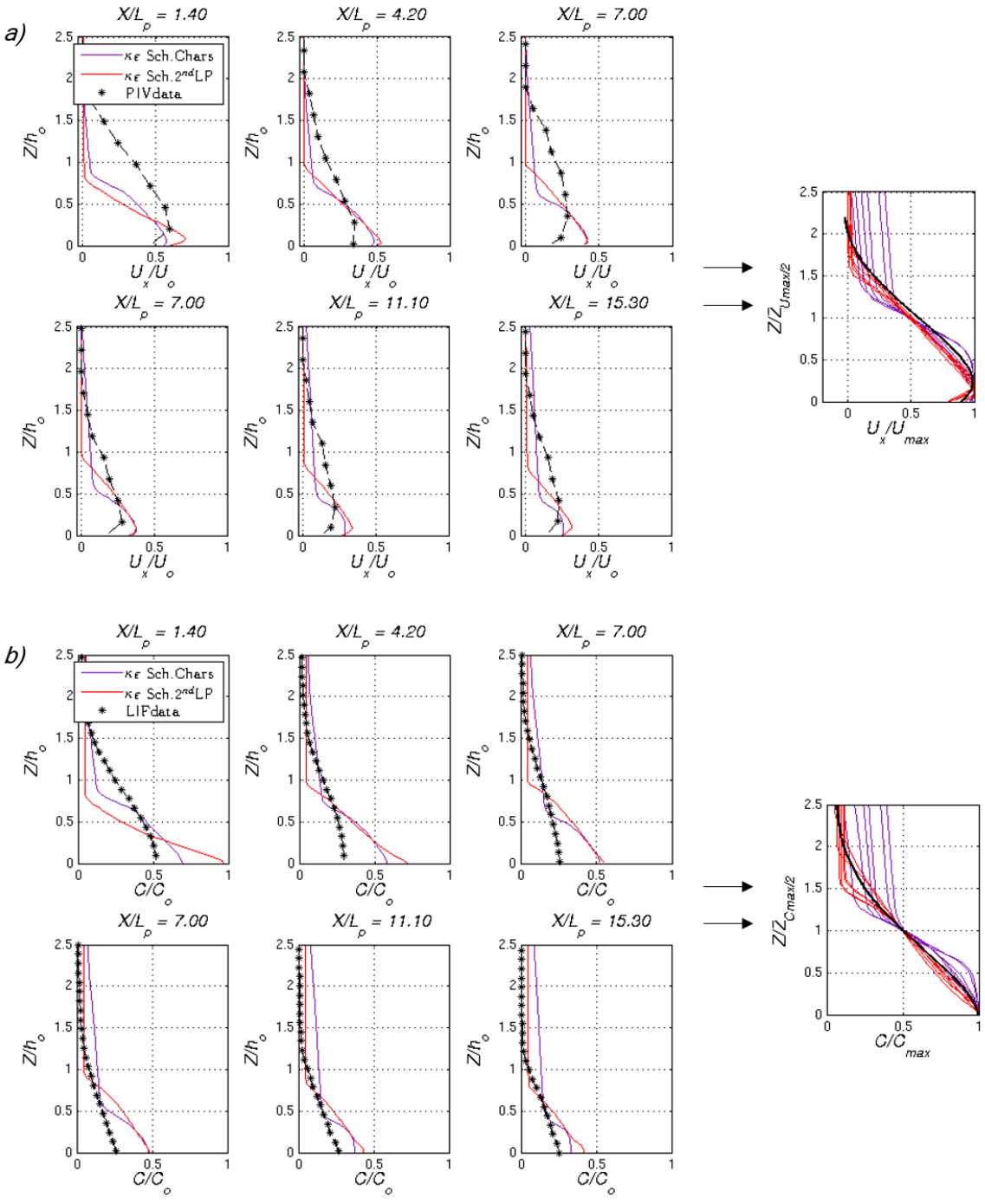

Figure 3.7: Downstream variation and similarity cross profiles for cases with $TCMv = \kappa$-ε: a) horizontal velocity and b) salinity concentration

In order to study the influence of these empirical constants on the density currents modelling, the results of several simulations varying the values of these constants are analyzed. The range of values of $c_{3\varepsilon}$ and c_μ is chosen based on the state of the art conclusions: $c_{3\varepsilon}$ values from 1 to 0.6 and c_μ values from 0.09 to 2.5. Another important parameter is the Schmidt number σ_c, which takes part in the eddy diffusivity definition and has values between 0.7 and 1. However, due to its lesser impact on the results compared to the $c_{3\varepsilon}$ and c_μ constants' impact, it is assumed to be equal to 0.7, a common value for heat and salinity transport. Taking advantage of the experimental results, a comparison between the results obtained from different simulations is carried out using of the Root Mean Square absolute Error (RMSE) formula:

$$RMSE = \sqrt{\frac{1}{N}\sum_{i=1}^{N}(x_{exp} - x_{num})^2} \tag{3.14}$$

where x_{exp} represents the experimental values of the variable studied - in this case the salinity concentration and the horizontal velocity; x_{num} represents the corresponding numerical value; and N is the number of pairs of comparable values. In this case, due to the large amount of data obtained from the PIV-PLIF techniques, the N value corresponds to the number of cross profiles evaluated, multiplied by the number of data points measured within the density current thickness (which varies depending on the variable). In order to obtain a kind of relative error, the Normalized $RMSE$ ($NRMSE$) is obtained by dividing the $RMSE$ by the initial value of the evaluated magnitude (C_0 or U_0) and multiplying by 100 to obtain the percentage. As a calibration assessment, the Table 3.6 compiles the error obtained for each simulation varying the $c_{3\varepsilon}$ and c_μ constants.

Table 3.6 reveals that the results of the simulation with $c_{3\varepsilon}$ equal to 0.7 and c_μ equal to 0.2 provides the smallest errors: 0.135 psu for salinity, and 0.005 m/s for velocity (2.8 % and 4.8 %, respectively). Figure 3.8 shows the downstream variation and similarity cross profiles for that simulation. As can be seen, the displayed results agree fairly well, both in terms of the shape as well in terms of the absolute values.

The optimum value of $c_{3\varepsilon}$ obtained in this study ($\sim [0.7-0.6]$) agrees with the values published in the scientific literature concerning density currents (e.g. Hossain and Rodi (1982); Rodi (1987) and Choi and Garcia (2002)). It has to be mentioned that some researchers define the empirical constant in the form $(1 - c_{3\varepsilon})$ instead

TABLE 3.6: Calibration of empirical coefficients c_μ and $c_{3\varepsilon}$ of κ-ε model

κ-ε coefficients		Salinity errors		Velocity errors	
$c_{3\varepsilon}$	c_μ	$RMSE$ (psu)	$NRMSE_{C_0}$ (%)	$RMSE$ (m/s)	$NRMSE_{U_0}$ (%)
1	0.09	0.496	10.3	0.012	11.7
	0.15	0.396	8.2	0.011	10.5
	0.2	0.244	5.0	0.008	7.9
	0.25	0.253	5.3	0.008	8.2
0.9	0.09	0.450	9.4	0.010	10.2
	0.15	0.358	7.5	0.010	9.8
	0.2	0.210	4.4	0.007	7.2
	0.25	0.219	4.6	0.007	7.5
0.8	0.09	0.427	8.9	0.011	10.6
	0.15	0.318	6.6	0.009	9.0
	0.2	0.177	3.7	0.007	6.7
	0.25	0.187	3.9	0.006	6.4
0.7	0.09	0.318	6.6	0.008	8.3
	0.15	0.199	4.1	0.007	6.8
	0.2	0.135	2.8	0.005	4.8
	0.25	0.139	2.9	0.006	5.6
0.6	0.09	0.355	7.4	0.009	9.0
	0.15	0.238	4.9	0.007	7.3
	0.2	0.137	2.8	0.006	5.7
	0.25	0.140	2.9	0.006	5.7

of $c_{3\varepsilon}$, so that the corresponding optimum value would then be ($\sim [0.3 - 0.4]$). On the other hand, the optimum value of c_μ obtained (~ 0.2) is included in the range of values established by the function $c_\mu = f(\overline{P/\varepsilon})$, defined by Rodi (1972). This function is only valid for thin shear layers like density currents, where the argument $\overline{P/\varepsilon}$ is the average value of P/ε across the layer. Launder et al. (1973) demonstrated that the use of this function significantly improves the κ-ε model's ability to predict these kinds of flows. Far from the standard value ($c_\mu = 0.09$), which is accepted for flows with the production P and dissipation ε of the turbulence kinetic energy in balance ($\overline{P/\varepsilon} \simeq 1$), the optimum value obtained corresponds to a $\overline{P/\varepsilon}$ value of ~ 0.5. That is, the average production term is approximately half of the average dissipation of turbulence kinetic energy. Figure 3.9 displays the downstream variation of the terms involved in the κ-ε equations like the above mentioned P and ε.

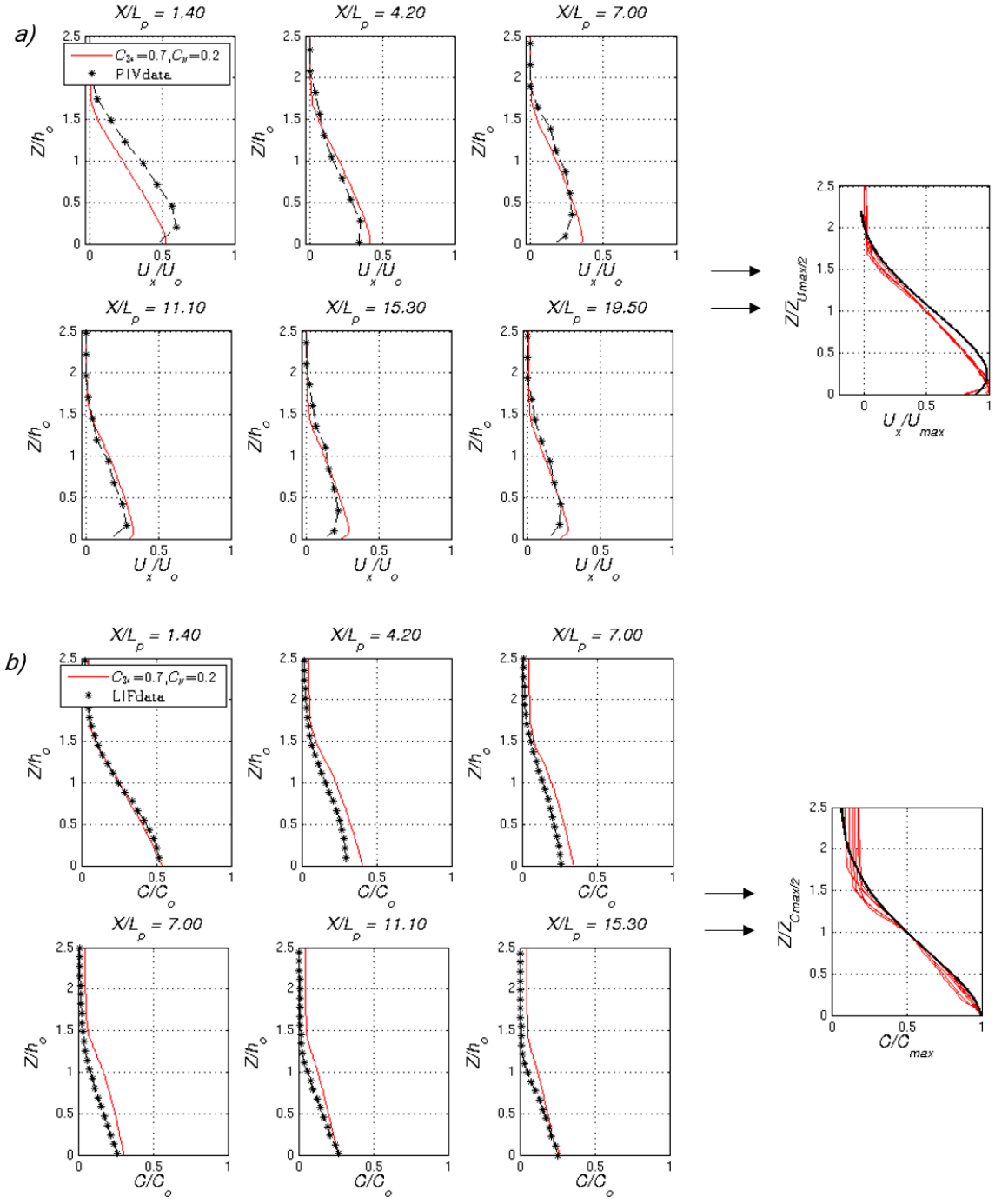

Figure 3.8: Downstream variation and similarity cross profiles for cases with calibrated $TCMv = \kappa$-ε: a) horizontal velocity and b) salinity concentration

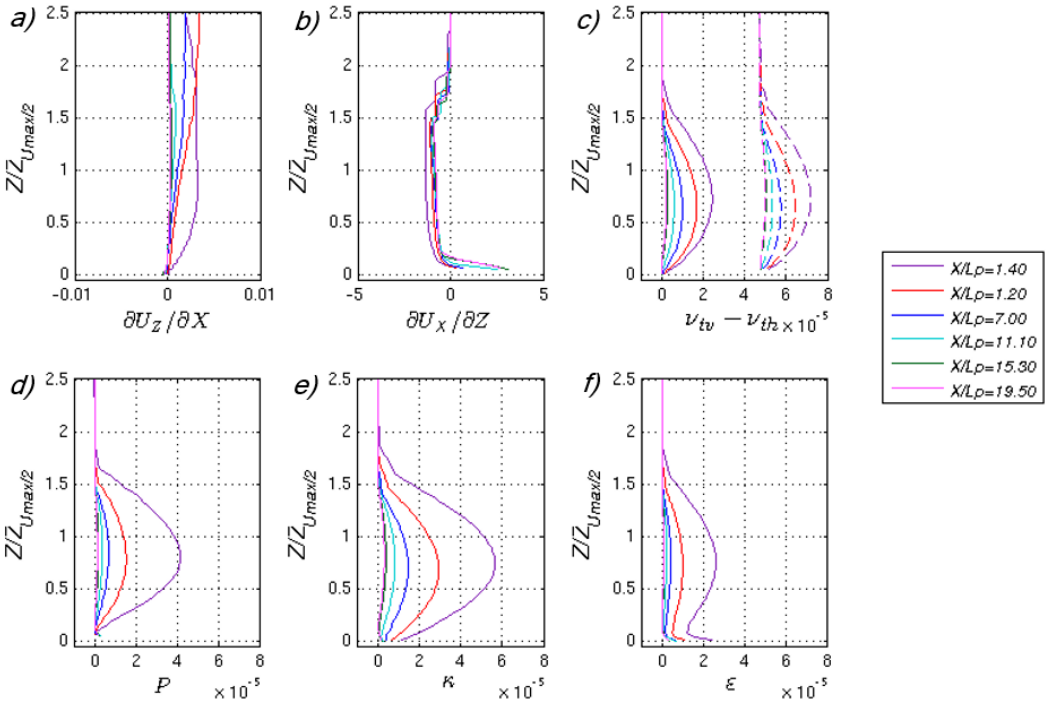

Figure 3.9: Downstream variation of the terms involved in κ-ε equations (3.8)-(3.9) for the calibrated test: a) horizontal gradient of vertical velocity; b) vertical gradient of horizontal velocity; c) horizontal (dashed line) and vertical (continuous line) eddy viscosities; d) production term; e) turbulent kinetic energy; f) dissipation of turbulent kinetic energy

Focusing on the graphs plotted in Figure 3.9, the horizontal gradient of vertical velocity ($\partial U_Z/\partial X$), the vertical gradient of horizontal velocity ($\partial U_X/\partial Z$) and the vertical eddy viscosity (ν_{tv}) are extracted in order to obtain the production term (P) following the equation (3.10). The tiny values of $\partial U_Z/\partial X$ were expected due to the horizontal nature of the flow studied, and the range of values ($[-2, 3]$ $1/s$) obtained for $\partial U_X/\partial Z$ agrees well with the experimental data ($[-2, 2]$ $1/s$) presented in Chapter 2. As expected, the eddy viscosities reduce their values according to the velocity decay. It is worth emphasizing that these two numerical magnitudes, ν_{tv} and ν_{th}, are part of the Boussinesq approach to establishing a closure model for the RANS equations (see section 3.2). Thus, their values cannot be directly compared to their experimental values obtained from velocity fluctuations. The Figure 3.9d presents the production term (P), which shows really small values close to the bottom compared to the dissipation of turbulent kinetic energy (ε), plotted in 3.9f. Finally, the turbulent kinetic energy (κ) is displayed in 3.9e. The shape

of the κ cross profiles and their order of magnitude (10^{-5}) match with the experimental horizontal Reynolds stress component (the main component of turbulent kinetic energy in these horizontal flows) presented in Chapter 2. Regarding to the shape of the cross profile, both the numerical and experimental profiles present a clear peak corresponding to the upper flow boundary and a zone of minimum turbulence energy at the location of the maximum velocity.

3.4. Proposed modelling set-up

Having presented the main results of the sensitivity test are presented, this section summarizes the proposed modelling set-up in order to simulate the behavior of a density current. According to the nomenclature used throughout this manuscript, the optimum numerical aspects used to configure any of the well-known 3D hydrodynamic models that solve the equations described in section 3.2, are listed in Table 3.7.

TABLE 3.7: The optimum numerical aspects for predicting density currents

$\boldsymbol{\Delta x}$	$\boldsymbol{\Delta z}$	$\boldsymbol{Sce}$	$\boldsymbol{Hyd}$	$\boldsymbol{TCMh}$	$\boldsymbol{TCMv}$	$\boldsymbol{AdSch_{\kappa\varepsilon}}$
$\Delta x_1 \leq bo/4$	$\Delta z_{min} \leq ho/16$	$Q\&V$	with	Cst.	κ-ε c_μ=0.2, $c_{3\varepsilon}$=0.7	Most conserv. (p.e. $2^{nd}O$-KP)

Applying these recommendations to the $CASE1$ density current analyzed (see Table 3.1), a relative error of the front position ($NRMSE_{X_{fexp}}$) of less than 6% is obtained. For the evolution of the density current in the streamline where the dilution of the current is the lowest (line 0°), the error is about 4% for the main velocity component ($NRMSE_{U_0}$), and less than 1.3% for the dilution ($NRMSE_{S_{min}}$). Figure 3.10 shows the evolution of the main magnitudes described and their graphically comparison with the experimental data. Moreover, Figure 3.11a presents a plan-view comparison in terms of concentration between the numerical and the experimental spreading results at different times. For consistency, the longitudinal symmetry profile views of the numerical and the experimental concentration results are shown in Figures 3.11b and 3.11c. It has to be taken into account that the vertical scale in the profile plots is distorted, thus, to properly check the

turbulence structures' characteristics at the upper boundary and the head of the density current, a review of Chapter 2 is recommended.

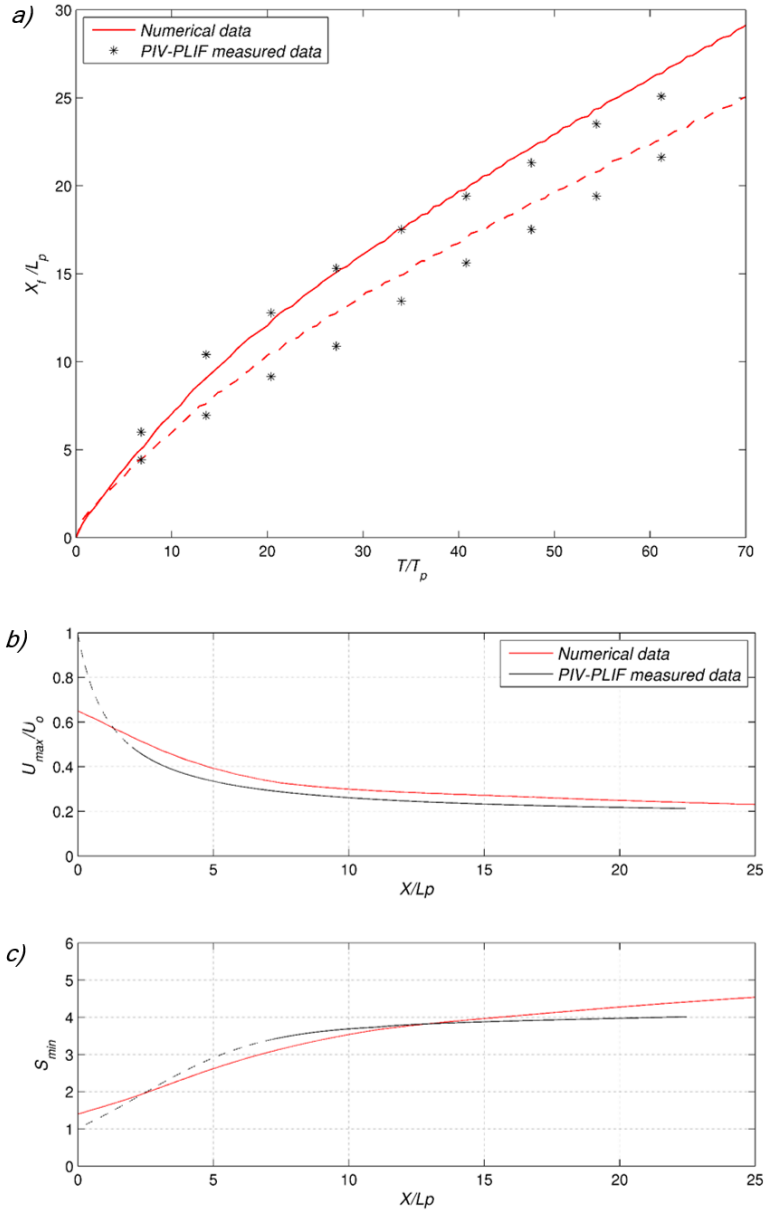

Figure 3.10: Comparison between the numerical and the experimental results: a) dimensionless front position versus dimensionless time in line 0° (continuous line) and in line 45° (dashed line); b) longitudinal profile of normalized maximum velocity; c) longitudinal profile of minimum dilution

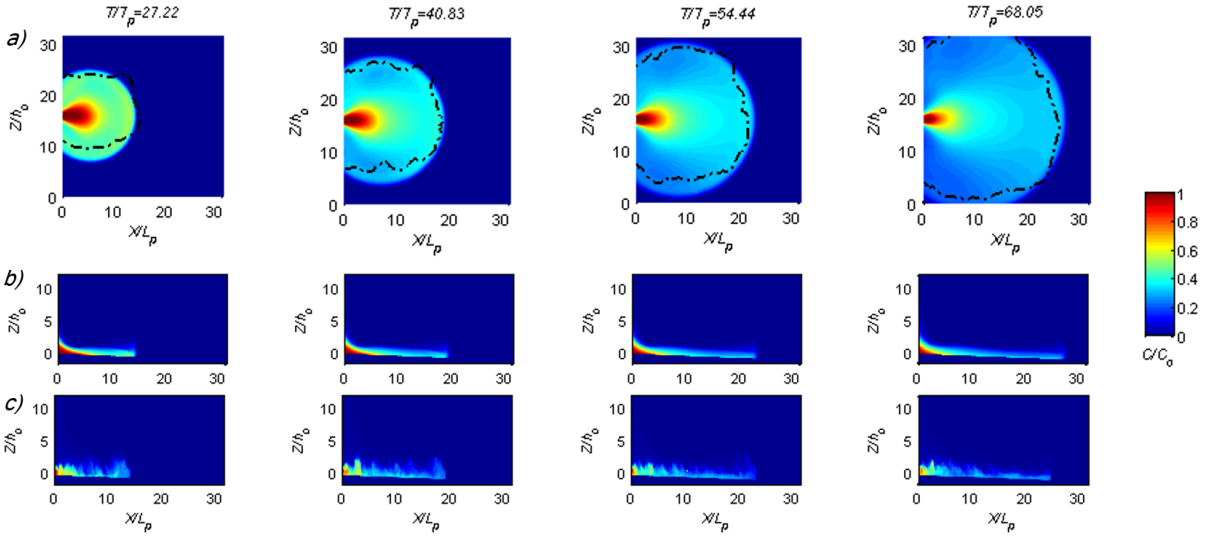

Figure 3.11: Comparison between the numerical and the experimental spreading results at different times: a) plan view (experimetal results are the dashed line); b) profile view of modelled results; c) profile view of LIF experimental results

3.5. Validation under different flow conditions

To ensure that the proposed modelling set-up is valid for density currents generated under different flow conditions, the present section compares the numerical results obtained taking into account this set-up with the experimental data obtained from different laboratory tests.

This study applies the proposed optimum modelling set-up to simulate the complete set of experimental density currents presented in Chapter 2 (Pérez-Díaz et al. (2017b)), which main parameters are gather in Table 3.8. A comparison between the experimental and numerical results is carried out using the minimum dilution obtained from the last section of the density currents (S_{minF}), which represents the result of the transport and mixing processes. Table 3.9 shows the mentioned comparison, denoting the experimental and the numerical results with the sub-indices $_E$ and $_N$, respectively. As can be observed, a good agreement between experimental and numerical values is obtained for all cases. Furthermore, the modelled values S_{minF_N} maintain the correlation revealed in the experiments S_{minF_E}. That is, establishing the value of *CASE1* as the base case $S_{minF_{Nb}}$, the rates $S_{minF_N}/S_{minF_{Nb}}$ agree with the corresponding experimental ratio $S_{minF_E}/S_{minF_{Eb}}$, showing that steeper slopes (*CASE4* and *CASE5*) and higher initial momentum (*CASE2* and *CASE3*) enhance the dilution, unlike in the case with higher initial buoyancy

Table 3.8: Main characteristics of the complete set of the laboratory configurations

CASES	Slot dimensions $(b_0 \cdot h_0)$ m	Water depth (Ha_0) m	Slope (α) %	Density difference $(\rho_a - \rho_0)$ Kg/m^3	Discharge flow-rate (Q_0) l/min	Buoyancy flux (Bf_0) cm^4/s^3
CASE1	$0.100 \cdot 0.026$	0.460	1.0	3.145	14.600	749
CASE2	$0.100 \cdot 0.016$	0.460	1.0	3.100	15.100	765
CASE3	$0.100 \cdot 0.026$	0.460	1.0	3.130	19.200	984
CASE4	$0.100 \cdot 0.026$	0.420	2.5	3.070	14.980	753
CASE5	$0.100 \cdot 0.026$	0.360	4.5	3.140	14.09	775
CASE6	$0.100 \cdot 0.026$	0.460	1.0	11.080	14.890	2700

(*CASE6*). Another comparison between measured and modelled data based on the Normal Entrainment coefficient E_N (explained in Section 3.3.1) also displays a good accordance between the two datasets, revealing that all the E_N values are of the same order of magnitude, within the range of 0.007 to 0.031.

Table 3.9: Minimum dilution comparison at the last section of the density currents studied

CASES	Modified parameter	S_{minF_E}	S_{minF_N}	$S_{minF_E}/S_{minF_{Eb}}$	$S_{minF_N}/S_{minF_{Nb}}$
CASE1	–	4.3	4.5	$S_{minF_{Eb}}$	$S_{minF_{Nb}}$
CASE2	$\downarrow h_0$	7.2	7.2	1.66	1.60
CASE3	$\uparrow Q_0$	6.8	5.8	1.56	1.28
CASE4	$\uparrow \alpha$	5.3	5.9	1.23	1.31
CASE5	$\uparrow\uparrow \alpha$	6.6	6.8	1.525	1.51
CASE6	$\uparrow (\rho_a - \rho_0)$	4.1	3.7	0.94	0.83

Choi and Garcia (2001) published a set of density current experiments carried out in a $2.44x3.66x1.22m^3$ tank. They studied the spreading rates of three-dimensional density currents on sloping beds, varying the density difference and the angle of the slope. The sloping bed was made of fiberglass, i.e. a roughness equivalent to glass or Plexiglass. The initial flow parameters of these experiments are clearly detailed in the Table 1 of Choi and Garcia (2001)). In an effort to continue validating the recommendations for the configuration of the hydrodynamic models to properly simulate the density currents, experiments from $DEN1$ to $DEN9$ (see Table 1 of Choi and Garcia (2001)) are numerically reproduced and compared to the corresponding measurements. Figure 3.12a shows the good agreement on the graph of dimensionless maximum half-width versus dimensionless time. In addition, Figure 3.12b shows the comparison for longitudinal spreading using of the

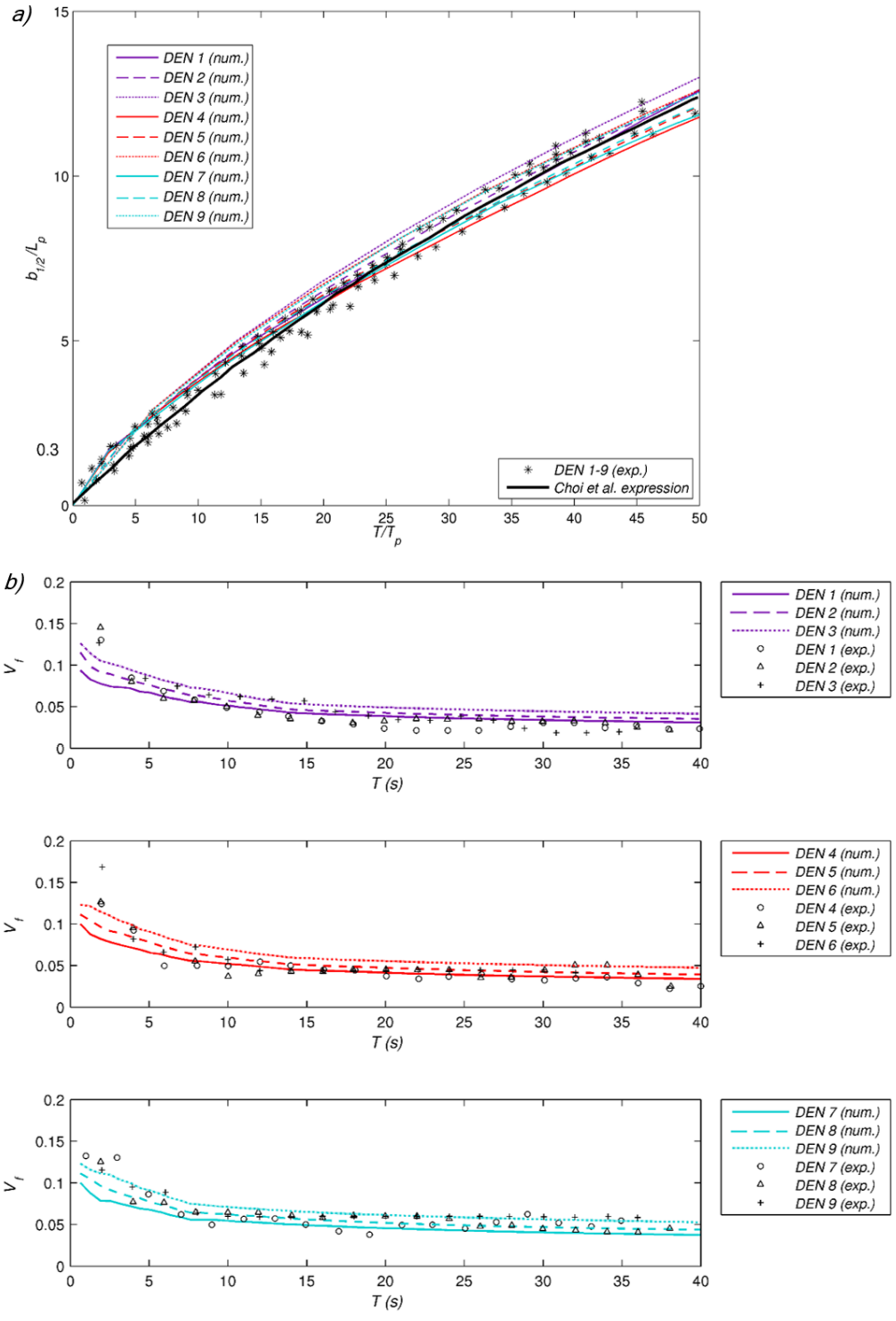

Figure 3.12: Comparison between the numerical and the experimental results (Choi and Garcia (2001)): a) dimensionless maximum half-width versus time; b) velocity front

front velocity evolution. In this case, it can be observed that the velocity is fairly well reproduced when the initial high momentum region is developed. Beyond the comparison, some remarks regarding the different densities and slopes' influence on the current behavior can be made from observing these graphs. Agreeing with previous studies (Alavian (1986); Choi and Garcia (2001)), steeper slopes favor rapid longitudinal spreading and hinder the lateral spreading (i.e. higher front velocities and lower half-widths), and a higher density difference favors both longitudinal and lateral spreading (i.e. higher front velocities and higher half-widths).

3.6. Conclusions

Drawing from the set of sensitivity tests and the calibration-validation efforts, this study reveals that appropriately configured 3D hydrodynamic models are able to simulate the behavior of saline density currents with a high level of accuracy. Then, the main numerical guidelines for solving these kinds of flows with these models are summarized:

- Variable spacing horizontal discretization (e.g. unstructured mesh-grids) is recommended inn order to obtain a high resolution near the source. This way, a lower resolution can be set in the farthest part of the source, making the application more computationally efficient. Assuming a slot-shaped source ($b_0 \times h_0$), which is a common approximation at the beginning of the far field region of the brine discharges, minimal spacing at least equal to the width of the slot b_0 is needed to ensure the momentum and mass conservation as much as possible. Specifically, for the cases analyzed in this study, spacing higher than $b_0/4$ is recommended.

- In the vertical direction, a high resolution is mandatory to prevent the vertical numerical diffusion. For the type of density currents studied in this work, and considering the a slot-shaped source, the vertical spacing has to be at least $h_0/16$. Since this fine resolution cannot maintained along the whole water column (i.e. there are too many numbers of layers), a gradual vertical spacing with the highest resolution near the bottom (within the density current body) is recommended. In such cases, a sigma-layer coordinate

(i.e. terrain-following) in the vertical domain discretization is recommended, in order to keep the finest layers at the bottom.

- Full momentum-source specification is advisable, i.e. both the flow rate and the also velocity information ($Q\&V$) should be detailed.

- The hydrostatic hypothesis is considered well assumed for cases over a plain bathymetry since it significantly ($1.5 \sim 2$ times) reduces the computational time and because the equivalent case without the hypothesis does not present significantly improved results.

- The Constant model is recommended as horizontal turbulence closure model ($TCMh$), varying the eddy coefficient values according to the mesh-grid resolution.

- Several vertical turbulence closure model ($TCMv$) can be successfully applied, such as Constant, Mixing-Length or κ-ε models. However, given the demonstrated influential role the $TCMv$ has in the numerical simulation of these flows, a calibration effort for each case study is recommended to be performed. Specifically, for the cases analyzed in this study, the calibrated κ-ε model (empirical constants $c_{3\varepsilon}$ and c_{μ} equal to ~ 0.7 and ~ 0.2, respectively) in conjunction with the most conservative advection scheme for the κ-ε equations, provides the best results. It has to be taken into account that the use of the κ-ε turbulence model, which solves two more equations, is highly demanding in terms of computational time. Both the Mixing Length model and the Constant model can give good approximate results in a more reasonable timeframe for field applications.

The results obtained in this study demonstrate that by applying these guidelines, 3D hydrodynamic models can reproduce laboratory-generated density current flows with errors lower than 1.3% for the minimum dilution line and 6% for the maximum velocity line. Due to the previous guidelines having been obtained from the validations using measurements obtained taken under laboratory controlled conditions, this contribution represents a first step on the validation of these 3D hydrodynamic models to solve real field-scale saline current flows. Accordingly, the logical next step should be to check and validate the previous guidelines in field-scale applications, where the bathymetry and the environmental conditions can have a significant influence on the density current evolution. It is noteworthy

that these models have been widely validated in terms of the reproduction of main coastal dynamics, either by themselves or by robust coupling with other models (e.g. atmospheric and wave models).

Chapter 4

Coupled modelling methodology of brine discharges. Validation case: Maspalomas desalination plant [1][2]

Abstract

The main sub-product of seawater desalination plants is brine, an hypersaline effluent which is commonly discharged into the sea through submerged jets and may cause harmful impact on the Environment as well as on the desalination technology efficiency if it reaches the seawater intakes. This contribution presents a coupled modelling methodology using *ad hoc* validated models (i.e. BrIHne and TELEMAC-3D) to accurately predict the Near Field (NF) and Far Field (FF) behavior of these brine discharges in an integral way. Furthermore, the developed methodology is validated against concentration measurements in the brine plume generated by the discharge of Maspalomas desalination plant (Canary Island, Spain) under different environmental conditions. Results obtained reveals that the proposed methodology performs accurately in terms of spatial extent of the density current, in terms of salinity excesses obtained close to and far form the

[1]This study is under preparation to be submitted for publication in a SCI journal.

[2]This study was developed during a placement at I+D center HR Wallinford (part of the management consortium of the suite of solvers TELEMAC-MASCARET), in collaboration with the Hydrodynamics and Metocean group

discharge point as well as in terms of vertical distribution of the salinity within the water column. Therefore, this contribution constitutes and advance in predicting these negatively-buoyant discharges, which is fundamental in the outfall design phase of desalination plant whose objective is to mitigate the negative effect of brine both in the NF and FF regions.

4.1. Introduction

The scarcity of water in highly populated areas near the coast (e.g. the Mediterranean and the Middle East regions or the coast of California, China and Australia) has promoted the construction of many seawater desalination plants to supply with fresh water the local population (Cánovas Cuenca (2012); Laspidou et al. (2010) and Dawoud and Al Mulla (2012)). At the time of this thesis, the most highest yielding desalination technology worldwide is the seawater reverse osmosis (SWRO), whose main sub-product is brine, and hypersaline effluent which is commonly discharged into the sea through submerged jets and may cause harmful impact on marine ecosystems (Laspidou et al. (2010); Lattemann and Höpner (2008) and Sánchez-Lizaso et al. (2008)). The behavior of brine discharges within the marine environment are usually split into the Near Field (NF) and Far Field (FF) regions according to the proximity to the discharge point and to spatial and temporal scales of the downstream developed flow. Knowing that the highest dilution rates are obtained in the NF region, where the mixing characteristics are dominated by small scales (∼metres and ∼minutes), discharge devices are specially designed to achieve maximum dilution and to meet environmental requirements within the NF region. However, in the following cases a FF region prediction is required: (1) the minimum dilution required is not achieved in the NF region, (2) there are sensitive ecosystems to brine far from the discharge point but within the potential impact area of the FF, (3) there is a risk of recirculation problems, i.e. brine effluent discharged can reach the seawater intake, (4) the effluent has chemical pollutants (e.g. those present in the sub-product of thermal desalination plants, or in membrane cleaning waters of SWRO desalination plants). In these cases, a global hydrodynamic study that allow to predict the complex brine effluent behavior far from the discharge point (i.e. both NF and FF regions) is required. Due to the large differences in time and spatial scales, the NF and FF regions have to be separately predicted by using different simulation tools. Therefore, a

reliable coupling procedure between NF and FF region models is needed to obtain a prediction of the global behavior of the brine discharges, covering distance far from the disposal point.

Regarding the NF region, where the mixing obtained depends on the brine discharge configuration and the effluent and ambient properties, several software have been used to provide an approximate environmental impact assessment of submerged discharges: VISJET (Cheung et al. (2000)), CORMIX (Doneker and Jirka (2001)) and VISUAL-PLUMES (Frick (2004)). Although these tools, based on dimensional analysis and integration of differential equations, were programmed and validated for simulating the flow of positively-jets, they have been also used for modelling negatively buoyant jets arising from brine discharges. More recently, a new set of tools called BrIHne (www.BrIHne.ihcantabria.com), based on mathematical approaches scientifically supported for brine effluents (Palomar et al. (2013)), have been developed and validated with experimental tests (Palomar (2014)). Several research works such as Plumb (2008) and Garcia Alba (2011) used computational fluid mechanics (CFDs) advanced models as the CFD FLUENT to achieve approximate predictions for single port discharges. Oliver et al. (2008) and Robinson et al. (2016) focussed in the comparison of their advanced modelling results with measurements from experiments of inclined negatively buoyant discharges, showing the difficulties encountered. These CFDs models are the closest to DNS (Direct Numerical Simulation) by using complex turbulence closure models of either time (Reynolds equations), or spatially averaged Large Eddy Simulation (LES). However, although very refined information can be extracted from them, these models are still very time-consuming compared to the integral model approach.

In the FF region, where the transport and mixing characteristics are dominated by large scales (∼kilometres and ∼hours), the behavior of the saline density current generated depends on the ambient conditions (bathymetry, currents, waves, wind, etc.) and the differences between the flow properties of the density current and receiving waters. As a broad classification, two modelling techniques are available for studying these flows numerically: integral models (e.g. (Parker et al., 1986) and Ungarish (2007a)) and those which solve the vertical structure of the flow such as 3-Dimensional hydrodynamic models (Bombardelli and García (2002) and Firoozabadi et al. (2009)). Since the integral models do not take into

account the real ambient conditions (i.e. bathymetry and meteo-ocean conditions), the calibrated modelling with 3-Dimensional hydrodynamic models such as Delft3D-Flow (Roelvink and Van Banning (1994) and Hydraulics (2005)), SELFE (Zhang and Baptista (2008)) and TELEMAC-3D (Hervouet (2007) and LNHE and Laboratory (2007)) can provide more realistic predictions. Recently, Mahgoub et al. (2015) validated a TELEMAC-3D model application through the spreading measurements of a set of experimental density currents. In addition the work presented in Chapter 3 (Pérez-Díaz et al. (2017a)) have recently showed a full calibration&validation in terms of velocity and dilution of TELEMAC-3D model through a wide range of laboratory-generated non-confined density currents. On this basis, an optimum modelling set-up to predict the behavior of these kind of flows with 3D hydrodynamic models was presented. Simulations with CFDs models have been also scope of certain density current studies (Patterson et al. (2006) and Cantero et al. (2007)), but as well as in the previous NF region, these simulations are still very time-consuming to be applied at real scales.

In the scientific literature there are several research works regarding the coupling procedures of NF and FF models, mainly focused on waste water and thermal single port discharges (i.e. positively buoyant effluents). Roughly speaking, there are two main coupling strategies, the "passive" and "active" coupling. The most current and realistic version of "passive" coupling consist of introducing the values of diluted concentration and/or flow rates determined by the NF model at specific locations of the FF model as source terms (Zhang and Adams (1999)). Choi and Lee (2007) refers to this procedure as "Diluted Source at Trapped Level" (DSTL) and was applied in the algorithm developed by Bleninger (2006) to couple the NF model CORMIX and the FF model Delft3D (Hydraulics Delft (2001)). It is noteworthy that "passive" couplings are suitable for relatively small discharges, whose NF characteristics do not change the flow characteristics of the FF (Stamou and Nikiforakis (2013)). For thermal discharges, whose large flow rates may affect significantly the flow field in FF and vice versa, Choi and Lee (2007) and Stamou and Nikiforakis (2013) developed similar "active" couplings that are capable to introduce the NF action on the ambient flow by a collection of sink/sources along the jet trajectory and a diluted source at the terminal level. Although Nikiforakis and Stamou (2015) adapted the coupling procedure developed by Stamou and Nikiforakis (2013) for brine discharges, this procedure has not been validated with real field measurements of this kind of effluents. Recently, NF and FF modelling using coupling procedures has been validated for brine discharges by Wood

et al. (2014). The authors considered brine generated from salt cavern leaching operations, which result in high salinity, or "hypersaline" brines. They found that "passive" coupling with TELEMAC-3D produced good comparisons with field measurements of salinity in the FF region.

The scope of this contribution is to carry out more detailed field validation, using measurements of reject brine concentrations near a desalination plant, whose salinities are lower than those from solution mining activities. The TELEMAC-3D and BrIHne models were selected for the present research, based on their previous successful validation. The present work seeks to couple the two models, and eventually lead to a full dynamic coupling capability. In addition, all the coupling modelling methodology steps, from the initial analysis of environmental databases to the visualization of the results, are clearly explained with detail through the validation case

The manuscript is organized as follows: the main characteristics of the NF model, the FF model and the coupling methodology are explained in Section 4.2. Then, in Section 4.3, the proposed methodology is validated against data of Maspalomas desalination plant and field measurements of Portillo et al. (2014). Finally, conclusions are presented in section 4.4.

4.2. Coupled modelling methodology

The proposed coupled modelling methodology to assess the potential impact of brine discharges to the environment is reflected in the diagram of 4.1. The orange dashed square highlights the four main steps of the proposed methodology, which are explained below and detailed through and example in section 4.3. It is worth mentioning that, since the most convenient and increasingly used discharge configuration are those through submerged jets, the present methodology focus on this kind of discharges. However, it can be adapted and extrapolated to other discharge configurations.

The external databases needed for the coupled modelling methodology can be classified in two set of data: (1) the desalination plant data as the discharge location (i.e. the geographic reference), the fluid-flow characteristics (i.e. the flow rate, the saline concentration and the density of the effluent) and the discharge device characteristics (i.e. the port diameter, the discharge angle, the port height, the initial

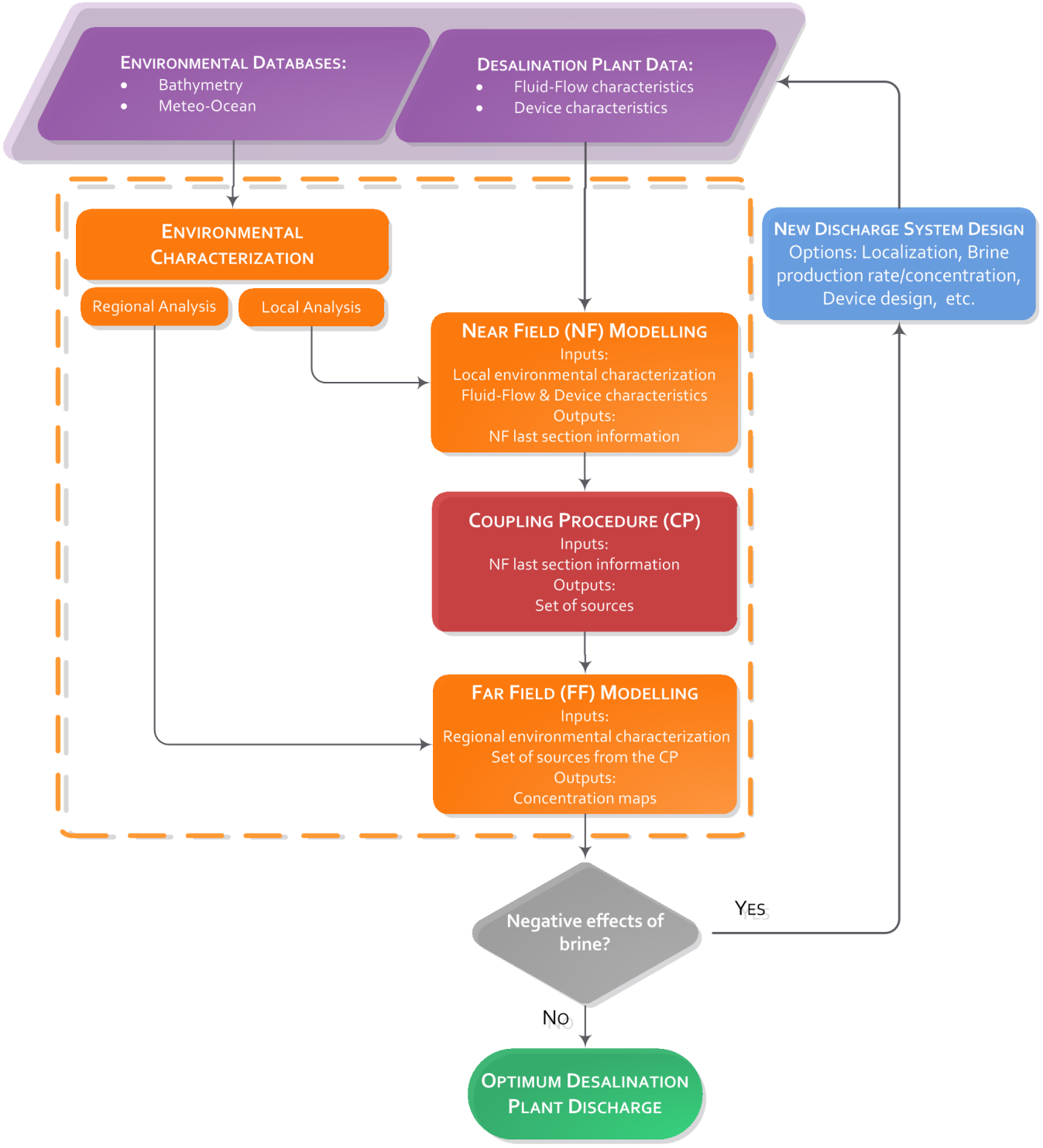

Figure 4.1: Diagram of the general methodology to assess the global impact of a brine discharge.The orange dashed square include the coupled modelling methodology

discharge velocity, etc.); and (2) the environmental data, i.e. the bathymetry and the meteo-ocean information in the desalination plant area. The first ones are inputs to the NF modelling step, while the second ones are inputs to a previous step, the environmental characterization step, which transforms them into inputs to the NF and FF modelling steps.

Therefore, this environmental characterization step feeds the methodology at two spatial levels: at a local level, where is located the discharge device (i.e. NF region); and at regional level, where is expected to impact the density current (i.e. FF region). The local characterization consist of analyzing the average depth, the ambient velocity, the temperature and the salinity of the receiving water at the discharge location. On the other hand, the regional characterization consist of analyzing the hydrodynamics of the study area (i.e. currents, sea level, temperature and salinity) as well as the meteorology (i.e. wind and sea level pressure) to generate the Initial Conditions (IC), Boundary Conditions (BC) and atmospheric forcing to the FF model. According to the available meteo-ocean databases for the study region, their nature (i.e. numerical or instrumental databases), their quality, and their spatial-temporal resolution, different techniques can be used to develop this environmental characterization step. For example, these techniques can range from a statistical analysis of numerical reanalysis databases to generate synthetic scenarios, to the implementation of a dynamic downscalling methodology. It is noteworthy that obtaining good results from the FF modelling step is highly dependent on the environmental characterization of the study area, thus, a big effort has to be made in this first step to obtain environmental reliable results.

The following methodology steps, the NF modelling, the coupling procedure and the FF modelling, are interrelated steps, in such a way that the outputs of the predecessor step feeds the following step. The NF and FF models used in this methodology are BrIHne tools and TELEMAC-3D, respectively. In the following sections, a brief description of both models, their strengths and limitations, and a detailed explanation of the coupling procedure designed for these kind of effluents are explained.

4.2.1. Models description

4.2.1.1. NF model: BrIHne tools

As mentioned in section 4.1, for the NF modelling there are several commercial software based on dimensional analysis and integration of differential equations such as VISJET, CORMIX and VISUAL-PLUMES. However, significant uncertainties and lack of validation and recommendations have been detected in the use of these tools when applied to brine effluents (Palomar et al. (2012b) and Palomar et al. (2012a)). To overcome the detected shortcoming, the Environmental Hydraulics Institute of The University of Cantabria (IH Cantabria) developed a set of numerical models to specifically simulate the behavior of brine discharges. These tools are based on dimensional analysis and integration of differential equations with mathematical approaches scientifically supported. They have an instantaneous online execution (from the user-friendly web-interface www.BrIHne.ihcantabria.com), and provide the flow main variables evolution to characterize the behavior at the NF region. An important advantage of BrIHne NF tools in comparison to previous cited commercial models is that they are validated with experimental data obtained by the use of non-intrusive optical laser techniques PIV (Particle Image Velocimetry) and PLIF (Planar Laser Induced Fluorescence) (Palomar et al. (2013) and Palomar (2014)). Therefore, BrIHne tools have been selected because they represent the only validated and open-source alternative for this kind of dense effluents.

Within the set of BrIHne tools, the NF models to simulate brine discharges through submerged jets are the BrIHne-jet, the BrIHne-MJets and the BrIHne-Jet-Spreading. These models differ in the mathematical approach applied to solve the flow equations and in the modelling scope. BrIHne-Jet and BrIHne-MJets are based on the integration of differential equations along the jet centelines, assuming an unlimited environmental and self-similarity between cross-sections (numerical approach and equations proposed by Jirka (2004)). The first one can be applied for single-port jet submerged brine discharges, while the second one is adequate for multi-port jet submerged brine discharges. In case of merging between jets, the BrIHne-MJets applies the hypothesis of an equivalent slot diffuser, maintaining the fluxes, and transforming three dimensional jets into a bi-dimensional plume (Jirka (2006)). The modelling scope of both tools described is from the jet nozzle to the point where the jet impact the bottom. Finally, the BrIHne-Jet-Spreading

can be also applied for single-port jet submerged brine discharges but it is based on calibrated dimensional analysis formulas (Palomar (2014)), which consider the variables with greater influence on the processes such as the port diameter (d_o), the densimetric Froude number (F_{rd}) and the initial discharge angle (θ) (see Fischer (1979) and Roberts et al. (1997)). The modelling scope of this tool is from the jet mouth to the end of the near field region, including the jet path and the spreading layer. Hence, the latter model presents an improvement over the BrIHne-Jet model because it does not neglect the important dilution that can occur in the spreading layer (Palomar (2014)). It has to be take into account that this model assumes stagnant receiving water, which is an acceptable assumption in the majority of the cases for brine discharges, since the ambient velocities near the seabed are usually negligible in comparison with the discharge velocity.

Figure 4.2 shows the decision diagram to select the suitable BrIHne tool. In this diagram, the first decision parameters are the number of ports (Np), and in cases of more than 1 port, the separation between them (Sp) and their critical separation ($S_{p_{cr}}$). The latter parameter depends on the individual study case, and it has to be obtained from the width result at the impact point of a previous auxiliary simulation with the BrIHne-Jet by assuming a single port (with the corresponding flow fluxes). The other decision parameters are the expression $U_r F_{rd}$ and directly de Froude densimetric number (F_{rd}), where U_r refers to the ambient velocity (U_a) relative to the jet discharge velocity (U_o), $U_r = U_a/U_o$, and the Froude densimetric number refers to $F_{rd} = U_o/(g'_0 d_o/2)^{1/2}$, being $g'_o = g(\rho_o - \rho_a)/\rho_a$. The threshold value of $U_r F_{rd}$ is established using the observations revealed in Gungor and Roberts (2009); Roberts and Toms (1987) and Palomar (2014), which study different jet discharges varying the port angle and the ambient current, among others. The last decision parameter, F_{rd}, was established by Palomar (2014), since the dimensional analysis formulas in which are based on, were validated for studies with greater F_{rd} values than 10. In function of the model selected for the study case, the input data required, as well as their output data, are different. Table 4.1 gathers the kind of input and output data must be expected in each case.

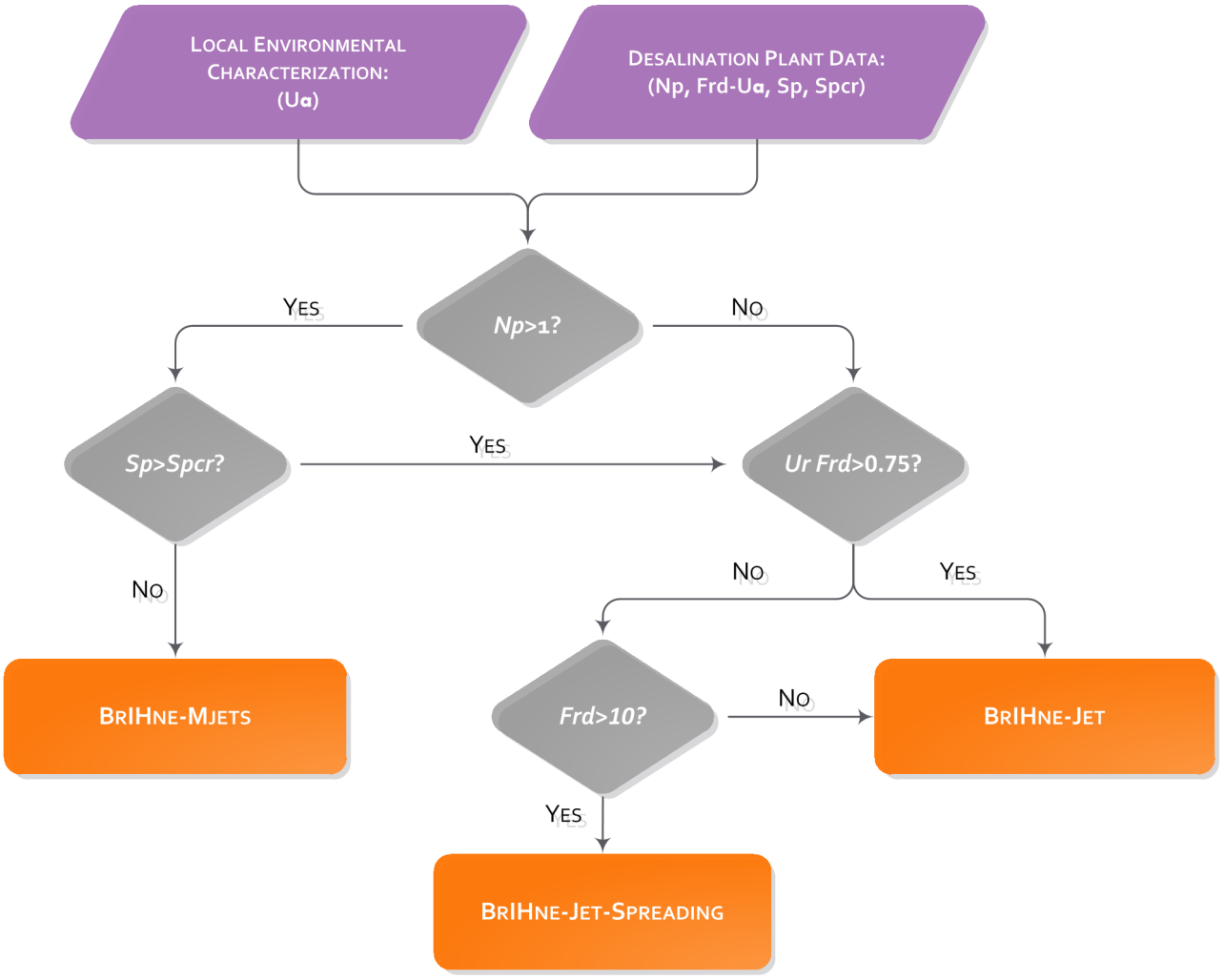

Figure 4.2: Decision diagram to select the suitable BrIHne model

4.2.1.2. FF model: TELEMAC-3D

TELEMAC-3D model has been chosen in this work due to some of its special features such as the large number of subroutines based on scientific literature to reproduce processes of different scale; its sigma-layer coordinate (i.e. terrain-following) in the vertical domain discretization; and its unstructured horizontal domain discretization, that allows to work with variable spacing meshes, hence, to obtain computationally-efficient high resolution results in specific areas (e.g. areas of sources and sinks of water). It solves the 3-Dimensional free surface flow equations and the transport equations of intrinsic quantities such as salinity and temperature. For each point in the grid, TELEMAC-3D main results are the water depth, the velocity vector and the concentrations of transported quantities (LNHE and Laboratory (2007) and (Hervouet (2007)).

Furthermore, TELEMAC-3D was the model used in Chapter 3, which establishes a calibrated and validated modelling set-up to predict the behavior of saline density currents under laboratory conditions. The saline density currents generated in that study were designed (i.e. their discharge characteristics such as the geometry, the flow rate and fluid characteristics, as well as the bottom slope) to reproduce wide range of saline plumes characteristic of the FF of brine discharges from common SWRO desalination plants. This proposed modelling set-up is considered in the present study to obtain accurate results in the FF modelling with TELEMAC-3D. The main numerical recommendations are outlined below:

- Variable spacing horizontal discretization (e.g. unstructured mesh-grids) is recommended in order to obtain a high resolution near the source. Assuming a slot-shaped source ($b_{0FF} \times h_{0FF}$), which is a common approximation at the beginning of the far field region of the brine discharges, a minimal spacing at least of equal to the width of the slot (b_{0FF}) is needed.

- In the vertical direction, a high resolution is mandatory to prevent the vertical numerical diffusion. Considering the slot-shaped source, the vertical spacing has to be at least $h_{0FF}/16$ within the density current. A sigma-layer coordinate (i.e. terrain-following) in the vertical domain discretization is mandatory, in order to keep the finest layers at the bottom and to establish a gradual spacing.

- Full momentum-source specification is advisable, i.e. both the flow rate and the velocity information ($Q\&V$) should be detailed.

- The Constant model is recommended as a horizontal horizontal turbulence closure model $TCMh$)

- Several vertical turbulence closure models ($TCMv$) can be successfully applied, such as Constant, Mixing-Length or κ-ε models. However, given the demonstrated influential role the $TCMv$ has in the numerical simulation of these flows, a calibration effort for each case study is recommended to be performed. It has to be taken into account that the use of the κ-ε turbulence model, which solves two more equations, is highly demanding in terms of computational time. Both the Mixing Length model and the Constant model can give good approximate results in a more reasonable timeframe for field applications.

Therefore, the FF application (i.e. TELEMAC-3D application) for the study case should be configured based on the previous recommendations, the coupling procedure outputs, and the CI and BC generated in the environmental characterization step.

4.2.2. Coupling procedure

In this section, the coupling procedure step, which is the one in charge to ensure the continuity and dynamism between both modelling regions (NF and FF), is detailed through their three main aspects: the dynamic, temporal and spatial aspects. While the dynamic aspect focus on the main magnitudes transformation from the NF to the FF region (i.e. flow rate and salinity concentration), the temporal and spatial aspects specify how is the temporal and spatial distribution of these magnitudes.

4.2.2.1. Dynamic aspects

According to the scientific literature revealed presented in the Introduction section, a kind of DSTL coupling procedure, the most realistic version of those gathered by Zhang and Adams (1999), is applied in this methodology. This coupling consists on specifying an increased flow and diluted source concentration at the computational nodes of the FF mesh-grid at the terminal level indicated by the NF modelling (i.e. at the end of the NF region modelled). If the initial discharge is a flow rate of Q_o with a concentration of C_o, the ambient concentration is C_a, and the concentration and the dilution factor predicted at the end of the NF are C and $S = (C_o - C_a)/(C - C_a)$, respectively, then the source is introduced to the FF model at a concentration of $C_{oFF} = C = (C_o - C_a)/S + C_a$ and at a flow rate of $Q_{oFF} = S \cdot Q_o$. Taking into account a slot shape-approximation (Bleninger (2006)) for the terminal level predicted by the NF model, this global source from NF to FF model is transformed in a set of sources according to the FF mesh-grid resolution and the width and thickness of the terminal level (see Figure 4.3).

Some differences among the inputs to the FF model depending on the NF BrIHne model used are appreciated. In those cases where the BrIHne-Jet and BrIHne-MJets models are used, the width (b_{oFF}) and thickness (h_{oFF}) of the discharge to the FF are directly defined by output variables at the jet impact point: the

jet/s radius (R) and the maximum height (Z), respectively. However, in those ideal cases where the BrIHne-Jet-Spreading model (since it takes into account the dilution in the spreading layer) is applied, while the thickness (h_{oFF}) is also directly defined by the corresponding NF output variable (h), the width (b_{oFF}) has to be defined by applying the buoyancy flux conservation ($B_f = B_{fo} = g'_o \cdot Q_o$). By considering the slot shape-approximation at the NF terminal level, the buoyancy flux can be expressed by:

$$B_f = g' \cdot Q = g' \cdot b_{oFF} \cdot h_{oFF} \cdot U \tag{4.1}$$

where $g' = g(\rho - \rho_a)/\rho_a$, being ρ and ρ_a the plume density and the ambient density, respectively. Since the velocity (U) at the end of the spreading layer is also an NF output variable of the BrIHne-Jet-Spreading model, the only unknown of this equation is the width (b_{oFF}). Table 4.1 shows the main NF outputs needed for the coupling procedure depending on the NF model used, and their transformation to be included in the FF model. Regarding the X, Y coordinates, it is important to mention that they are referred to an origin localized at the discharge point.

TABLE 4.1: BrIHne inputs, BrIHne outputs and their transformation to be included in the FF model using the Coupling Procedure (CP)

NF Model	NFinputs[a]	NFoutputs[b]/CPinputs	CPoutputs/FFinputs$^{c}_{NF}$
BrIHne-Jet (BrIHne-MJets)	Environment: H_a, C_a, ρ_a, U_a. Discharge: d_o, θ, h_o, σ, C_o, ρ_o, U_o, (N_p, S_p).	S: dilution Z: maximum height R: jet/s radius X,Y: coordinates	$Q_{oFF} = S \cdot Q_o$ $C_{oFF} = (C_o - C_a)/S + C_a$ $h_{oFF} = Z$ $b_{oFF} = 2 \cdot R$
BrIHne-Jet-Spreading	Environment: H_a, C_a, ρ_a. Discharge: d_o, θ, h_o, σ, C_o, ρ_o, U_o.	S: dilution U: velocity h: thickness X,Y: coordinates	$Q_{oFF} = S \cdot Q_o$ $C_{oFF} = (C_o - C_a)/S + C_a$ $h_{oFF} = h$ $b_{oFF} = B_{fo}/(h \cdot U \cdot g')$

[a] Meaning of symbols:
H_a: average depth at the discharge point; C_a: ambient salinity; ρ_a: ambient density; U_a, ambient velocity; d_o: port diameter; θ: initial discharge angle; h_o: port height; σ: horizontal angle between the jet and the environment crossflow; C_o: effluent salinity; ρ_o: effluent density; Q_o: initial flow rate; U_o: initial discharge velocity; N_p: number of ports; S_p: separation between ports.

[b] They are outputs at the end of the NF, i.e. at the impact point for BrIHne-Jet and BrIHne-MJets, and at the end of the spreading layer for BrIHne-Jet-Spreading.

[c] These FF Inputs$_{NF}$ defined are those from the CP step. Inputs from the regional environmental characterization step are not included (i.e. IC, BC and atmospheric forcing)

4.2.2.2. Temporal aspects

Since BrIHne models are capable of including time varying inputs, that is, temporal series of all the variables required, the coupling time-step (Δt_{CP}) is function of both the calculation time-step of the NF model (Δt_{NF}) and the FF model (Δt_{FF}), following the expression: $\Delta t_{CP} = max(\Delta t_{NF}, \Delta t_{FF})$. The time-step of the NF model (Δt_{NF}) is only dependent on the temporal resolution of the inputs from the desalination plant and, in case of using BrIHne tools that consider not stagnant receiving water, of the ambient velocity. Δt_{FF} is dependent on a more complex concept related to the convergence criterion of the FF model, such us the Courant condition. Due to the usual lack of temporal information of the desalination plant data (it is common to work with nominal values of certain potential scenarios), and the tiny values of the Δt_{FF} (order of seconds or minutes), the Δt_{CP} for common situations where the receiving water is considered to be in calm, is equal to the value of Δt_{NF}. For those study cases of nominal scenarios, this results in constant-flux discharges both in NF and FF region during the study period.

4.2.2.3. Spatial aspects

As it has been explained in the previous section 4.2.2.1, the flow and concentration values at the terminal level predicted by the NF model, have to be transform in a set of sources to be included in the FF model. The location and number of the set of sources (N_s) are dependent on width (b_{oFF}) and thickness (h_{oFF}) of the terminal level and the mesh-grid definition in the coupling area, which has to be designed following the recommendations summarised in section 4.2.1.2. Apart from this, the magnitude (flow and concentration) and the location values of this set of sources are also dependent on the NF model used and the coupling time step (Δt_{CP}).

In those cases where the NF model is the BrIHne-Jet or BrIHne-Mjets, hence, the magnitude values are only dependent on the average dilution factor, the flow rate (Q_i) for each source are equally distributed among the number of sources: $Q_i = Q_{oFF}/N_s$ with the same concentration $C_i = C_{oFF}$. In those ideal cases where the NF model applied is the BrIHne-Jet-Spreading model the previous flow magnitude values per source can be more realistically distributed in the vertical direction by applying the vertical shape profile functions obtained by Palomar

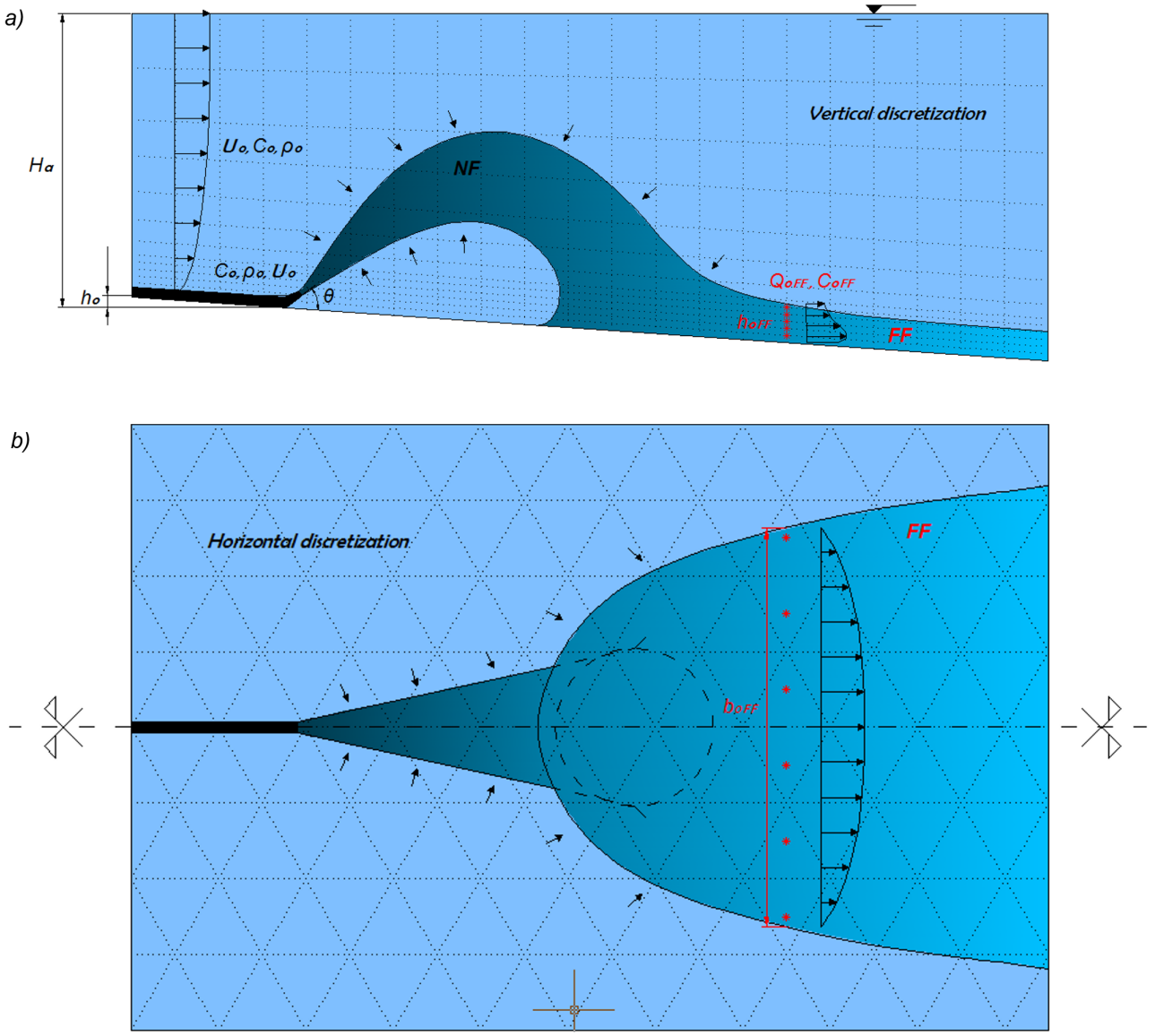

Figure 4.3: Coupling procedure scheme: a) profile view and b) plan view

(2014) from a great number of spreading layer experiments. As far as the authors of this work are aware, there are not published works with detailed information about the horizontal distribution at the end of the spreading layer. Although it is supposed to have a kind of Gaussian shape because of the inertia from their previous region and the bottom slope, due to the lack of data, in this study it is considered equally distributed along the width.

In addition, from one coupling time-step (Δt_{CP}) to the following, the location and magnitude values of the sources can changed. Thus, the high resolution region near the potential coupling area has to be large enough to take into account

possible changes in the sources location. Figure 4.3 shows a plan and profile view of the coupling procedure between BrIHne-Jet-Spreading and TELEMAC-3D for a certain coupling time-step.

4.3. Validation case: Maspalomas desalination plant

The present section reveals the application of the coupling methodology proposed in section 4.2 for the study of the brine discharge of the Maspalomas II SWRO desalination plant. Finally, the methodology results are compare with concentration measurements of the brine density current generated under different environmental conditions.

The Maspalomas II SWRO desalination plant is in the south of the island of Gran Canaria (Canary Islands, Spain), around 500 m from the sea between the beaches Playa de Las Burras and Playa de Cochino (see Figure4.4). Nowadays, the plant has an average production of potable water around 944 m^3/h with a final conversion factor of 50 %. This results in a brine production of 944 m^3/h with and average salinity of 73.6 *psu*. Due to water spills out of the storage tank of the plant into the brine drain, the brine product is diluted before its discharge to the marine environment. The final mixture discharge flow is around 1.062 m^3/h with a average salinity of 69.5 *psu*. The discharge is channeled through an underground PVC pipeline with a length of 500 m which joins onto a 300 m underwater outfall made of cast iron, both with diameter of 0.6 m. The discharge device is a simple outlet elbow with the same diameter as the outfall, at a vertical angle of 42.5° to the sea bottom. The discharge point is at a depth of 4 m at mean low water spring tide and the brine effluent is discharged over a wide sandy bottom with a mild slope of 1.6 %.

The sandy bottom where the study brine density current flows is home to the island's largest and most ecologically important seagrass meadow of *Cymodocea nodosa* which was declared both a Site of Comunity Interest under the name of *Sebadales de Playa del Inglés-ES7010056* (OJEC (2002)) and a Special Area of Conservation (BOE (2009)). Under the framework of the Spanish National project $Venturi - Project$ (*www.proyectoventuri.com*), in order to assess the spatial extent of the brine density current, several sampling campaigns were conducted

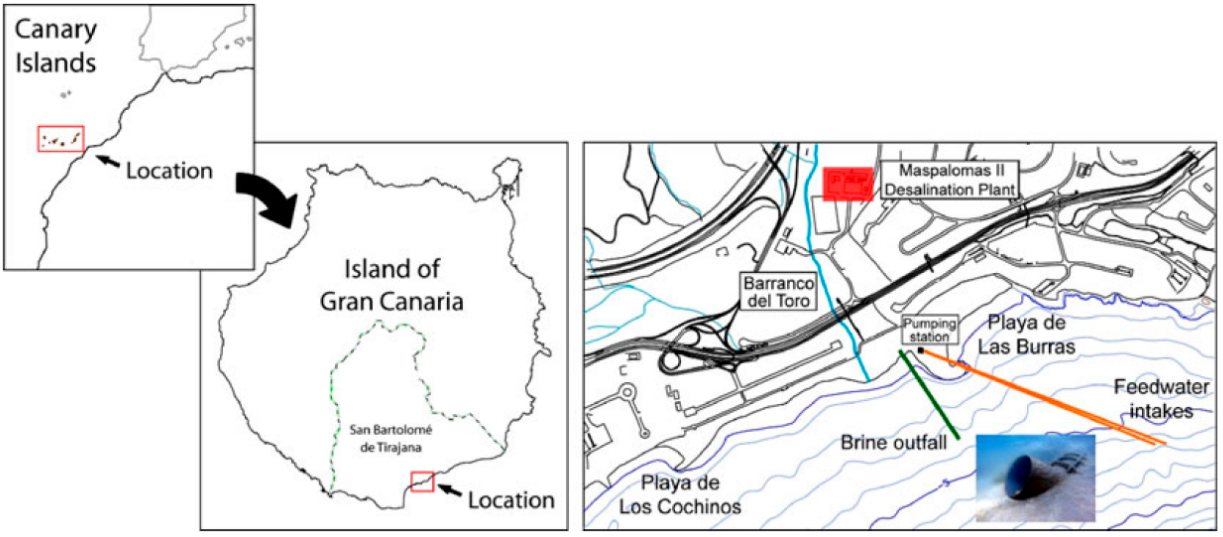

Figure 4.4: Location of Maspalomas II desalination plant and its facilities. Source: Portillo et al. (2014)

measuring the salinity field in the influence zone when the desalination plant was operating under normal conditions. Sampling periods were chosen looking for mean meteorological and oceanographic conditions of the area, but with some differentiations so as to have a certain amount of variability in the hydrodynamic conditions between campaigns. The bottom salinity measurement technique consisted of a sonde with a conductivity sensor attached to a weight to keep it as close as possible to the bottom. The sampling grid was defined over the influence zone of the discharge with different grid spacing to capture from the closest to most remote region. More details regarding the sampling and data gathering as well as the instrumentation characteristics are explained in the published work Portillo et al. (2014).

Table 4.2 shows the main characteristics of the field campaigns such as the date, the discharge flow rate, and the temperature and salinity of both the brine and the receiving water close to the discharge port.

4.3.1. Methodology application

In this section the methodology explained in the previous section 4.2 and outlined briefly in the Figure 4.1 is applied for the 7 scenarios corresponding to the set of Maspalomas campaigns.

TABLE 4.2: Main characteristics of the field campaigns

	C1	C2	C3	C4	C5	C6	C7
Date $(yy/mm/dd)$	9/7/22	9/7/23	9/9/29	9/9/30	10/1/21	10/1/22	11/1/17
Start time $(hh:mm)$	∼7:00	7:15	∼8:00	7:48	10:37	11:38	9:05
End time $(hh:mm)$	∼11:00	11:15	∼11:45	11:30	13:22	14:07	13:35
Duration (h)	∼4.00	4.00	∼3.75	3.70	2.75	2.48	4.50
Flow rate, Q_o (m^3/s)	0.280	0.299	0.307	0.309	0.396	0.347	0.321
Brine salinity, C_o (psu)	73.20	73.20	68.4	73.00	53.24	60.89	67.00
Brine temperature, T_o $(°C)$	23.00	24.61	26.00	26.03	21.82	22.43	22.90
Sea salinity, C_a (psu)	36.80	36.80	36.80	36.80	36.80	36.80	36.80
Sea temperature, T_a $(°C)$	22.70	22.74	24.00	24.01	20.46	20.89	20.70

4.3.1.1. Databases

Desalination plant data

The localization and the general device characteristics of the Maspalomas desalination plant were explained in the previous section. However, to be more specific, the location of the discharge port is at the coordinates [445726, 3071119] m (referenced to the geographic coordinate system WGS84), the port diameter (d_o) is 0.6 m, the port angle (θ) is 42.5°, and the port height (h_o) is close to 0 m. The direction of the discharge pipeline and port, hence the initial jet direction, is perpendicular to isobath lines.

The basic fluid and flow characteristics of the brine effluent (i.e. flow rate Q_o, salinity C_o and temperature T_o) for each scenario are summarised in Table 4.2. Other derived fluid and flow characteristics required by the NF models (see section 4.2.1.1) are the density (ρ_o) and the velocity discharge (U_o). The latter variables are directly obtained by the temperature and salinity measurements (i.e. UNESCO equation of state) and through the knowledge of the flow rate and the port diameter (i.e. $U_o = Q_o/(\pi \cdot d_o^2/4)$, respectively.

Environmental databases

Around the same time as the first salinity field campaigns, a high resolution bathymetry data with well-defined isobaths each 1 m were provided for the whole continental shelf of Gran Canaria. Regarding the receiving water characteristics,

the temperature (T_a) and salinity (C_a) close to the discharge port are nearly invariants among campaigns. Their measured values are gathered in Table 4.2. Apart from this characteristics, an ADCP was located close to the discharge port during several days/hours around the campaign periods to capture the hydrodynamic characteristics of the area. In addition, the meteorological station located at the beach Playa de las Burras provided wind data for the period of the campaigns. Figure 4.5 shows the ambient current (speed and direction) measured for the longer ADCP record. It belongs to the $C7$ campaign. Simultaneously, Figure 4.6 shows the wind speed and direction for the same period.

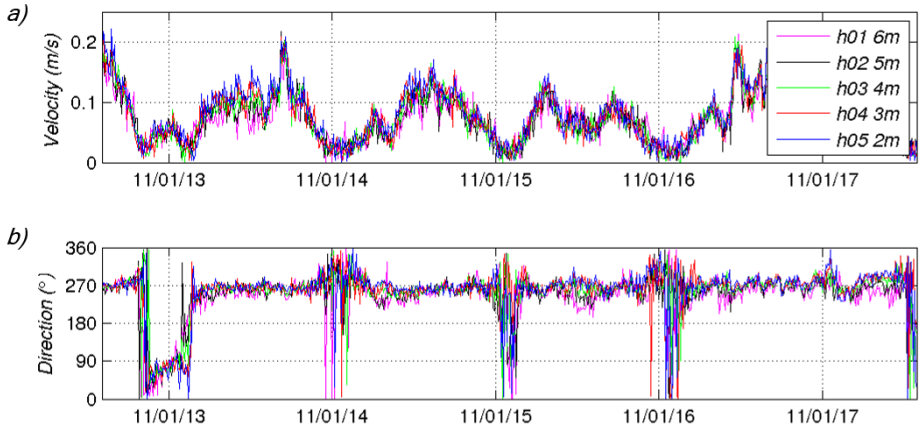

Figure 4.5: Currents measured by the ADCP near the discharge location: a) speed and b) direction. h01 corresponds to the measurements near the bottom and h06 to the measurements near the surface.

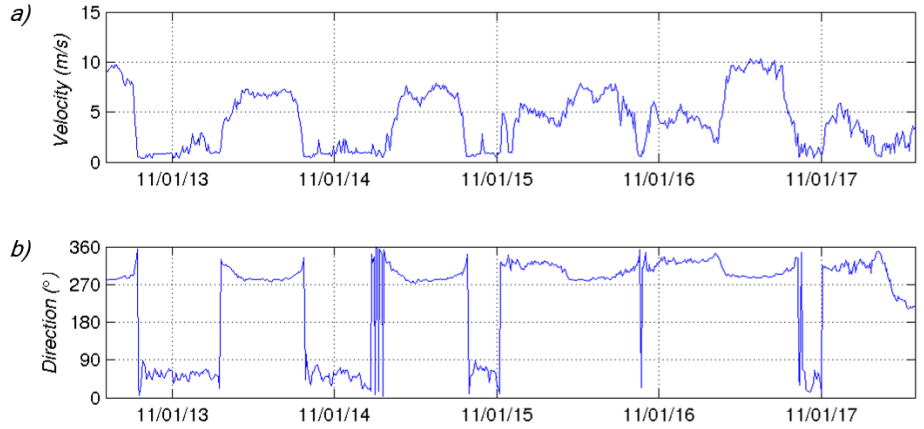

Figure 4.6: Wind measured by the Meteorological station at the beach Playa de las Burras

As can be observed, the vertical distribution of the ambient current is nearly uniform (almost the same values at the bottom and the surface), and the current direction exhibits a clear influence of wind magnitudes. That is, when the wind

speed is significant, the ambient current direction is totally oriented by the wind direction. This behavior, which is common in shallow water areas, is observed in all the field campaigns.

4.3.1.2. Environmental characterization

As described in the Modelling Methodology section, the environmental characterization has to be at local and regional scale to feed both NF model and FF model.

Specifically, the regional characterization is necessary to generate the Initial Conditions (IC) and Boundary Conditions (BC) to the domain of the FF application (i.e. to the mesh-grid of TELEMAC-3D application, see Figure 4.7). In this case, a dynamic downscalling methodology from the IBI-MyOcean reanalysis 2002-2012 (Sotillo et al. (2015)) to the FF TELEMAC-3D application through the Regional Ocean Modelling System (ROMS, Shchepetkin and McWilliams (2005)) is applied to obtain a good hydrodynamic characterization in the study area (for each campaign period). The bi-dimensional ROMS application consist of two nested mesh-grid with different resolution (see Figure 4.7) in order to have enough data in terms of spatial coverage at the boundaries of the FF model. Apart from being forced by hydrodynamic data from MyOcean (sea level height and barotropic currents), ROMS model is also forced by meteorological data from Seawind II reanalysis 1989-2013 (Menendez et al.) (sea level pressure and wind stresses). The high hydrodynamic resolution results of this downscalling procedure (i.e. the sea level height and the barotropic currents), are post-processed into IC and BC to feed the FF TELEMAC-3D application. Figure 4.7 shows the modelling domains of the described dynamic downscalling.

Two kind of TELEMAC-3D applications in terms of BC are considered in this study. The first one (ROMS-T3D) generates the BC by interpolating the results of the ROMS application (sea level height and barotropic velocity), while the second one (ROMS-T3D-Assimilation) takes also advantage of the instrumental measurements by integrating them as a prescribed rate at one of the boundaries (in this case, the east one). Figure 4.8 presents a comparison between the velocity results from both applications at the location of the discharge device for the $C7$ period. Moreover, the ADCP measurements for the corresponding period are also plotted.

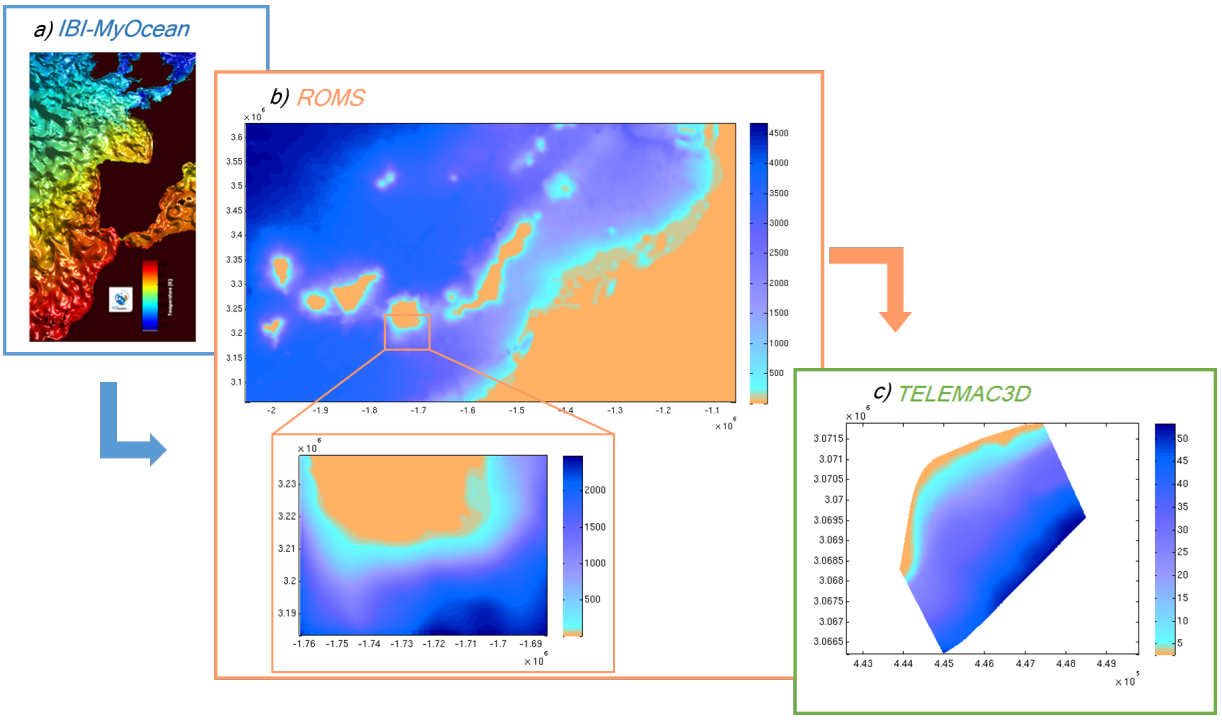

Figure 4.7: Modelling domains of the dynamic downscalling to regionally characterize the study area: a) IBI-Myocean domain (source: http://marine.copernicus.eu/), b) ROMS nested domains, and c) TELEMAC-3D domain

As one might expect, the application with instrumental data assimilation (ROMS-T3D-Assimilation) gives better results than the other case (ROMS-T3D). However, since it is unlikely to have instrumental data in common scenarios, it has to be highlighted that the results from the pure numerical methodology shown a pretty good agreement with the ADCP measurements (see Figure 4.8). Regarding the magnitude of velocities encountered, Table 4.3 gathers the main validation statistical parameters for each numerical simulation. As can be observed they are good results, especially considering the low values of the velocity magnitude (they are lower than 0.2 m/s for all the study scenarios).

TABLE 4.3: Validation statistical parameters of the velocity modelled through the two simulation techniques

Parameter	ROMS-T3D	ROMS-T3D-Assimilation
RMSE[a]	0.038	0.0271
R2[b]	0.707	0.869
Pearson[c]	0.572	0.911
RSI[e]	0.379	0.268

[a] Root Mean Square Error; [b] Correlation Index; [c] Pearson Index; [d] Residual Scatter Index

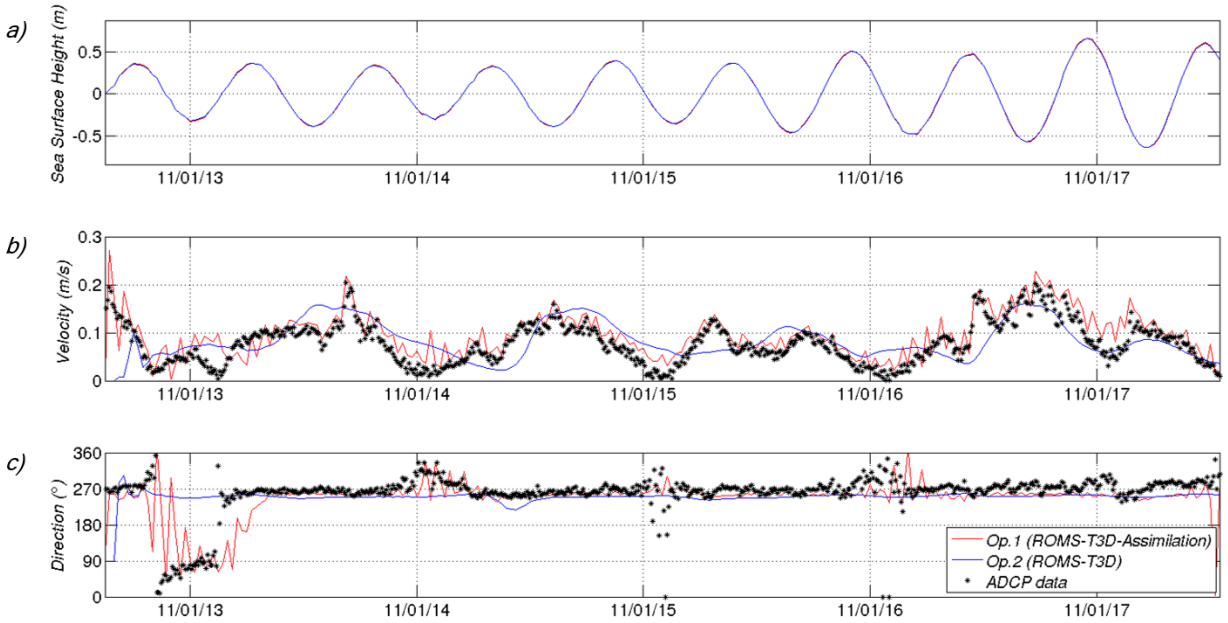

Figure 4.8: Comparison between numeric results and ADCP measurements where the discharge device is located: a) Sea surface height, b) velocity, c) velocity direction

4.3.1.3. Near Field modelling

Following the decision diagram of Figure 4.2 and taking into account the information provided in previous methodology steps, the suitable NF BrIHne model to each study scenario is chosen. Due to the common single port device for all the scenarios the option of using BrIHne-MJets model is rejected. Then, considering the low ambient velocities ($U_a < 0.2\ m/s$) and the low Froude densimetric values ($F_{rd} \simeq 3$) for all the cases, the parameter $U_r F_{rd}$ is always lower than its threshold value. Therefore, the BrIHne-Jet model is the suitable model for the studied scenarios.

The inputs required by BrIHne-Jet model for each scenario are gathered at Table 4.2 and section 4.3.1.1. Figure 4.9 shows some graphs about the jet trajectory from the BrIHne results report. The main results at the end of the NF region for the same example scenario ($C7$) are gathered in Table 4.4.

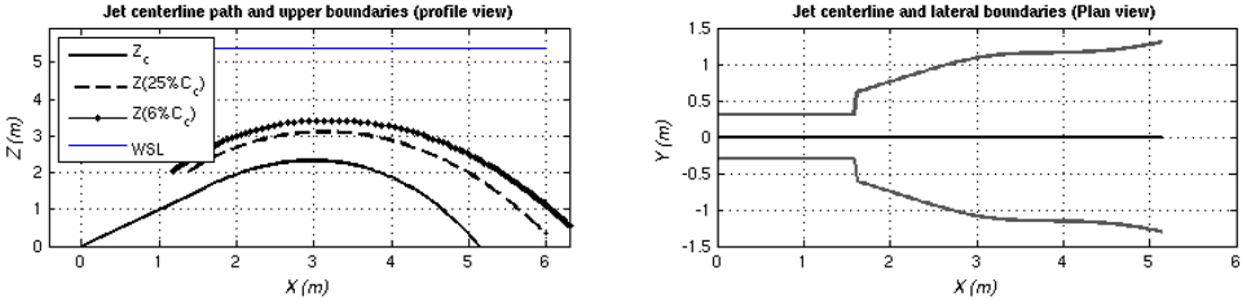

Figure 4.9: Example of graphs from the BrIHne result report of scenario $C7$

4.3.1.4. Coupling procedure

Table 4.4 shows the main BrIHne outputs for the coupling procedure and their transformation to be included in the FF model.

TABLE 4.4: Example of BrIHne outputs and their transformation to be included in the FF model for the scenario $C7$

NF Outputs/CP Inputs	CP Outputs / FF Inputs$_{NF}$
$S = 2.5$	$C_{oFF} = 0.8\ m^3/s$
$Z = 1.07\ m$	$C_{oFF} = 48.9\ psu$
$R = 1.31$	$h_{oFF} = 1.07\ m$
X,Y: $[6, 0]$	$b_{oFF} = 2.62\ m$

Regarding the temporal aspects, since the studied scenarios present an invariant flow rate (see Table 4.2) and the parameter $U_r F_{rd}$ has such a low value that the receiving water can be considered to be in calm, a constant-flux discharge can be assumed during the study periods. In terms of the spatial distribution of the discharge in the FF region, the total discharge rate (Q_{oFF}) for each scenario was equally distributed among the Np sources. Following the recommendations described in section 4.2.1.2, the Np resulted in 16 sources (one per layer within the density current), which locations are dependent on the corresponding XY coordinates, h_{oFF} and b_{oFF}. To properly define these locations, the TELEMAC-3D mesh-grid used at the environmental characterization, has to be adapted according to the same recommendations.

4.3.1.5. Far Field modelling

Following the recommendations described in section 4.2.1.2, and the number of sources defined at the coupling procedure, a mesh-grid of 676251 elements is used

for the scenario $C7$ (for the rest of the scenarios the number of elements is around this value, too). This grid has higher horizontal resolution (horizontal discretization, Δx) in the plume area (from Δx equal to b_{oFF} near the discharge, to Δx equal to $6 \times b_{oFF}$) and lower horizontal resolution in the boundary regions. Regarding the vertical layers, the application is defined with 16 fixed layers within the density current thickness (this layers are always at the same distant to the bottom) and 14 layers gradually spaced to the surface. Taking into account the turbulence modelling, the Constant model was used at the horizontal dimension and the calibrated κ-ε model, the Mixing-Length model and also the Constant model has been considered at vertical dimension. The latter casuistry was tested to study de influence of the turbulence model on the dispersion results as well as on the computational time.

Figure 4.10 shows the maps of modelled salinity concentration at the bed layer for two instants with ambient velocity in opposite directions for scenario $C7$. As can be observed, even considering this kind of heavy density currents (due to the low mixing capacity of the discharge device installed in this case), and a low ambient velocity magnitude, the behavior of the density current along the FF is mainly driven by the bottom slope (i.e. the density current follows the line of maximum depth gradient) but also by the environment flow conditions (that is, the density current turns slightly to the right in the first case, and to the left in the second).

In this case the turbulence closure model used is the calibrated κ-ε model. However, in a preliminary comparison among modelling results, κ-ε turbulence appears to enhance the dilution compared with the Mixing-Length and the Constant models (in case of Constant model after calibrating the eddy viscosity and diffusivity parameters). In addition, it is noteworthy that the computational time demand is reduced by a 25% and by a 50%, respectively, when the Mixing-Length and the Constant models are applied, instead of κ-ε.

4.3.2. Validation

Due to the fact that the only temporal reference of the salinity data sampling is the campaign period, i.e. there are not information about the temporal instant at which each sample of each campaign was gathered, the validation is performed considering the maximum salinity values reached by the modelled density current in the corresponding period. As expected, within the water column, the maximum

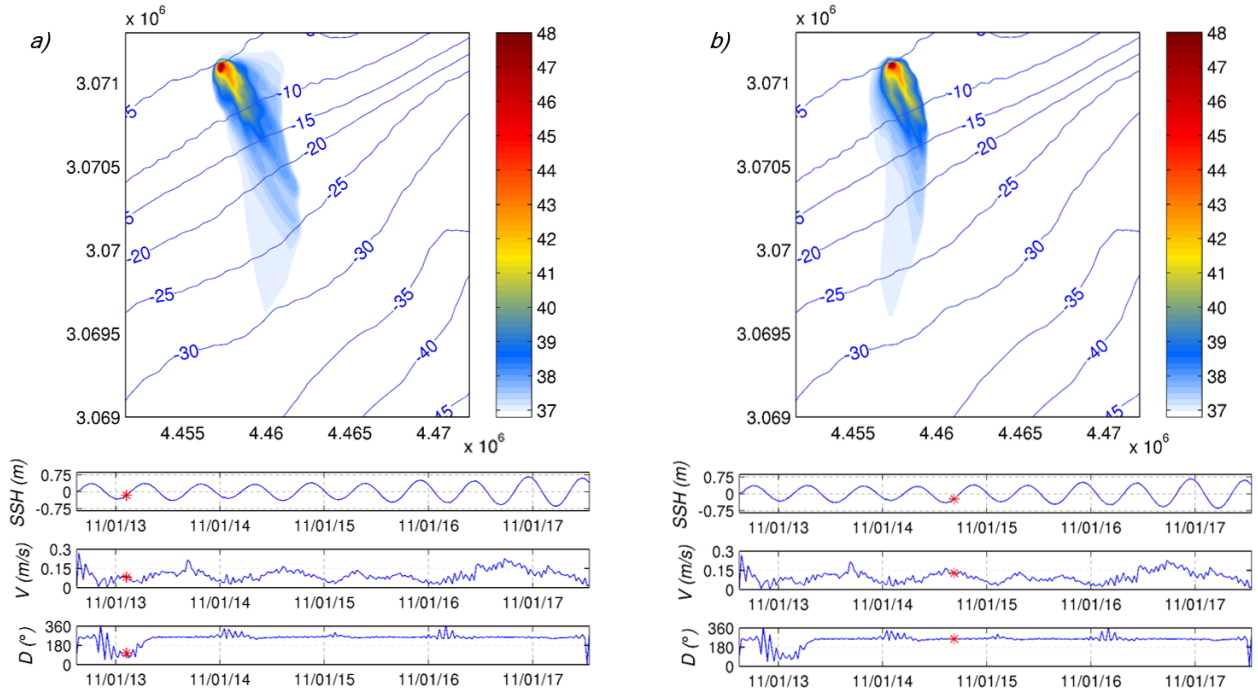

Figure 4.10: Modelled salinity concentration at the bottom layer for two instants with ambient velocity in opposite directions for scenario $C7$

values are always found in the bottom layer. This way, a good validation would be that the salinity values measured within the density current are equal or lower than the maximum calculated values from the modelled results (since it gathers the maximum values obtained during the study period). Otherwise, the modelled results would be underestimating the spatial extent of the density current, i.e. the potential negative impact over the environment.

Figures 4.11 and 4.12 show the validation salinity maps for the campaigns $C7$ and $C6$, two of the most dissimilar from each other (in terms of discharge conditions and density current extent). These figures reveal the maximum bottom salinity as well as the salinity measurements in a full view of the FF region and in a zoom of the closer region to the discharge. As can be observed, all the measured values are within the maximum bottom salinity footprint, moreover, the majority of the values are within their corresponding contour line. In addition, Figure 4.13 shows the validation salinity maps (the full view of the FF region) for the rest of the campaigns. It is noteworthy that for all the scenarios studied several tests were carried out varying the turbulence closure model together with the domain discretization. Finally, by considering the computational time demand as well as the agreement with the field measurements, best results (Figures 4.11, 4.12 and

4.13) were achieved for those tests that use the discretization specified in section 4.3.1.5 (following the recommendations presented in 3) and apply the Mixing-Length turbulence model.

Since common statistical parameters such as Root Mean Square Error (RMSE) and Pearson correlation coefficient need temporal correspondence to provide meaningful values, the percentage of the measured values that are inside the corresponding contour line from modelling results (considering the contour lines from 37 to 42 *psu* each *psu* variation) are revealed in Table 4.5. This parameter provide a general idea of the quality of the modelled results.

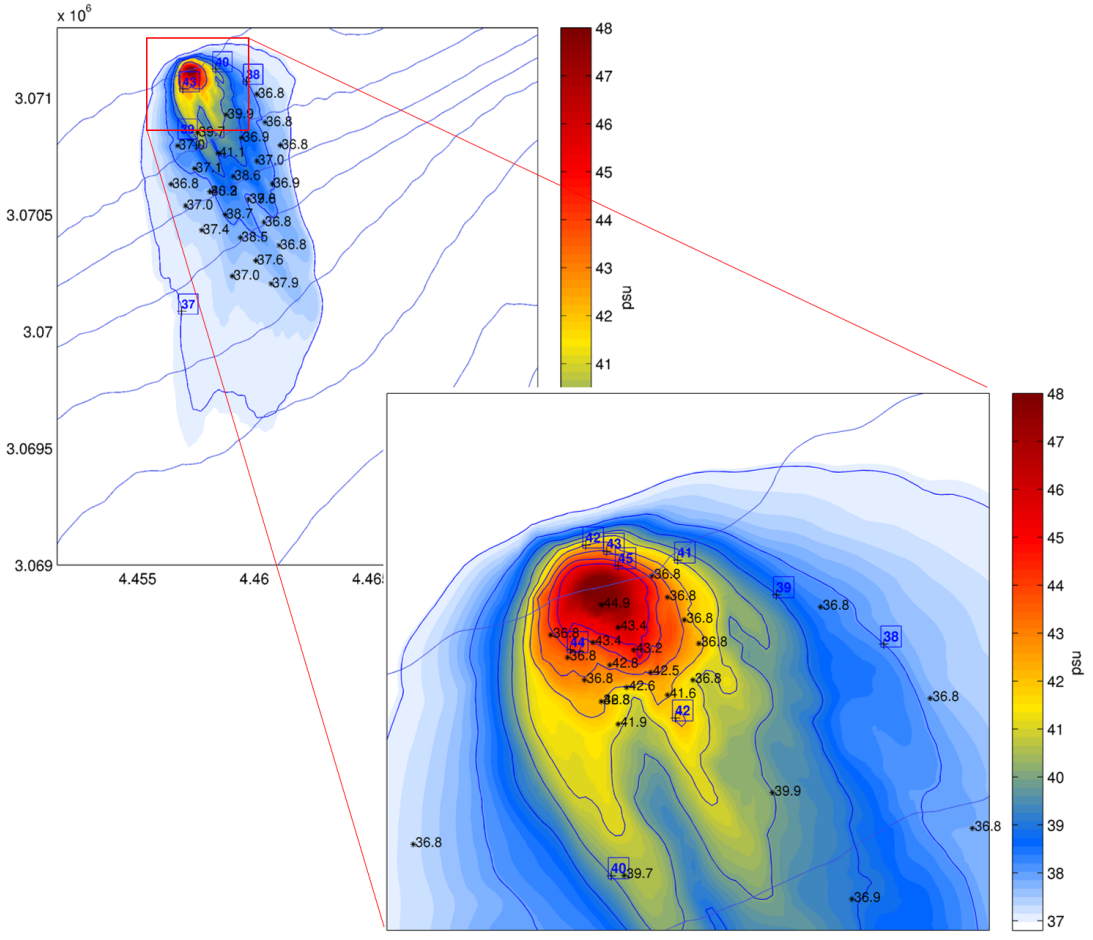

Figure 4.11: Maximum bottom modelled salinity (contours and filled colors) and measurements (asterisks) of scenario *C*7

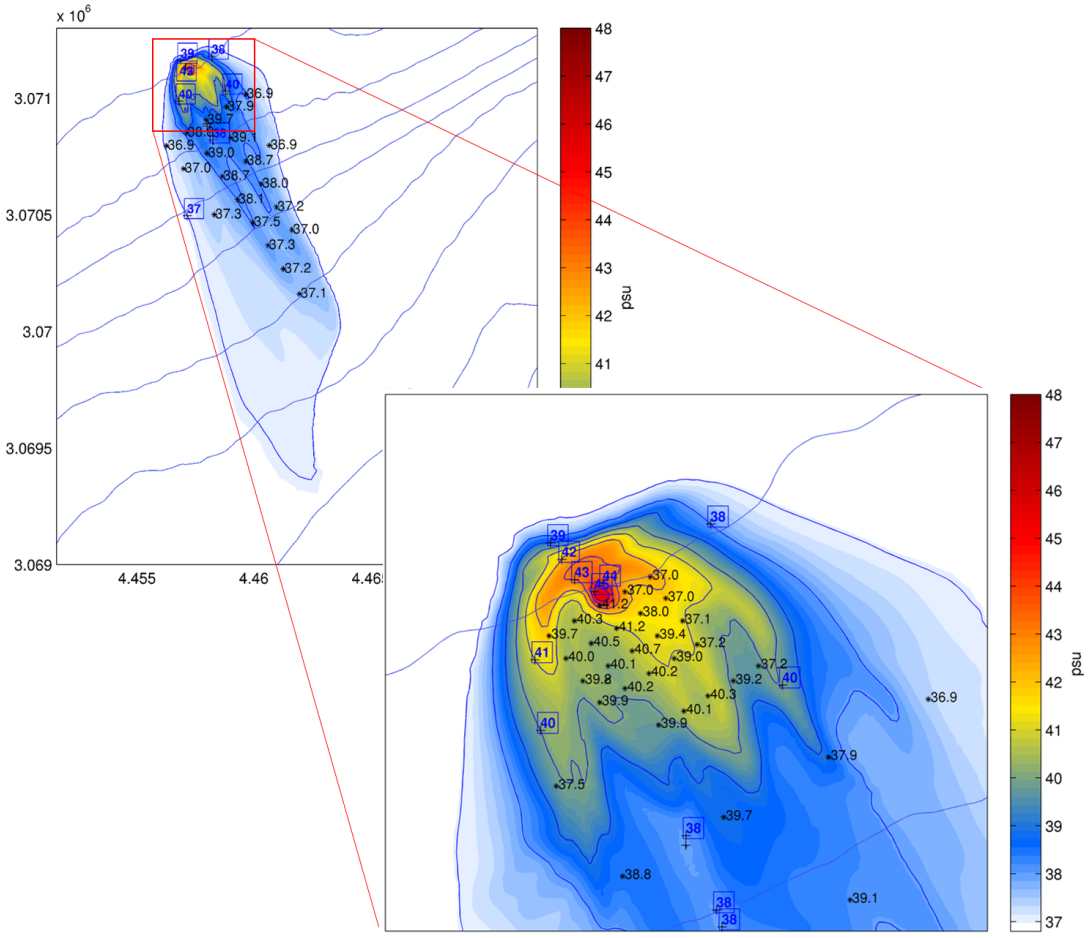

Figure 4.12: Maximum bottom modelled salinity (contours and filled colors) and measurements (asterisks) of scenario *C*6

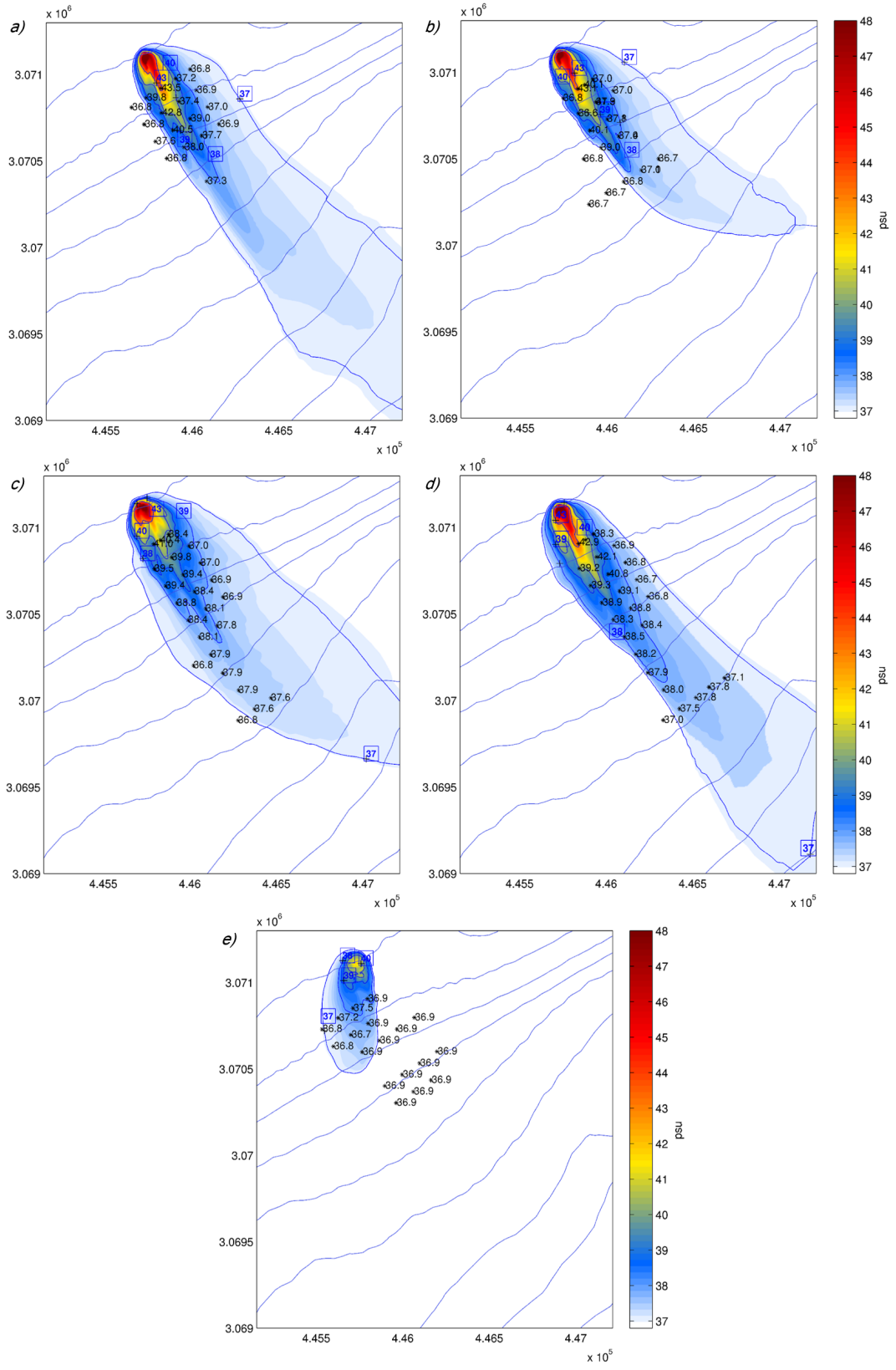

Figure 4.13: Maximum bottom modelled salinity (contours and filled colors) and measurements (asterisks) of scenarios: a) $C1$, b) $C2$, c) $C3$, d) $C4$, e) $C5$

TABLE 4.5: Percentage of the measured values that are inside the corresponding contour line from modelling results

	C1	C2	C3	C4	C5	C6	C7
percentage	86.4	92.5	91.6	93.7	100.0	93.5	92.8

During the campaign *C*4, apart from the bottom velocity measurements, several salinity measurements along the water column in the point with the coordinates [445742,3071082] were gathered by a CTD for a known temporal reference (30/09/2009 08:16-08:17). Figure 4.14a shows the modelled salinity concentration at bed layer for this moment and the point location, and Figure 4.14b shows the quite approximate agreement between the modelled salinity profile and the measured one.

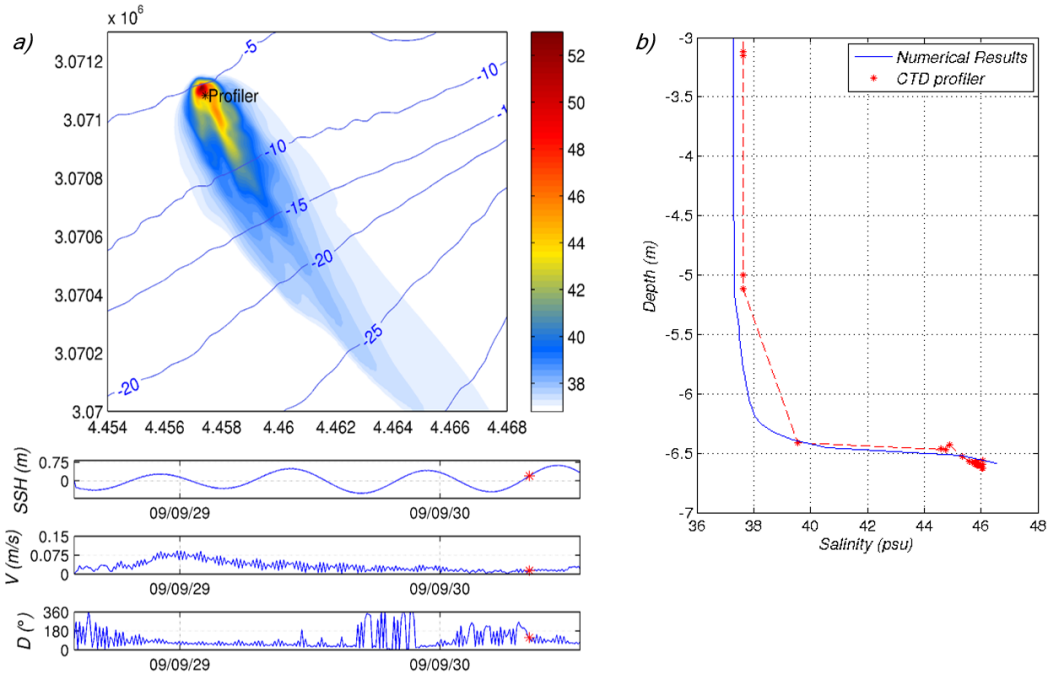

Figure 4.14: a) Modelled salinity concentration at the bottom layer for (30/09/2009 08:16-08:17) instant of scenario *C*4 and the profiler location; b) comparison of the salinity profile between the numeric results and the field measurements

4.4. Conclusions

This work presents a validated numerical methodology to predict the behavior of increasingly common brine discharges through submerged jets. This methodology includes from the preparedness of the desalination plant scenarios and the environmental characterization to the NF modelling and their coupling to the FF modelling. The NF and FF numerical models proposed are the BrIHne tools and TELEMAC-3D, respectively, both of them widely validated in terms of modelling this negatively-buoyant flows (Palomar (2014) and Mahgoub et al. (2015)).

Throughout a set of scenarios that simulate the real discharge conditions specified at several field campaigns of Maspalomas desalination plant (Portillo et al. (2014)), the present methodology steps, from the initial analysis of environmental databases to the visualization of the results, are explained in this work. It is noteworthy that due to the understanding of the importance of the environmental conditions within the FF density current behavior, this work also presents a dynamic downscalling using ROMS-TELEMAC-3D hybrid model to obtain the hydrodynamic characterization of the study area. Thanks to the availability of ambient current measurements during the field campaigns, this downscalling is validated, providing values of $RMSE$ lower than 0.038 m/s of the current velocity.

Finally, since the scope of these field campaigns was to obtain salinity concentration measurements in the brine plume, the modelled salinity footprint results are compared with the field measurements. From these comparisons it can be concluded that the proposed methodology performs quite well in terms of the spatial extent of the density current (both datasets agrees that the extent can reach values up to 1500 meters in favour of the slope) and in terms of the salinity excesses obtained close to and far from the discharge point. In addition, through a set of salinity profile measurements at a certain point and a certain period, the proposed methodology also performs quite well the density current thickness and the distribution of salinity values within the water column. Due to the accurate validation results, it can be concluded that the proposed coupling procedure based on a "passive" strategy, which considers a slot-shaped FF source assumption and follows the recommendations established in Chapter 2, is a suitable coupling procedure for this kind of low-flow negatively-buoyant discharges.

This validated methodology presents a more accurate alternative than other known simplified models based on integral equations such as and the BrIHne-PLUME model and the FF module of CORMIX. The latter approximations only can provide an order of magnitude of the dilution obtained in the FF region, since it takes into account neither the fluctuation of the environmental conditions nor the real bathymetry. Furthermore, the present methodology is an *ad hoc* procedure to study the behavior of these negatively-buoyant discharges, as until now they have been studied through methodologies only validated for positively-buoyant discharges. Thus, this contribution constitutes an advance in predicting brine effluent behavior, which is fundamental in the outfall design phase of a SWRO desalination plant whose objective is to mitigate the negative effects of brine.

Chapter 5

Conclusions and future research

5.1. Summary of contributions

The overall aim of this thesis was to broaden the knowledge of brine effluent's behaviour as well as into their modelling to predict their spacial extent far from the discharge point. This general goal was accomplished by fulfilling the three specific objectives set out in Chapter 1. In this section the main conclusions obtained in pursuit of each objective are summarized:

Objetive 1: To deep into the knowledge of the behaviour of non-confined saline density currents

This specific objective was satisfactorily achieved thanks to the high-quality (with high spatial and temporal resolution) experimental data obtained using PIV and PLIF measurement techniques. In virtue of the detailed examination of flow fields in the planes of symmetry, a global spatial outlook of the behavior of transport and mixing processes of these density currents was obtained:

- The direct analysis of the mean flow fields revealed that the main component (i.e. the horizontal component) of the mean velocity decreases sharply along the non-confined density current due to the influence of friction with the surrounding stagnant fluid, bottom friction and lateral spreading. Velocity turbulent fluctuations present higher values too in the zone close to the

discharge slot, and they rapidly decay downstream of the flow, revealing the collapse of higher length scales of turbulence. Analogous results were shown about concentration fields. Therefore, turbulent mass transport is significantly close to the discharge slot, where the higher Momentum flux takes place, but rapidly decays along the saline current.

- Regarding the vertical structure, mean flow cross profiles revealed that these kinds of flows present self-similarity properties. Concentration shape parameters took values around $S1 : 0.7-0.86$; $S2 : 0.57-0.77$ for the cases tested. These values correspond to supercritical density currents with smooth shape concentration profiles.

- The analysis of the turbulence vertical structure at different downstream locations showed a common zone of minimum turbulence, occurring at the position of maximum velocity. Just below this position, the concentration fluctuation presents its minimum, related to a slow diffusion zone (area with less turbulent mass transport).

- By means of an order of magnitude analysis of the energy exchange, the study density currents (with range of Richardson number from 10^{-1} to 1) revealed a stable stratification with Schmidt numbers close to 1.

- Through the assessment of the longitudinal profiles of maximum values of horizontal mean velocity and mean concentration, the "Normal Status" was observed to be reached at an almost common distance from the source for all the casuistry tested.

- From the "Normal Status", the horizontal mean velocity and the dilution rate (designed as the Normal Entrainment coefficient E_N) reach a quasi-constant value. Since the E_N values obtained agrees well with several existing parameterizations for confined density currents, this study reveals that vertical mixing beyond the "Normal Status" is the main mixing mechanism in the plane of symmetry for non-confined density currents (agreeing with Yuan et al. (2013))

- As a general finding from the comparison among the whole set of density current generated, it can be concluded that steeper slopes (tests within a range from 1% to 4.5%) and higher initial momentum fluxes enhance the dilution. More specifically, the final minimum dilution obtained at the last section of

density currents (S_{minF}) was found to increase around 1.6 times when the Momentum flux was doubled and around 1.6 times for each percentage unit of increment of bottom slope. Contrarily, the S_{minF} was reduced ~ 0.9 times when the Buoyancy flux was tripled.

- A comparison between the three-dimensional integrated equation approximation model proposed by Alavian (1986) and the PIV and PLIF experimental data of the present work shows that this approximation cannot correctly simulate the behavior of these non-confined density currents.

Objetive 2: To establish an optimum numerical set-up to model non-confined saline density currents

Throughout a comprehensive sensitivity analysis to the main numerical aspects and a validation against the experimental data detailed in Chapter 3, this thesis establishes an optimum numerical set-up to model saline density currents with 3D hydrodynamic models. Then, the main numerical guidelines to obtain this set-up for any application are summarized:

- Variable spacing horizontal discretization (e.g. unstructured mesh-grids) is recommended in order to obtain a high resolution near the source. Assuming a slot-shaped source ($b_0 \times h_0$), minimal spacing at least equal to the width of the slot b_0 is needed to ensure the momentum and mass conservation as much as possible.

- In the vertical direction, a high resolution is mandatory to prevent the vertical numerical diffusion. For the type of density currents studied in this work, and considering a slot-shaped source, the vertical spacing has to be at least $h_0/16$. Since this fine resolution cannot be maintained along the whole water column (i.e. there are too many numbers of layers), a gradual vertical spacing with the highest resolution near the bottom (within the density current body) is recommended. In such cases, a sigma-layer coordinate (i.e. terrain-following) in the vertical domain discretization is recommended, in order to keep the finest layers at the bottom.

- Full momentum-source specification is advisable, i.e. both the flow rate and the velocity information ($Q\&V$) should be detailed.

- The hydrostatic hypothesis is considered well assumed for cases over a plain bathymetry since it significantly reduces the computational time ($1.5 \sim 2$ times) and because the equivalent case without the hypothesis does not present significantly improved results.

- The Constant model is recommended as horizontal turbulence closure model ($TCMh$), varying the eddy coefficient values according to the mesh-grid resolution.

- Several vertical turbulence closure model ($TCMv$) can be successfully applied, such as Constant, Mixing-Length or κ-ε models. However, given the demonstrated influential role the $TCMv$ has in the numerical simulation of these flows, a calibration effort for each case study is recommended to be performed. Specifically, for the cases analyzed in this study, the calibrated κ-ε model (empirical constants $c_{3\varepsilon}$ and c_{μ} equal to ~ 0.7 and ~ 0.2, respectively) in conjunction with the most conservative advection scheme for the κ-ε equations, provides the best results. It has to be taken into account that the use of the κ-ε turbulence model, which solves two more equations, is highly demanding in terms of computational time. Both the Mixing Length model and the Constant model can give good approximate results in a more reasonable timeframe for field applications.

The validation results obtained in this study demonstrate that by applying these guidelines, 3D hydrodynamic models can reproduce laboratory-generated density current flows with errors lower than 1.3% for the minimum dilution line and 6% for the maximum velocity line.

Objetive 3: To implement a coupling methodology between NF and FF models

Taking advantage of the existence of validated NF and FF models such as BrIHne and TELEMAC-3D, this thesis presents a numerical methodology to predict the behavior of increasingly common brine discharges through submerged jets. This methodology includes from the preparedness of the desalination plant scenarios and the environmental characterization to the NF modelling and their coupling to the FF modelling.

Finally, the validation of the proposed methodology against concentration measurements in the brine plume generated by the discharge of Maspalomas desalination plant (Canary Island, Spain), demonstrates the applicability of this methodology for studying real field-scale cases. From this validation the following specific conclusions are drawn:

- The dynamic downscalling used to obtain the hydrodynamic characterization of the study area (ROMS-TELEMAC-3D hybrid model) provides values of $RMSE$ lower than 0.038 m/s of the current velocity close to the discharge point.
- Regarding the density current generated in the FF region, the global proposed methodology performs properly in terms of the spatial extent of the density current (both datasets agrees that the extent can reach values up to 1500 meters in favour of the slope) and in terms of the salinity excesses obtained close to and far from the discharge point.
- Throughout a set of salinity profile measurements at a certain point and a certain period, the proposed methodology also performs accurately the density current thickness and the distribution of salinity values within the water column.
- Due to the accurate validation results, it can be concluded that the proposed coupling procedure based on a "passive" strategy, which considers a slot-shaped FF source assumption and which follows the recommendations established in Chapter 2, is a suitable coupling procedure for this kind of low-flow negatively-buoyant discharges.

5.2. Future research

The studies carried out within this thesis have lead to future research topics. Here, some of these challenges are outlined.

Regarding the experimental characterization:

- Having observed that the bathymetry is one of the determining factors in the behaviour evolution of the saline density currents, it would be advisable

to perform additional experiments with a wide range of plain bathymetry slopes and with obstacles that mimic sharp bathymetry gradients sometimes common in marine bottoms.

- For a better understanding of lateral spreading of non-confined saline density currents, the experiments presented in this thesis should be repeated taking PIV-PLIF measurements in perpendicular planes to the plane of symmetry (i.e. perpendicular to the main flow direction). Other option would be to apply three-dimensional PIV-PLIF measurement techniques.

- Taking into account the brine effluent behaviour in both NF and FF region, a set of experiments that cover the NF and the initial part of the FF region under different initial conditions (i.e. both ambient and discharge conditions) should be designed and carried out. Recently, Palomar (2014) and Costa González (2016) studied in detail the intermediate region between NF and FF region (i.e. the spreading layer). However a comprehensive study considering the FF region is still lacking and further efforts are needed to characterize the whole behaviour.

Regarding the FF numerical modelling:

- By performing extra numerical sensitivity tests with a wide range of initial discharge conditions, a general rule based on any significant parameter related to the mixing processes such as Richardson or Péclet numbers should be established to define the minimum horizontal and vertical discretization in the initial region (slot-shaped source).

- Taking into account those regions where large bathymetry gradients can be presented, hence where the numerical diffusion can be mistakenly the governing mixing process within the modelling, further sensitivity tests regarding the horizontal and vertical discretization, the TCMs as well as the assumption of the hydrostatic hypothesis should be carried out.

- To explore the use of flexible vertical meshes that allow the layer locations to evolve in time and space, based on chosen physical variables, such as vertical density gradients. TELEMAC-3D has this option, which is called the Automatic Mesh Redistribution (AMR) method, based on a generalization of the traditional sigma-layer coordinate (Mead et al. (2011)).

- Further sensitivity test considering low-Reynolds number κ-ε TCM (Hwang and Lin (1998)) to improve the modelling of the near-bottom region (Paik et al. (2009)).

Regarding the coupled modelling methodology:

- To conduct a comparative study between "passive" and "active" coupling procedures for several brine discharges with a wide range of flow rates.
- To adapt the proposed methodology to positively-buoyant discharges such as urban waste water discharges and thermal discharges. This way, through a validation effort similar to the previous one, a useful tool would be presented to study human-induced discharges within marine environments.
- Since common 3D-hydrodynamic models such as TELEMAC-3D are robustly coupled with well-known water quality, wave and atmospheric models, the present methodology could be adapted to consider additional environmental conditions within the FF region. If deemed necessary, far beyond the latter adaptation regarding the FF models, a big effort should be done to adapt NF models in order to take into account these new conditions.

Bibliography

Adduce, C., Sciortino, G., Proietti, S., 2012. Gravity Currents Produced by Lock Exchanges: Experiments and Simulations with a Two-Layer Shallow-Water Model with Entrainment. Journal of Hydraulic Engineering 138, 111–121, doi:10.1061/(ASCE)HY.1943-7900.0000484.

Akiyama, J., Stefan, H., 1985. Turbidity Current with Erosion and Deposition. Journal of Hydraulic Engineering 111, 1473–1496, doi:10.1061/(ASCE)0733-9429(1985)111:12(1473).

Alavian, V., 1986. Behavior of Density Currents on an Incline. Journal of Hydraulic Engineering 112, 27–42, doi:10.1061/(ASCE)0733-9429(1986)112:1(27).

Almgren, A.S., Bell, J.B., Szymczak, W.G., 1996. A Numerical Method for the Incompressible Navier-Stokes Equations Based on an Approximate Projection. SIAM Journal on Scientific Computing 17, 358–369, doi:10.1137/S1064827593244213.

Birman, V., Margin, J., Meigurg, E., 2005. The non-Boussinesq lock-exchange problem. Part 2. High-resolution simulations. Journal of Fluid Mechanics 537, 125, doi:10.1017/S0022112005005033.

Bleninger, T., 2006. Coupled 3D hydrodynamic models for submarine outfalls: Environmental hydraulic design and control for multiport diffusers. Ph.D. thesis. University Karlsruhe, Germany.

BOE, 2009. BOE, Orden ARM/3521/2009, de 23 de diciembre, por la que se declaran zonas especiales de conservación los lugares de importancia comunitaria marinos marítimo terrestres de la región Macaronésica de la RedNatura 2000 .

Bombardelli, F.A., García, M.H., 2002. Three-dimensional Hydrodynamic Modeling of Density Current in the Chicago River, Illinois.

Bourban, S.E., 2013. Stratified shallow flow modelling. Ph.D. thesis.

Bournet, P.E., Dartus, D., Tassin, B., Vinçon-Leite, B., 1999. Numerical Investigation of Plunging Density Current. http://dx.doi.org/10.1061/(ASCE)0733-9429(1999)125:6(584) , doi:10.1061/(ASCE)0733-9429(1999)125:6(584).

Bradford, S.F., Katopodes, N.D., Parker, G., 1997. Characteristic of turbid underflows. Journal of Hydraulic Engineering 123(5), 420–431.

Britter, R.E., 1979. The spread of a negatively buoyant plume in a calm environment. Atmospheric Environment - Part A General Topics 13, 1241–1247, doi:10.1016/0004-6981(79)90078-7.

Britter, R.E., Linden, P.F., 1980. The motion of the front of a gravity current travelling down an incline. Journal of Fluid Mechanics 99, 531, doi:10.1017/S0022112080000754.

Britter, R.E., Simpson, J.E., 1978. Experiments on the dynamics of a gravity current head. Journal of Fluid Mechanics 88, 223, doi:10.1017/S0022112078002074.

Brø rs, B.r., Eidsvik, K.J., 1992. Dynamic Reynolds stress modeling of turbidity currents. Journal of Geophysical Research 97, 9645, doi:10.1029/92JC00587.

Buckee, C., BC, K., Peakall, J., 2009. Particulate Gravity Currents. volume 31. Blackwell Publishing Ltd., Oxford, UK, doi:10.1002/9781444304275.

Cánovas Cuenca, J., 2012. Report on water desalination status in the mediterranean countries. Technical Report. Instituto Murciano de Investigación y Desarrollo Agrario y Alimentario. Murcia.

Cantero, M.I., Balachandar, S., Garcia, M.H., Ferry, J.P., 2006. Direct Numerical Simulations of Planar and Cylindrical Density Currents. Journal of Applied Mechanics 73, 923, doi:10.1115/1.2173671.

Cantero, M.I., Lee, J.R., Balachadar, S., Garcia, M.H., 2007. On the front velocity of gravity currents. Journal of Fluid Mechanics 586, 1, doi:10.1017/S0022112007005769.

Cenedese, C., Adduce, C., 2008. Mixing in a density-driven current flowing down a slope in a rotating fluid. Journal of Fluid Mechanics 604, 369–388, doi:10.1017/S0022112008001237.

Cenedese, C., Adduce, C., Cenedese, C., Adduce, C., 2010. A New Parameterization for Entrainment in Overflows. Journal of Physical Oceanography 40, 1835–1850, doi:10.1175/2010JPO4374.1.

Cheung, S., Leung, D., Wang, W., Lee, J., Cheung, V., 2000. VISJET-a computer ocean outfall modelling system, in: Proceedings Computer Graphics International, IEEE Comput. Soc. pp. 75–80, doi:10.1109/CGI.2000.852322.

Choi, K.W., Lee, J.H., 2007. Distributed Entrainment Sink Approach for Modeling Mixing and Transport in the Intermediate Field. Journal of Hydraulic Engineering 133, 804–815, doi:10.1061/(ASCE)0733-9429(2007)133:7(804).

Choi, S.U., 1999. Layer-averaged modeling of two-dimensional turbidity currents with a dissipative-Galerkin finite element method Part II: Sensitivity analysis and experimental verification. Journal of Hydraulic Research 37, 257–271, doi:10.1080/00221689909498310.

Choi, S.U., Garcia, M.H., 1995. Modeling of one-dimensional turbidity currents with a dissipative-Galerkin finite element method. Journal of Hydraulic Research 33, 623–648, doi:10.1080/00221689509498561.

Choi, S.U., Garcia, M.H., 2001. Spreading of Gravity Plumes on an Incline. Coastal Engineering Journal 43, 221–237, doi:10.1142/S0578563401000359.

Choi, S.U., Garcia, M.H., 2002. kϵ Turbulence Modeling of Density Currents Developing Two Dimensionally on a Slope. Journal of Hydraulic Engineering 128, 55–63.

Chowdhury, M.R., Testik, F.Y., 2014. A review of gravity currents formed by submerged single-port discharges in inland and coastal waters. Environmental Fluid Mechanics 14, 265–293, doi:10.1007/s10652-014-9334-7.

Chu, V.H., Jirka, G.H., 1987. Surface buoyant jets and plumes, Encyclopedia of Fluid Mechanics.

Cortés, A., Rueda, F.J., Wells, M.G., 2014. Experimental observations of the splitting of a gravity current at a density step in a stratified water body. Journal of Geophysical Research: Oceans 119, 1038–1053, doi:10.1002/2013JC009304.

Costa González, F., 2016. Estudio en modelo físico de los procesos de mezcla producidos en vertidos hiperdensos y corrientes de gravedad. Ph.D. thesis.

Crimaldi, J.P., 2008. Planar laser induced fluorescence in aqueous flows. Experiments in Fluids 44, 851–863, doi:10.1007/s00348-008-0496-2.

Dallimore, C.J., Hodges, B.R., Imberger, J., 2003. Coupling an Underflow Model to a Three-Dimensional Hydrodynamic Model. Journal of Hydraulic Engineering 129, 748–757, doi:10.1061/(ASCE)0733-9429(2003)129:10(748).

Dallimore, C.J., Imberger, J., Ishikawa, T., 2001. Entrainment and Turbulence in Saline Underflow in Lake Ogawara. Journal of Hydraulic Engineering 127, 937–948, doi:10.1061/(ASCE)0733-9429(2001)127:11(937).

Dawoud, M.A., Al Mulla, M.M., 2012. Environmental Impacts of Seawater Desalination: Arabian Gulf Case Study. International Journal of Environment and Sustainability ISSN 1, 22–37.

Doneker, R.L., Jirka, G.H., 2001. CORMIX-GI systems for mixing zone analysis of brine wastewater disposal. Desalination 139, 263–274, doi:10.1016/S0011-9164(01)00318-6.

Eidsvik, K.J., Brø rs, B.r., 1989. Self-accelerated turbidity current prediction based upon (k) turbulence. Continental Shelf Research 9, 617–627, doi:10.1016/0278-4343(89)90033-2.

Ellison, T.H., Turner, J.S., 1959. Turbulent entrainment in stratified flows. Journal of Fluid Mechanics 6, 423, doi:10.1017/S0022112059000738.

Farrell, G.J., Stefan, H.G., 1988. Mathematical modeling of plunging reservoir flows. Journal of Hydraulic Research 26, 525–537, doi:10.1080/00221688809499191.

Fernandez, R.L., Imberger, J., 2006. Bed roughness induced entrainment in a high Richardson number underflow. Journal of Hydraulic Research 44, 725–738, doi:10.1080/00221686.2006.9521724.

Ferrier, A., Funk, D., Roberts, P., 1993. Application of optical techniques to the study of plumes in stratified fluids. Dynamics of Atmospheres and Oceans 20, 155–183, doi:10.1016/0377-0265(93)90052-9.

Firoozabadi, B., Afshin, H., Aram, E., 2009. Three-Dimensional Modeling of Density Current in a Straight Channel. Journal of Hydraulic Engineering 135, 393–402, doi:10.1061/(ASCE)HY.1943-7900.0000026.

Fischer, H.B., 1979. Mixing in inland and coastal waters. Academic Press.

Frick, W., 2004. Visual Plumes mixing zone modeling software. U.S. Environmental Protection Agency Papers .

Fukuoka, S. and Fukushima, Y., 1980. Reservoir, On Dynamic Behavior of the Head of the Gravity Current in a Stratified, in: Proc. Second Int. Symp. Stratified Flow, IAHR, 1, pp. 224–227.

Garcia, M.H., 1993. Hydraulic Jumps in Sediment Driven Bottom Currents. Journal of Hydraulic Engineering 119, 1094–1117, doi:10.1061/(ASCE)0733-9429(1993)119:10(1094).

Garcia, M.H., Parsons, J.D., 1996. Mixing at the front of gravity currents. Dynamics of Atmospheres and Oceans 24, 197–205, doi:10.1016/0377-0265(95)00442-4.

Garcia Alba, J., 2011. Estudio de chorros turbulentos con modelos CFD: Aplicación en el diseño de emisarios submarinos. Ph.D. thesis, doi:10.13140/RG.2.1.3592.0729.

Gerber, G., Diedericks, G., Basson, G.R., 2011. Particle Image Velocimetry Measurements and Numerical Modeling of a Saline Density Current. Journal of Hydraulic Engineering 137, 333–342, doi:10.1061/(ASCE)HY.1943-7900.0000304.

Gerhard H. Jirka, Abrahan, G. and Harleman, D., 1976. An assessment of techniques for hydrothermal prediction (1976 edition) — Open Library, in: Department of Civil Engineering, MIT for U.S. Nuclear Regulatory Commision, Cambridge.

Gray, T.E., Alexander, J., Leeder, M.R., 2006. Longitudinal flow evolution and turbulence structure of dynamically similar, sustained, saline density and turbidity currents. Journal of Geophysical Research 111, C08015, doi:10.1029/2005JC003089.

Gungor, E., Roberts, P.J.W., 2009. Experimental Studies on Vertical Dense Jets in a Flowing Current. Journal of Hydraulic Engineering 135, 935–948, doi:10.1061/(ASCE)HY.1943-7900.0000106.

Härtel, C., Meiburg, E., Necker, F., 2000. Analysis and direct numerical simulation of the flow at a gravity-current head. Part 1. Flow topology and

front speed for slip and no-slip boundaries. Journal of Fluid Mechanics 418, S0022112000001221, doi:10.1017/S0022112000001221.

Hebbert, B., Patterson, J., Loh, I., Imberger, J., 1979. Collie River Underflow into the Wellington Reservoir. Journal of the Hydraulics Division 105, 533–545.

Heller, V., 2011. Scale effects in physical hydraulic engineering models. Journal Journal of Hydraulic Research 493, 22–1686, doi:10.1080/00221686.2011.578914.

Hervouet, J.M., 2007. Hydrodynamics of free surface flows : modelling with the finite element method. Wiley.

Hodges, B.R., Furnans, J.E., Kulis, P.S., 2011. Thin-Layer Gravity Current with Implications for Desalination Brine Disposal. Journal of Hydraulic Engineering 137, 356–371, doi:10.1061/(ASCE)HY.1943-7900.0000310.

Hossain, M.S., Rodi, W., 1982. Turbulent buoyant jets and plumes. Pergamon Press.

Hosseini, S., Shamsai, a., Ataie-Ashtiani, B., 2006. Synchronous measurements of the velocity and concentration in low density turbidity currents using an Acoustic Doppler Velocimeter. Flow Measurement and Instrumentation 17, 59–68, doi:10.1016/j.flowmeasinst.2005.05.002.

Huppert, H.E., 2006. Gravity currents: a personal perspective. Journal of Fluid Mechanics 554, 299, doi:10.1017/S002211200600930X.

Huppert, H.E., Simpson, J.E., 2006. The slumping of gravity currents. Journal of Fluid Mechanics 99, 785, doi:10.1017/S0022112080000894.

Hwang, C.B., Lin, C.A., 1998. Improved Low-Reynolds-Number k Model Based on Direct Numerical Simulation Data. AIAA Journal 36, 38–43, doi:10.2514/2.349.

Hydraulics, W., 2005. Delft3D-FLOW users manual, v 3.12. Technical Report. WL—Delft Hydraulics. Delft, The Netherlands.

Hydraulics Delft, 2001. Delft3d user interface. Capabilities and applications.

Imran, J., Parker, G., Katopodes, N., 1998. A numerical model of channel inception on submarine fans. Journal of Geophysical Research: Oceans 103, 1219–1238, doi:10.1029/97JC01721.

Islam, M.A., Imran, J., 2010. Vertical structure of continuous release saline and turbidity currents. Journal of Geophysical Research 115, C08025, doi:10.1029/2009JC005365.

Jirka, G.H., 2004. Integral Model for Turbulent Buoyant Jets in Unbounded Stratified Flows. Part I: Single Round Jet. Environmental Fluid Mechanics 4, 1–56, doi:10.1023/A:1025583110842.

Jirka, G.H., 2006. Integral Model for Turbulent Buoyant Jets in Unbounded Stratified Flows Part 2: Plane Jet Dynamics Resulting from Multiport Diffuser Jets. Environmental Fluid Mechanics 6, 43–100, doi:10.1007/s10652-005-4656-0.

Joseph Boussinesq, 1877. Essai sur la théorie des eaux courantes. Mémoire présenté par divers savants à l'Académie des Sciences de Paris. Paris.

Kashefipour, S., Kooti, F., Ghomeshi, M., 2010. Effect of reservoir bed slope and density current discharge on water entrainment.

Kneller, B.C., Bennett, S.J., McCaffrey, W.D., 1999. Velocity structure, turbulence and fluid stresses in experimental gravity currents. Journal of Geophysical Research 104, 5381, doi:10.1029/1998JC900077.

Kulis, P., Hodges, B.R., 2006. Modeling gravity currents in shallow bays using a sigma coordinate model, in: The 7th Int. Conf. on Hydroscience and Engineering, Philadelphia, USA.

Kurganov, A., Petrova, G., 2007. A second-order well-balanced positivity preserving central-upwind scheme for the Saint-Venant system 5, 133–160.

La Rocca, M., Adduce, C., Sciortino, G., Pinzon, A.B., 2008. Experimental and numerical simulation of three-dimensional gravity currents on smooth and rough bottom. Physics of Fluids 20, 106603, doi:10.1063/1.3002381.

La Rocca, M., Adduce, C., Sciortino, G., Pinzon, A.B., Boniforti, M.A., 2012. A two-layer, shallow-water model for 3D gravity currents. Journal of Hydraulic Research 50, 208–217, doi:10.1080/00221686.2012.667680.

La Rocca, M., Pinzon, A.B., 2010. Experimental and Theoretical Modelling of 3D Gravity Currents, in: Numerical Simulations - Examples and Applications in Computational Fluid Dynamics. InTech, doi:10.5772/13251.

Laspidou, C., Hadjibiros, K., Gialis, S., 2010. Minimizing the Environmental Impact of Sea Brine Disposal by Coupling Desalination Plants with Solar Saltworks: A Case Study for Greece. Water 2, 75–84, doi:10.3390/w2010075.

Lattemann, S., Höpner, T., 2008. Environmental impact and impact assessment of seawater desalination. Desalination 220, 1–15, doi:10.1016/j.desal.2007.03.009.

Launder, B.E., Morse, A., Rodi, W., Spalding, D.B., 1973. Prediction of free shear flows: A comparison of the performance of six turbulence models .

Launder, B.E., Spalding, D.B., 1974. The numerical computation of turbulent flows. Computer Methods in Applied Mechanics and Engineering , 269–289.

Liao, Q., Cowen, E., 2010. Relative dispersion of a scalar plume in a turbulent boundary layer. Journal of Fluid Mechanics 661, 412–445, doi:10.1017/S0022112010003058.

LNHE, N.H., Laboratory, E., 2007. Telemac Modelling System: Telemac-3D Code, Operating manual [online].

Lowe, R.J., Rottman, J.W., Linden, P.F., 2005. The non-Boussinesq lock-exchange problem. Part 1. Theory and experiments. Journal of Fluid Mechanics 537, 101, doi:10.1017/S0022112005005069.

MacDonald, D.G., Chen, F., 2012. Enhancement of turbulence through lateral spreading in a stratified-shear flow: Development and assessment of a conceptual model. Journal of Geophysical Research: Oceans 117, doi:10.1029/2011JC007484.

Madsen, P., Rugbjerg, M., Warren, I., 1988. Subgrid modelling in depth intergrated flows, in: 21st Coastal Engineering Conference, ASCE, New York. pp. 505–5011.

Mahgoub, M., Hinkelmann, R., Rocca, M.L., 2015. Three-dimensional non-hydrostatic simulation of gravity currents using TELEMAC3D and comparison of results to experimental data. Progress in Computational Fluid Dynamics, An International Journal 15, 56, doi:10.1504/PCFD.2015.067325.

Martin, J.E., Garcia, M.H., 2008. Combined PIV/PLIF measurements of a steady density current front. Experiments in Fluids 46, 265–276, doi:10.1007/s00348-008-0556-7.

Maxworthy, T., Nokes, R.I., 2007. Experiments on gravity currents propagating down slopes. Part 1. The release of a fixed volume of heavy fluid from an enclosed lock into an open channel. Journal of Fluid Mechanics 584, 433, doi:10.1017/S0022112007006702.

Mead, C., Bourban, S., Cawthorn, C., Turnbull, M., 2011. The importance of model plane location and movement in dense discharge assessment .

Menendez, M., García-Díez, b.M., Fita, b.L., Fernández, b.J., Méndez, b.F.J., Gutiérrez, b.J.M., . High-resolution sea wind hindcasts over the Mediterranean area , doi:10.1007/s00382-013-1912-8.

Morton, B.R., Taylor, G., Turner, J.S., 1956. Turbulent Gravitational Convection from Maintained and Instantaneous Sources. Proceedings of the Royal Society A: Mathematical, Physical and Engineering Sciences 234, 1–23, doi:10.1098/rspa.1956.0011.

Munk, W., Anderson, E., 1948. Notes on a theory of the thermocline. Journal of Marine Research 3, 276–295.

Nezu, I., Nakagawa, H., 1993. Turbulence in Open Channel Flows (IAHR Monographs): Amazon.es: Hiroji Nakagawa, Iehisa Nezu: Libros en idiomas extranjeros, in: IAHR monograph series, Balkema.

Nikiforakis, I., Stamou, A., 2015. Integrated modelling for the discharge of brine from desalination plants into coastal waters. Desalination and Water Treatment 53, 3214–3223, doi:10.1080/19443994.2014.933629.

Nogueira, H.I.S., Adduce, C., Alves, E., Franca, M.J., 2014. Dynamics of the head of gravity currents. Environmental Fluid Mechanics 14, 519–540, doi:10.1007/s10652-013-9315-2.

Nokes, R., McBryde, J., Davidson, M., Allis, M., 2010. Modelling the front conditions of rigid boundary gravity currents, in: 6th International Symposium on Environmental Hydraulics, Athens. pp. 183–188.

OJEC, 2002. OJEC, Official journal of the European Communities 9.1.2002 (L 5/16) adopting the list of sites of Community importance for the Macaronesian biogeographical region, pursuant to Council Directive 92/43/EEC .

Oliver, C.J., Davidson, M.J., Nokes, R.I., 2008. kϵ Predictions of the initial mixing of desalination discharges. Environmental Fluid Mechanics 8, 617–625, doi:10.1007/s10652-008-9108-1.

Ottolenghi, L., Adduce, C., Inghilesi, R., Roman, F., Armenio, V., 2016. Mixing in lock-release gravity currents propagating up a slope. Physics of Fluids 28, 056604, doi:10.1063/1.4948760.

Özgökmen, T.M., Chassignet, E.P., 2002. Dynamics of Two-Dimensional Turbulent Bottom Gravity Currents. Journal of Physical Oceanography 32, 1460–1478, doi:10.1175/1520-0485(2002)032<1460:DOTDTB>2.0.CO;2.

Paik, J., Eghbalzadeh, A., Sotiropoulos, F., 2009. Three-Dimensional Unsteady RANS Modeling of Discontinuous Gravity Currents in Rectangular Domains. Journal of Hydraulic Engineering 135, 505–521, doi:10.1061/(ASCE)HY.1943-7900.0000034.

Palomar, P., 2014. Experimental and Numerical optimization of brine discharges in the marine environment. Ph.D. thesis. Universidad de Cantabria.

Palomar, P., Lara, J., Losada, I., 2012a. Near field brine discharge modeling part 2: Validation of commercial tools. Desalination 290, 28–42, doi:10.1016/j.desal.2011.10.021.

Palomar, P., Lara, J., Losada, I., Rodrigo, M., Alvárez, A., 2012b. Near field brine discharge modelling part 1: Analysis of commercial tools. Desalination 290, 14–27, doi:10.1016/j.desal.2011.11.037.

Palomar, P., Lara, J., Losada, I., Tarrade, L., 2013. Numerical modeling of brine discharge: commercial models, MEDVSA online simulation tools and advanced computational fluid dynamics. Desalination and Water Treatment 51, 543–559, doi:10.1080/19443994.2012.714625.

Papakonstantis, I.G., Christodoulou, G.C., 2010. Spreading of round dense jets impinging on a horizontal bottom. Journal of Hydro-environment Research 4, 289–300, doi:10.1016/j.jher.2010.07.001.

Parker, G., Fukushima, Y., Pantin, H.M., 1986. Self-accelerating turbidity currents. Journal of Fluid Mechanics 171, 145, doi:10.1017/S0022112086001404.

Parker, G., Garcia, M., Fukushima, Y., Yu, W., 1987. Experiments on turbidity currents over an erodible bed. Journal of Hydraulic Research 25, 123–147, doi:10.1080/00221688709499292.

Patterson, M.D., Simpson, J.E., Dalziel, S.B., van Heijst, G.J.F., 2006. Vortical motion in the head of an axisymmetric gravity current. Physics of Fluids 18, 046601, doi:10.1063/1.2174717.

Patterson, M.D., Simpson, J.E., Dalziel, S.B., Nikiforakis, N., 2005. Numerical modelling of two-dimensional and axisymmetric gravity currents. International Journal for Numerical Methods in Fluids 47, 1221–1227, doi:10.1002/fld.841.

Pérez-Díaz, B., Castanedo, S., Palomar, P., 2017a. Modelling non-confined density currents using 3D hydrodynamic models: finding the key numerical guidelines. (Under Review) .

Pérez-Díaz, B., Palomar, P., Castanedo, S., 2016a. PIV-PLIF characterization of density currents, in: 4th IAHR Europe Congress, Liege, Blegium. pp. 174–178, doi:10.1201/b21902-34.

Pérez-Díaz, B., Palomar, P., Castanedo, S., 2017b. PIV-PLIF global characterization of non-confined saline density currents under different flow conditions. Journal of Geophysical Research: Oceans (Under Review) .

Pérez-Díaz, B., Palomar, P., Castanedo, S., Álvarez, A., 2016b. Caracterización experimental del campo lejano de los vertidos de salmuera al mar. RIBAGUA - Revista Iberoamericana del Agua 3, 66–75, doi:10.1016/j.riba.2016.07.003.

Plumb, B.R., 2008. Modelling of Desalination Plant Outfall Sedimentation. Ph.D. thesis. School of Aeronautical, Civil and Mechanical Engineering, UNSW@ADFA, ACT 2610.

Portillo, E., Ruiz de la Rosa, M., Louzara, G., Quesada, J., Ruiz, J., Mendoza, H., 2014. Dispersion of desalination plant brine discharge under varied hydrodynamic conditions in the south of Gran Canaria. Desalination and Water Treatment 52, 164–177, doi:10.1080/19443994.2013.795349.

Princevac, M., Fernando, H.J.S., Whiteman, C.D., 2005. Turbulent entrainment into natural gravity-driven flows. Journal of Fluid Mechanics 533, 259–268, doi:10.1017/S0022112005004441.

Roberts, P.J.W., Ferrier, A., Daviero, G., 1997. Mixing in Inclined Dense Jets. Journal of Hydraulic Engineering 123, 693–699, doi:10.1061/(ASCE)0733-9429(1997)123:8(693).

Roberts, P.J.W., Toms, G., 1987. Inclined Dense Jets in Flowing Current. Journal of Hydraulic Engineering 113, 323–340, doi:10.1061/(ASCE)0733-9429(1987)113:3(323).

Robinson, D., Wood, M., Piggott, M., Gorman, G., 2016. CFD modelling of marine discharge mixing and dispersion. Journal of Applied Water Engineering and Research 4, 152–162, doi:10.1080/23249676.2015.1105157.

Rodi, W., 1972. The prediction of free turbulent boundary layers by use of a two-equation model of turbulence. Ph.D. thesis. Imperial College London. University of London.

Rodi, W., 1975. A Note on the Empirical Constant in the Kolmogorov-Prandtl Eddy-Viscosity Expression. Journal of Fluids Engineering 97, 386, doi:10.1115/1.3447325.

Rodi, W., 1984. Turbulence models and their application in hydraulics : a state of the art review. Technical Report. International Association for Hydraulic Research (Section on Hydraulics Instrumentation). Delft, The Netherlands.

Rodi, W., 1987. Examples of calculation methods for flow and mixing in stratified fluids. Journal of Geophysical Research 92, 5305, doi:10.1029/JC092iC05p05305.

Rodi, W., Chow, W., 1980. Turbulence Models and Their Application in Hydraulics. CRC Press.

Roelvink, J., Van Banning, G., 1994. Design and Development of DELFT3D and Application to Coastal Morphodynamics, in: International Association for Hydraulic Research in Hydroinformatics, pp. 451–456.

Sánchez-Lizaso, J.L., Romero, J., Ruiz, J., Gacia, E., Buceta, J.L., Invers, O., Fernández Torquemada, Y., Mas, J., Ruiz-Mateo, A., Manzanera, M., 2008. Salinity tolerance of the Mediterranean seagrass Posidonia oceanica: recommendations to minimize the impact of brine discharges from desalination plants. Desalination 221, 602–607, doi:10.1016/j.desal.2007.01.119.

Sequeiros, O.E., 2012. Estimating turbidity current conditions from channel morphology: A Froude number approach. Journal of Geophysical Research: Oceans 117, n/a–n/a, doi:10.1029/2011JC007201.

Sequeiros, O.E., Spinewine, B., Beaubouef, R.T., Sun, T., García, M.H., Asce, M., Parker, G., 2010. Characteristics of Velocity and Excess Density Profiles of Saline Underflows and Turbidity Currents Flowing over a Mobile Bed. J. Hydraul. Eng 13600, 7–412, doi:10.1061/(ASCEE)HY.1943-7900.0000200.

Shao, D., Law, A.W., Li, H., 2008. Brine discharges into shallow coastal waters with mean and oscillatory tidal currents. Journal of Hydro-environment Research 2, 91–97, doi:10.1016/j.jher.2008.08.001.

Shchepetkin, A.F., McWilliams, J.C., 2005. The regional oceanic modeling system (ROMS): a split-explicit, free-surface, topography-following-coordinate oceanic model. Ocean Modelling 9, 347–404, doi:10.1016/j.ocemod.2004.08.002.

Simpson, J.E., 1982. Gravity Currents in the Laboratory, Atmosphere, and Ocean. Annual Review of Fluid Mechanics 14, 213–234, doi:10.1146/annurev.fl.14.010182.001241.

Simpson, J.E., 1997. Gravity currents: the environment and the laboratory. Cambridge Univ. Press, doi:10.2277/0521561094.

Smagorinsky, J., 1963. General circulation experiments with the primitive equations. Monthly Weather Review 91, 99–164, doi:10.1175/1520-0493(1963)091<0099:GCEWTP>2.3.CO;2.

Smyth, W.D., Moum, J.N., 2000. Length scales of turbulence in stably stratified mixing layers. Physics of Fluids 12, 1327, doi:10.1063/1.870385.

Sotillo, M.G., Cailleau, S., Lorente, P., Levier, B., Aznar, R., Reffray, G., Amo-Baladrón, A., Chanut, J., Benkiran, M., Alvarez-Fanjul, E., 2015. The MyOcean IBI Ocean Forecast and Reanalysis Systems: operational products and roadmap to the future Copernicus Service. Journal of Operational Oceanography 0, doi:10.1080/1755876X.2015.1014663.

Stacey, M.W., Bowen, A.J., 1988a. The vertical structure of density and turbidity currents: Theory and observations. Journal of Geophysical Research 93, 3528, doi:10.1029/JC093iC04p03528.

Stacey, M.W., Bowen, A.J., 1988b. The vertical structure of turbidity currents and a necessary condition for self-maintenance. Journal of Geophysical Research 93, 3543, doi:10.1029/JC093iC04p03543.

Stamou, A.I., Nikiforakis, I.K., 2013. Integrated modelling of single port, steady-state thermal discharges in unstratified coastal waters. Environmental Fluid Mechanics 13, 309–336, doi:10.1007/s10652-012-9266-z.

Strang, E.J., Fernando, H.J.S., 2001. Entrainment and mixing in stratified shear flows. Journal of Fluid Mechanics 428, 349–386, doi:10.1017/S0022112000002706.

Tennekes, H., Lumley, J.L., 1972. A First Course in Turbulence. MIT Press.

Tsihrintzis, V.a., Alavian, V., 1996. Spreading of three-dimensional inclined gravity plumes. Journal of Hydraulic Research 34, 695–711, doi:10.1080/00221689609498466.

Turner, J.S., 1973. Buoyancy Effects in Fluids. Cambridge University Press, Cambridge, doi:10.1017/CBO9780511608827.

Turner, J.S., 1986. Turbulent entrainment: the development of the entrainment assumption, and its application to geophysical flows. Journal of Fluid Mechanics 173, 431, doi:10.1017/S0022112086001222.

Ungarish, M., 2007a. A shallow-water model for high-Reynolds-number gravity currents for a wide range of density differences and fractional depths. Journal of Fluid Mechanics 579, 373, doi:10.1017/S0022112007005484.

Ungarish, M., 2007b. Axisymmetric gravity currents at high Reynolds number: On the quality of shallow-water modeling of experimental observations. Physics of Fluids 19, 036602, doi:10.1063/1.2714990.

Ungarish, M., 2008. Energy balances and front speed conditions of two-layer models for gravity currents produced by lock release. Acta Mechanica 201, 63–81, doi:10.1007/s00707-008-0073-z.

Viollet, P.L., 1988. On the Numerical Modelling of Stratified Flows, in: Physical Processes in Estuaries. Springer Berlin Heidelberg, Berlin, Heidelberg, pp. 257–277, doi:10.1007/978-3-642-73691-9_14.

Wells, M., Cenedese, C., Caulfield, C.P., 2010. The Relationship between Flux Coefficient and Entrainment Ratio in Density Currents. Journal of Physical Oceanography 40, 2713–2727, doi:10.1175/2010JPO4225.1.

Westerweel, J., 1993. Digital Particle Image Velocimetry - Theory and Application. Ph.D. thesis. Delft University.

Willert, C., 1996. The fully digital evaluation of photographic PIV recordings. Applied Scientific Research 56, 79–102, doi:10.1007/BF02249375.

Wood, M., Henno, F., Mead, C., 2014. Validation of computational models for hypersaline and other dense marine discharges, in: 7th International Symposium on Environmental Hydraulics, 5-7 January, Singapore.

Yuan, Y., Horner-Devine, A.R., Yuan, Y., Horner-Devine, A.R., 2013. Laboratory Investigation of the Impact of Lateral Spreading on Buoyancy Flux in a River Plume. Journal of Physical Oceanography 43, 2588–2610, doi:10.1175/JPO-D-12-0117.1.

Zhang, X.Y., Adams, E.E., 1999. Prediction of Near Field Plume Characteristics Using Far Field Circulation Model. Journal of Hydraulic Engineering 125, 233–241, doi:10.1061/(ASCE)0733-9429(1999)125:3(233).

Zhang, Y., Baptista, A.M., 2008. SELFE: A semi-implicit Eulerian–Lagrangian finite-element model for cross-scale ocean circulation. Ocean Modelling 21, 71–96, doi:10.1016/j.ocemod.2007.11.005.